Wave modulation by strong currents: A study in the Lofoten Maelstrom and surrounding areas.

Trygve Halsne

Thesis for the degree of Philosophiae Doctor (PhD)
University of Bergen, Norway
2024

UNIVERSITY OF BERGEN

Wave modulation by strong currents: A study in the Lofoten Maelstrom and surrounding areas.

Trygve Halsne

Thesis for the degree of Philosophiae Doctor (PhD)
at the University of Bergen

Date of defense: 07.06.2024

Year: 2024

Title: Wave modulation by strong currents: A study in the Lofoten Maelstrom and surrounding areas.

Name: Trygve Halsne

Print: Skipnes Kommunikasjon / University of Bergen

Scientific environment

This study is carried out at the Geophysical Institute, University of Bergen, and in the Division for Maritime Meteorology and Oceanography at the Norwegian Meteorological Institute (MET Norway), in Bergen, Norway. The author has been enrolled in the Norwegian Research School on Changing Climates in the coupled Earth System (CHESS) throughout the period. Parts of the research was also carried during a three month exchange at the Institute of Marine Sciences in Venice, Italy, partly funded by the EU Erasmus+ scholarship, under the guidance of Dr. Alvise Benetazzo. The work presented herein have been conducted under the supervision of Prof. Øyvind Breivik at the University of Bergen and MET Norway, and Prof. Kai Håkon Christensen at the University of Oslo and MET Norway. Project related work have included data management activities related to Copernicus Sentinel data within the Division of Remote Sensing and Data Management at MET Norway under Dr. Øystein Godøy.

CHESS
Research school on changing climates in the coupled earth system

UNIVERSITAS BERGENSIS

Norwegian Meteorological Institute

Acknowledgements

First and foremost, I want to thank my supervisors Øyvind and Kai: It has been a true pleasure to collaborate with both of you! To some extent, it is true when I say that I chose supervisors before choosing topic. You both possess a very strong physical intuition, which has been very helpful when I've been lost in the equations. More importantly, you have recognized that this PhD project has been carried out in combination with a (more important) family project. In that context, you have helped me to balance and invest in both.

A Big (yes, with a capital) thanks goes to my leader Øystein for giving me the opportunity to follow my research interests, and for your always positive attitude—it is very much appreciated! Further, I would like to thank all my co-authors, which have encouraged me and provided me constructive feedback throughout the paper-writing process. A special thanks goes to Ana for running the WAM models that have been used extensively throughout the thesis and to Øyvind Sætra for constructive discussions. Moreover, I want to express my gratitude to the wave people at ISMAR in Venice, in particular to Alvise Benetazzo and Francesco Barbariol, for your hospitality and fruitful discussions during my research stay. Furthermore, to all my great colleagues at MET Norway and GFI Bergen: Thanks for being so positive, helpful, and cheering.

To some extent, this thesis is a result of a larger system that proves to work: Ever since I started at MET Norway, I have been surrounded by leaders and colleagues that have been flexible, encouraging, and constructive, such that a layman like me, with family and kids, have been able to seamlessly conduct a PhD project within a governmental institution. So, this is a thanks to the public system(s) of Norway, or in broader terms to the democracy, that actually works pretty well!

To my family and friends who have followed me closely during this process: Your cheering and support have been very much appreciated! So has your questions about what I've been doing and, in particular, the perseverance you have shown when I have told you this "very interesting story" on how currents affect ocean waves. Martin: We almost reached the Maelstrom by boat (thanks!), but the weather prevented us to go further. To my parents, close family, and in–laws: Thank you for being who you are, and for teaching me the important lessons in life. By the grace of God, I am lucky to have you all in my life. Finally, to my beloved wife Katrine and my children Filip, Oline, and Jakob: You are my favorite crew. So let's leave this (boring) book and go out to see some waves!

Trygve Halsne
Bergen, 2024-03-20

"The Maelstrom!" they cried. "The Maelstrom!"

Jules Verne 1869

Abstract

Ocean waves and currents—ubiquitous features of the sea—are in a constant state of mutual interaction, which causes strongly inhomogeneous sea states. Their interplay regulates air–sea interaction processes in space, time, and magnitude and also poses a threat to marine activities because of, for example, substantial wave height modulations. The imprint of currents on the sea state is still not properly understood, largely due to the lack of observations. The research presented in this thesis aims to understand the current-induced physical processes that modulate the sea state, and the degree to which it changes. Furthermore, the aim is to evaluate the reliability of sea state predictions by spectral wave models including current forcing in realistic, energetic, flow fields.

These aspects are quantified in a very strong tidal current in northern Norway—namely the Lofoten Maelstrom—and its surrounding coastal area. A set of conventional, and unconventional, metrics for validation have been utilized; this includes novel in situ observations of waves, currents, and wave breaking-induced air bubble penetration depths, as well as satellite remote sensing observations, in addition to local knowledge. These assets have been carefully evaluated against a range of modeling tools, including high-resolution spectral wave models both with and without surface current forcing, in combination with order-of-magnitude estimates.

The Lofoten Maelstrom strongly modulates the sea state. This includes the wave breaking statistics, wave heights (up to 90 % increase), directional spectrum, as well as the short-term extreme wave statistics (up to 15 % increase). Both in the Maelstrom and the coastal area of northern Norway surrounding it, the wave–current interaction mechanisms include local and non-local effects. These take place over a range of spatio-temporal scales that are closely related to the flow field dynamics and wave conditions. Such variability is mapped out using a novel diagnostic method. The modeling results agree well with the available observations, in particular the wave spectrum modulations. However, more observations are needed to draw even more firm conclusions on the effect of currents on waves, which, by nature, is a strongly inhomogeneous problem in both the temporal and horizontal domain.

Sammendrag

Bølger og strøm – allestedsnærværende trekk ved havet – er i en konstant tilstand av gjensidig vekselvirkning. Disse prosessene forårsaker sterkt inhomogene sjøtilstander. Samspillet dem imellom regulerer utvekslingsprosesser mellom hav og atmosfære i både tid, rom, og omfang. Bølge-strøm veskelvirkninger utgjør også en trussel for maritime aktiviteter på grunn av, eksempelvis, betydelige modulasjoner av bølgehøyden. Det er fortsatt stor usikkerhet knyttet til hvor stort avtrykk strømmen setter på bølgefeltet, som i stor grad skyldes mangel på observasjoner. Formålet med denne oppgaven er å forstå de strøm-induserte fysiske prosessene som modulerer bølgefeltet, og i hvilken grad bølgefeltet endres. Målet er også å evaluere påliteligheten til bølgeprognoser fra spektrale bølgemodeller med strøm-pådrag i realistiske og energiske strømningsfelt.

Disse aspektene er analysert i en svært kraftig tidevannsstrøm i Nord-Norge – nemlig Moskstraumen – samt i det omkringliggende kystområdet. Et bredt utvalg av konvensjonelle og ukonvensjonelle metoder er blitt brukt i valideringsarbeidet. Blant annet: Særegne in situ-observasjoner av bølger, strøm og dybden til luftbobler injisert via brytende bølger, fjernmålings-observasjoner fra satellitt, og lokal kunnskap. Disse har blitt nøye evaluert mot en rekke modelleringsverktøy, som høyoppløselige spektrale bølgemodeller både med og uten strøm-pådrag, i kombinasjon med størrelsesorden-estimater.

Moskstraumen har en stor innvirkning på bølgefeltet; den modulerer bølgebrytningsstatistikken, bølgehøydene (opptil 90 % økning), retningsspekteret, i tillegg til korttidsekstrembølgestatistikken (opptil 15 % økning). I Moskstraumen, og de omkringliggende områdene, er bølge-modulasjonene preget av lokale og ikke-lokale effekter. Disse inntreffer på rom- og tidsskalaer som er nært knyttet til strømningsfeltets dynamikk, i tillegg til de rådende bølgeforholdene. En slik type variasjon er kartlagt ved hjelp av en ny diagnostisk metode. Modellresultatene stemmer godt overens med de tilgjengelige observasjonene. Dette gjelder særlig modulasjonene i bølgespekteret. Det er imidlertid behov for flere observasjoner for å kunne trekke enda sikrere konklusjoner om effekten av strøm på bølgefeltet, siden dette er et problem – som av natur – er sterkt inhomogent i tid og rom.

Outline

This thesis consists of an introductory part and four scientific papers. Chapter 1 establishes the motivation and objectives for the thesis on the topic of wave–current interaction. An introduction to the theoretical basis and some relevant concepts are given in Chapter 2, which also delimits the problem. Then follows a description of the region of interest in northern Norway, together with an overview of the relevant data and methods that have been used in the scientific results (Chapter 3). The results are briefly summarized in Chapter 4, and followed by the conclusions and suggestions for future work (Chapter 5). Finally, the scientific papers included in this thesis are (Chapter 6):

1. Saetra, Ø., **Halsne, T.**, Carrasco, A., Breivik, Ø., Pedersen, T. and Christensen, K. H., (2021) *Intense interactions between ocean waves and currents observed in the Lofoten Maelstrom*, Journal of Physical Oceanography **51** (11)

2. **Halsne, T**., Bohlinger, P., Christensen, K. H., Carrasco, A., and Breivik, Ø, (2022) *Resolving regions known for intense wave–current interaction using spectral wave models: A case study in the energetic flow fields of Northern Norway*, Ocean Modelling **176**

3. **Halsne, T**., Christensen, K. H., Hope, G., and Breivik, Ø, (2023) *Ocean wave tracing v. 1: a numerical solver of the wave ray equations for ocean waves on variable currents at arbitrary depths*, Geoscientific Model Development **16** (22)

4. **Halsne, T**., Benetazzo, A., Barbariol, F., Christensen, K. H., Carrasco, A., and Breivik, Ø, (2023) *Wave modulation in a strong tidal current and its impact on extreme waves*, Journal of Physical Oceanography **54** (1)

Contents

1 Introduction

1.1 Motivation

The size and appearance of wind–generated ocean surface waves are proportional to the wind speed and fetch (*Hasselmann et al.*, 1973; *Holthuijsen*, 2007). When at sea, however, significant wave field modulations may occur, seemingly out of nowhere—even during calm winds and in deep waters. These abrupt changes are caused by interactions between the ambient current and waves. Ambient currents dictate the horizontal wave field variability at scales from $\mathcal{O}(10^0)$ km to $\mathcal{O}(10^2)$ km (*Ardhuin et al.*, 2017; *Romero et al.*, 2020); this is particularly evident in coastal[1] environments since they often host tidal currents, river mouths, and small-scale flows caused by frontogenesis processes—either separately or in combination. Such environments are very vulnerable to waves due to the presence of man-made structures, coastal erosion, and their implication for ship navigation, among others. It is therefore of societal and economical importance to obtain accurate estimates of the wave field and its current-induced modulations.

Strong currents are particularly undersampled due to the complexity of deploying instruments and the associated risk of losing them. A current of this kind is the Lofoten Maelstrom, which is an exceptionally strong tidal current in northern Norway (Fig. 1.1). The tidal current—known locally as *Moskstraumen*—is a critical dynamic component for its surroundings. For example, Lofoten is a primary spawning area for the pelagic Northeast Arctic cod (*Hjermann et al.*, 2007), and the Maelstrom is a main driver in the dispersion of eggs and larvae on their way to the Barents Sea (*Lynge et al.*, 2010; *Ommundsen*, 2002; *Vikebø et al.*, 2007). The flow field dynamics of the Maelstrom have been studied extensively (*Børve et al.*, 2021; *Gjevik et al.*, 1997; *Moe et al.*, 2002), but no studies have accurately verified the results against observations. Moreover, though this area has long been an infamously dangerous place to sail, this study is the first to demonstrate the impact of the Maelstrom on the wave field.

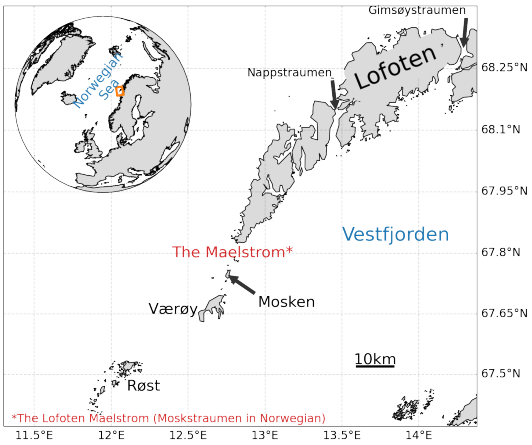

Figure 1.1: The Lofoten Maelstrom in northern Norway (orange bounding box). The Maelstrom is locally known as Moskstraumen; "straum" is current in Norwegian.

Energetic flow fields, like the Agulhas and Kuroshio currents, are notorious for their hazardous wave conditions (*Barnes and Rautenbach*, 2020; *Kudryavtsev et al.*, 1995;

[1] Here, coastal is the part of the ocean being closer than about 200 km from land.

Quilfen and Chapron, 2019; *Tamura et al.*, 2009). Such complicated conditions involves at least three facets: It refers to a sea state of high significant wave height, despite the wind speed suggesting otherwise (*Quilfen et al.*, 2018); a complex sea state due to crossing and choppy waves (*Kudryavtsev et al.*, 1995, 2017); a sea state more prone to individual extreme waves (*Lavrenov*, 1998; *Onorato et al.*, 2011; *Toffoli et al.*, 2011), which are also known as "freak" waves (*Dysthe et al.*, 2008). These different facets need be verified—a task that becomes increasingly complex in their respective order. Statistically speaking, recent studies show that the modeled wave height variability (or inhomogeneity[2]) caused by realistic ocean currents agree with the variability measured by remote sensing instruments (*Ardhuin et al.*, 2017; *Romero et al.*, 2020). Nevertheless, the accuracy of such forcing in a deterministic wave modeling perspective is more challenging (*Babanin et al.*, 2017, 2019; *Kanarik et al.*, 2021; *Palmer and Saulter*, 2016; *Rapizo et al.*, 2018; *Staneva et al.*, 2015); this is linked to the uncertainties associated with the underlying flow field dynamics, together with the lack of observations.

The recurring and predictable nature of the tides makes tidal currents suitable locations for studying wave–current interaction at oceanic scales (*Baschek*, 2005). However, the wave field modulation by tides is a multifaceted problem, which is largely related to the variety in met–ocean[3] conditions. Such variety includes the range of flow field properties (e.g., linked to the bathymetry and topography), in combination with the prevailing wind and wave conditions. This variability influences the dominating interaction mechanism, which may be either local or non-local. An exact quantification of their respective contribution is, however, difficult to provide (*Ardhuin et al.*, 2012; *Davidson et al.*, 2008; *Romero et al.*, 2017; *Tolman*, 1990a; *Vincent*, 1979). Therefore, careful considerations of simplified theoretical models are an essential step in the process of diagnosing the dominant cause of the observed modulations (e.g., *Ardhuin et al.*, 2017; *Ho et al.*, 2023; *Holthuijsen and Tolman*, 1991; *Masson*, 1996). Moreover, recent discoveries suggests that the horizontal variability of sea state parameters of higher-order spectral moments are different than those of lower order (*Ardhuin et al.*, 2017; *Romero et al.*, 2020). Hence, one might expect that sea state parameters like the expected extreme waves, say, (relying on higher-order moments) respond differently to currents than the significant wave height (the zeroth-order moment).

1.2 Objectives

The primary aim of my thesis is to analyze and assess the effects of mean ocean currents on the short-term statistics of surface gravity waves. More specifically, I want to properly assess the extent to which the Lofoten Maelstrom modulates the *sea state*—which denotes the short-term statistical characteristics of the wave field. For instance, how much does the Maelstrom influence the wave heights? Does it alter the occurrence probability of extreme waves? In that case, what are the driving mechanisms for such modulations, and to what extent are they predictable? Central to this thesis, and these questions, are the novel in situ wave and current observations that were collected in the Lofoten Maelstrom during the winter season of 2018–2019. In addition, I want to examine the wave field modulations caused by currents in the larger coastal region surrounding the

[2]Here and throughout, "inhomogeneous" refers to spatial, or horizontal, variability.

[3]Met–ocean is an abbreviation for the meteorological and oceanographic conditions.

Maelstrom. Here, certain areas are known for intense wave–current interaction, but there have been no attempts at resolving them using state-of-the-art wave models. Moreover, and in contrast to the Maelstrom, the currents in these areas are made up of several flow field components, which further complicates the task.

From the scientific literature, I found that it was not straightforward to either assess or interpret the observed wave modulations in the Maelstrom. For example, remote sensing observations showed bands of wave breaking at the tidal front when the Maelstrom and waves were heading in the same direction, thus suggesting that other mechanisms than the typical opposing waves and currents were important (*Baschek*, 2005). Moreover, few works have addressed the influence of currents on the extreme wave statistics. The recent implementation of space–time extreme waves in spectral wave models by *Barbariol et al.* (2017) and *Benetazzo et al.* (2021) made it possible to conduct such a study in the Maelstrom. Furthermore, the considerable lack of observations of both waves and currents in the coastal area surrounding the Maelstrom made it difficult the verify wave model results. Therefore, I hypothesized that local knowledge could be used as a source of information to judge whether numerical model results were realistic or not.

Based on these considerations, the following objectives were addressed in the thesis:

- Present the novel observations in the Lofoten Maelstrom, and discuss how the tidal current interacts with the wave field (Paper I).
- Assess the physical processes that cause the strong wave field modulations in the Maelstrom (Papers I–IV). Here, the non-local contribution of refraction was a most essential component (Paper III).
- Assess wave field predictions in northern Norway when using ocean surface currents as forcing by, among others, using local knowledge as a qualitative indicator (Paper II).
- Characterize the spatio-temporal variability in wave field modulations due to currents of different origin (Paper II).
- Evaluate how, and to what extent, the Maelstrom modulates the wave spectrum and the associated short-term extreme wave statistics.(Paper IV).

2 Scientific background

2.1 Stochastic ocean waves

Ocean waves are commonly characterized by their period T, which is the time it takes between two consecutive crests to pass a fixed point. Long waves (like tides and tsunamies) have large periods, while short waves (like ripples) have short periods. This thesis focuses on the wind–wave regime, i.e., waves in the approximate range of $T \in (0, 30]$ s, which are generated by surface winds (*Munk*, 1950). Furthermore, emphasis is put on studying *surface gravity waves* such that the forces associated with surface tension can be neglected. Wind generated surface gravity waves are hereafter referred to as waves, for brevity.

2.1.1 Wave theory

Linear wave theory assumes that the magnitude of the sea surface elevation η, which is made up by a set of waves with amplitude a and wave number $\kappa = |\mathbf{k}| = |(k_x, k_y)|$, is small compared with a characteristic wave length $\lambda = 2\pi/\kappa$. Formally, the assumption requires that the wave steepness (also referred to as the wave slope) $\varepsilon = a\kappa \ll 1$. As a consequence, an arbitrary sea surface can be considered a linear superposition of a given number N monochromatic plane surface waves with different amplitudes and frequencies $f_i = 1/T_i$ as

$$\eta(\mathbf{x}, t) = \sum_{i=0}^{N} a_i \sin(\chi_i), \tag{2.1}$$

where $\mathbf{x} = (x, y)$ is the position vector and t is time. Indeed, such waves are uncorrelated and prescribes a Gaussian wave field. The phase function for the ith component is

$$\chi = \mathbf{k} \cdot \mathbf{x} - \sigma t + \delta_r, \tag{2.2}$$

which specifies the stage in the wave cycle between 0 and 2π, where δ_r is arbitrary. The wave angular frequency $\sigma = 2\pi f$ is interconnected with the wave number κ through the *dispersion relation*

$$\sigma^2 = g\kappa \tanh(\kappa d), \tag{2.3}$$

where d and g are the water depth and gravitational acceleration, respectively. From the phase function, $\mathbf{k} = \partial\chi/\partial\mathbf{x}$ and $\sigma = -\partial\chi/\partial t$. The wave phase speed, i.e., the propagation speed of the wave crest, is

$$c = \frac{\sigma}{\kappa}. \tag{2.4}$$

Two important limits for waves and their propagation occurs at *deep* and *shallow* waters. Deep water means that $d \gg \lambda/2$ such that $\kappa d \gg \pi$, and the dispersion relation reduces to $\sigma^2 = g\kappa$. Such waves are known as *dispersive*, meaning that their phase speed depends on the wave length since $c = \sqrt{g/\kappa}$. As a consequence, long waves (i.e., small κ) propagate faster than short waves (large κ). In shallow water, $\tanh(\kappa d) \simeq \kappa d$ such that

$c = \sqrt{gd}$; such waves are *non-dispersive* since they propagate with the same phase speed independent of their wave length. The range between deep and shallow waters is know as intermediate depths.

Ocean waves are essentially a reservoir of energy and momentum. The wave energy (per unit area) is equally partitioned in a kinetic and a potential term, and their sum E_{tot}, for a single wave component, is

$$E_{\text{tot}} = \frac{1}{2}\rho_w g a^2, \tag{2.5}$$

where ρ_w is the density of water. The wave momentum is related to the wave energy by

$$\mathbf{M} = \frac{E_{\text{tot}}}{c}\,\frac{\mathbf{k}}{\kappa}. \tag{2.6}$$

It is worth noticing that the wave energy is a scalar while the momentum is a vector. The wave energy propagates with the wave group velocity

$$c_g = \frac{\partial \sigma}{\partial \kappa}, \tag{2.7}$$

which in vector form is $\mathbf{c}_g = c_g \mathbf{k}/\kappa$, and oriented in the direction normal to the wave crest. In the deep–water limit $c_g = c/2$ while in the shallow–water limit $c_g = c$.

2.1.2 The wave spectrum

A cost-efficient and convenient approach is to consider waves as a stochastic process using a spectral (or phase-averaged) representation, instead of the deterministic phase-resolved description. The one-sided unidirectional wave variance density spectrum can formally be described by the continuous Fourier transform of the auto-covariance function C as

$$E(\sigma) = 2\int_0^\infty C(\tau)\cos(\sigma\tau)\,d\tau. \tag{2.8}$$

Here, it is assumed that $\eta = \eta(t)$ is a weakly-stationary Gaussian zero-mean process, by applying the central limit theorem. Therefore, $C(\tau) = \mathrm{E}\{\eta(t)\eta(t+\tau)\}$, where $\mathrm{E}\{\cdot\}$ and τ denote the statistical expected value and a time difference, respectively. Wind–waves are generated by the synoptic mean wind conditions. Stationarity can therefore be obtained at time scales in-between synoptic variability and the fluctuations associated with single waves; this is a reasonable assumption for a duration $D \in (15, 30)$ minutes. It follows directly that $C(0)$ is the variance of η such that

$$\mathrm{var}(\eta) = \mathrm{E}\{\frac{1}{2}a_i^2\}, \tag{2.9}$$

(for a discrete sea surface) which is proportional to the total wave energy in (2.5). Therefore, the wave spectrum—as it will be referred to here—is interchangeably referred to as the wave variance and wave energy density spectrum. The wave spectrum can be presented in its unidirectional form $E(\sigma)$ (i.e., integrated over all directions) and directional form $E(\sigma, \theta)$, where θ denotes wave direction. Furthermore, it can be written as a function of frequency $f = \sigma/2\pi$, wave number κ, or wave number vector $\mathbf{k}$. Since the total variance is conserved, these different forms are related by their Jacobian; a

complete derivation of the Jacobian from an absolute to intrinsic frame of reference (to be introduced later) is shown in the Appendix of Paper IV.

Some characteristics about the wave field can be inferred from the wave spectrum. *Swell waves* are located at low frequencies and recognized by a narrow frequency and directional spectrum. Consequently, in physical space, they appear as long-crested. Such waves originate from distant storms due to deep–water dispersion (2.4), i.e., long waves propagate faster than short waves and can escape the storm. Formally, swell can be characterized by requiring that the wave age $c/U_{10} > 1.2$ or $c/U_{10}\cos(\theta - \theta_{\text{wind}}) > 1.2$ (*Grachev and Fairall*, 2001), where U_{10} is the mean wind speed 10 m above sea level and θ_{wind} the wind direction. Contrary, *active wind–waves* are characterized by a wide frequency and directional spectrum, and typically reside on higher frequency; these are waves that are actively generated (and fed) by the wind. More details about the wave generation by wind is provided later and in Appendix A. Sometimes, swell and active wind–wave appear simultaneously. The resulting spectrum is then commonly referred to as being *bi-modal*; such cases are treated in Paper II and Paper IV.

Under the assumption of linear long-crested waves, *Longuet-Higgins* (1952) showed that the wave amplitude a_i and wave height H_i follow a Rayleigh distribution. Therefore, the statistical characteristics of the wave field, which is commonly referred to as the *sea state*, can be expressed by spectral moments on the form (here also using the unidirectional spectrum for simplicity)

$$m_j = \int_0^\infty \sigma^j E(\sigma)\, d\sigma. \tag{2.10}$$

Such bulk parameters provide important descriptors of the sea state. For instance, the zeroth-order moment $m_0 = \text{var}(\eta)$. Furthermore, m_0 is related to the *significant wave height* $H_{\text{s}} \simeq H_{m0} \approx 4.004\sqrt{m_0}$, which is the maybe most important sea state parameter for seafarers and in engineering contexts. In a wave record, H_{s} is similar to the mean of the one-third highest waves. Other standard *physical* variables include mean wave periods like $T_{m01} = m_0/m_1$ and $T_{m02} = \sqrt{m_0/m_2}$. Here, it is important to note that higher order moments are more sensitive to the higher frequencies; this is particularly important in wave measurements since higher frequencies are typically more sensitive to noise, which may thus contaminate higher order spectral variables. In addition to physical parameters, spectral *shape* parameters (like the frequency bandwidth) provide insight on the type of sea state. A number of such parameters are computed in Paper IV, and some are introduced below.

2.1.3 Short-term extreme wave statistics

For engineering and practical purposes, it is of interest to know the size of the highest wave one is *most likely* to encounter in a given sea state; this includes the maximum wave crest $\eta_{\max}$ and crest-to-trough height $H_{\max}$. In wave statistics, the highest wave represents an outlier—or extreme—in the wave height distribution. The degree to which waves are considered extreme is characterized by their ratio with H_{s}. Those that exceed the limits $\eta_{\max} > 1.25H_{\text{s}}$ and $H_{\max} > 2H_{\text{s}}$ are usually referred to as *freak* or *rogue* (*Dysthe et al.*, 2008). Such events are considered rare, but do appear in wave records in all sea states. Still, they are not possible to deterministically predict (*Bitner-Gregersen et al.*, 2024).

An in-depth treatment of the deterministic and stochastic models related to extreme waves is outside the scope of this thesis. However, a brief summary of the traditional short-term statistics for a single point, together with the extension to a space–time domain, is provided below.

Time extremes

The expected extreme waves computed from the Rayleigh distribution agrees reasonably well against observations (*Forristall*, 1978). However, ocean waves are not strictly linear, and active wind–waves are short-crested. Concerning nonlinearity, it is recognized that the largest wave crests in storm conditions deviate from the linear theory (*Dysthe et al.*, 2008; *Malila et al.*, 2023). An extension to the linear wave theory was proposed already by Sir George Gabriel Stokes in the 1840s by which η is made up by a perturbation series of bound harmonics in ε to a given order (see *Lamb*, 1932). As a result, the probability density function of η is skewed towards lower values, since the nonlinear contributions makes the troughs wider and crests narrower. The maybe most known nonlinear wave crest distributions are those up to second-order by *Tayfun* (1980) and *Forristall* (2000). *Tayfun and Fedele* (2007) found that the nonlinear contributions have an insignificant impact on $H_{\max}$. This can be reasoned by the fact that nonlinear crests and troughs are higher and shallower, respectively, compared with linear theory. As a consequence, the crest-to-trough wave height becomes, to some extent, conserved.

In a short-crested sea state, the crest-to-trough heights H are, in a time series, generally lower than that of narrow-banded sea states. *Naess* (1985) and *Boccotti* (1982) suggested to account for frequency bandwidth effects through the auto–covariance function C. As a consequence, $H_{\mathrm{s}} \simeq 2\sqrt{2(1+|\Psi^*|)m_0)}$ where $\Psi^* \in [-1, 0]$ is the ratio between the absolute maximum and the absolute minimum of the autocovariance (see *Boccotti*, 2000, ch. 4.7.3.). It is a spectral bandwidth parameter, and usually referred to as the *narrow-bandedness* parameter. If $\Psi^* = -1$, the spectrum is infinitely narrow which leads to the common $H_{\mathrm{s}} \approx 4\sqrt{m_0}$. For a parametric JONSWAP spectrum (*Hasselmann et al.*, 1973), $\Psi^* \in [-0.75, -0.65]$. As a consequence, the extreme wave height distribution also becomes a function of Ψ^* (see *Boccotti*, 2000, ch. 5.7.3.).

Space–time extremes

The study of stochastic extreme waves has emerged from the traditional single-point observations. It is, however, acknowledged that single point observations are unlikely to capture the highest sea surface elevation—particularly for short-crested sea states. Thus, a three dimensional domain that spans both space and time is more appropriate. Recent developments have applied the exceedance probability of the general geometric field statistics by *Adler* (1981) and *Piterbarg* (1996) to the three dimensional sea surface elevation $\eta = \eta(\mathbf{x}, t)$ (*Fedele*, 2012; *Fedele et al.*, 2013; *Krogstad et al.*, 2004). Following *Tayfun* (1980), *Benetazzo et al.* (2015) recently proposed a correction of the space–time crest height distribution to second-order in ε. In a space–time domain, the number of waves (or sample size) is much larger than that of a single-point time series domain (*Krogstad et al.*, 2004). Thus, the magnitude of the expected extremes increases. Finally, and building upon the so-called quasi-determinism theory by *Boccotti* (2000), it is more likely to capture the highest wave in a wave group during its propagation in a space–time

domain.

In short-term statistics, the homogeneity assumption enables us to compute the aforementioned variables (together with other ancillary variables) from the directional wave spectrum. In other words, the expected space–time extreme waves can be computed from the directional spectrum. This was recently implemented in *spectral wave models* (to be introduced in the subsequent section) by *Barbariol et al.* (2017) and *Benetazzo et al.* (2021). Furthermore, and as will be seen later, ambient currents modulate the wave spectrum, and thus the spectral moments and associated variables. Their impact on the expected space–time extreme waves is demonstrated in Paper IV.

2.2 Waves on mean currents

The ocean flow field can be considered a linear superposition of different current components like those associated with the mean flow $\mathbf{U} = (u, v)$, the wave orbital motion $\tilde{\mathbf{u}}$, and turbulent fluctuations $\mathbf{u}'$. Here, I consider waves riding on a preexisting *ambient* current $\mathbf{U}$. Generically, this problem includes wave lengths that are much smaller than the *scale of observations*, for instance wave lengths of visible light observed at scales of meters. Such a treatment is known as the *geometric optics approximation*. At oceanic scales, it means that $\mathbf{U}$ varies slowly in space and time compared with wave properties like the wave length λ and wave period T (*Peregrine*, 1976). The formal limit is treated in Paper IV. Indeed, such a treatment involves a simplification of the problem. For instance, phenomena like diffraction are not included. This is, however, a reasonable assumption for length scales at the order of a kilometer and larger (*Ardhuin et al.*, 2012). In light of geometric optics, this section is devoted to the theory of wave–current interactions.

2.2.1 Wave kinematics

For waves on an ambient current $\mathbf{U}$, it is possible to make a distinction between two reference frames: Moving with the current and at a fixed position in space. The first is known as the *intrinsic*, or *relative*, frame of reference, and the second as the *absolute*. A position $\mathbf{x}$ in the fixed frame is related to the relative position $\hat{\mathbf{x}}$ by

$$\hat{\mathbf{x}} = \mathbf{x} - \mathbf{U}t. \tag{2.11}$$

Inserting into (2.2), we obtain the *Doppler shift equation* that relates the absolute angular frequency ω to the now so-called intrinsic frequency σ by

$$\omega = \Omega(t, \mathbf{k}, \mathbf{x}) = \sigma + \mathbf{k} \cdot \mathbf{U}. \tag{2.12}$$

It also becomes necessary to distinguish between the absolute and intrinsic versions of other variables like the absolute group velocity $\mathbf{c}_{g,a} = \mathbf{c}_g + \mathbf{U}$. Similarly, the phase function (2.2) can be formulated in terms of ω. Note that if $\mathbf{k} \cdot \mathbf{U} = 0$, there is no interaction.

In a fixed control volume, the number of wave crests is conserved (also known as the wave number density conservation; for details see Note D in *Holthuijsen*, 2007, Appendix

D). In combination with (2.12), one can derive the wave ray equations

$$\frac{d\mathbf{x}}{dt} = \frac{\partial \Omega}{\partial \mathbf{k}}, \tag{2.13}$$

$$\frac{d\mathbf{k}}{dt} = -\frac{\partial \Omega}{\partial \mathbf{x}}, \tag{2.14}$$

$$\frac{d\omega}{dt} = \frac{\partial \Omega}{\partial t}, \tag{2.15}$$

which govern the kinematics related to wave propagation. Here d/dt is the material derivative. Equations (2.13)–(2.15) express the evolution in position, wave number, and absolute frequency along a ray, respectively. A ray is a parametric curve in the x–y plane. At zero currents, rays are directed normal to $\mathbf{k}$; this is not the case for non-zero currents. Any change in σ, $\mathbf{k}$, and $\mathbf{U}$ affect the ray through (2.12). Owing to wave number density conservation, such changes are particularly related to the intrinsic dispersion relation (2.3), which is also sensitive to the water depth. Paper III presents a numerical solver of (2.13)–(2.15), and further details are given therein.

The advection (2.13) is essentially the group velocity in the absolute reference $\mathbf{c}_{g,a}$. For large parts of the wind–wave regime, the *weak current assumption* $\delta = U/c_g \ll 1$, where $U = |\mathbf{U}|$ holds (e.g., *Dysthe*, 2001). Consequently, the advection is to leading order governed by the (intrinsic) group velocity. In the form presented here, (2.14) includes the change in both $\mathbf{k}$ and κ. The first is associated with refraction since the wave propagation direction θ is normal to the wave crest, and the second represents the change in wave number and thus the wave length. The change in κ is at times referred to as the "concertina effect" which alludes to the instrument (*Ardhuin et al.*, 2017; *Wang and Sheng*, 2018). Refraction due to currents and bathymetry is an important effect that causes strongly inhomogeneous wave fields (e.g., *Bôas et al.*, 2020). This topic will be discussed in more detail later. *Kenyon* (1971) was the first to show that the wave deflection angle, in deep water, is a function of the vertical component of the current vorticity $\zeta = \partial v/\partial x - \partial u/\partial y$ (to first order in δ); this was also derived in detail by *Dysthe* (2001).

The change in ω through (2.15) is for most applications considered to be negligible. The bathymetry is most often steady, meaning $d = d(\mathbf{x})$, and the current changes little in time compared with the time scales of the waves (i.e., $\partial \mathbf{U}/\partial t \approx 0$). However, such simplifications are not always true—particularly in shallow regions with strong tidal modulation (*Ho et al.*, 2023; *Tolman*, 1990b).

An example of numerically integrating the ray equations with respect to waves at intermediate depths is shown in Fig. 2.1. Here, only the change in water depth is taken into account. Nevertheless, it is clear that the set of equations captures the leading order change in wave propagation direction when compared against the background satellite image (note the factor 30 lower resolution in the bathymetry field [using GEBCO[1]] compared with the satellite image).

Some of the earliest wind–wave forecasting models were based on ray tracing frameworks, however most often neglecting the currents (e.g., *Cavaleri and Rizzoli*, 1981). This includes the first coastal wave forecasting model in Norway, where estimates of crossing waves were based on the work by *Mathiesen* (1987) (*Christakos*, 2021).

[1] https://www.gebco.net/data_and_products/gridded_bathymetry_data/ accessed 2024-01-18

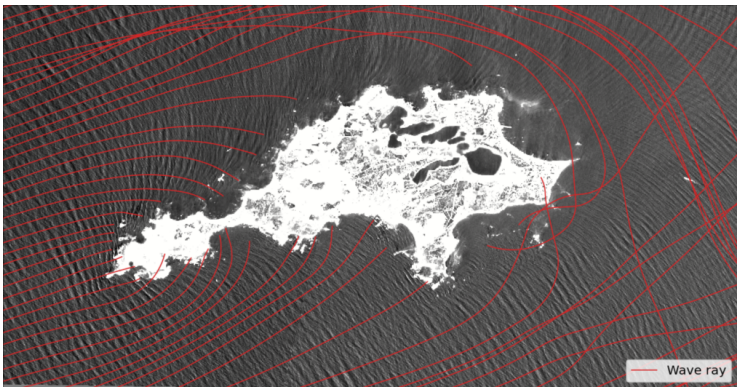

Figure 2.1: Wave rays computed from the solver in Paper III in the vicinity of the Rottnest iceland on the west coast of Australia. Background image has 10 m pixel resolution and is acquired by the Copernicus Sentinel-2 mission (band B4). For the wave rays, only refraction due to the changing bathymetry (300 m resolution) is taken into account. Image contains modified Copernicus Sentinel-2 data [2021], processed by ESA.

2.2.2 Wave dynamics

The seminal series of papers by Michael S. Longuet-Higgins and Ross W. Stewart laid the foundation on how to physically understand, and mathematically describe, the interaction between ocean waves and mean currents (*Longuet-Higgins and Stewart*, 1960, 1961, 1962, 1964). They essentially argued that *transport* of the wave induced momentum $\mathbf{M}$ is equivalent to a stress, and that horizontal variations in this stress act as forces on the water (as body forces). The stress is known as the *Radiation stress*, and is proportional to E_{tot}. It is usually written in its tensor form $S_{\alpha\beta}$ $(\alpha, \beta = x, y)$. The different directional contributions depend on the alignment with the reference coordinate system.

The governing equation for modeling waves on ambient mean currents arises from applying the conservation laws for energy, momentum and mass. In its simplest form, i.e., considering a vertically uniform current profile and disregarding dissipative processes, the wave energy balance equation becomes (see *Phillips*, 1977, ch. 3.6 for details)

$$\frac{\partial E_{\text{tot}}}{\partial t} + \frac{\partial}{\partial x_\alpha}\left[E_{\text{tot}}(u_\alpha + c_{g,\alpha})\right] + S_{\alpha\beta}\frac{\partial U_\beta}{\partial x_\alpha} = 0. \tag{2.16}$$

The frequency shift caused by current gradients according to (2.12) can be physically interpreted as a *straining* mechanism; waves become longer on positive current gradients and vice versa. According to Longuet-Higgins and Stewart, the interaction between the radiation stress and the current-induced straining results in an exchange of energy between the current and the waves, since the rate-of-strain (i.e., the current gradient) does work against the radiation stress. In the case of a constant ambient current, energy is conserved; there is no current-induced straining involved, and the last term on the left hand side vanishes. Conversely, wave energy is not conserved with the presence of varying currents; the product between the radiation stresses and current gradient appear as either a source or sink of wave energy. In Paper I, (2.16) is considered in more detail.

2.2.3 Wind–wave modeling

In a modeling context, it is inconvenient to work with a non-conservative property like E. However, a related quantity known as the *wave action density* $N = E/\sigma$, or wave action in short, is conserved in the presence of currents (*Bretherton and Garrett*, 1968; *Whitham*, 1965). State-of-the-art spectral wave models now solve the *wave action balance equation*, which is similar to (2.16) but formulated for N and with a non-zero right-hand-side that includes non-conservative and nonlinear processes (*Komen et al.*, 1994);

$$\frac{\partial N}{\partial t} + \nabla_{\mathrm{h}} \cdot \left(\dot{\mathbf{x}} N\right) + \nabla_{\mathrm{k}} \cdot \left(\dot{\mathbf{k}} N\right) = \frac{S_{\mathrm{in}} + S_{\mathrm{nl}} + S_{\mathrm{ds}} + S_{\mathrm{bot}}}{\sigma}. \tag{2.17}$$

Such a model has been used in Paper II and Paper IV. In (2.17), $N = N(\mathbf{k}; \mathbf{x}, t)$ is a five-dimensional variance density spectrum. The horizontal gradient operator $\nabla_{\mathrm{h}} = (\partial/\partial x, \partial/\partial y)$ and the wave number gradient operator $\nabla_{\mathrm{k}} = (\partial/\partial k_x, \partial/\partial k_y)$ denote the gradients in physical and spectral space, respectively. The terms with overdots represent material derivatives $\dot{\langle\rangle} = d\langle\rangle/dt$, and we recognize that wave action propagates along rays defined by (2.13)–(2.14). The wave action spectrum can also be written $N = N(\kappa, \theta; \mathbf{x}, t)$ by which (2.17) would involve other, interrelated, terms like (2.15); this form is used in the Wave Watch III spectral wave model (*WW3DG*, 2019).

The right hand side of (2.17) contains non-conservative physical and nonlinear processes; the S_{in} (in = input) represent the momentum transfer from surface winds into the wave field, which is proportional to U_{10}^2; the S_{nl} (nl = nonlinear) redistributes the wave action density in the frequency–directional space because of triple (shallow water) and quadruple (deep water) nonlinear wave-wave interactions; the S_{ds} (ds = dissipation) is a sink of wave momentum, primarily due to wave breaking (called whitecapping in deep–water). Nearshore, wave energy is also dissipated through the bottom friction source term S_{bot}. In shallower regions, terms like depth-induced wave breaking should also be included. A thorough review of these parameters is outside the scope of the present thesis, but can be found in *Komen et al.* (1994). In this thesis, I have primarily focused on including currents in the wave kinematics, i.e., the left hand side of (2.17). Such a choice is supported by *Ardhuin et al.* (2012) who reviewed the performance of spectral wave models in areas of strong currents. They suggested that most important for the accuracy of influence by currents on waves was, in decreasing order: The accuracy of the forcing fields; the behaviour of the source terms; and the accuracy of the model numerical schemes. A more in-depth discussion on the appearance of mean currents in the source terms, including the importance of the numerical resolution, is provided in Appendix A.

2.3 Currents effects on waves

In the previous section, I introduced how preexisting currents enters the governing equations for ocean waves. Hence, currents impact the advection of wave energy, its direction and frequency [i.e., (2.12)–(2.15)], but also their amplitude and associated energy [(2.16)–(2.17)]. However, it is difficult to directly attribute how, why, and where, in the governing equations—but also in the physical space—the interaction appear. Such knowledge is key to further understand the physical processes. Here, a review of currents effects on waves is first considered by simplified models, then by highlighting their mod-

ulation of the wave spectrum, and lastly by considering how they cause inhomogeneous wave fields in space and time.

2.3.1 Idealized and simplified models

It is not readily seen from (2.16) and (2.17) how the wave spectrum responds to ambient currents. Therefore, some considerations of idealized cases are helpful in pinpointing the leading order mechanisms. Such cases are often sensitive to the type of sea state, i.e., if it is of swell type or (active) wind–sea type (*Holthuijsen and Tolman*, 1991). For swell conditions, and on horizontal length scales below 100 km, the source terms can often be considered negligible (*Ardhuin et al.*, 2010). On the other hand, an actively forced wind–sea generates a broad frequency–directional spectrum, and the high frequency part of the spectrum becomes saturated (*Phillips*, 1984). Under constant wind, for sufficiently long duration, the spectrum (or sea state) may reach a state of *equilibrium*; the terms S_{in}, S_{nl}, S_{ds}, and S_{bot} balance each other (*Phillips*, 1985).

Quasi-stationary solutions

The non-dissipative wave action equation, i.e., with a zero right-hand-side in (2.17), can be further simplified by considering a quasi-stationary (or steady in short) wave train on deep water, and a unidirectional action spectrum $N = N(f; \mathbf{x})$. By using the Doppler shift equation (2.12), and by only considering waves propagating in the x–direction with $u = u(x)$, we obtain

$$\frac{E}{E_0} = \frac{c_0^2(1 + \frac{2u_0}{c_0})}{c^2(1 + \frac{2u}{c})}. \tag{2.18}$$

This is maybe the most well-known solution describing how currents modulate the wave field—shown already by *Longuet-Higgins and Stewart* (1961). The subscript "0" refers to a region with a specific current u_0; it usually refers to conditions where $u = 0$. According to (2.18), the wave energy increase as the denominator becomes small, which occurs on negative, or opposing currents (Fig. 2.2). A singularity occurs when $u = -c_0/4$ which is known as the blocking velocity (see Appendix B). In (2.18), one assumes that there is an upwelling flow to compensate for the current gradient; another solution—with less impact on the spectrum—can be found for a current being compensated by a transverse, horizontal, inflow velocity such that $\nabla_h \cdot \mathbf{U} = 0$ (*Longuet-Higgins and Stewart*, 1961). To first order in the *relative* weak current assumption $|\delta_r| = |u/c_{\text{g},0}| \ll 1$, (2.18) can be evaluated by the simple expression

$$\frac{E}{E_0} \simeq \frac{1}{1 + 2\delta_r}, \tag{2.19}$$

by assuming $u_0 = 0$; the derivation of this expression is shown in detail in Appendix B. A comparison between the exact (2.18) and the approximate (2.19) is shown in Fig. 2.2. As expected, these two solutions diverge for large values of $|\delta_r|$. High frequency waves are most sensitive to this current modulation, since δ_r increase with frequency.

Throughout the literature, different versions of (2.18) have been used to emphasize the effects of currents on the wave field (e.g., *Baschek*, 2005; *Baschek et al.*, 2006; *Chawla and Kirby*, 2002; *Holthuijsen and Tolman*, 1991; *Huang et al.*, 1972; *Lai et al.*, 1989; *Masson*, 1996; *Ris and Holthuijsen*, 1996; *Rusu and Guedes Soares*, 2011; *Vincent*, 1979;

Wang and Sheng, 2018). It has proven to be quite robust in determining wave height modulations in strong currents, particularly where active wind sea is dominating, but also when compared with more advanced—but still simplified—models like the transient version by *Ardhuin et al.* (2012).

Based on (2.18), *Rapizo et al.* (2017) proposed to modify the S_{ds} term by *Rogers et al.* (2012) to enhance the dissipation on opposing currents. They found the modification to provide satisfactory wave height results in a tidal inlet (more details are found in Appendix A).

The convenience of working with (2.18) is that it can also express modulations in other parameters by utilizing wave interrelations. For instance, in Paper IV a reformulated version of (2.18) is used to express the change in wave steepness ε.

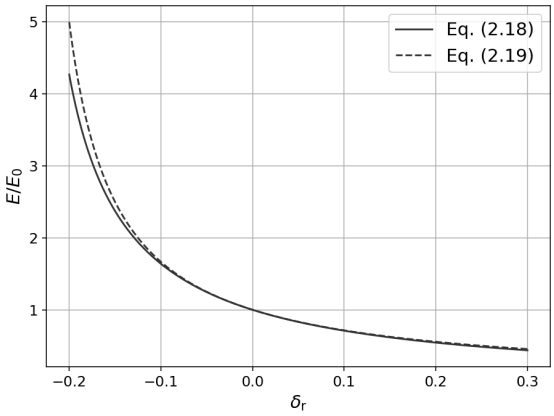

Figure 2.2: Wave energy modulation by steady currents. The exact solution (2.18) *(with* $u_0 = 0$*) is plotted in solid line, while the leading order approximation* (2.19) *is plotted in dashed line.*

In the scientific community, there is no clear naming for the wave modulation mechanism in (2.18). It is often referred to as the "blocking effect" (e.g., *Chawla and Kirby*, 2002), "energy bunching" (e.g., *Ardhuin et al.*, 2012), or "the combined effects of wavelength shortening and energy focusing" (*Rapizo et al.*, 2017). Here, the latter is the most precise, since shortening and energy bunching are associated with negative current gradients. However, most of the aforementioned expressions only consider the negative current gradients, while the modulation also occurs for positive current gradients (Fig. 2.2). Therefore, in Paper IV, we called it the *wave straining* mechanism (partly based on a constructive comment by one of the anonymous reviewers). Here, *wave* alludes to the wave action and *straining* the lengthening or shortening by the current gradients as described in Section 2.2.2; this is similar to *Holthuijsen and Tolman* (1991), but they separated between the energy contributions from the wave length modulation (i.e., current-induced shoaling) and the radiation stresses.

Another interesting steady case is that of horizontally sheared currents oblique to the wave propagation direction, like $u = u(y)$. This was originally treated by *Johnson* (1947), but the energy modulation due to the radiation stresses was corrected by *Longuet-Higgins and Stewart* (1961). In such cases, the current also causes wave refraction, which will be treated in more detail in the subsequent section. Under such conditions, however, some approximate analytical solutions for energy modulations owing to specific effects exists; these were used to study waves in the Gulf Stream by *Holthuijsen and Tolman* (1991), a work that was recently reproduced and extended by *Allahdadi et al.* (2023).

Wave action conservation along rays

Since wave action is conserved along wave rays, the wave energy modulation can be computed from the change in distance between two initially parallel, say, rays; a shortening yield higher waves and vice versa (*Mathiesen*, 1987). Such a treatment gives qualitatively good results, which is why ray density maps can be used to assess the impact by refraction on wave heights (see e.g., *Quilfen and Chapron*, 2019; *Rapizo et al.*, 2014; *Ying et al.*, 2011). Such maps should, however, be evaluated carefully since ray tracing frameworks often specify a single initial direction of all rays, and the ray paths are very sensitive to the initial direction and thus not representative for an ocean wave field (*Holthuijsen and Tolman*, 1991; *Smit and Janssen*, 2019). Therefore, an ensemble of rays, ideally reflecting the frequency-directional distribution of the directional spectrum should be used. We used a ray density map in Paper I to assess the importance of refraction in the Lofoten Maelstrom. However, the linear theory breaks down as the distance between the rays approaches zero, or they coalesce (*Peregrine*, 1976). Such singularities are called caustics. More precisely, caustics are the envelopes that enclose points of crossing rays. Wave ray tracing frameworks—as the one in Paper III—are essentially Lagrangian frameworks, which are unable to properly take into account non-conservative and nonlinear interactions. However, ray tracing analysis can be very powerful when combined with a full, Eulerian, spectral wind–wave model. Such analyses were carried out in Paper II and Paper IV.

Transient solution: the relative wave convergence

A scaling analysis of (2.16), accompanied by a discussion of the effects of currents on wave energy, is provided in Paper I. Essentially, under conditions of following waves and currents (assuming a coordinate system aligned with the wave propagation direction), (2.16) reduces to

$$\frac{\partial E}{\partial t} = -E\Big[\Big(2\frac{c_g}{c} + \frac{1}{2}\Big)\frac{\partial u}{\partial x} + \Big(\frac{c_g}{c} + \frac{1}{2}\Big)\frac{\partial v}{\partial y}\Big]. \tag{2.20}$$

Here, it is possible to evaluate the *relative* impact by current gradients on the transient wave field; this is readily done by considering the deep and shallow–water limits as

$$\frac{1}{E}\frac{\partial E}{\partial t} = \begin{cases} -\Big(\frac{3}{2}\frac{\partial u}{\partial x} + \frac{\partial v}{\partial y}\Big), \text{ deep water,} \\ -\Big(\frac{5}{2}\frac{\partial u}{\partial x} + \frac{3}{2}\frac{\partial v}{\partial y}\Big), \text{ shallow water.} \end{cases} \tag{2.21}$$

In this special case, the change in wave energy per time is proportional to the horizontal divergence $\nabla_h \cdot \mathbf{U}$. We recognize the minus sign in front of the divergence such that a convergent flow field causes an increase in wave energy. Thus, we named the term "relative wave convergence". The convenience with (2.21) is that a first-order approximation of the temporal modulation in E can be assessed directly by using a current field from an ocean model. In Paper I we only considered the deep–water limit, but the wave spectrum is even more sensitive to the current gradients in shallow waters.

2.3.2 Spectral modulation

Using the relative current–wave ratio δ_r, and only considering waves in x–direction, the Doppler shift equation becomes

$$\omega = \sigma(1 + \delta_r). \tag{2.22}$$

Thus, for a given u, the shortest waves is most sensitive to current modulations. Consequently, the high frequency part of the spectrum is most sensitive to current gradients; this explains the formation of bright narrow bands that are often observed along ocean fronts in remote sensing imagery, which are due to spectral saturation causing wave breaking (*Phillips*, 1984)—as those shown in Paper I. Bright and dark narrow bands in remote sensing imagery also reveal internal waves, where the saturated and non-saturated spectrum fluctuates as a result of the current gradients caused by the oscillating pycnocline (*Alpers*, 1985; *Lenain and Pizzo*, 2021).

In terms of directional distribution, the spread often increase due to varying currents (*Ardhuin et al.*, 2012; *Holthuijsen and Tolman*, 1991; *Mathiesen*, 1987). *Rapizo et al.* (2016) found that the broadening in direction was more pronounced the narrower the initial wave system prior to entering the current. *Dysthe* (2001) and *Kenyon* (1971) showed that the shortest waves are most sensitive to current-induced refraction, which often causes an increase in the spreading. However, refraction may also cause a local decrease in the directional spread. Particularly in caustics if the current and waves are such that they become aligned and not necessarily crossing (*Wang et al.*, 1994). Furthermore, the directional spread may also decrease down-wave because of short waves breaking, as is nicely illustrated by the orthophotos by *Johnson* (1947) at a tidal inlet in California. Indeed, in such situations, the currents become a high-pass filter down-wave because of the breaking-induced dissipation.

In summary, currents may cause substantial modulations within the unidirectional and directional spectrum. However, such modulations are not necessarily seen in the integrated spectral parameters (*Tolman*, 1990a). Locally, for instance, δ_r decrease with frequency such that changes in the lower order moments—most sensitive to the energy carrying frequencies—may be small. The impact by currents on spectral parameters in a bi-modal sea state, i.e., having a distinct wind–wave and swell component, can be particularly difficult to assess. In Paper IV we provide an in-depth discussion on such a case. To introduce the subsequent section: An interesting feature is the non-local impact by currents on the spectrum that occur down-wave. Such modulation is mainly caused by refraction, that occur locally, but the most substantial changes in the spectrum occur down-wave.

2.3.3 Spatio-temporal wave field variability

Local and non-local influence on wave height

Indeed, waves constantly interact with the current while propagating. This is a challenge in interpreting observations, particularly those that have limited horizontal coverage (*Vincent*, 1979). This is the reason why the simplified models introduced above are worthwhile (*Masson*, 1996). The wave energy—represented by H_s—is the maybe most important wave parameter for practical use and therefore studied most extensively. Later, parameters associated with higher order spectral moments are also considered.

In the ocean, the most important non-local effect on H_s is refraction. The current gradients causes areas with focusing and de-focusing of wave rays, which induces a strongly inhomogeneous wave field (*Ardhuin et al.*, 2017; *Irvine and Tilley*, 1988; *Romero et al.*, 2020). *Bôas et al.* (2020) showed that the horizontal variability in narrow-banded wave fields was dictated by the rotational component of the mean current flow field. Conversely, they found insignificant changes in the wave field by increasing the kinetic energy in the irrotational component of the flow field. Moreover, and for such wave fields, *Bôas and Young* (2020) and *Smit and Janssen* (2019) showed that the refraction-induced wave scattering causes a directional diffusion in wave energy. In deep water, a characteristic wave deflection angle θ_c can be computed from the ray curvature expressions by *Dysthe* (2001) and *Kenyon* (1971), by assuming a constant vertical current vorticity ζ_c over a certain distance l_c (*Gallet and Young*, 2014)

$$\theta_c = \frac{\zeta_c l_c}{c_g}. \tag{2.23}$$

Using values of $\zeta = 2 \times 10^{-5}$ s^{-1}, and $l_c = 100$ km, a swell with $T = 10$ s deflects about 14.5 degrees while a $T = 17$ s wave deflects about 8.5 degrees. The importance of refraction is evaluated in all the papers of this thesis. Interestingly, and as pointed out in Paper II and Paper III, refraction due to currents and bathymetry occurs simultaneously at intermediate and shallow waters, where one may act as a wave guide for the other.

The transient relative wave convergence solution of (2.21) is another example of a non-local effect in H_s. Here, the growth in wave energy is associated with the time a wave train experiences a certain current convergence, and vice versa for current divergence. A more detailed evaluation of (2.21) is given in Paper I.

Local modulations in H_s occur through (2.18). Here, "local" means length scales by which the ambient current vary in space. Modulations in (2.18) becomes evident when δ is of $\mathcal{O}(1)$, and particularly when approaching the blocking velocity (*Chawla and Kirby*, 2002). For small–scale wind generated waves, *Phillips* (1984) showed how the current gradients, in combination with the scale of variability in the current field, could have a significant local influence on the waves; negative current gradients induces local spectral saturation—as referred to in the previous section.

Temporal variability due to different current regimes

Ocean currents of different origin typically vary on different time scales—the wave field is modulated accordingly. In descending order of spatio-temporal scales, such modulations have been demonstrated in the Antarctic Circumpolar Current (*Rapizo et al.*, 2018), at mesoscales (*Marechal and Ardhuin*, 2021; *Quilfen and Chapron*, 2019; *Tan et al.*, 2023), in tidal currents (*Ardhuin et al.*, 2012; *Masson*, 1996), and at submesoscales (*Ardhuin et al.*, 2017; *Lenain et al.*, 2023; *Romero et al.*, 2020). However, current regimes of different origin may occur simultaneously, which makes it difficult to discern their impact on the wave field (*Gemmrich and Garrett*, 2012). In Paper II, we address how to map the temporal variability of different current regimes in northern Norway by introducing a diagnostic method; it is repeated in a more generic form in Appendix C.

Horizontal variability for higher order spectral moments

This topic has not been particularly emphasized in the present thesis. However, it has been discussed indirectly in Paper IV. Recent studies show that the horizontal variability in higher order spectral moments is different than those of lower order. *Romero et al.* (2020) pointed out that wave parameters like the mean square slope ($\propto m_2$) and stokes drift ($\propto m_3$) were more collocated in space with the current divergence and vertical vorticity than, for example, H_s ($\propto m_0$). They also pointed out that the current gradients dictated areas of wave breaking; this agrees with the works by *Rascle et al.* (2016, 2017, 2018), which highlighted how the mean square slope was modified locally by the current gradients—in agreement with the theory by *Phillips* (1984). Moreover, *Ardhuin et al.* (2017) showed how the moments m_0–m_4 had similar variability at scales above 100 km. However, larger variability was found for the highest moments at scales below approximately 10 km. Together with the work by *Romero et al.* (2020), this supports the idea that the horizontal variability of the bulk energy in the spectrum—typically residing on the lower frequencies—is governed by mechanisms like refraction, while the high-frequency part is more locally affected by the ambient current.

3 Methods, data, and region of interest

In this chapter, I provide an overview of the most important datasets and methods that have been used in the scientific papers, together with an introduction to the region of northern Norway. The Lofoten Maelstrom is introduced first. Note that within the all the papers included in this thesis (Chapter 6), I have mostly referred to the Maelstrom by its local name Moskstraumen. Here, however, I continue by using the Lofoten Maelstrom, or simply Maelstrom in short.

3.1 The Lofoten Maelstrom

In the region from the north–east Atlantic to the Barents Sea, the tide propagates as a shallow–water wave, across the Norwegian Sea, in a north-eastward direction (Fig. 1.1). Close to the coast of Norway, it becomes a topographically steered Kelvin wave that reaches phase speeds around 100 m s^{-1} at the continental shelf (while reaching higher speeds further offshore). For the tidal wave, the Lofoten archipelago appears as a funnel shaped vertical wall, which hinders its propagation. Besides the narrow straits across the archipelago (see Nappstraumen and Gimsøystraumen in Fig. 1.1), the only way around is through the Moskenes sound. It is located between the westernmost tip of Lofoten and the island Mosken, and is about 8 km wide. The sound is a shallow bottom ridge of about 50 m depth which connects the Norwegian Sea to the west with the semi-enclosed basin *Vestfjorden* to the east. The sea surface level difference across the sound reaches about 0.4 m, and the associated pressure gradient generates a strong semidiurnal tidal current—the Lofoten Maelstrom. It is strongest about 2 h after high and low tide where it is flowing west and east, respectively (*Gjevik*, 2009). During spring tide, the Maelstrom reaches speeds of at least 3 m s^{-1}, and the volumetric flow rate is estimated to reach 0.6 Sv (*Gjevik*, 2009; *Lynge et al.*, 2010). This is about twice that of the Amazon river. The dominating tidal components are the semidiurnal lunar (M_2) and solar (S_2) constituents (*Moe et al.*, 2002).

Historically, the Maelstrom has been infamous for its ferocity and dangerous whirls. It was known as the "Charybdis of the North"—the ancient Greek sea monster in the Messina Strait described in Homer's Odyssey (*Homer*, 1919)—and was mentioned in tales as early as the Viking age (*Guerber*, 1909). Among the abundance of references, the best known are the classical works "A Descent into the Maelström" by Edgar Allan Poe (*Poe*, 1841) and "Twenty Thousand Leagues Under the Seas" by Jules Verne (*Verne*, 1891). Poe's novel inspired the American composer Phillip Glass, and his music was recently filmatized[1]. The word Maelstrom stems from the Dutch "malen" meaning grinding, or in some contexts pulverizing. For reference, Røst (the name of the archipelago located south-west of the Maelstrom [Fig. 1.1]) originates from the Norse "Rost" which means whirl in English. Consequently, the currents in the area are known for their strong vortex-like appearance. In many of the historical references, the sea surface manifestation of the Charybdis (or any of the other associated creatures) took the form as high

[1] https://www.nfi.no/eng/film?name=descent-into-the-maelstrom&id=2046–accessed 2024-01-16

waves. An example is shown in Fig. 3.1 where the Italian cartographer Vincenzo Maria Coronelli (1650–1718) depicted the Maelstrom as monstrous waves that arose from the deep. The Danish priest and poet Anders Arrebo (1587–1637) claimed that the Maelstrom generated waves so high that they shaded the view of the sun (*Spaans*, 2023). In the post-medieval era (around 1500–1750), where many of these references stem from, the ocean was indeed mysterious. This is nicely illustrated in the "Carta Marina" by the Swedish priest and chartographer Olaus Magnus from 1539 (reproduced over the Maelstrom in Paper I). However, and in contrast to these contemporary mythical descriptions, a more physical reasoning about the origin of the Maelstrom was proposed by the Norwegian poet and priest Petter Dass in 1685 (*Gjevik et al.*, 1997). He was able to attribute the flow of the Maelstrom with the phases of the moon. His considerations also included the modulation of the waves entering the Maelstrom (see Appendix in Paper I). A more complete historical review of the Maelstrom is given by *Gjevik et al.* (1997), and a condensed version is provided in Paper I.

Figure 3.1: The sea surface manifestation of the Lofoten Maelstrom by the Venetian (Italian) cartographer Vincenzo Maria Coronelli around 1690. The text reads in English "Waves formed by the sinkhole of Moskstraumen". Here, the Mosken island is to the left in the painting.

The different tidal stages of the Lofoten Maelstrom is shown in Fig. 3.2: The Maelstrom flows west at high tide (panel a), while accelerating to its maximum around 2 h after high tide (panel b). The front is associated with a strong current shear and thus subject to breaking waves. Slack tide occurs a couple of hours before low tide (panel c). The west-going branch of the Maelstrom decelerates and turns in a clockwise direction, starting with the southernmost part and then gradually northwards. Such turning causes a strong horizontal current shear within the sound and is locally known as *Strinna*; it causes complicated sailing conditions for smaller vessels (*Den norske los*, 2018). This region of strong current shear is elaborated upon in Paper II. Note that the currents just east of Lofoten turns anti-clockwise in contrast to the rest of the area (*Moe et al.*, 2002). The Maelstrom starts flowing west at low tide (panel d), while accelerating to maximum

eastward flowing current about 2 h after low tide (panel e). Eddies and whirls—which have given name to the Maelstrom—occur in the vicinity of current. Around 2 h before high tide (panel f), the current turns gradually from north to south (again causing the *Strinna*) and continues to accelerate westwards against high tide. In Paper I and Paper II, and the stages where the Maelstrom were flowing west (Fig. 3.2 a–c) and east (Fig. 3.2 d–f) were called falling and rising tide, respectively.

The flow field associated with the Maelstrom takes different shapes when flowing west and east; it becomes a narrow jet when flowing west, while being broader and more horizontally uniform when flowing east. Such flow field asymmetry was also suggested in the model study by *Børve et al.* (2021). However, the asymmetry has only been qualitatively verified by satellite imagery (as in Paper I). Nevertheless, as ocean models (including the one used in this thesis) suggests that such asymmetry exists, it allows to investigate how different flow fields affect the wave field. This is studied in Paper IV.

Satellite imagery and ocean model current fields of the Maelstrom are shown in Figure 3.3; this is a situation after high tide (Fig. 3.2b) and the Maelstrom is thus flowing west. The satellite image reveals the tidal flow direction, but also the fronts that are associated with strong current gradients and wave breaking. The extent and shape of the current is also represented by the 800 m resolution ocean model (to be introduced in Section 3.3.3). From the vertical cross-sections, we see that the model predicts a barotropic current. This is in agreement with the measurements that are presented in Paper I, and also with the previous model studies by *Moe et al.* (2002).

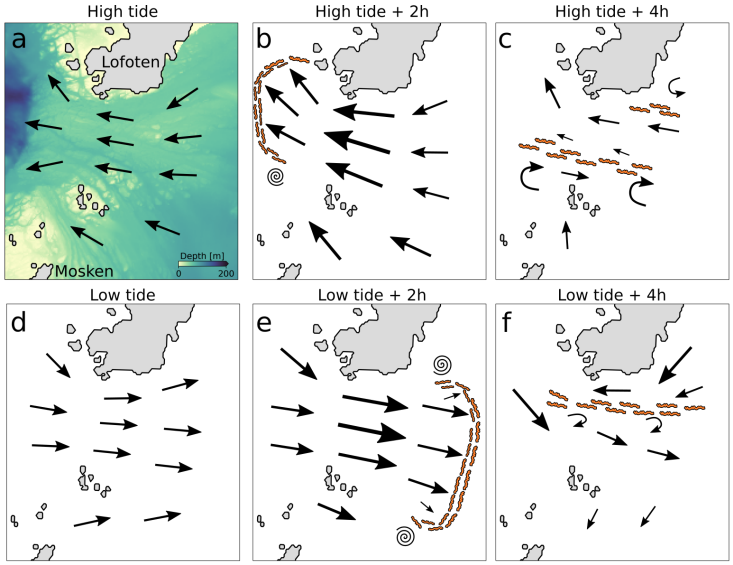

Figure 3.2: A conceptual illustration of the flow field evolution of the Lofoten Maelstrom during a tidal cycle. Different stages are shown in panels a–f, where maximum current speed of the Maelstrom occur about 2 h after high and low tide. Arrows denote the approximate direction and relative magnitude of the current. Ridged orange lines denote areas associated with strong horizontal current shear and thus wave breaking. Spirals indicate typical areas where whirls (radiating from the Maelstrom) appear. The illustration is based on the descriptions by Den norske los (2018) and Gjevik (2009).

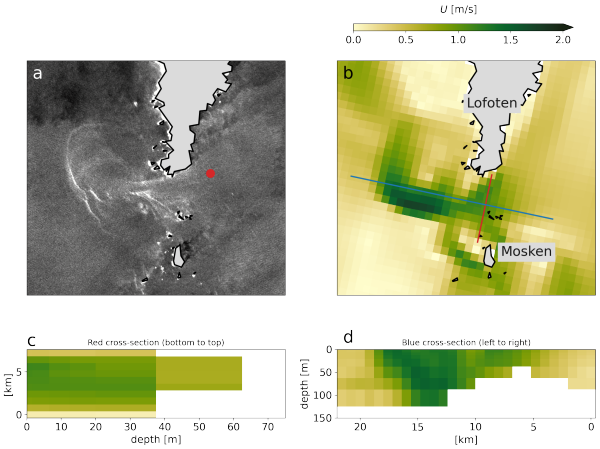

Figure 3.3: Snapshot of the Lofoten Maelstrom while flowing west at October 10 2021. Panel a show the sea surface signature of the Maelstrom depicted by the Copernicus Sentinel-1B satellite. Panel b show modeled surface current speed closest in time (i.e., T=17 UTC from the NK800 ROMS model [Tab. 3.1]). Vertical cross-sections across and along the Moskenes sound are shown in panels c and d, respectively. The red dot in panel a indicates the location of the ADCP. Note that the small isles in the middle of the sound are not included in the NK800 topography. Image contains modified Copernicus Sentinel-1 data (2021), processed by ESA.

The Moskenes sound combines the Vestfjorden basin to the east with the Norwegian Sea to the west (Fig. 1.1). Therefore, the wave conditions are constrained by the limited fetch (about 100 km) from the east, while in practice having unlimited fetch from the west. Due to the location in the belt of westerlies, the wave field often becomes multi-modal typically consisting of a (local) wind sea and remote swell component. Such wave fields, together with the asymmetric flow field conditions of the Maelstrom, are treated in Paper IV.

Its history, intensity, and strong gradients makes the Maelstrom a popular site for remote sensing imagery for both popular science communication[2] and in the so-called gray literature (e.g., *Dokken and Wahl*, 1995). The tides also generate internal waves in the Moskenes sound, that propagate into Vestfjorden (*Dokken et al.*, 2001). The associated currents caused by internal waves also affect surface waves (e.g., *Lenain and Pizzo*, 2021), but the current gradients are typically much lower than those associated with the Maelstrom. The role of internal waves on surface waves in the area has not been addressed in this thesis. As a sidenote, the strongest tidal current in Norway, *Saltstraumen*, is located just across Vestfjorden. This is an inshore tidal current which is among the strongest tidal currents in the world, with claims of speeds up to 10 m s^{-1} (*Gjevik*, 2009).

[2] https://earthobservatory.nasa.gov/images/89984/ungovernable-fury–accessed 2024-01-16

3.2 Met–ocean conditions in northern Norway

Northern Norway is surrounded by open ocean from the Barents Sea to the north, to the Norwegian Sea to the southwest (Fig. 1.1). It is located in the belt of westerlies and thus exposed to extratropical cyclones, but also polar lows. Moreover, the region has a set of ocean circulation systems. Here I introduce the regions' characteristic met–ocean conditions that are relevant for this work.

3.2.1 Ocean currents

The offshore ocean circulation is dominated by the Norwegian Atlantic Current (NwAC), while the Norwegian Coastal Current (NCC) is wedged between the NwAC and the coast of Norway. The NwAC is a two-branch system of the North Atlantic Current flowing northwards bringing saline water into the Arctic (*Mork and Skagseth*, 2010). In this thesis, the relevant branch is the topographically trapped barotropic current that closely follows the continental slope (Fig. 3.4). The NCC is colder and fresher as it consists of river runoff and Baltic sea water, and thus provides a low-salinity inflow to the Barents Sea (*Christensen et al.*, 2018). The NwAC and NCC mix gradually as they flow northward. As seen in Fig 3.4, mean current speeds reaches about 1 m s^{-1} offshore, while maximum values exceeds 2 m s^{-1}. Furthermore the circulation also comprise wind-driven near-inertial currents at the Coriolis frequency f_{cor} (*Röhrs and Christensen*, 2015). These are, however, difficult to discern from the semidiurnal tides; at these latitudes (between 67–72 degrees north) $f_{\mathrm{cor}}^{-1} \in [12.6, 13]$ h and is thus close to the M_2 ($\simeq 12.42$ h) tidal period. Submesoscale features like eddies and fronts typically arise from baroclinic instabilities in the NCC, as seen visually in Fig. 2 of Paper II. Details about their generation and origin is outside the scope of this thesis. A more in-depth description is given by *McWilliams* (2016). However, their horizontal extent is typically between 0.1–10 km (i.e., lower than the Rossby radius) and their life time varies from sub-daily to a couple of days.

3.2.2 Wave conditions

Indeed, most waves entering the region from offshore have in practice no fetch limitation. Therefore, and because of the westerlies, the wave climate includes a regular influx of remotely generated swell, which often appear in combination with an active wind–sea component. Furthermore, the sea state may become extraordinarily high; the 100-year return value of H_{s} is around 17 m (*Aarnes et al.*, 2012; *Haakenstad et al.*, 2020). There is a strong seasonal variability in wave heights, with the largest occurring during the winter season. In summary, the wave climate is multi-faceted, with a strong seasonal dependence.

Of particular interest to this thesis are the near–coastal locations (in addition to the Maelstrom) that are known for dangerous sea states—treated in detail in Paper II. These locations have been reported to be particularly complicated to navigate, and overlap with areas that throughout history have been known for shipwrecks. A total of 24 such areas have been identified along the coast of Norway, and eight out of these are located in northern Norway. Here, the severe wave conditions are almost exclusively attributed to the interaction with the ambient currents (*Den norske los*, 2018).

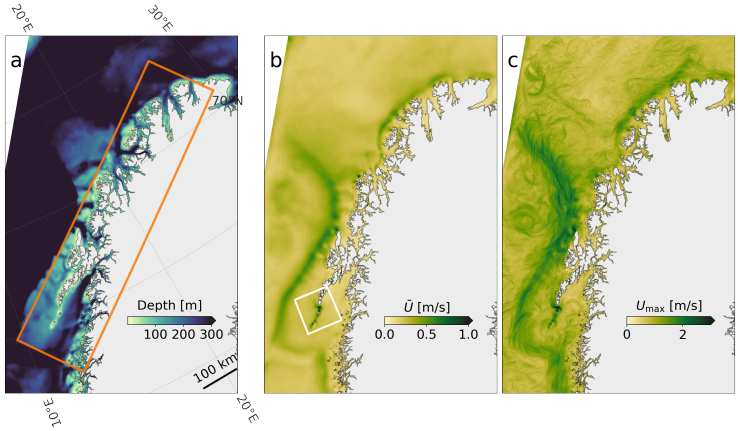

Figure 3.4: Bathymetry (panel a), mean surface current speed ($\bar{U}$ panel b), and maximum surface current speed (panel c) in northern Norway. Current statistics are computed for the period January–September 2019 using NK800 (see Tab. 3.1). Orange contour in panel a highlight the WAM model domains used in Paper II and Paper IV. White contour in panel b highlight the area covering the Lofoten Maelstrom.

3.3 Data: Observations and models

Here I provide an overview of the most important datasets and sources that are used in the papers. A summary is provided in Tab. 3.1.

3.3.1 In situ

The most central data set in this thesis is the acoustic Doppler current profiler (ADCP) observations that were acquired in the Maelstrom during the winter season 2018–2019 (Fig. 3.5). The successful ADCP deployment and recovery operation was a collaborative effort between the Norwegian Coastal Administration, Nortek AS, and the Norwegian Meteorological Institute. This was the first-of-its-kind measurements of waves and currents in the Maelstrom. That is, *Moe et al.* (2002) used some current recordings from a 21-day period in 1972 at four locations, each with three vertical depths. Other attempts measuring the current profile have been abandoned due to the harsh conditions. To my knowledge, waves in the Maelstrom have not been measured previously. Moreover, and throughout the world, very few moored observations of waves and currents exists in such intense environments similar to the Maelstrom. Our instrument—a five-beam (four slanted and one vertical) NORTEK Signature 500 kHz ADCP[3]—was mounted in a tripod frame with a gimbal to compensate for a potentially slanted bottom topography, and deployed at about 50 m depth southeast of Lofoten (see Fig. 3.3a). The instrument operated in a concurrent plan by alternating between average and burst mode. A description of the acquisition setup and data is presented in Paper I, Paper II, and

[3] https://www.nortekgroup.com/products/signature-500–accessed 2024-01-31.

Table 3.1: Summary of the most important data that are used in the papers (including observations and those from community models). RS–Remote Sensing.

Name	Type	Short summary	Duration	Location	Paper(s)
ADCP	In situ	Nortek Signature 500 ADCP	3 months	The Maelstrom	I, II, IV
WR	In situ	Datawell Wave rider	3 months	Vestfjorden	II
Sentinel-1	RS	Sentinel-1 SAR imagery	Instant	The Maelstrom	I
Sentinel-2	RS	Sentinel-2 MSI imagery	Instant	The Maelstrom, Rottnest Island	I, III
CMEMS S3A	RS	Sentinel-3A Level-3 altimeter	Swaths	Entire domain	II
ESA CCI	RS	ESA CCI altimeter multi-mission	Swaths	Entire domain	II
NK800	Model	800 m horizontal resolution ROMS model	-	Entire domain	I–IV
NORA10	Model	Wave and surface pressure fields from 10 km resolution hindcast	-	Entire domain	I
WAM_{ref}	Model	WAM 800 m resolution with wind forcing only	-	Entire domain	II
WAM_{curr}	Model	WAM 800 m resolution with wind + NK800 current forcing	-	Entire domain	II
WAM_{W}	Model	WAM 800 m + Latemar package with wind forcing only	-	Entire domain	IV
WAM_{W+C}	Model	WAM 800 m + Latemar package wind + NK800 current forcing	-	Entire domain	IV

Paper IV, in decreasing order of detail, respectively. However, the aforementioned papers used different parts of the data set. Therefore, I give a brief summary here. After Paper I got published, Nortek AS also made their own story about the deployment in the Lofoten Maelstrom[4].

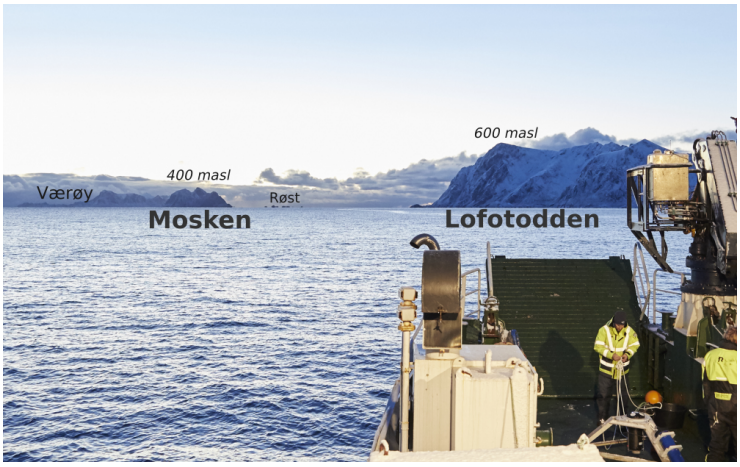

Figure 3.5: On the way to deploy the Nortek Signature 500 ADCP in the Maelstrom in December 2018. The up-looking ADCP was mounted in a tripod (see bottom right) and deployed in the sound between the Mosken island and Lofotodden. The photograph field-of-view is oriented in a west-southwest direction.

An overview of the deployment setup and data acquisition plan is shown in Fig. 3.6. In average mode, 1 Hz current profiles (2 m vertical resolution) were acquired every 10th minute (starting at full hours) with a duration of 1 minute. In burst mode, the five-beam configuration measured horizontal currents (with the four slanted beams) at 2 Hz (2.4 m vertical resolution) for 20-minute segments every 30 minutes (starting at whole hours). Vertical currents were also measured by the slanted beams, as well as by the vertically oriented fifth beam. This beam also measure the sea surface elevation η by filtering out the ocean surface from the backscatter intensity in vertical echogram profiles. Moreover, a pressure sensor at the instrument is also used for wave measurements. A standard routine during burst measurements is to acquire a single vertical raw echogram profile in order to properly detect the sea surface. In our setup, such profiles were acquired every 15th minute with 2.4 cm vertical resolution.

In Paper I, Paper II, and Paper IV, vertical ocean current profiles and wave statistics were computed using Nortek's OceanContour (v. 2.1.2) software. Wave parameters also include the directional wave spectrum, which is inferred from correlating the uppermost velocities from the slanted beams. The frequency limit for such velocities, and thus the directional spectrum, is about 0.2 Hz waves at 50 m depth. The raw echograms were used in Paper I to evaluate the bubble penetration depth from breaking waves, which is elaborated upon in Section 3.4.1. In Paper IV, the raw η from the burst segments was used for evaluating the tendency to wave extremes.

In addition to the ADCP, a third-generation directional Datawell Waverider[5] buoy

[4] https://www.nortekgroup.com/knowledge-center/userstory/improving-metocean-forecasts-with-wave-and-current-data–accessed 2024-01-31.

[5] https://datawell.nl/products/directional-waverider-mkiii/–accessed 2024-01-31

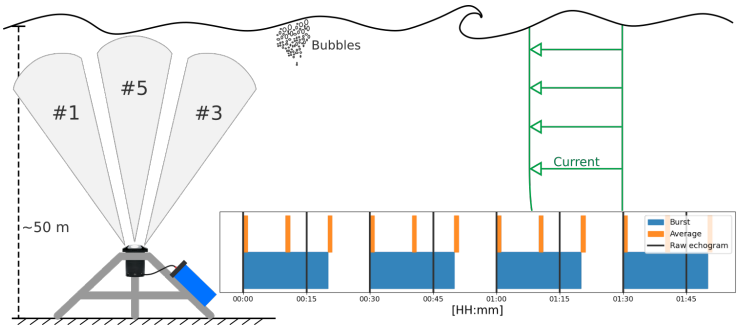

Figure 3.6: An illustration of the Nortek Signature 500 ADCP setup in the Maelstrom during the three month deployment. The ADCP was mounted in a tripod about 50 m below mean sea level. For illustrative purposes, the figure only shows two of the in total four slanted beams (i.e., #1 and #3) together with the vertical fifth beam. Green vertical profile indicate the barotropic current and direction (arrows). The instrument acquisition plan is outlined in the insert figure: Burst mode (blue) includes wave and current measurements (beams #1–#5) , average mode (orange) includes currents only (beams #1–#4), and raw echograms (black) were acquired every 15th minute (beam #5).

located in Vestfjorden was used in Paper II to evaluate wave model results (Table 3.1).

3.3.2 Satellite remote sensing

Broad and narrow swath satellite remote sensing have essentially been used for two purposes: Assessing the impact by currents on the wave field through H_s retrievals (Table 3.1), and to visualize the imprint of ocean dynamics on the sea surface (e.g., see Fig. 2 in Paper II). In Paper I, both synthetic aperture radar and optical imagery, from the respective Copernicus Sentinel-1 & 2 missions, were used to qualitatively verify the shape of the modeled flow field of the Maelstrom. In addition, they provide evidence for increased wave breaking during maximum current strength. For wave refraction at small scales, the Sentinel-2 snapshot in Fig. 2.1 is a qualitative verification of the ray tracing model in Paper III (in Paper III the Sentinel-2 image is only used to highlight the concept of refraction). These broad swath products were primarily accessed through the Norwegian ground segment for Sentinel data (*Halsne et al.*, 2019). In Paper II, H_s retrievals from a number of satellite altimeter missions were used to to verify wave model output. These are 1 Hz Level-3 products processed by the Copernicus Marine Service (CMEMS) and the European Space Agency Climate Change Initiative (ESA CCI). The H_s retrievals, and the accompanied model verification parameters, were accessed and computed using the open-source *wavy*[6] package. More specifications about the aforementioned sensors and products are found in the respective papers.

3.3.3 Community models

Spectral wave model

Different versions of the third-generation spectral wave model WAM (WAve Modelling group, *Komen et al.*, 1994) have been used to model the wind–wave field in northern

[6] https://wavyopen.readthedocs.io/en/latest/–accessed 2024-01-31

Norway (Table 3.1); a 10–11 km horizontal resolution hindcast model (*Reistad et al.*, 2011) provided the environmental conditions in Paper I; different versions of an 800 m resolution setup were employed for Papers II and IV. The domain of the latter WAM simulations are outlined in Fig. 3.4a, and is similar to the operational wave model operated by the Norwegian Meteorological Institute for the specific domain. Most of the model specifications are listed in the respective papers. In short, the 800 m resolution model in Paper II was a 4.7 version provided through the MyWave project (*Behrens et al.*, 2013). In Paper IV, a more recent version was used which included the computation of expected space–time extreme waves. This latter procedure was documented and implemented by *Barbariol et al.* (2017) and *Benetazzo et al.* (2021), and is known as the *Latemar* package[7].

Norkyst800 ROMS model

The Norkyst800 (NK800) is a ROMS (Regional Ocean Modeling System, *Shchepetkin and McWilliams*, 2005) implementation which is used as ocean current forcing in the aforementioned 800 m WAM simulations. It is an operational forecasting model operated by the Norwegian Meteorological Institute. The most relevant model specifications for the works in this thesis are listed in Paper I and Paper II, and a complete overview is given by *Albretsen et al.* (2011). Note that there is a difference in number of vertical levels in Papers I and II, due to updates in the NK800 setup during the period. The ocean model domain includes the northermost parts of the NwAC and NCC, and is forced with eight tidal constituents. Statistically speaking, the ocean model is expected to be representative of the coastal waters. However, NK800 is not expected to give deterministic prediction of all the dynamics; this particularly involves the submesoscale features that radiate from the NCC.

3.4 Methods

Here I present some of the key methods that were used in the scientific papers (Chapter 6).

3.4.1 Echogram bubble depth retrievals

During maximum current speed of the Lofoten Maelstrom, the tilt of the ADCP, *at times*, exceeded the limit (i.e., 10 degrees from zentih) by which wave measurements can be used with a sufficient degree of accuracy. However, the raw vertical echogram data are still valid observations. From such measurements, it is possible to estimate the penetration depth by wave breaking induced air bubbles (e.g., *Strand et al.*, 2020; *Vagle and Farmer*, 1998; *Wang et al.*, 2016). In the context of our measurements (with sparse temporal resolution [Fig. 3.6]), the interesting parameter were not the maximum depths reached by the bubbles, but rather the tidal modulation of the bubble depths.

Bubble penetration depths were estimated by a thresholding procedure on the high resolution vertical echogram data (see Fig. 4 in Paper I). Since bubbles are a well-known feature in echograms close to the surface, the algorithm required continuous exceedance of the threshold level in order to remove other spurious features further down in the water column. This includes fish with limited vertical extent. The threshold was set

[7] https://www.mercator-ocean.eu/en/portfolio/latemar/–accessed 2024-01-20

to 40 dB. Bubble penetration depths are computed to be the vertical distance from the lowermost point exceeding the threshold and up to the sea surface elevation.

3.4.2 Twin model experiments

Twin model runs (i.e., with and without ocean surface current forcing) were conducted for the 800 m resolution WAM models in Paper II and Paper IV. Such pairs allows us to assess the sea state modulations caused by the currents, and is a frequently used method in the scientific and operational community (e.g., *Kanarik et al.*, 2021; *Olabarrieta et al.*, 2012; *Palmer and Saulter*, 2016; *Rapizo et al.*, 2018). Since the wind forcing is the same in both models, the differences in model fields are solely due to currents. A more quantitative approach—that has not been considered here—can be enabled within the wave model framework. That is to turn on and off the different kinematic terms in (2.17), as well as within the source terms, to assess the model sensitivity to each of them. Indeed, this is a very powerful approach to evaluate the contribution by specific mechanisms in (2.17). This approach have been used by, e.g., *Ardhuin et al.* (2017), *Guimarães et al.* (2022), *Marechal and Ardhuin* (2021), *Romero et al.* (2020), and *Wang and Sheng* (2018). In such cases, however, the model output fields should be carefully evaluated. Because, by turning off certain mechanisms, like refraction, also implies that the other processes, like wave-wave interaction, will adjust an already artificial model field.

3.4.3 Frequency modulation

Some current regimes can be characterized by their temporal modes, like the M_2 and S_2 components in the Maelstrom. Therefore, it is convenient to analyse time series of wave modulations in frequency space. In particular, a power spectral density (PSD) analysis is commonly used to separate between different dynamics (e.g., *Gemmrich and Garrett*, 2012). In Paper I, the tidal modulation in bubble depths was quantified by computing the PSD on specific subsets of the bubble depth time-series presented above. Moreover, in Paper II, PSD analysis were carried out for both single and multiple grid points on the model difference fields (e.g., WAM with minus WAM without surface current forcing) to single out the temporal variability. Such analysis led to the diagnostic method proposed in Paper II, which can be applied to map the spatio-temporal variability for certain temporal modes. The method is presented in a more general form in Appendix C.

4 Introduction to the papers

Paper I: Intense interactions between ocean waves and currents observed in the Lofoten Maelstrom

Øyvind Saetra, Trygve Halsne, Ana Carrasco, Øyvind Breivik, Torstein Pedersen, and Kai Håkon Christensen

The Lofoten Maelstrom appeared very strong in the NK800 model, but its strength and flow field properties had never been properly verified. Moreover, the sea state modulation caused by the Maelstrom had only been described in folklore and pilot guide reports, without any quantitative information. Furthermore, and throughout the world, very few moored observations exists in such intense environments. Therefore, the in situ current and wave measurements acquired in the Lofoten Maelstrom were novel (Section 3.3.1). We assessed the impact by the current gradients on the wave field by using (2.21) with modeled currents from NK800, and by physical reasoning. The results were compared against the ADCP observations. We found that the standard wave observations were *at times* corrupted during maximum currents due to the high tilt of the instrument. Therefore, bubble penetration depths were estimated from the raw vertical echogram data, and were considered a proxy for the current-induced wave height modulations (Section 3.4.1). The main findings from Paper I are summarized below.

- We verify that the Maelstrom reaches speeds of at least 3 m s^{-1}, and that the Maelstrom is barotropic. This is in line with the NK800 output and corroborate previous estimates by *Gjevik et al.* (1997) and *Moe et al.* (2002).
- The observed tidal modulation in bubble depths suggests that the current gradients cause a strong energy exchange between the current and wave field, which leads to steeper waves. Another likely cause of the bubble depth modulations is that waves steepen as the Maelstrom decelerates relative to the waves riding on the current.
- The apparent strong tidal modulation of the wave field, and the good agreement between the observed and modeled current, suggests that current forcing can give added value to wave forecasting models.

The findings were also summarized in a dedicated news article by the Norwegian Broadcasting Corporation[1], and by forskning.no[2]—a national digital platform for scientific news.

Erratum: Equation (16) in Paper I includes a term E_k, where the k-index is a typo. The typo is corrected in the subsequent Equation (17), which was solved numerically.

[1] https://www.nrk.no/nordland/for-forste-gang-har-de-malt-farten-pa-den-verdensberomte-strommen-moskstraumen-1.15911428–accessed 2024-02-09

[2] https://www.forskning.no/havet-historie-meteorologisk-institutt/sa-raskt-strommer-tidevannet-i-den-beryktede-moskstraumen/1998858–accessed 2024-02-09

Paper II: **Resolving regions known for intense wave–current interaction using spectral wave models: A case study in the energetic flow fields of Northern Norway**

Trygve Halsne, Patrik Bohlinger, Kai Håkon Christensen, Ana Carrasco, and Øyvind Breivik

In Paper I, we found that the NK800 model gave a reasonable representation of the Lofoten Maelstrom. Therefore, I wanted to check if forcing a high-resolution WAM model with surface currents from NK800 would improve the predicted wave heights. I also found that the aforementioned corrupted wave height measurements only occurred during some of the spring tide periods. In other words, measured wave parameters like H_s were available most of the time. Furthermore, the near–coastal area in northern Norway surrounding the Maelstrom is also subject to strong currents on different spatio–temporal scales. Some specific sub-regions are known for dangerous sea states—all linked to the ambient current—but no measurements other than scattered satellite altimeter H_s retrievals were available. However, detailed descriptions of supposedly dominating interaction mechanisms existed in the Norwegian Pilot Guide for Maritime Navigation (*Den norske los*, 2018). I hypothesized if such information could be of any value when assessing the difference in a twin-model experiment. The main findings from Paper II are:

- Most of the areas known for dangerous waves were qualitatively resolved by the model including current forcing.
- Local knowledge can be a valuable source of information in terms of wave model assessments.
- Absolute model differences in H_s around 2 m (up to 90 % increase) were found in regions with strong tides. The ADCP observations in the Maelstrom corroborated the modeled wave field modulations when including currents.
- A new diagnostic method to map the spatio–temporal variability was presented. The method was employed to distinguish between the tidal and sub-mesoscale currents influence on the H_s field.

Erratum: The "2D spectrum" in the caption of Fig. 12 is a typo. It should be "1D" or "unidirectional" spectrum.

Paper III: **Ocean wave tracing v. 1: a numerical solver of the wave ray equations for ocean waves on variable currents at arbitrary depths**

Trygve Halsne, Kai Håkon Christensen, Gaute Hope, and Øyvind Breivik

In order to qualitatively assess how variable currents modulate the wave field, simplified solutions are a most essential tool. By those listed in Section 2.3, the inhomogeneous wave field caused by current-induced refraction is the most difficult to assess. Refraction analysis by ray tracing has played a central role in numerous recent wave–current interaction papers (e.g., *Ardhuin et al.*, 2012; *Bôas and Young*, 2020; *Gallet and Young*, 2014; *Romero et al.*, 2017, 2020; *Sun et al.*, 2022). In Paper I, I used a version that only took current-refraction into account. It was extended in Paper II to also support varying depths. Therefore, and since no such model was available as open source, I decided to make a robust implementation with the aim of supporting the scientific community. The main features and results in Paper III are:

- It is is implemented for arbitrary currents at variable depths.
- The joint effect of current and depth-induced refraction, occurring at intermediate depths, can be decisive for the horizontal wave height variability.
- The solver is verified against analytical solutions and tested for numerical convergence.
- The model follows an object-oriented, and modular, approach such that new functionality can easily be added and old components easily substituted, without changing the entire system.
- The solver is enclosed by a set of relevant ancillary methods which simplifies further analysis.

Paper IV: Wave modulation in a strong tidal current and its impact on extreme waves

Trygve Halsne, Alvise Benetazzo, Francesco Barbariol, Kai Håkon Christensen, Ana Carrasco, and Øyvind Breivik

Tidal currents have been proposed to be ideal locations for studying the effect of currents on extreme waves (e.g., *Baschek*, 2005). However, very few attempts have been reported in the scientific literature. Moreover, the vast portion of preexisting works have focused on the deterministic aspect of extreme waves, and to a much lesser extent the stochastic approach. With the exceptions of *Barbariol et al.* (2015) and *Romero et al.* (2017), no previous studies have considered the influence of currents on the recent stochastic extreme waves formulated for a space–time domain (see Section 2.1.3). In particular, the sensitivity of space–time extreme wave heights to currents have never been assessed. In Paper II, we found that the flow field of the Maelstrom appeared different when heading east and west, suggesting that different interaction mechanisms could dominate. Such situations, and their impact on the space–time extremes, were further investigated in Paper IV. The key findings in Paper IV are:

- We find an increase up to 15 % in the expected second-order space–time extreme wave crests when the Maelstrom opposes the dominating wave field. In particular, the increase is sensitive to the currents modulation in spectral steepness.
- The Maelstrom, at times, cause an increase in the expected space–time extreme wave heights up to 12 %. However, the extreme wave heights correlated strongly the narrow-bandedness parameter, which resulted in a decrease during long-crested sea states.
- Our results suggests that tidal-induced modulations in expected extremes are sensitive to the dominant wave–current interaction mechanism. Particularly, refraction and wave straining affect the spectral steepness differently.

5 Synthesis, conclusions and future perspectives

5.1 Synthesis of scientific results

This thesis is a story about how energetic currents modulate the short-term statistics of ocean waves in coastal and near–coastal environments. Here, I present a linkage between the scientific results that, together, compose the thesis (Chapter 6). Papers I, II, and IV focused on different aspects of the sea state modulation in northern Norway. Paper I presented the novel ADCP measurements in the Lofoten Maelstrom, and demonstrated the connection between the increase in bubble depths and the horizontal current gradients. Hence, it focused on the current-induced modulations in wave breaking. Paper II focused more on the sea state modulations in terms of H_{s}, and the performance of wave models including realistic surface current forcing. That is, in the Maelstrom but also in the larger coastal region surrounding it. A third aspect of the sea state was addressed in Paper IV, namely current-induced modulations in the short-term space–time extreme wave statistics. Expected extremes are computed from a number of spectral (sea state) variables, and are thus sensitive to the influence by ambient currents.

The physical processes that govern the sea state modulations were addressed in all papers. This is an important task, since it brings a more generalized view of the interactions, which may be applicable elsewhere. Refraction analyses has been a most essential step in this process, which resulted in the solver presented in Paper III.

Another way to consider the connection between the scientific papers is in terms of spectral modulation. To some extent, Paper I focused on the high frequency part of the spectrum: The high frequency components are saturated first, which results in an increased wave dissipation. The dissipation was manifested as air bubble injection due to wave breaking. Paper II focused more on the energy carrying frequencies in the spectrum, located at lower frequencies, through H_{s} ($\propto m_0$). In terms of spectral modulation, Paper IV was sort of a combination of Papers I and II since the expected extremes are computed from a set of spectral variables of different order. For instance, expected space–time extreme wave crests grow with increasing spectral steepness ($\propto m_1^2/m_0^2$), while at the same time, the "extremeness" of such large waves are found through normalization by H_{s}. As a consequence, the normalized expected extreme wave estimates are to some extent balanced by moments of different order, which are sensitive to the underlying interaction mechanism.

5.2 Main conclusions the from scientific results

The works within this thesis are the first to demonstrate the impact of the Lofoten Maelstrom on the sea state. The ADCP observations provide evidence that these changes include the wave breaking statistics (Paper I), wave heights (Paper I, Paper II, Paper IV), the wave spectrum (Paper II, Paper IV), and also the occurrence probability of extreme waves (Paper IV). For the latter point, Paper IV is the first work to demonstrate the sensitivity of stochastic space–time extremes in realistic currents. Furthermore, the results show that the Maelstrom is adequately represented in NK800, and that using the current fields as forcing in WAM800 provide realistic spectra (Paper II, Paper IV). Moreover, the associated spectral variables validates well against the observations. As a conse-

quence, spectral wave models give more realistic wave forecasts when including tidal currents as forcing; this beneficial in both an operational context (wave forecasts) as well as for engineering applications (hindcasts or reanalysis). Furthermore, the Maelstrom causes more intense wave breaking and is thus an important dynamic component in driving upper ocean mixing and air–sea fluxes.

In the coastal region of northern Norway, the model results suggest that including surface current forcing improves the sea state representation, particularly in areas with strong tidal currents. The results are, however, less conclusive in areas subject to ocean dynamics of less predictability, like submesoscale fronts. Nevertheless, the wave model with current forcing qualitatively resolves most of the areas known for dangerous waves, thus giving credibility to such forcing to be included in an operational context.

Indeed, in geographical terms, the objectives of this thesis are rather narrow; it is centered on the region of northern Norway, and to a large extent the Lofoten Maelstrom. This region, and more importantly its dynamics, is, however, representative of many places around the world. In particular intense tidal environments[1]—keeping in mind that some areas have very characteristic met–ocean conditions. Nonetheless, the convenient *relative wave convergence* solution (2.21) (Paper I), order of magnitude reasoning [e.g., (2.19) and Paper IV], and wave ray tracing (Paper III) are convenient methods that easily can be applied to assess the influence of currents on the wave field. Furthermore, ocean currents occur on different spatio-temporal scales throughout the world's oceans (*Gemmrich and Garrett*, 2012; *Romero et al.*, 2017; *Lenain et al.*, 2023). As such, their variability and space and time can be singled out using the diagnostic method proposed in Paper II (see Appendix C). In summary, the scientific results presented here are expected to have a general applicability.

5.3 Future perspectives

The scientific results suggest that the spectral modulation is sensitive to the underlying, or dominant, interaction mechanism. However, more observations are needed in order to draw more precise conclusions on this topic. Tidal currents are well suited locations for further investigation. The Maelstrom is still heavily undersampled, particularly its horizontal variability. Such variability can be explored in detail by applying quantitative 2D wave field measurement techniques like those reported by *Hansen et al.* (2016), *Kudryavtsev et al.* (2017), *Lenain et al.* (2023), and *Rascle et al.* (2018). This also allows to target the strong variability that occurs at scales smaller than 800 m. However, the aforementioned measurement techniques will only provide a short temporal coverage. Such limitations can be mitigated by, for instance, deploying an array of ADCPs covering different parts of the Maelstrom. Moreover, as wave buoys become more lightweight, cheaper, and thus expendable, deploying an array of such freely drifting devices could also resolve the inhomogeneities. Such measurements should preferably be compared with high-resolution numerical models, potentially also including phase–resolving models. Furthermore, recent work in the community (following *Bôas et al.*, 2020; *Bôas and Young*, 2020) aims at providing a mapping between the rotational component of the

[1] Like the Cape of St. James (British Columbia, see *Masson*, 1996), the Gulf of Main (Eastern Canada, see *Wang and Sheng*, 2018), the Pentland Firth (Great Britain, see *Saruwatari et al.*, 2013), the Dover Strait (English Channel, see *Mackay and Hardwick*, 2022), the Messina strait (Italy), Ushant (Iroise sea, see *Ardhuin et al.*, 2012), Port Phillips Head (Australia, see *Rapizo et al.*, 2017), and the Fraser Estuary (British Columbia, see *Baschek*, 2005)

current and the horizontal variability in H_s for swell–wave regimes; such a comparison would be interesting to perform in the Maelstrom.

Proper wave breaking statistics, including whitecaps at the sea surface and the depth of which the bubbles reach, are of interest to quantify the mixing and dispersion of matter due to waves. Such work is also interesting in the context of momentum transfer from the waves to the current. The effect by vertical mixing on transport of substances may not be pivotal within strong barotropic currents like the Maelstrom, but may be more impactful on strong vertically sheared currents.

With regards to current forcing, this study has exclusively focused on using surface currents. Even though this is a valid assumption in the barotropic Maelstrom, most other places it is not. Recent studies have shown that strong shear can lead to substantial changes in wave energy (*Quinn et al.*, 2017) as well as in wave breaking statistics (*Zippel and Thomson*, 2017). However, the uppermost currents are the most important, and their vertical shear is less important the shorter the waves (*Ellingsen and Li*, 2017; *Stewart and Joy*, 1974; *Kirby and Chen*, 1989). With regards to wave kinematics on vertically sheared currents, the ray tracing model in Paper III is a good candidate to perform a sensitivity analysis.

Lastly, this thesis has focused on the impact by currents on the wave field. Waves, however, also impact the mean flow (e.g., *Hypolite et al.*, 2021). In a tidally dominated estuary, *Olabarrieta et al.* (2011) found that the momentum transfer from waves to currents, particularly because of wave breaking, could change current speeds up to 0.5 m s^{-1}. Fully coupled model experiments are therefore good candidates to gain further insight on the broader range of interaction processes that occur between ocean waves and currents (*Breivik et al.*, 2015).

6 Scientific results

Paper I

Intense interactions between ocean waves and currents observed in the Lofoten Maelstrom

Øyvind Saetra, Trygve Halsne, Ana Carrasco, Øyvind Breivik, Torstein Pedersen, and Kai Håkon Christensen
Journal of Physical Oceanography, **51/11** (2021)

Intense Interactions between Ocean Waves and Currents Observed in the Lofoten Maelstrom

ØYVIND SAETRA,[a] TRYGVE HALSNE,[a,b] ANA CARRASCO,[a] ØYVIND BREIVIK,[a,b] TORSTEIN PEDERSEN,[c] AND KAI HÅKON CHRISTENSEN[a]

[a] *Norwegian Meteorological Institute, Oslo, Norway*
[b] *University of Bergen, Bergen, Norway*
[c] *Nortek AS, Oslo, Norway*

(Manuscript received 20 November 2020, in final form 3 September 2021)

ABSTRACT: The Lofoten Maelstrom has been known for centuries as one of the strongest open-ocean tidal currents in the world, estimated to reach 3 m s^{-1}, and by some estimates as much as 5 m s^{-1}. The strong current gives rise to choppy seas when waves enter the Moskenes Sound, making the area extremely difficult to navigate. Despite its reputation, few studies of its strength exist, and no stationary in situ measurements for longer time periods have been made due to the challenging conditions. By deploying for the first time in situ wave and current instruments, we confirm some previous estimates of the strength of the current. We also show that its strength is strongly connected with wave breaking. From a consideration of specific forcing terms in the dynamical energy balance equation for waves on a variable current, we assess the impact of the underlying current using a convenient metric formulated as a function of the horizontal current gradients. We find that the horizontal gradients are a likely explanation for the observed enhanced wave breaking during strong currents at a rising tide.

KEYWORDS: Currents; Gravity waves; Wave breaking; Tides

1. Introduction

The Lofoten Maelstrom, locally (and hereafter) referred to as Moskstraumen, is a very strong open-ocean tidal current in northern Norway. It is caused by the large difference in tidal amplitude between Vestfjorden and the Norwegian Sea. Moskstraumen is located in the Moskenes Sound between the Lofoten peninsula and the island of Mosken (Figs. 1a and 2). The Lofoten peninsula acts as a barrier for the northward-propagating tidal Kelvin wave, building up a water level difference. The tidal currents are thus driven by the pressure gradient across the Moskenes Sound (Gjevik et al. 1997; Moe et al. 2002; Ommundsen 2002). Its ferocity made it notorious as early as the Viking Age (Guerber 1909), with notable references in the classical literature like "A Descent into the Maelström" by Edgar Allan Poe (Poe 1841), and *Twenty Thousand Leagues Under the Seas* by Jules Verne (Verne 1869). In the first nautical chart covering Scandinavia, the "Carta Marina" (see Fig. 1b), the Swedish priest Olaus Magnus depicted the current as a giant whirlpool engulfing ships (Peterson et al. 1996). The word Maelstrom originates from the Dutch "malen" meaning *grinding*, referring to the ocean eddies generated by the current. These were thought of as sinks of water, whereby the water was drawn into the holes of large magical millstones grinding salt on the ocean floor (Guerber 1909), supposedly explaining the mechanism that makes the ocean salty.

Maritime navigation in the Moskenes Sound is considered safe only on slack tide. A recent incident involved the fishing vessel *Iselin* (see Fig. 1c), which capsized in the middle of the Moskenes Sound, fortunately without loss of human life (Smith 2017). The Norwegian Pilot Guide (Den norske los 2018) claims that ships with up to 10-kt speed (about 5 m s^{-1}) have been unable to advance. Their claim, however, is based solely on observations from ships and other eye-witness accounts.

Model studies (Gjevik et al. 1997; Moe et al. 2002; Ommundsen 2002) have estimated current speeds to reach 3 m s^{-1}, using a 500-m resolution barotropic ocean circulation model, but the authors noted the lack of observations to corroborate their results. Ship-based measurements with an acoustic Doppler current profiler (ADCP) were taken in 2009, where current speeds up to 1.7 m s^{-1} (Lynge 2011) were observed. The Institute of Marine Research tried to deploy current moorings in 1977, but the speed of the current made it too risky, and the attempt was abandoned (S. Sundby 2020, personal communication). Thus, to our knowledge, the ADCP observations reported here are the first in situ observations of its kind in Moskstraumen. That is, simultaneous observations of waves and currents spanning a considerable time period.

The theory describing wave–current interactions is well established (e.g., Longuet-Higgins and Stewart 1960; Phillips 1977; Andrews and McIntyre 1978; Phillips 1984). However, the response of surface waves to different current regimes at both mesoscale and submesocale is still an active field of research (e.g., Gallet and Young 2014; Quilfen et al. 2018; Vincent 1979; Ardhuin et al. 2017; Gemmrich and Garrett 2012; Masson 1996; Romero et al. 2020; Marechal and Ardhuin 2021). Recent studies include further development of modeling frameworks taking wave–current interactions into account (e.g., Moreira and Peregrine 2012; Ardhuin et al. 2012; Romero 2019; Villas Bôas et al. 2020) as well observational case studies (e.g., Quilfen and Chapron 2019; Romero et al. 2017; Kudryavtsev et al. 2017). In nearshore environments, wave–current interactions depend on the local wave and current

Denotes content that is immediately available upon publication as open access.

Corresponding author: Trygve Halsne, trygve.halsne@met.no

DOI: 10.1175/JPO-D-20-0290.1

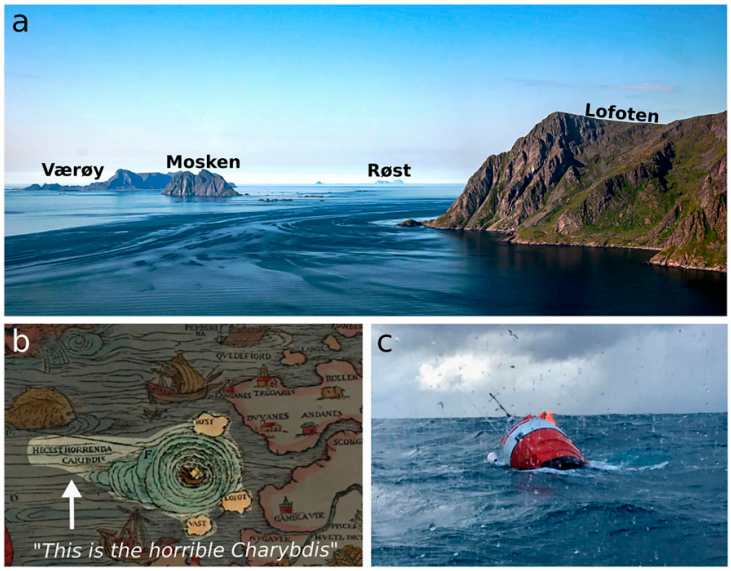

FIG. 1. The many views of Moskstraumen. (a) A photograph of Moskstraumen in the Moskenes Sound from 2009 by Jørn Røssvoll taken from a helicopter. The photograph is most likely taken during a falling tide, as seen from the geometry of the current bending northward around Lofoten. (b) Moskstraumen drawn in "Carta Marina" from 1539 by the Swedish priest Olaus Magnus. Moskstraumen is located in the center of the panel engulfing a ship. (c) The distressed fishing vessel *Iselin* photographed from a rescue vessel (picture courtesy of the Norwegian Sea Rescue Society). *Iselin* capsized in the Moskenes Sound in 2017 due to the fishing nets and ropes getting tangled up in the propeller.

conditions which, in turn are affected by the bathymetry, atmospheric and tidal conditions (Masson 1996; Rapizo et al. 2017). At the same time, wave–current interactions are also nonlocal with regards to the current's influence on the waves along their propagation path. This includes current-induced refraction, which is shown to play a key role in modulating the wave field for both swell and wind sea at scales up to several hundreds of kilometers (Gallet and Young 2014; Ardhuin et al. 2017; Romero et al. 2017; Kudryavtsev et al. 2017; Quilfen et al. 2018; Quilfen and Chapron 2019; Villas Bôas et al. 2020; Marechal and Ardhuin 2021). Both Vincent (1979) and Masson (1996) reported that their local observations of significant wave height variability needed to be adjusted for current-induced refraction. In the field studies of Romero et al. (2017), they found that wave breaking at scales ≤ 1 km was sensitive to the local gradients in the current, but the areas of enhanced wave breaking also overlapped with areas of convergent wave rays. In general, observations reflect cumulative effects as well as local processes.

The aim of this paper is to present the observations of waves and currents in Moskstraumen, shedding some light on dominant interaction processes. The paper is organized as follows. In section 2, we present the governing equations for waves on a variable current together with a simplified expression assessing the importance of the local current gradients on the wave field. We also present the various data, i.e., observed and modeled, which were used in the analysis. In section 3, we present the environmental conditions during the case study periods selected from our field campaign. In section 4 we present the results which are further discussed in section 5. Finally, our conclusions are presented in section 6.

2. Methods, data, and observations

a. Governing equations

1) WAVES ON A VARIABLE CURRENT

A plane surface wave propagating in a slowly varying medium can be described as

$$\eta(\mathbf{x}, t) = ae^{i\chi}, \tag{1}$$

where $\chi = \mathbf{k}\cdot\mathbf{x} - \sigma t + \phi$ is the wave phase function. Here, a, $\mathbf{k}$, $\mathbf{x}$, σ, t, and ϕ denote the wave amplitude, wavenumber vector, horizontal spatial coordinates, angular intrinsic frequency, time coordinate, and random phase, respectively. For waves on a current, the absolute angular frequency is

$$\omega = \sigma + \mathbf{k}\cdot\mathbf{u}, \tag{2}$$

where $\mathbf{u} = (u, v)$ is the horizontal Eulerian velocity vector representing an ambient current. We thus have

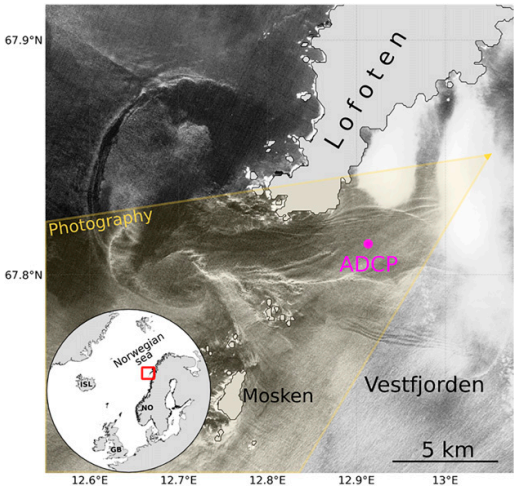

FIG. 2. The area of Moskstraumen. Moskstraumen is located in the Moskenes Sound between Lofoten and the island of Mosken in northern Norway, as indicated by the red square. The sea surface signature of Moskstraumen during a falling tide is captured by the Copernicus *Sentinel-2A* optical satellite at 21 Jul 2017. The signature is characterized by the plume-like structures west of Lofoten with the narrow white bands indicating areas of breaking waves. The plumes are heading westward. The yellow shaded area and magenta dot shows the area depicted in Fig. 1a and the location of the bottom-mounted ADCP, respectively. Iceland (ISL), Great Britain (GB), and Norway (NO) are marked for reference.

$$\frac{\partial \mathbf{k}}{\partial t} + \nabla \omega = 0, \tag{3}$$

which describes conservation of wave crests within any given area (see, e.g., Phillips 1977, p. 23). The angular intrinsic frequency and wavenumber are related through the general dispersion relation

$$\sigma^2 = g\kappa \tanh(\kappa d), \tag{4}$$

where d is the water depth and $\kappa = |\mathbf{k}|$.

Instead of resolving the phase of each single wave component it is also possible to apply a phase averaging model for the wave energy density E, which is common in wave forecasting. Without ambient currents, E is a conserved quantity. But in the presence of currents there is an exchange of energy between the wave field and the mean Eulerian current, and E is no longer conserved (Longuet-Higgins and Stewart 1964). The dynamical aspects of wave evolution could alternatively be formulated as an equation for the wave action, $N = E/\sigma$, which is a conserved quantity in the presence of currents (Bretherton and Garrett 1968; Phillips 1977). From a spectral wave modeling perspective it is common to consider $N = N(t, \mathbf{x}, \kappa, \theta)$, and the evolution of a wave field is modeled through the wave action conservation equation (e.g., WW3DG 2019), here using index notation

$$\frac{\partial N}{\partial t} + \frac{\partial}{\partial x_i}(\dot{x}_i N) + \frac{\partial}{\partial k_i}(\dot{k}_i N) + \frac{\partial}{\partial \theta}(\dot{\theta} N) = \frac{\hat{S}}{\sigma}. \tag{5}$$

Here, $i, j = (1, 2)$ represent the horizontal components, and θ is the direction of the wavenumber vector. The term $\hat{S}$ represents sources and sinks of E like wind forcing and wave breaking in addition to nonlinear interactions. The total time derivative terms (denoted with overdots) constitute the wave ray equations

$$\dot{x}_i = \frac{\partial \omega_i}{\partial k_i}, \tag{6}$$

$$\dot{k}_i = -\frac{\partial \sigma}{\partial d}\frac{\partial d}{\partial s} - k_i \frac{\partial u_i}{\partial s}, \tag{7}$$

$$\dot{\theta} = -\frac{1}{\kappa}\left[\frac{\partial \sigma}{\partial d}\frac{\partial d}{\partial m} - k_i \frac{\partial u_i}{\partial m}\right], \tag{8}$$

where s is a coordinate in the direction of θ and m is orthogonal to s. In Eq. (5), the terms in Eqs. (6)–(8) represent wave advection by the total group velocity, the evolution in wavenumber, and the change in wave direction, respectively.

2) HORIZONTAL CURRENT GRADIENTS AND WAVE FIELD MODULATION

Tidal fronts can be considered to be natural laboratories for studying wave–current interactions (Baschek 2005). When considering the processes in the small region with the most intense tidal currents, we chose to disregard the wind forcing in Eq. (5) in order to qualitatively assess the impact of the tides on the wave field. With no wind forcing, the evolution of the wave field would not be realistically represented under conditions with high wind speed. Although the wave field in Moskstraumen is known to become even more complicated under certain weather and wave conditions [see Den norske los (2018) and also the appendix], the spatiotemporal variations in the wind controls scales larger than those by the ocean currents and tides in our area of interest. Thus, local wind wave growth occurs at longer time scales than those associated with the tide (Tolman 1990). Furthermore, we will first disregard the dissipation in the region with most intense tidal currents since we are primarily interested in the period where the tidal currents impact the wave growth, before the waves break. We look more closely at the wave breaking process later on, however, in section 4. In the following, we turn to the equations for E. Wave energy density E is proportional to the square of the significant wave height, and is a common and convenient variable in wave measurements.

Following Phillips [1977, Eq. (3.6.21)], the nondissipative barotropic energy balance equation for waves on a variable current can be written as

$$\frac{\partial E}{\partial t} + \frac{\partial}{\partial x_i}(\dot{x}_i E) + S_{ij}\frac{\partial u_i}{\partial x_j} = 0, \tag{9}$$

where $\dot{x}_i = u_i + c_i^{(g)}$ from Eq. (6), where $c_i^{(g)}$ is the intrinsic group velocity. The last term in Eq. (9) is the radiation stress, which denotes the nonlinear transfer of energy between the

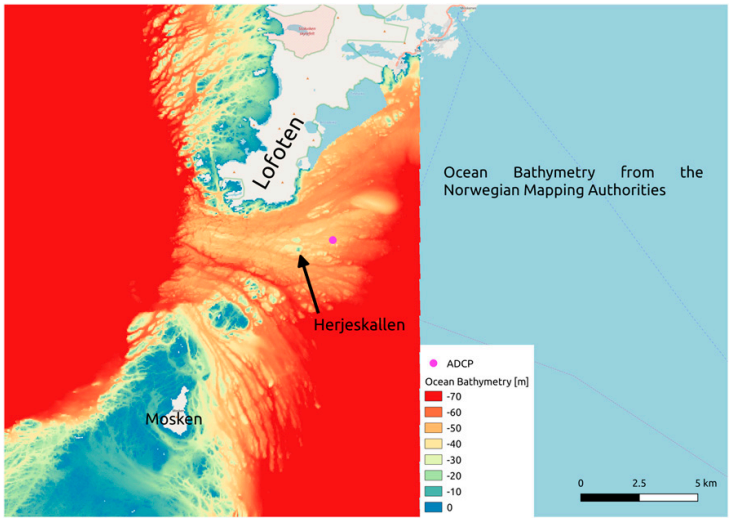

FIG. 3. The bathymetry in the Lofoten area. Red indicates areas with depth > 70 m. The ADCP instrument location is denoted with the magenta dot, located about 2 km east of the seamount Herjeskallen. The 50-m horizontal resolution bathymetry data are freely available from the Norwegian Mapping Authorities.

waves and the mean Eulerian currents. Equation (9) can be rewritten as

$$\frac{\partial E}{\partial t} = \underbrace{-\frac{\partial u_i}{\partial x_i}E}_{\text{current convergence}} \underbrace{-\frac{\partial c_i^{(g)}}{\partial x_i}E}_{\text{refraction}} \underbrace{-(u_i + c_i^{(g)})\frac{\partial E}{\partial x_i}}_{\text{wave advection}} \underbrace{-S_{ij}\frac{\partial u_i}{\partial x_j}}_{\text{radiation stresses}}. \quad (10)$$

The terms on the right-hand side are convergence/divergence of wave energy by the current field, refraction from horizontal gradients in the group velocity due to variations in the water depth or the ambient current, wave energy advection, and the interaction between the radiation stresses and the current gradients.

3) SCALING ARGUMENTS AND TIDAL FORCING ASYMMETRIES

Lacking direct observations of the horizontal variations, it is difficult to quantify the contribution from each term on the right-hand side in Eq. (10). We do know, however, that the tidal flow is associated with very strong current gradients (see Fig. 2 and later Fig. 9). Since these gradients are primarily due to the geometry of the coastline, bathymetry, and the sharp fronts that develop as the flow entrains the more quiescent regions on both side of the Moskenes Sound, we keep open the possibility that the horizontal length scale L_u associated with the tidal flow is different from the horizontal length scale L_w of the waves (Tolman 1990). The obvious cases to consider are when the waves and currents are either opposed or aligned. Opposing wind and currents are known to contribute to significant local wave growth in the Moskenes Sound [see Den norske los (2018) and also the appendix], for which we assume L_w and L_u are of the same order of magnitude. There is obviously also a modulation of the waves when the waves and currents are heading in the same direction, but reports indicate that the coupling is not as pronounced: the prevailing wave direction is from the southwest, and the waters east of Herjeskallen (Fig. 3) are known to be covered by whitecaps during rising tide, that is, during both calm and rough weather conditions. Heading in the same direction, waves will also increase when the current decelerates. In this case, the decreasing current opposes the waves, relative to its maximum.

Letting E_0, u_0, c_0 denote typical values for the wave energy, the speed of the current, and the wave group velocity, respectively, and letting $\beta = c_0/u_0$, we find that the right-hand side terms of Eq. (10) scale as

$$u_0 E_0 \left[\frac{1}{L_u} + \frac{\beta}{L_w} + \frac{1}{L_w} + \frac{\beta}{L_w} + \frac{1}{L_u}\right]. \quad (11)$$

If now $L_w/\beta \gg L_u$, we see that the first and last terms on the right-hand side of Eq. (10) would dominate. Previous studies suggests that L_u decreases in coastal areas due to the influence of the bathymetry (Tolman 1990). In our case, reasonable values are $u_0 = 3\,\mathrm{m\,s^{-1}}$ and $c_0 \sim 10\,\mathrm{m\,s^{-1}}$, hence $\beta \simeq 3$ and we need to require that $L_u \ll L_w/3$. For $L_u = 10^2 - 10^3$ m we would require that $L_w > O(10^4)$ m, which is only realistic when the waves and currents are aligned. We will analyze this special case in some detail below.

4) SIMPLIFIED WAVE ENERGY EQUATION FOR ALIGNED WAVES AND CURRENTS

Assuming now that $L_w/\beta \gg L_u$ holds, we may simplify Eq. (10) such that

$$\frac{\partial E}{\partial t} = -\frac{\partial u_i}{\partial x_i}E - S_{ij}\frac{\partial u_i}{\partial x_j}. \tag{12}$$

If we align the x axis with the wave propagation direction, the nonzero diagonal components of the radiation stress tensor [Phillips 1977, Eq. (3.6.27)] yield

$$\frac{1}{E}\frac{\partial E}{\partial t} = -\left[\left(2\frac{c_g}{c}+\frac{1}{2}\right)\frac{\partial u}{\partial x}+\left(\frac{c_g}{c}+\frac{1}{2}\right)\frac{\partial v}{\partial y}\right], \tag{13}$$

where c is the phase velocity. The ratio between the phase and group velocity determines the relative weight given to the current gradient components in the x and y directions. Equation (13) gives an impression of how the temporal rate of change of wave energy is related to the horizontal current gradients. The deep water limit allows us to simplify Eq. (13) further,

$$\frac{1}{E}\frac{\partial E}{\partial t} = -\left(\frac{3}{2}\frac{\partial u}{\partial x}+\frac{\partial v}{\partial y}\right) = -R_{\mathrm{wc}}. \tag{14}$$

The right-hand side term, excluding the minus sign in front, we denote "relative wave convergence," with the general symbol R_{wc}. At 50-m depth, the mean depth in the Moskenes Sound (Fig. 3), this corresponds to waves with a wavelength of less than approximately 100 m ($\lambda < 2d$) with corresponding wave periods from 8 s and below.

The R_{wc} is a function of the horizontal current gradients and can easily be computed from an ocean circulation model. Where the current field is convergent, the wave energy will grow. Hence, negative R_{wc} leads to an increase in energy density, and vice versa where $R_{\mathrm{wc}} > 0$. In areas with strong current gradients and barotropic conditions, Eq. (14) can thus provide insight into how the currents modulate the wave field.

b. Observations and model representation of Moskstraumen

1) ADCP MEASUREMENTS

Continuous bottom-mounted ADCP measurements were acquired for a 3-month period (6 December 2018–25 February 2019), using a Nortek Signature 500. This is a five-beam instrument capable of measuring currents, waves and turbulence simultaneously. Contrary to traditional ADCPs, the instrument contains a vertically oriented fifth beam, which was used as an echo sounder to both measure distance to the surface and high-resolution backscatter in the water column. The instrument was deployed at the entrance of the Vestfjorden basin as indicated by the magenta dot in Fig. 2, at 50-m depth about 2 km east of the seamount Herjeskallen (Fig. 3). The instrument was mounted on a tripod in a gimbal to keep it vertically oriented. We used current and wave data from both the averaging mode (averaged values of 60 samples every 10 min with 1-Hz sample rate and vertical bins of 2 m) and burst mode (17 min sample window with 2-Hz sample rate and 13-min gaps between measurement windows), in addition to the raw altimeter echo burst (0.0011-Hz sample rate with vertical bins of 2.4 cm). Nortek's OceanContour (v. 2.1.2) software was used for processing the data.

Due to the strength of Moskstraumen, in particular during spring tide (i.e., maximum tide during lunar cycle), the instrument tilt sometimes exceeded the limit of what can be compensated by the gimbal. The limit used by Nortek was 10°. For measurements with high tilt, wave data cannot be estimated with sufficient degree of accuracy. Current measurements, however, can be used.

2) ATMOSPHERIC, OCEAN CIRCULATION, AND SPECTRAL WAVE MODEL DATA

The NORA10 hindcast (Reistad et al. 2011) was used to assess the wind conditions during the field campaign. The horizontal resolution is approximately 10 km, whereas the temporal resolution of the wind field is one hour.

The ocean surface currents were taken from NorKyst800, the Norwegian Meteorological Institute's operational version of the Regional Ocean Modeling System (ROMS; see Shchepetkin and McWilliams 2005). NorKyst800 is a three-dimensional ocean circulation model (hereinafter just referred to as the ocean model) with 800-m horizontal resolution. The vertical dimension is resolved using a terrain-following σ coordinate with 35 levels, with higher resolution close to the surface. The uppermost layers have a resolution of approximately 30 cm in the area of interest. Output fields have a temporal resolution of 1 h. Further specifications of the model setup are given by Albretsen et al. (2011).

A spectral wave model was used to assess the dominating wave conditions outside the area close to the observation site. The estimates are based on the Wave Analysis Model (WAM; Komen et al. 1994). This is an upgraded version of the third-generation WAM code developed under the EU-funded project MyWave (Behrens et al. 2013). The total wave spectrum is made up by the wind sea part and swell, where the wind sea is under influence of the local winds. A common separation of the two regimes is that the wind sea part of the spectrum consists of wave components with phase speed less than the local wind velocity projected onto the wave component direction. Swell is then defined as the remaining part of the spectrum. See Behrens et al. [2013, Eq. (18)] for the exact separation in the WAM model, which also includes the directional difference between the wind and waves.

3) SATELLITE OBSERVATIONS

Data from two of the Copernicus Sentinel missions, i.e., Sentinel-1 (S1) and Sentinel-2 (S2), have been used to look for sea surface signatures of wave–current interactions in Moskstraumen. Both missions consist of polar-orbiting satellites with 180° phase difference. The S1 satellites carry a C-band synthetic aperture radar (SAR) and the S2 satellites carry a Multispectral Instrument (MSI), sampling 13 spectral bands. For S1, we used the high-resolution ground range detected interferometric wide swath mode products with 20 m × 22 m horizontal resolution (range × azimuth). For S2, the spectral bands

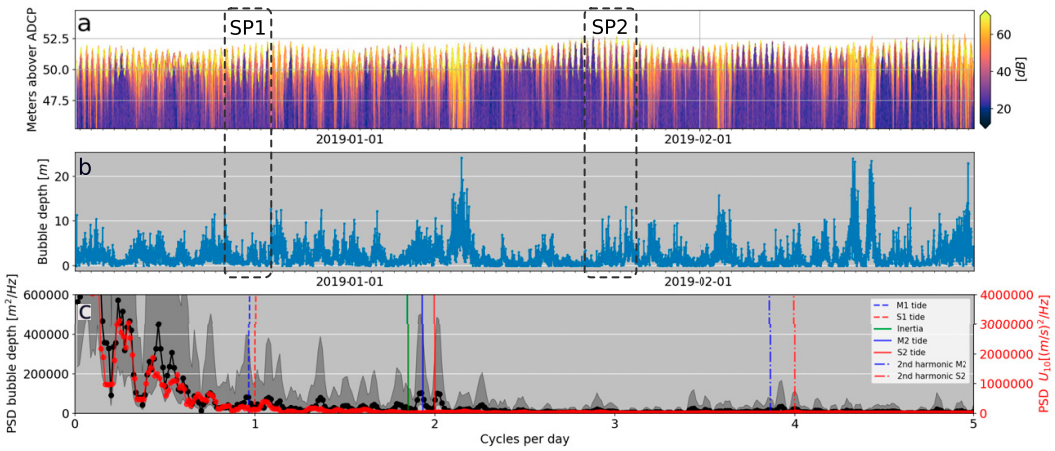

FIG. 4. Computation of approximate bubble depth from the full time series of ADCP measurements together with modeled wind. (a) The smoothed altimeter echo burst (AB) measurements where values above the sea surface are masked out by means of the pressure measurements. (b) The approximate bubble depth computed from the AB measurements and (c) the spectral representation of approximate bubble depth (black line) and U_{10} (red line) for the entire measurement period. The black shaded area denotes the 95% confidence limit for the bubble depth. SP1 and SP2 denote the case study periods in December 2018 and January 2019, respectively. Frequencies of tidal constituents and the inertial frequency are plotted in the lower panel.

either have 10 m × 10 m (4 bands), 20 m × 20 m (6 bands), or 60 m × 60 m (3 bands) horizontal resolution. We used the frequency band B4 with a central wavelength of 664.6 nm. As a consequence of the polar orbits, the temporal resolution for the Lofoten area is quite high, with approximately daily and subdaily coverage for S1 and S2, respectively. However, S2 MSI does not acquire images at low solar angles, which in practice means that there is no coverage in the period from late October until the end of February.

As an illustration of the surface signature of the current at a falling tide, where the flow is directed out of Vestfjorden, we included an optical image (acquired by *Sentinel-2A*) in Fig. 2. The image clearly shows the strong current gradient on the eastern side (upstream) as well as a plume-like structure on the western side of Moskstraumen, where the outgoing current meets the open ocean.

c. *Wave breaking derived from high-resolution raw altimeter echo bursts*

Events of enhanced wave breaking were identified using the raw altimeter echo bursts (hereinafter AB) from the ADCP (Fig. 4a). Such measurements can be used as a proxy for wave breaking (Thorpe 1986; Wang et al. 2016; Strand et al. 2020). The data were acquired by an upward-looking echo sounder with a vertical bin resolution of 2.4 cm. From the AB, we estimated a bubble penetration depth in the water column based on signal intensity. We define the bubble depth as the layer between the sea surface and the value from AB exceeding a threshold value, set to 40 dB. All values within the surface layer must exceed the threshold in order to be attributed to wave breaking.

Noise in the AB signal were smoothed column wise using a running mean filter. A time series of the smoothed vertical columns closest to the sea surface is shown in Fig. 4a. Here, values above the sea surface are masked out by means of the pressure measurements. The approximate bubble depth computed from the entire measurement period is shown in Fig. 4b. Outside the spring tide periods of investigation (denoted SP1 and SP2 in Fig. 4), we found that, qualitatively, the bubble penetration depth corresponded well with the wind speed. This was particularly evident during the strongest storms, with a bubble depth of more than 20 m (Fig. 4b). Moreover, it is possible to separate the six periods of spring tide during the three months measurement period from the envelope of the sea surface height, Fig. 4a.

3. Weather conditions during the case study periods

The area surrounding Moskstraumen, or the Lofoten area, is located in an area of prevailing southwesterly winds and waves, particularly during the storm season in fall and winter. In the current work, we focus on two periods during spring tide, i.e., 21–24 December and 22–26 January. These were chosen since they included periods with strong horizontal current gradients, sometimes combined with low wind speeds. Time references refer to UTC time. In the following we provide a brief description of the dominant weather pattern for both periods, which is summarized in Fig. 5.

a. *21–24 December 2018*

At noon 21 December, the synoptic weather situation was dominated by a strong high pressure centered over the Northern Scandinavian peninsula, which, together with a weak low pressure system developing between the Svalbard archipelago and the island of Jan Mayen, directed southerly winds

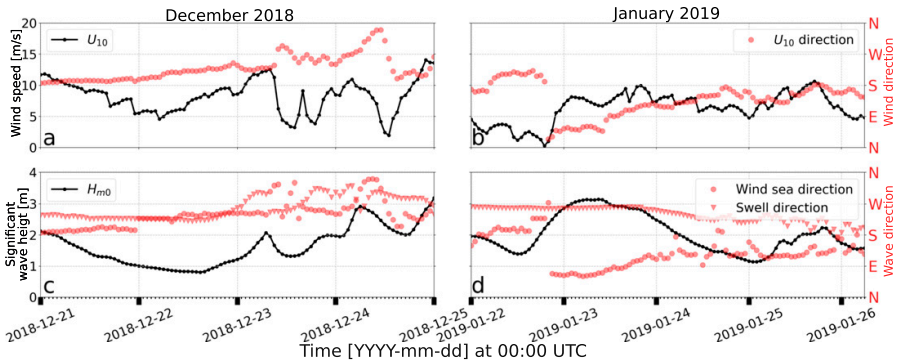

FIG. 5. Time series of the dominant wind and wave conditions during the two periods under consideration. (top) Wind speed at 10 m (U_{10}; black) and wind direction (red circles) from a grid point in the NORA10 hindcast close to the ADCP location. (bottom) Significant wave height (H_{m0}, black) together with the wave directions (red) from a WAM spectral wave model grid point close to the ADCP location. Wave directions are given for the wind sea regime (circle) and swell (triangle), where wind sea and swell are discriminated by a criterion based on the directional difference between wind and wave propagation as well as the inverse wave age. All directions follow the meteorological convention (coming from). N, E, S, and W denote north, east, south, and west, respectively.

over Moskstraumen (Fig. 5a). During 22 December the wind turned southwesterly, increasing in strength. On 24 December the synoptic weather situation was dominated by a rather intense low pressure system coming from the west/southwest. As this low approached the Norwegian coast, the wind speed increased to about 14 m s^{-1} in the late evening. The significant wave height was less than 3 m during the entire period (Fig. 5c). The wind sea and swell were mainly headed eastward.

b. 22–26 January 2019

On 22 January a weak high pressure ridge was located over the Lofoten peninsula, resulting in weak southerly winds (less than 5 m s^{-1}) and significant wave heights below 2 m (Figs. 5b,d). During the evening, a high pressure system built up over the Svalbard archipelago, while at the same time a more intense low pressure system came in from the southwest near Iceland. This resulted in a change to northeasterly winds at the observation site and steadily increasing wind speed. The large-scale wind pattern remained stationary for the rest of the study period, with the observation site located between these two synoptic systems.

4. Results

a. Current maxima

For the 3-month period of the ADCP deployment at the seabed in Moskstraumen, we measured current speeds up to 3 m s^{-1} at 10-m depth, confirming previous model studies (Gjevik et al. 1997; Moe et al. 2002; Ommundsen 2002). Due to the instrument's location, we do not expect this to represent the maximum strength of the tidal current, which is more likely to be found where the Moskenes Sound is at its narrowest.

b. Wind, waves, and enhanced wave breaking

There is a connection between the observed bubble depth and the modeled wind (Figs. 5 and 6). The wind affected the wave energy density spectrum and the bubble depth measurements in terms of both its strength and direction. This was particularly evident during the second part of January 2019. Here, the wind had shifted from heading east and northward to more westward (about 2000 UTC 22 January, Fig. 5b). It also ramped up in strength. The impact on the wave energy spectrum was a transition to a wider spectrum. This is seen at 2000 UTC 22 January and 1000 UTC 25 January with more energy on neighboring frequencies around 0.1 Hz and 0.2 Hz, respectively (Fig. 6d). Considering the AB, the sea surface got rougher, indicating enhanced wave breaking during larger portions of the period, in particular from 1000 UTC 25 January to 0000 UTC 26 January (Fig. 6b).

To compare the wind speed with enhanced wave breaking (or bubble depth), we performed a power spectral density (PSD) analysis on both these variables for the entire measurement period (Fig. 4c). Here we found that the low frequencies in the PSDs fitted well with the passage of synoptic weather systems. That is, from zero and up to about 0.75 cycles per day. For lower frequencies, the wind speed signal dropped close to zero while the enhanced wave breaking had spikes close to those of the semidiurnal tidal constituents, M_2 and S_2.

c. Wave breaking during a rising tide

The time series of relative wave convergence R_{wc}, computed from the ocean model at the ADCP location, are presented in Figs. 7a and 7e. Both panels consistently show negative wave convergence for approximately 3-hourly periods before pronounced peaks in the surface tracker signal from the ADCP (Figs. 7b,f). The peaks indicate enhanced wave breaking and are marked with gray vertical bars. Moreover, the enhanced wave breaking corresponded with the maximum current speed (Figs. 7c,g). This was further supported by the spectral representation of wave breaking during all spring tide situations in our ADCP data (Fig. 8). Here we found good agreement

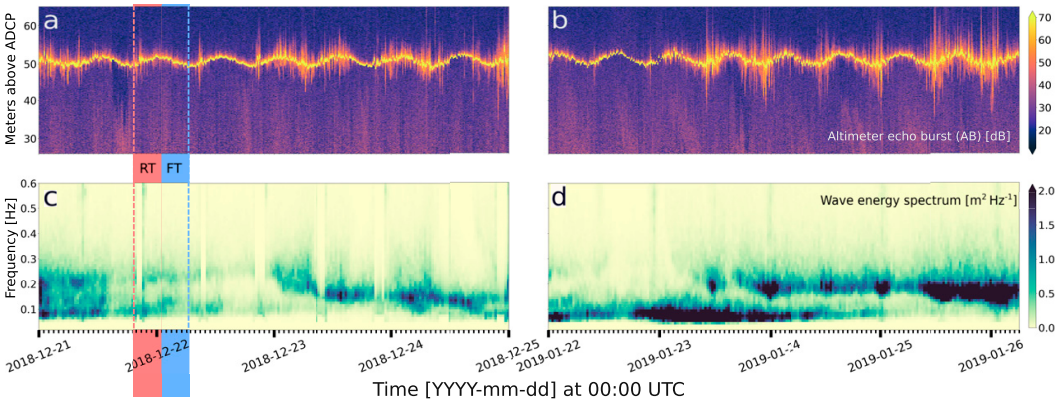

FIG. 6. Time series of altimeter echo burst (AB) and wave energy spectrum during the study periods from the ADCP measurements. (a),(b) AB inverse echo sounder signal from the ADCP. (c),(d) The wave energy spectrum from December 2018 and January 2019, respectively. The red and blue areas approximately show the phases of a rising tide (RT) and a falling tide (FT), respectively. At the location of the ADCP, the currents shift direction from eastward to westward during RT. During FT, the currents shift direction from westward to eastward. RT is also characterized with maximum current speed which corresponds with the spikes in the AB signal during RT.

between bubble depth and the M_1, S_1, and S_2 tidal frequencies, and in particular the M_2 constituent. The inertial frequency is close to the M_2 frequency in the Lofoten area. All these events happened at a rising tide, which means that the tidal flow was directed eastward into Vestfjorden (right panels, Fig. 9). The current speed shows an almost uniform vertical profile, confirming the assumption of predominantly barotropic conditions in Eq. (9).

The degree of alignment between the Eulerian current and mean wave direction is shown in Figs. 7d and 7h. Here, the directions are projected on to one another, with values of unity indicating that the current is headed in the mean wave propagation direction and going against for negative values. In December 2018 (left panel, Fig. 7), we found repeated events of enhanced wave breaking when the flow was in the direction of the waves at current maximum. This period was characterized by winds mostly below 10 m s^{-1} and a steady propagation of swell from the west (Figs. 5a,c). Likewise, in the beginning of January 2019, waves would also break when propagating in the direction of the current during current maxima (see between

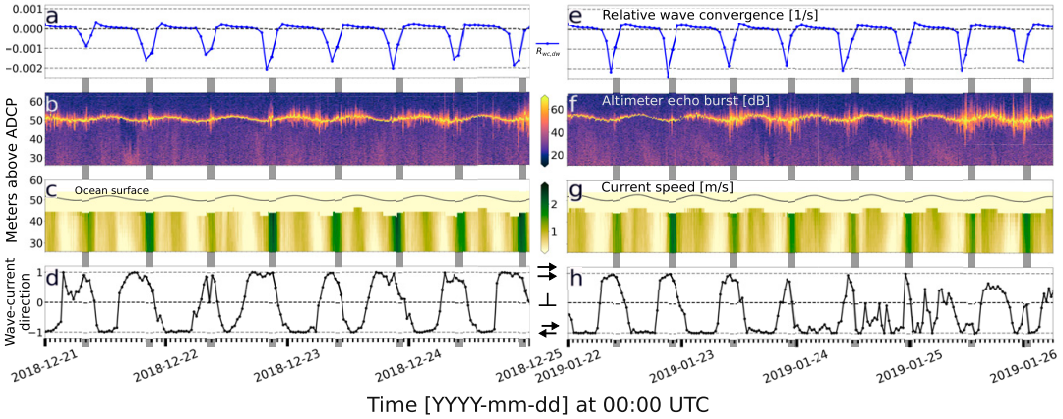

FIG. 7. Time series of wave and current properties for the two study periods. (a),(e) Relative wave convergence, $R_{wc,dw}$, computed from the ocean model. (b),(f) Altimeter echo burst (AB) data from ADCP. (c),(g) Vertical profile of current speed from ADCP and the sea surface from bottom pressure measurements. (d),(h) Projected wave and current direction where values 1, 0, and −1 denote same, orthogonal, and opposite direction for wave propagation and currents, respectively. Vertical gray bars indicate periods of max current speeds at the rising tide.

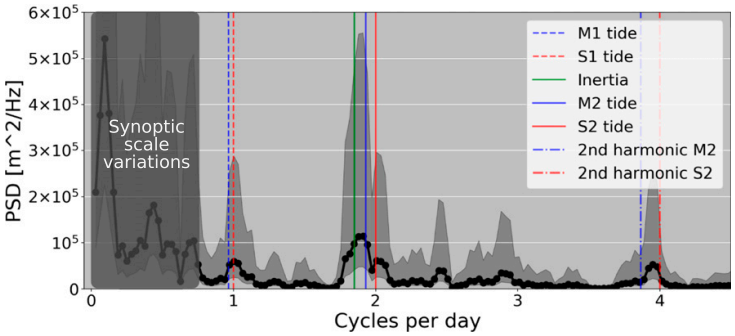

FIG. 8. Power spectral density of approximate bubble depth (black line) during spring tide situations from the ADCP measurements. The black shaded region around the PSD denotes the 95% confidence limit. The spectral representation shows increased wave breaking, which coincides with the frequency of the tidal constituents, in particular M_2, S_2, and the inertial. These frequencies correspond to the maximum current speed in Moskstraumen. The synoptic-scale variations in U_{10} coincide with wave breaking from zero up to approximately 0.75 cycles per day as seen in Fig. 4c.

0000 UTC 22 January and 1200 UTC 23 January in Figs. 7f–h). When the wind turned northwesterly and ramped up (around 0300 UTC 23 January, Fig. 5b), we ultimately observe a shift to higher frequencies in the wave energy spectrum (Fig. 6d). We also observe a general increase in wave breaking, mostly before and during current maxima (see between 1200 UTC 23 January and 0000 UTC 24 January in Figs. 7f,g). From 1200 UTC 24 January and out, the waves were opposing the current to a larger degree, including current during maxima (see 1200 UTC 25 January in Figs. 7f,h). This period was also characterized with enhanced wave breaking, still containing spikes around the current maxima.

d. *Moskstraumen from ocean model, satellite observations, and ADCP*

Figure 9 illustrates the sea surface signature of Moskstraumen at falling and rising tides. A falling tide is characterized by white narrow bands forming plume-like structures west of Lofoten in the optical S2 image (bottom left), and a wider white shaded area in the

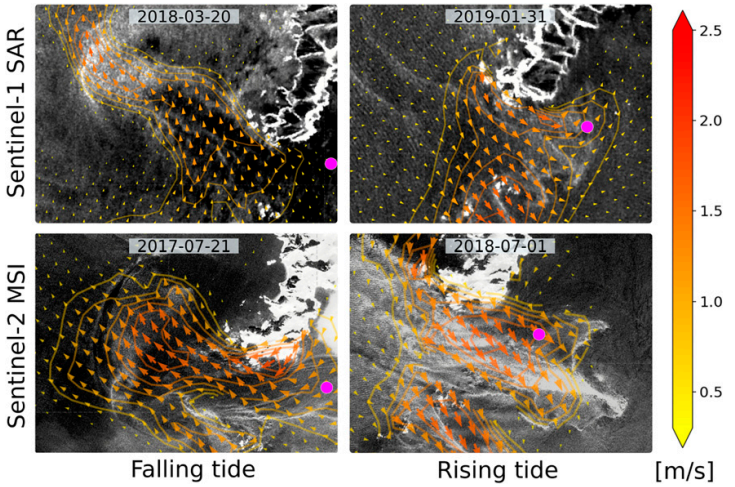

FIG. 9. Satellite and ocean model representation of Moskstraumen. Satellite imagery of Moskstraumen at (left) a falling tide and (right) a rising tide with modeled ocean surface currents overlaid. The satellite images in the top and bottom panels are from the Copernicus Sentinel-1 and Sentinel-2 missions, respectively. The magenta dot indicates the position of the bottom-mounted ADCP. The dates of the events are denoted in each of the images. The image in the top-right panel was taken during the ADCP deployment. The time difference between satellite acquisition and model time was within 30 min for all the cases.

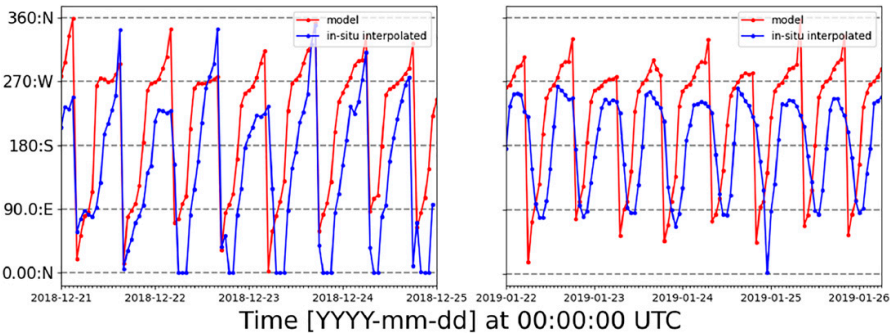

FIG. 10. Time series comparing the ocean current direction between the ocean model and the ADCP measurements for the two study periods. N, E, S, and W denote north, east, south, and west, respectively. The red line shows output from the ocean model interpolated to the location of the ADCP. The blue line shows the ADCP measurements interpolated to the temporal resolution of the ocean model. Direction here denotes where the current is heading to.

S1 SAR image (top left), both indicating zones of wave breaking (Kudryavtsev et al. 2005, 2017). The situations during a rising tide (right panels in Fig. 9) shows similar structures, but now the tidal current flow into Vestfjorden. We have overlaid the modeled surface currents on the satellite images in Fig. 9. The horizontal structure of the tidal flow appears to be well represented by the model.

Figure 10 compares the modeled ocean current with the ADCP measurements. The modeled currents were interpolated to the measurement location and the ADCP measurements were linearly interpolated to the temporal resolution of the model. Despite an overall satisfactory agreement between the two, there were differences in both the gradients of the current direction (i.e., the turning rate) and the phase. This is unsurprising given a model resolution of 800 m. The difference in time and direction was generally less than 2 h and 90°, respectively.

In Eq. (14), we are primarily interested in the duration of the periods of positive and negative relative wave convergence, and not necessarily the magnitude. These periods were estimated to last 4–5 h (Fig. 7). Hence, the discrepancies in terms of the direction and its phase between the model and the ADCP data were within the limits which we considered to be satisfactory for the time scales considered here.

e. Current gradients

The modeled horizontal current divergence, $\delta = \partial u/\partial x + \partial v/\partial y$, and the vertical vorticity $\zeta = \partial v/\partial x - \partial u/\partial y$ were computed for the area surrounding Lofoten. An example during a rising tide is shown in Fig. 11, where the divergence and vorticity are normalized by the inertial or Coriolis frequency f. During all the rising tide situations in the two study periods, the location and horizontal extent of the divergent and convergent areas in the Moskenes Sound were consistent with what is shown in Figs. 11d and 11e. That is, the tidal current formed two eddies, the northernmost located just east of the Lofoten peninsula, rotating counterclockwise, and the southernmost just east of Mosken, rotating clockwise (see the relative vorticity plot in Fig. 11e). As the current turned with the tide, the northernmost eddy disappeared while the southernmost eddy was advected out of the Moskstraumen branch before dissipating in Vestfjorden (not shown). The main structures in Moskstraumen resolved by the ocean model during a rising tide are in accordance with earlier studies by Lynge (2011).

Recent studies show that the current's vertical vorticity plays a key role in modifying several properties of the wave field like peak period, direction and significant wave height (e.g., Gallet and Young 2014; Quilfen et al. 2018; Quilfen and Chapron 2019). In idealized experiments, Villas Bôas et al. (2020) showed that refraction was the main mechanism leading to gradients in significant wave height, and that the effect of divergence was significantly smaller, even when adding an energetic divergent flow to a purely rotational one. Moreover, Villas Bôas and Young (2020) derived an expression for wave action diffusivity showing that the diffusivity was only a function of the rotational part of the current to first order. This is in accordance with the result showing that the curvature of a wave ray can be computed from the ratio between the vorticity and the group velocity

$$\chi_{\mathrm{rc}} = \zeta / c_g, \tag{15}$$

assuming $\delta_{\mathrm{cu}} = |\mathbf{u}|/c_g$ is small. The term χ_{rc} is the wave ray curvature (m^{-1}) (Kenyon 1971; Dysthe 2001).

In the area west and southwest of the Moskenes Sound, there were several regions with ζ of the same order as f, as seen in Fig. 11b. This was the case for both the study periods (not shown). The location of these regions varies with the flow and was in general advected northward by the Norwegian coastal current. To investigate the impact from current-induced refraction, we performed a simple ray-tracing analysis solving Eqs. (6)–(8) numerically. Figure 12a show the effect of refraction for an in incoming 7 s period long crested wave when exposed to the current field in Fig. 11c. The initial wave propagating direction $\alpha_{\mathrm{in},0}$ was chosen according to values from the spectral wave model. In this case the Moskenes Sound was subject to diverging wave rays. Wave ray paths are, however, sensitive to their initial direction as well as to the location of areas with strong ζ (Masson 1996). To assess the sensitivity with respect to the initial propagation direction, we computed the wave ray density from perturbing the incoming wave direction, which we denote $\alpha_{\mathrm{in},0}$. The area in Fig. 12a was further divided into grid boxes with size 5 times the grid resolution of the ocean model,

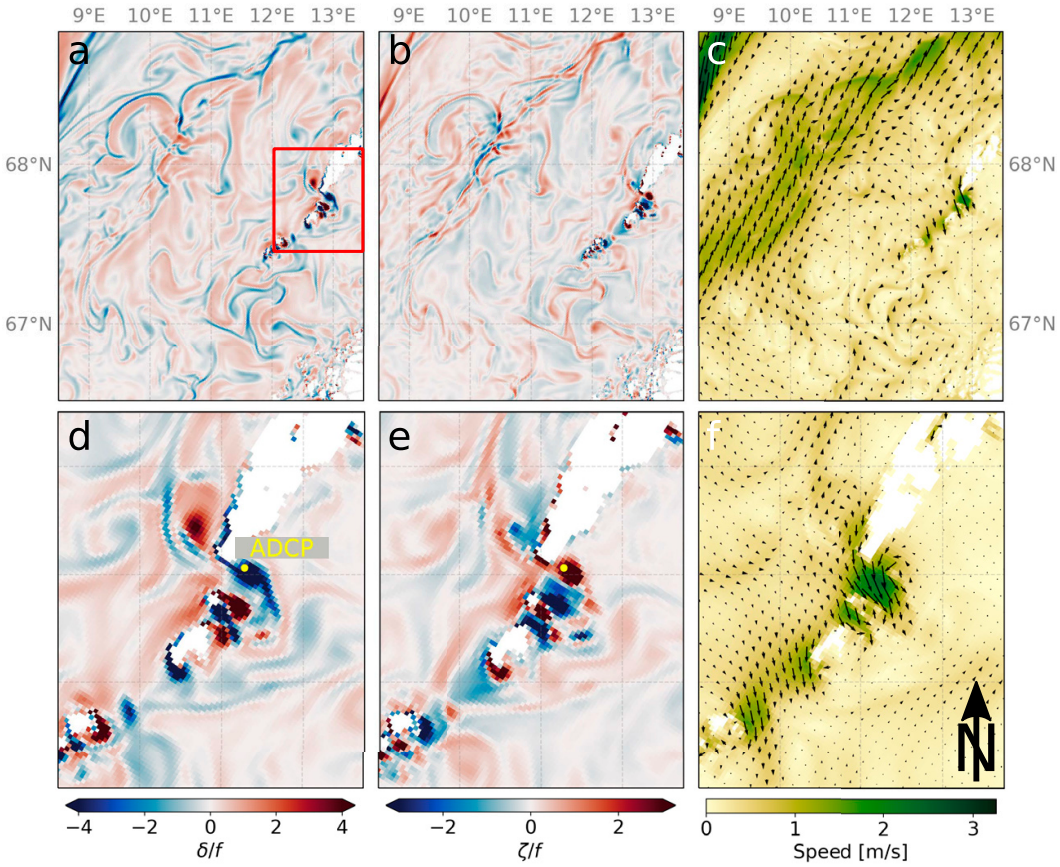

FIG. 11. An overview of the horizontal surface current gradients and speed at 2200 UTC 22 Jan 2019 during a rising tide computed from the ocean model showing the (a),(d) current divergence; (b),(e) vertical vorticity; and (c),(f) current velocity vectors overlaid the current speed. Divergence and vorticity are scaled by the inertial frequency. (top) The large-scale situation and (bottom) a zoom in on the area of interest covering the red square in (a). The yellow dot denotes the ADCP instrument location.

for which the wave ray density was computed for each grid box. The ray density is the ratio between the average number of wave rays for all realizations within the grid box and the number of incoming wave rays in the initial grid boxes, i.e., before refraction due to currents had happened. The wave ray density could be considered an indicator for wave energy, with dense areas having larger energy due to crossing waves (Rapizo et al. 2014). Figure 12b show the spatial distribution of wave ray density for five realizations of the 7-s period wave, i.e., four 2.5° directional increments around $\alpha_{in,0}$ including the result for $\alpha_{in,0}$. From the computation, the Moskenes sound was not exposed to focusing wave rays with wave ray density just below one.

f. *Evolution and horizontal extent of relative wave convergence*

Temporal evolution of relative wave convergence R_{wc} and ζ in the Moskenes Sound are presented in Fig. 13. Note that R_{wc} was computed with the x axis taken as the direction of wave propagation as in Eq. (14), implying waves coming from west. The areas of strong ζ and R_{wc} were collocated in space and time, in particular for the two cyclonic and anticyclonic eddies in the Moskenes Sound described above. The extent of the area with negative R_{wc} covering the ADCP was growing steadily from 2000 UTC 22 January (Fig. 13a) until 2200 UTC 22 January (Fig. 13c), with the latter being the time when enhanced wave breaking and maximum current speed was measured by the ADCP (Figs. 7f,g). At this point, the area had the shape of an ellipse with minor and major axes of approximately 5 km in north–south direction and 10 km in east–west direction, respectively. The location and extent of R_{wc} and ζ was about the same throughout January 2019 (not shown).

5. Discussion

a. *Estimating the effect of relative wave convergence*

According to Eq. (14), the wave energy density is expected to grow steadily during periods of negative wave convergence.

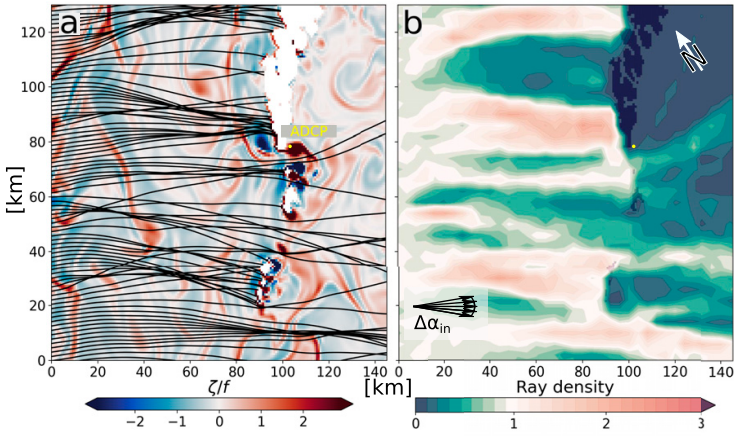

FIG. 12. Temporal evolution of wave rays from solving the wave ray equations for the current velocity field in Fig. 11c. (a) The evolution for a long crested 7-s period wave with initial propagation direction according to the WAM model. The wave rays are overlaid the vorticity field. (b) The density of wave rays computed from five realizations of the same wave in (a), but with five different initial propagation directions, i.e., waves with directional increments, $\Delta\alpha_{in}$, of 2.5° around the central initial propagation direction, as shown in (a). The directional increments are exaggerated for illustration purposes. The "ray density" is computed for grid boxes with size of 5×5 the grid resolution of the ocean model and is the ratio between the average number of wave rays for all realizations and the initial number of rays in the incoming grid boxes.

This means that energy accumulates in the wave field, leading to a net increase in wave height. A first-order estimate on the effect of relative wave convergence can be made by discretizing Eq. (14),

$$\frac{1}{E_k}\frac{E_{i+1}-E_i}{\Delta t} = -R_{\mathrm{wc}}. \tag{16}$$

Here i denotes the discrete time levels $\Delta t = t_{i+1} - t_i$. Temporal modulation of E due to R_{wc} is then obtained by rewriting the expression as

$$E_{i+1} = E_i - \Delta t E_i R_{\mathrm{wc}}. \tag{17}$$

Equation (17) was solved for a range of representative R_{wc} values computed from the ocean model. Figure 14 show the isolated effect of R_{wc} on the wave energy density in a wave field with initial value $E_0 = 1$. Figure 14b show two examples of how the wave energy density changes for waves propagating a representative distance of 10 km with varying R_{wc} (Figs. 13a–d). The 7-s period wave ($c_g = 5.5\,\mathrm{m\,s^{-1}}$) propagates 10 km in approximately 30 min. While propagating, the wave group experiences varying R_{wc}, and the resulting maximum positive change in wave energy density is $\Delta_{E,\max} = E_{\max} - E_0 \simeq 3\,\mathrm{m^2\,Hz^{-1}}$ (dashed line, duration = 25 min in Fig. 14b). The 5 s period wave ($c_g = 3.9\,\mathrm{ms^{-1}}$) propagates the distance in approximately 43 min, with a resulting $\Delta_{E,\max} \simeq 4.5\,\mathrm{m^2\,Hz^{-1}}$ (solid line, duration = 35 min in Fig. 14b).

Longer waves approaching the shallow water limit would also be modulated according to Eq. (17), using the shallow water solution of Eq. (13). The group velocity for shallow water waves would be larger than $22\,\mathrm{m\,s^{-1}}$ in the area of interest, which means they would propagate a distance of 10 km in less than 8 min. Even if the relative weight of the current gradients is larger for the shallow water solution than for deep water, the propagation speed limits the wave growth being bounded by the extent of the area with strong current gradients.

Relative wave convergence of $O(10^{-3})\ \mathrm{s^{-1}}$ produces the same effect as current gradients of $O(10^{-1})\ \mathrm{s^{-1}}$. We expect the current gradients in Moskstraumen to be higher for certain periods, in particular during spring tide, and capable of modulating the wave field according to Eq. (17). However, small-scale variability in the currents not resolved by the model could cause directional changes in the mean current for certain areas. The areas of convergent and divergent currents change accordingly, which in turn affects R_{wc}. In addition, if a wave is not propagating in the positive x direction, the cross terms in the radiation stress tensor (12) becomes nonzero and the contribution from each of the horizontal current gradient terms in Eq. (13) changes accordingly. This would again affect R_{wc}. Another important aspect is that Eq. (14) does not take dissipation through wave breaking into account nor input of energy from the wind, which obviously is present in our measurements (Figs. 7b,f).

Another interesting feature is the observation that the minimum relative wave convergence occurs halfway during the period of negative wave convergence (top panel, Fig. 7). One might expect the maximum growth rate to be associated with enhanced wave breaking. It is, however, the horizontal extent of the current gradients that is important for the waves to "feel" the effect of the current over a sufficiently long period.

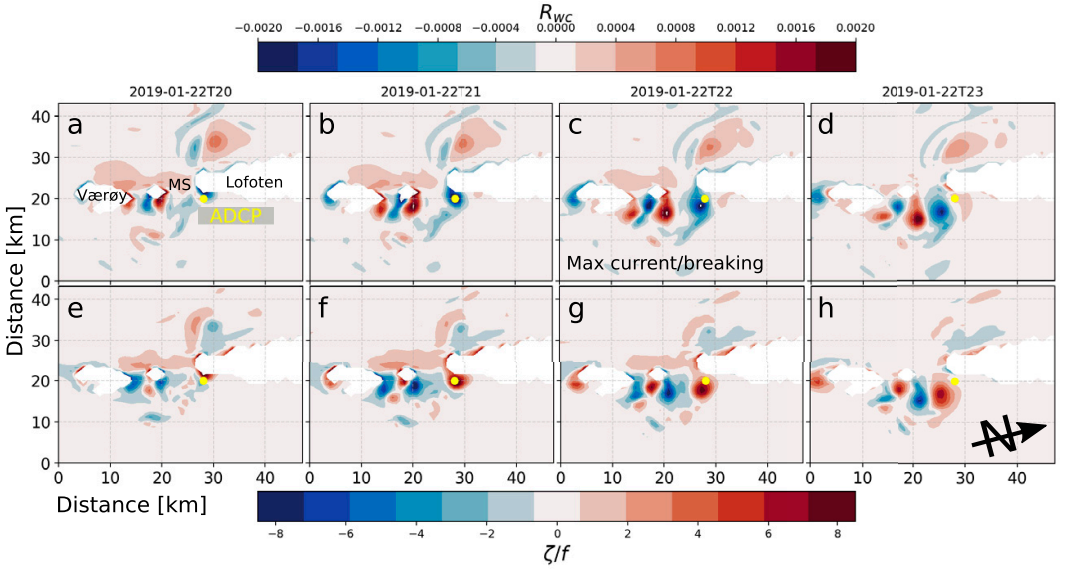

FIG. 13. The development of areas of relative wave convergence R_{wc} and normalized vertical vorticity ζ/f during a rising tide in Moskstraumen. The R_{wc} was computed with the x axis taken as the direction of wave propagation as in Eq. (14), implying waves coming from west. The island of Værøy and the southern tip of the Lofoten Penisula are shown in (a). "MS" denotes the Moskenes Sound. The location of the ADCP is indicated by the yellow dot.

As long as the relative wave convergence is negative, the waves will continue to grow despite a decrease in magnitude. This is clearly seen in Fig. 14b where $E = E_{max}$ occurs long after $R_{wc}(t) = R_{wc,min}$.

b. *Wave–current interactions and wave breaking*

From the observations, enhanced wave breaking systematically occurred during a period of negative wave convergence ($R_{wc} < 0$, see Figs. 7a,b,e,f), and coincided with the current maximum (Figs. 7c,g). From a spectral analysis, we found a good correspondence between the enhanced wave breaking and the semidiurnal tidal constituents M_2 and S_2 (Figs. 4c and 8). This was consistent during periods with wind speeds well below 10 m s^{-1} with steady swell from the west, but also in periods with higher wind speeds and local wind sea propagating eastward, like at the end of January 2019 (Figs. 5b,d).

Enhanced wave breaking also happened when the currents and waves were heading in the same direction (e.g., Fig. 7d). Wave breaking is related to steepening of waves, and thus to a modulation in wave amplitude and/or wavenumber. Several works have reported an increase in wave heights for waves and currents that are heading in the same direction (Vincent 1979; Masson 1996; Gemmrich and Garrett 2012; Romero et al. 2017). The modulation is mainly attributed to nonlocal cumulative effects such as current-induced refraction. The area of modulation could, however, be very sensitive to the direction of the wave rays (Masson 1996). Furthermore, if propagating along a collinear jet, wave rays could also diverge from the center and overlap at the edges of the jet depending on the properties of the wave field. A north–south transect across the Moskenes Sound during a rising tide shows that the current is spatially more uniform (Fig. 9), which is also confirmed in previous studies (Lynge 2011). The wave ray computations (Fig. 12) did not indicate that the Moskenes Sound was particularly exposed to converging wave rays during a rising tide. However, even if the tides are well represented in the ocean model (Fig. 9), we expect more uncertainty associated with the exact location of eddies and areas of strong vorticity. This would impact the ray tracks and potentially the spatial distribution of the wave ray density.

Regarding the propagation direction of the waves relative to the current direction, conservation of wave crests [Eq. (3)] together with the conservation of wave action yields the classical result of amplitude modulation due to the Doppler shift [i.e., Eq. (2)] (Phillips 1977). In their results from the Bodega Bay, Romero et al. (2017) found that white cap coverage was consistent with focusing of wave rays due to current-induced refraction. Moreover, they found that the area of enhanced wave breaking was at the edge of a current jet suggesting that the enhanced wave breaking was also due to opposing waves and currents in a frame of reference relative to the jet. Opposing waves and currents are known to be important in tidal inlets and upwelling jets (Baschek 2005; Rapizo et al. 2017). That is, the wavelength will increase for waves propagating into a current heading in the same direction and shorten for waves opposing a current. For opposing currents, in the x direction, say, the waves will grow until they reach the limit where $u = -c_g$, which is often referred to as the blocking velocity. Thus, wave steepening due

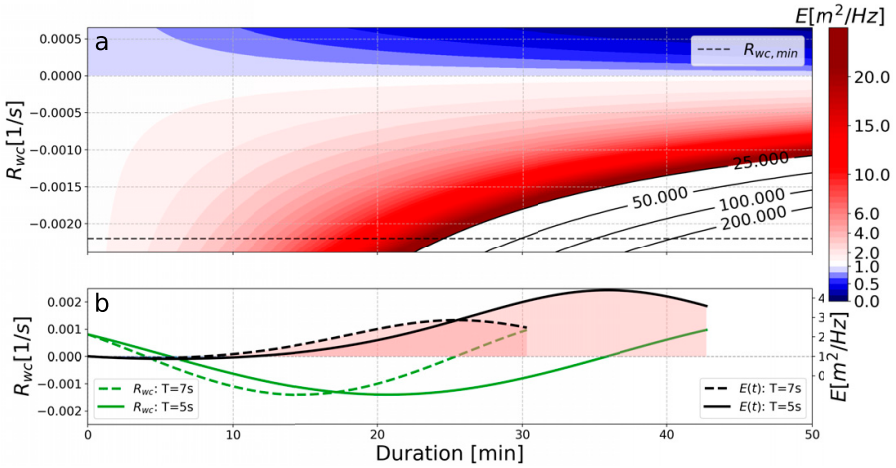

FIG. 14. A first-order estimate on the effect of relative wave convergence R_{wc} on wave energy density. (a) The temporal change in wave energy density E is plotted as a function of values of relative wave convergence with initial value $E_0 = 1$. Shades of red and blue denote increasing and decreasing wave energy density, respectively. The black dashed line denotes the minimum negative value computed for deep water waves from the ocean model (Fig. 7e). (b) Two examples of deep water waves with $E_0 = 1$ propagating over an area with varying R_{wc} (green lines). The waves have periods of $T = 7$ s (black dashed line) and $T = 5$ s (black solid line) with corresponding group velocities of $c_g = 5.5\,\mathrm{m\,s^{-1}}$ and $c_g = 3.9\,\mathrm{m\,s^{-1}}$, respectively. Their duration corresponds to propagating a distance of 10 km. The red and blue shaded areas correspond to an increase and decrease in E with respect to E_0, respectively.

to opposing waves and currents gives rise to wave breaking by altering the critical steepness limit. This was observed in Moskstraumen as early as the seventeenth century (see the appendix). A negative Doppler shift, yielding shorter waves, can also occur for waves riding on time-varying currents similar to that of Moskstraumen, even if their direction of propagation is the same. This can be explained by considering different reference frames. If viewing, say, Moskstraumen, from shore, the direction of the waves and currents will always be aligned during an event of rising tide (right panels, Fig. 9) for waves heading eastward, both before and after current maximum. However, when following the current, the waves in front of the current maximum (i.e., in the direction of the current) will increase their wavelength in accordance with the Doppler shift. The waves behind the current maximum will then be subject to a negative current and shorten. Such phases of positive and negative acceleration are present in Moskstraumen, as can be seen from the rapid increase and decrease in current speed before and after max speed (Figs. 7c,g).

If we assume ideal conditions with a spatially uniform, time-varying current going from rest (at $t = 0$) to a positive maximum ($t = T/2$) and back to rest again ($t = T$). Waves with no dissipation propagating in the direction of the current will be stretched as the current increases and shortened back to their original shape as the current decreases back to rest. In this case

$$\int_0^T R_{wc}\, dt = 0.$$

However, if the net wave convergence R_{wc} felt by the waves was negative before the current maximum occurs, then, as the waves are shortened again, they would become even steeper than before since they acquire energy due to the horizontal gradients of the current. Thus, the Doppler shift from the deaccelerating tidal current could possibly trigger wave breaking.

We expect mechanisms like current-induced refraction, wave steepening due to opposing currents as well as relative wind to also play a role in Moskstraumen. However, from the systematic occurrence of enhanced wave breaking at the M_2 frequency, we argue that the mechanism in Eq. (14) seemingly constitutes a significant part of the wave–current interaction processes during rising tides in Moskstraumen. In particular during periods with calm winds and waves coming from west. Further investigation is, however, needed to assess the importance of the other forcing terms in Eq. (10), and also how small-scale processes not resolved by our ocean model would affect the wave field.

6. Conclusions

We have presented the first simultaneous measurements of waves and currents in one of the strongest open-ocean tidal currents in the world, namely, the Lofoten Maelstrom, or Moskstraumen. By estimating the bubble depth from a bottom mounted ADCP, and using that as a proxy for wave breaking, we find that enhanced wave breaking occurs during a rising tide when Moskstraumen is at its strongest. That is, with a period equivalent to that of the M_2 tidal constituent. From a simplified expression considering specific forcing terms in the wave energy balance equation [Eq. (14)], we find that the horizontal gradients in the background flows qualitatively explain the

enhanced wave breaking, in particular during periods with low wind speed and with waves coming from the west (during rising tides). Under such conditions, the Doppler shift of the waves possibly contribute to further steepening of the waves. More measurements are however required to assess the importance of all the forcing terms in Eq. (10).

The ADCP measurements also confirm results from previous studies which estimated the strength of Moskstraumen to reach 3 m s^{-1} (Gjevik et al. 1997; Moe et al. 2002; Ommundsen 2002). We do, however, expect Moskstraumen to reach even higher speeds where the Moskenes Sound is at its narrowest.

The results presented here show the importance of adding currents as forcing in spectral wave models in nearshore environments. In addition, the expression in Eq. (14) can be utilized in areas of strong current gradients to estimate their role in modulating the wave field.

Acknowledgments. This research was partly funded by the Research Council of Norway through the project MATNOC, Grant 308796. We greatly appreciate all the help from employees at Nortek AS and the Norwegian Coastal Administration who made possible the instrument deployment as well as acquiring, processing, and analyzing the ADCP data. We thank Irena Jovic at the Petter Dass Museum for providing the English translation of "The Trumpet of Nordland."

Data availability statement. The Copernicus Sentinel-1 and Sentinel-2 data are available from the National Ground Segment for Satellite Data in Norway through colhub.met.no. Norkyst800 model data are available from https://thredds.met.no/thredds/dodsC/sea/norkyst800m/1h/aggregate_be. WAM and NORA10 data are available from the Norwegian Meteorological Institute upon request. In situ ADCP data are available from Nortek AS upon request.

APPENDIX

Early Wave–Current Interaction Observations in Moskstraumen

Increased wave amplitude, and thus increased wave breaking, as a result of opposing waves and currents was observed in Moskstraumen as early as in 1685 (first published 1739) by the Norwegian priest and naturalist Peter Dass in his work *Nordlands Trompet* (*The Trumpet of Nordland*) (Dass 2007). In the following, we cite the novel observation by Dass, first in Norwegian then translated into English (translation by Theodore Jorgenson, 1954):

Og skeer det, at Vinden er Strømmen imod,
Da reyses de Bølger i dybeste Flod
Saa høye som Klippernes Toppe:
Skull' nogen fordristes at fare der da,
Han reiste der alrig med Livet ifra,
Men maatte til Bunden ned hoppe.

and

And if it so happens that counterwinds blow,
The waves will as high as the mountaintops flow
And have nothing comparable elsewhere.
Should anyone dare to attempt the sea then,
He would not see near ones or dear ones again;
His grave would be watery bottom.

REFERENCES

Albretsen, J., A. K. Sperrevik, A. Staalstrøm, A. D. Sandvik, F. Vikebø, and L. Asplin, 2011: Norkyst-800 report no. 1: User manual and technical descriptions. Fisken og havet 2, Institute of Marine Research, 48 pp., https://www.hi.no/en/hi/nettrapporter/fisken-og-havet/2011/fh_2-2011_til_web.

Andrews, D. G., and M. E. McIntyre, 1978: An exact theory of nonlinear waves on a Lagrangian-mean flow. *J. Fluid Mech.*, **89**, 609–646, https://doi.org/10.1017/S0022112078002773.

Ardhuin, F., and Coauthors, 2012: Numerical wave modeling in conditions with strong currents: Dissipation, refraction, and relative wind. *J. Phys. Oceanogr.*, **42**, 2101–2120, https://doi.org/10.1175/JPO-D-11-0220.1.

——, S. T. Gille, D. Menemenlis, C. B. Rocha, N. Rascle, B. Chapron, J. Gula, and J. Molemaker, 2017: Small-scale open ocean currents have large effects on wind wave heights. *J. Geophys. Res. Oceans*, **122**, 4500–4517, https://doi.org/10.1002/2016JC012413.

Baschek, B., 2005: Wave-current interaction in tidal fronts. *Rogue Waves: Proc. 14th 'Aha Huliko'a Hawaiian Winter Workshop*, Honolulu, HI, University of Hawai'i at Mānoa, 131–138.

Behrens, A., J. Staneva, Ø. Saetra, and P. Janssen, 2013: Documentation of a web based source code library for WAM. Helmholtz-Zentrum Geestacht Tech. Rep., 79 pp., http://met-xpprod.customer.enonic.io/sokeresultat/_/attachment/inline/c1fdc351-1109-47fc-9d9e-65c9f31eaccb:b52dfe2b5953103564a339bb290b83c66b1315f6/MyWave_Report_D1.1.pdf.

Bretherton, F. P., and C. J. R. Garrett, 1968: Wavetrains in inhomogeneous moving media. *Proc. Roy. Soc. London*, **302A**, 529–554, https://doi.org/10.1098/rspa.1968.0034.

Dass, P., 2007: *Nordlands Trompet.* Gyldendal, 120 pp.

Den norske los, 2018: *The Norwegian Pilot Guide—Sailing Directions for the Norwegian coast, Svalbard and Jan Mayen*. The Norwegian Mapping Authority, https://www.kartverket.no/en/at-sea/nautical-publications/the-norwegian-pilot-guide-sailing-directions.

Dysthe, K. B., 2001: Refraction of gravity waves by weak current gradients. *J. Fluid Mech.*, **442**, 157–159, https://doi.org/10.1017/S0022112001005237.

Gallet, B., and W. R. Young, 2014: Refraction of swell by surface currents. *J. Mar. Res.*, **72**, 105–126, https://doi.org/10.1357/002224014813758959.

Gemmrich, J., and C. Garrett, 2012: The signature of inertial and tidal currents in offshore wave records. *J. Phys. Oceanogr.*, **42**, 1051–1056, https://doi.org/10.1175/JPO-D-12-043.1.

Gjevik, B., H. Moe, and A. Ommundsen, 1997: Sources of the maelstrom. *Nature*, **388**, 837–838, https://doi.org/10.1038/42159.

Guerber, H. A., 1909: *Myths of the Norsemen - From the Eddas and Sagas*. George G. Harrap and Company Limited, 416 pp.

Kenyon, K. E., 1971: Wave refraction in ocean currents. *Deep-Sea Res. Oceanogr. Abstr.*, **18**, 1023–1034, https://doi.org/10.1016/0011-7471(71)90006-4.

Komen, G. J., L. Cavaleri, M. Doneland, K. Hasselmann, S. Hasselmann, and P. A. E. M. Janssen, Eds., 1994: *Dynamics and Modelling of Ocean Waves*. Cambridge University Press, 554 pp., https://doi.org/10.1017/CBO9780511628955.

Kudryavtsev, V., D. Akimov, J. Johannessen, and B. Chapron, 2005: On radar imaging of current features: 1. Model and comparison with observations. *J. Geophys. Res.*, **110**, C07016, https://doi.org/10.1029/2004JC002505.

——, M. Yurovskaya, B. Chapron, F. Collard, and C. Donlon, 2017: Sun glitter imagery of surface waves. Part 2: Waves transformation on ocean currents. *J. Geophys. Res. Oceans*, **122**, 1384–1399, https://doi.org/10.1002/2016JC012426.

Longuet-Higgins, M. S., and R. W. Stewart, 1960: Changes in the form of short gravity waves on long waves and tidal currents. *J. Fluid Mech.*, **8**, 565–583, https://doi.org/10.1017/S0022112060000803.

——, and ——, 1964: Radiation stresses in water waves; a physical discussion, with applications. *Deep-Sea Res. II*, **11**, 529–562, https://doi.org/10.1016/0011-7471(64)90001-4.

Lynge, B. K., 2011: High resolution tidal models for the Norwegian coast. Ph.D. thesis, University of Oslo, 92 pp., https://www.duo.uio.no/bitstream/handle/10852/10729/2/dravhandling-lynge.pdf.

Marechal, G., and F. Ardhuin, 2021: Surface currents and significant wave height gradients: Matching numerical models and high-resolution altimeter wave heights in the Agulhas current region. *J. Geophys. Res. Oceans*, **126**, e2020JC016564, https://doi.org/10.1029/2020JC016564.

Masson, D., 1996: A case study of wave–current interaction in a strong tidal current. *J. Phys. Oceanogr.*, **26**, 359–372, https://doi.org/10.1175/1520-0485(1996)026<0359:ACSOWI>2.0.CO;2.

Moe, H., A. Ommundsen, and B. Gjevik, 2002: A high resolution tidal model for the area around the Lofoten Islands, northern Norway. *Cont. Shelf Res.*, **22**, 485–504, https://doi.org/10.1016/S0278-4343(01)00078-4.

Moreira, R., and D. Peregrine, 2012: Nonlinear interactions between deep-water waves and currents. *J. Fluid Mech.*, **691**, 1–25, https://doi.org/10.1017/jfm.2011.436.

Ommundsen, A., 2002: Models of cross shelf transport introduced by the Lofoten maelstrom. *Cont. Shelf Res.*, **22**, 93–113, https://doi.org/10.1016/S0278-4343(01)00069-3.

Peterson, R. G., L. Stramma, and G. Kortum, 1996: Early concepts and charts of ocean circulation. *Prog. Oceanogr.*, **37**, 1–115, https://doi.org/10.1016/S0079-6611(96)80002-4.

Phillips, O. M., 1977: *The Dynamics of the Upper Ocean*. 2nd ed. Cambridge University Press, 336 pp.

——, 1984: On the response of short ocean wave components at a fixed wavenumber to ocean current variations. *J. Phys. Oceanogr.*, **14**, 1425–1433, https://doi.org/10.1175/1520-0485(1984)014<1425:OTROSO>2.0.CO;2.

Poe, E. A., 1841: "A Descent into the Maelström." *Graham's Magazine*, Vol. 18, 235–241.

Quilfen, Y., and B. Chapron, 2019: Ocean surface wave-current signatures from satellite altimeter measurements. *Geophys. Res. Lett.*, **46**, 253–261, https://doi.org/10.1029/2018GL081029.

——, M. Yurovskaya, B. Chapron, and F. Ardhuin, 2018: Storm waves focusing and steepening in the Agulhas current: Satellite observations and modeling. *Remote Sens. Environ.*, **216**, 561–571, https://doi.org/10.1016/j.rse.2018.07.020.

Rapizo, H., A. V. Babanin, O. Gramstad, and M. Ghantous, 2014: Wave refraction on southern ocean eddies. *Proc. 19th Australasian Fluid Mechanics Conf.*, Melbourne, Victoria, Australian Fluid Mechanics Society, 1–4.

——, ——, D. Provis, and W. E. Rogers, 2017: Current-induced dissipation in spectral wave models. *J. Geophys. Res. Oceans*, **122**, 2205–2225, https://doi.org/10.1002/2016JC012367.

Reistad, M., Ø. Breivik, H. Haakenstad, O. J. Aarnes, B. R. Furevik, and J.-R. Bidlot, 2011: A high-resolution hindcast of wind and waves for the North Sea, the Norwegian Sea, and the Barents Sea. *J. Geophys. Res.*, **116**, C05019, https://doi.org/10.1029/2010JC006402.

Romero, L., 2019: Distribution of surface wave breaking fronts. *Geophys. Res. Lett.*, **46**, 10 463–10 474, https://doi.org/10.1029/2019GL083408.

——, L. Lenain, and W. K. Melville, 2017: Observations of surface wave–current interaction. *J. Phys. Oceanogr.*, **47**, 615–632, https://doi.org/10.1175/JPO-D-16-0108.1.

——, D. Hypolite, and J. C. McWilliams, 2020: Submesoscale current effects on surface waves. *Ocean Modell.*, **153**, 101662, https://doi.org/10.1016/j.ocemod.2020.101662.

Shchepetkin, A. F., and J. C. McWilliams, 2005: The regional oceanic modeling system (ROMS): A split-explicit, free-surface, topography-following-coordinate oceanic model. *J. Phys. Oceanogr.*, **9**, 347–404, https://doi.org/10.1016/j.ocemod.2004.08.002.

Smith, G., 2017: Fishing trawler Iselin capsized at Moskstraumen near Norway. *Maritime Herald*, 30 March, accessed 3 November 2020, www.maritimeherald.com/2017/fishing-trawler-iselin-capsized-at-moskstraumen-near-norway/.

Strand, K., Ø. Breivik, G. Pedersen, F. Vikebø, S. Sundby, and K. Christensen, 2020: Long-term statistics of observed bubble depth versus modeled wave dissipation. *J. Geophys. Res. Oceans*, **125**, e2019JC015906, https://doi.org/10.1029/2019JC015906.

Thorpe, S., 1986: Measurements with an automatically recording inverted echo sounder; ARIES and the bubble clouds. *J. Phys. Oceanogr.*, **16**, 1462–1478, https://doi.org/10.1175/1520-0485(1986)016<1462:MWAARI>2.0.CO;2.

Tolman, H. L., 1990: The influence of unsteady depths and currents of tides on wind-wave propagation in shelf seas. *J. Phys. Oceanogr.*, **20**, 1166–1174, https://doi.org/10.1175/1520-0485(1990)020<1166:TIOUDA>2.0.CO;2.

Verne, J., 1869: *Vingt mille lieues sous les mers*. Magasin d'éducation et de récrátion, 449 pp.

Villas Bôas, A. B., and W. R. Young, 2020: Directional diffusion of surface gravity wave action by ocean macroturbulence. *J. Fluid Mech.*, **890**, R3, https://doi.org/10.1017/jfm.2020.116.

——, B. D. Cornuelle, M. R. Mazloff, S. T. Gille, and F. Ardhuin, 2020: Wave–current interactions at meso- and submesoscales: Insights from idealized numerical simulations. *J. Phys. Oceanogr.*, **50**, 3483–3500, https://doi.org/10.1175/JPO-D-20-0151.1.

Vincent, C. E., 1979: The interaction of wind-generated sea waves with tidal currents. *J. Phys. Oceanogr.*, **9**, 748–755, https://doi.org/10.1175/1520-0485(1979)009<0748:TIOWGS>2.0.CO;2.

Wang, D., H. Wijesekera, E. Jarosz, W. Teague, and W. Pegau, 2016: Turbulent diffusivity under high winds from acoustic measurements of bubbles. *J. Phys. Oceanogr.*, **46**, 1593–1613, https://doi.org/10.1175/JPO-D-15-0164.1.

WW3DG, 2019: The WAVEWATCH III development group. User manual and system documentation of WAVEWATCH III. Tech. Note 333, NOAA/NWS/NCEP/MMAB, 465 pp., https://github.com/NOAA-EMC/WW3/wiki/files/manual.pdf.

Paper II

Resolving regions known for intense wave–current interaction using spectral wave models: A case study in the energetic flow fields of Northern Norway

Trygve Halsne, Patrik Bohlinger, Kai Håkon Christensen, Ana Carrasco, and Øyvind Breivik
Ocean Modelling, **176** (2022)

II

Ocean Modelling 176 (2022) 102071

Contents lists available at ScienceDirect

Ocean Modelling

journal homepage: www.elsevier.com/locate/ocemod

Resolving regions known for intense wave–current interaction using spectral wave models: A case study in the energetic flow fields of Northern Norway

Trygve Halsne [a,b,*], Patrik Bohlinger [a], Kai Håkon Christensen [a,c], Ana Carrasco [a], Øyvind Breivik [a,b]

[a] Norwegian Meteorological Institute, Henrik Mohns Plass 1, Oslo, 0371, Norway
[b] University of Bergen, Allégaten 41, Bergen, 5020, Norway
[c] University of Oslo, Problemveien 7, Oslo, 0315, Norway

ARTICLE INFO

Keywords:
Wave–current interaction
Tidal dynamics
Wave trapping
Water waves

ABSTRACT

Oceanic current forcing in spectral wave models have recently been demonstrated to have a large impact on wave heights at scales between one and up to several hundred kilometers. Here we investigate the impact of such forcing on open-ocean wave heights in Northern Norway using a high-resolution spectral wave model with currents from an ocean circulation model of similar resolution. We find that the wave model, to a large extent, resolves regions identified in the Norwegian Pilot Guide for maritime navigation as having dangerous sea states due to wave–current interaction. This is in contrast to a wave model forced with surface wind fields only. We present a novel diagnostic method to map the spatio-temporal scales associated with the wave height modulation between the two wave model predictions. The method is employed to map areas where significant wave–current interaction can be expected. In many cases, we are also able to confirm the physical mechanisms reported in the Pilot Guide, which are leading to an increase in wave energy due to currents. The largest wave height differences between the two models occur when waves and currents are opposing each other. In such situations, refraction and wave blocking are the dominating effects for the swell and wind sea parts of the spectrum, respectively. Furthermore, including current forcing significantly improves the agreement with in situ observations in strong tidal currents. Here, we see an increase in significant wave height of up to 50%. Even larger relative differences, exceeding 100%, are found in sheltered areas, with one specific region showing a reduction in model errors of 18% due to refraction and advection of wave action.

1. Introduction

Inclusion of ocean currents as forcing in spectral wave models is an active field of research, since it is one of the least developed and least verified parts in such models (Babanin et al., 2017, 2019). This is obviously important for day-to-day wave forecasting in regions with strong currents, but also for other aspects like modeling air–sea interactions due to the exchange of properties through the interface, which is key for climate predictions (Cavaleri et al., 2012). Ocean currents can modulate wave heights significantly, and even dominate the variability in the open ocean at scales of 10–100 km (Ardhuin et al., 2017). For shorter scales, sub-mesoscale fronts have been found to increase significant wave heights up to 30% (Romero et al., 2017), and twin model experiments have revealed wave height modulations up to 80% due to current-induced refraction in low wind conditions (Romero et al., 2020). Furthermore, periodic interactions in tidal currents is known to induce intense local wave height modulations, such as reported by Masson (1996).

Northern Norway is known for its extraordinarily strong open-ocean tidal currents (Gjevik et al., 1997). In addition, the region is subject to a turbulent flow field with strong eddies in the Norwegian Atlantic Current (NAC) and the Norwegian Coastal Current (NCC) (Mork, 1981), see Figs. 1, 2. Further to this, the northeast Atlantic is home to the most extreme wave climate globally (Aarnes et al., 2012). This makes Northern Norway an interesting region to study wave–current interaction as there is a steady influx of swell in addition to local windsea. Specific areas are known for intense interactions, described in detail in The Norwegian Pilot Guide (Den norske los, 2018, hereinafter NPG). Some are also mentioned in the classical literature (Gjevik et al., 1997). In the NPG, they are referred to as "areas of dangerous waves" (Fig. 3). This information was collected from an extensive survey among experienced sailors and local fishermen. In addition to mapping these areas, the survey also addressed the characteristic current and wave conditions presumed responsible for the choppy, and sometimes dangerous, sea states. However, there have been no attempts to resolve these areas

* Corresponding author at: Norwegian Meteorological Institute, Henrik Mohns Plass 1, Oslo, 0371, Norway.
Trygve Halsne (T. Halsne).
E-mail addresses: trygve.halsne@met.no (T. Halsne), patrikb@met.no (P. Bohlinger).

https://doi.org/10.1016/j.ocemod.2022.102071
Received 14 April 2022; Received in revised form 11 June 2022; Accepted 7 July 2022
Available online 14 July 2022

using spectral wave models. In this work, we aim to map areas known (or not known) for high and dangerous sea states presumed due to wave–current interaction using state-of-the-art wave and ocean models. Moreover, as different flow regimes (e.g., tidal and sub-mesoscale) are associated with various temporal and horizontal scales, we investigate if such a model coupling also resolves spatio-temporal variability in the wave field, including the extreme values in specific regions like strong tidal currents.

Only a few studies have investigated the impact of currents on the wave field in Northern Norway. Segtnan (2014) used the wave refraction model by Mathiesen (1987) and found that the wave propagation direction close to the coast was often misaligned with the wave direction offshore. The misalignment was attributed to current-induced refraction due to the eddies associated with the NCC. Saetra et al. (2021, hereinafter OS21) investigated wave–current interaction in the Lofoten Maelstrom, which is one of the world's strongest open-ocean tidal currents. They found that wave breaking increased during maximum current speeds. This was associated with an increase in wave height due to horizontal gradients in the tidal current. Neither of these studies sufficiently examined the flow fields impact on the wave height, and the associated horizontal variability.

Here we investigate the impact of currents by comparing the results from a twin experiment with identical spectral wave models (hereinafter wave models) with different forcing, i.e., one with wind and currents and one forced with wind only. Similar model setups have recently been shown to yield acceptable results on large (e.g. Marechal and Ardhuin, 2021), intermediate (e.g. Kanarik et al., 2021) and small horizontal scales (e.g. Romero et al., 2020), including tidal currents (Ardhuin et al., 2012). We assess the impact by different current regimes on the wave field by analyzing specific events and by comparing them with in situ and remote sensing observations. We also present a novel, generic, method to map spatio-temporal variability in twin experiments based on time series analysis, which in this context is used to map regions with strong wave–current interaction. More generally, we assess the usefulness of such an approach for sensitivity analysis in twin model experiments.

The paper is structured as follows: In Section 2, we provide a description of the models, forcing, and observations together with metrics and methods used for validation. In Section 3, we present our results, which are further discussed in Section 4. We then present our concluding remarks in Section 5.

2. Materials and methods

2.1. Models and observations

2.1.1. Model domain and study period

The model domain covers the coast of Northern Norway (Fig. 1), an area with extensive maritime activity, including ship traffic, fisheries, marine engineering, and marine harvesting (fish farming). The domain is identical to the high resolution operational wave forecast model at the Norwegian Meteorological Institute for this region. Northern Norway is located in the belt of westerlies and is thus dominated by westerly winds and waves. Specific areas in the region are subject to vigorous tidal currents due to the semi-diurnal northward propagating Kelvin wave. One of these is the aforementioned Lofoten Maelstrom located on the southern tip of *Lofoten* (location 7—Fig. 1 local names are referred to in italic). The tidal current's local name is *Moskstraumen*, which we will use here (see B—Fig. 1). Combined with the Norwegian Coastal Current that meanders northward, loosely following the bathymetry of the shelf, these strong tidal currents give rise to very strong current gradients.

This study covers the period from 2018-12-01 until 2019-02-28, which includes six spring tide periods and some storms mainly approaching the continental shelf from the west outside *Lofoten*. Six times during the period, H_s reached values above 6 m (not shown). The particular period was chosen since it overlaps with in situ observations from a measurement campaign in *Moskstraumen* (Saetra et al., 2021). We pay particular attention to the locations denoted A and B and those numbered 2–8 in Fig. 1. The first (A and B) denote the location of the in situ observations while the latter (2–8) denote areas known for dangerous waves according to their numbering in the NPG (see Fig. 3). The reason why we start counting on 2, is that area 1 is outside our model domain.

2.1.2. The WAM spectral wave model

We used a recent version of the wave model WAM, Cycle 4.7 (Komen et al., 1994; Behrens et al., 2013). WAM solves the wave action balance equation

$$\frac{\partial N}{\partial t} + \frac{1}{\cos(\phi)}\frac{\partial}{\partial \phi}\left(\dot{\phi}\cos(\phi)N\right) + \frac{\partial}{\partial \lambda}\left(\dot{\lambda}N\right) + \frac{\partial}{\partial \omega}\left(\dot{\omega}N\right) + \frac{\partial}{\partial \theta}\left(\dot{\theta}N\right) = \left(S_{\text{in}} + S_{\text{nl}} + S_{\text{ds}} + S_{\text{bot}}\right)\sigma^{-1}, \tag{1}$$

where $N = E/\sigma$, the wave action density, is the ratio of the spectral wave energy density, $E = E(t, \phi, \lambda, \omega, \theta)$, and the intrinsic wave angular frequency, σ. Furthermore, t, ϕ, λ, ω, and θ denote time, latitude, longitude, angular frequency, and direction, respectively. The right hand side in (1) denotes the parameterized physical processes which represents the wind input (S_{in} from Ardhuin et al., 2010), non-linear wave–wave interactions (S_{nl} from Hasselmann et al., 1985), wave dissipation due to white capping (S_{ds} from Ardhuin et al., 2010), and bottom friction (S_{bot} from Hasselmann et al., 1985). The terms denoted with overdots in Eq. (1) describe the wave kinematics governed by

$$\dot{\phi} = \left(c_g \cos(\theta) - U\right) R^{-1}, \tag{2}$$

$$\dot{\lambda} = \left(c_g \sin(\theta) - V\right)\left(R\cos(\theta)\right)^{-1}, \tag{3}$$

$$\dot{\omega} = \frac{\partial \Omega}{\partial t}, \tag{4}$$

$$\dot{\theta} = c_g \sin(\theta)\tan(\phi)R^{-1} + \dot{\theta}_D, \tag{5}$$

where $\mathbf{U} = (U, V)$ is the horizontal surface current velocity vector, R is the radius of the earth, c_g is the wave group velocity, and

$$\dot{\theta}_D = \left(\sin(\theta)\frac{\partial}{\partial \phi}\Omega - \frac{\cos(\theta)}{\cos(\phi)}\frac{\partial}{\partial \lambda}\Omega\right)(kR)^{-1}. \tag{6}$$

Here, $\mathbf{k}$ is the wave number vector and $k = |\mathbf{k}|$. Latitudinal and longitudinal advection of wave action by the wave group velocity and the ambient current are represented by Eqs (2)–(3). The temporal change of angular frequency is given by Eq. (4), where Ω is the Doppler-shift dispersion relation

$$\omega = \Omega(\mathbf{k}, \mathbf{x}, t) = \sigma + \mathbf{k}\cdot\mathbf{U}, \tag{7}$$

where $\mathbf{x} = (x, y)$ is the horizontal positional vector. The intrinsic frequency follows the linear dispersion relation

$$\sigma = \sqrt{gk\tanh(kd)}. \tag{8}$$

Here g, d are the gravitational acceleration and water depth, respectively. The refraction, or turning, of waves due to gradients in the ambient current and bathymetry is dictated by Eq. (5).

The model was set up on a regular grid with 800 m horizontal grid resolution. It had a spectral resolution of 24 directional and 30 frequency bins, ranging from $f_0 = 0.034523$ Hz to $f_{29} = 0.5476419$ Hz in logarithmic increments such that $f_i = f_0 \times 1.1^i$ where $i = 1, 2, \ldots, 29$. Model integration time steps of 30 s were used for both the propagation and source term computations. For the boundaries, we used hourly 2D spectra from the European Centre for Medium-Range Weather Forecasts (ECMWF).

We performed a twin model experiment using the same model specifications and physical parameterizations. Both were forced with surface winds, but one also included current forcing. These two runs are hereinafter referred to as the reference run, $\text{WAM}_{\mathbf{ref}}$, i.e., with zero currents, and the run including currents, $\text{WAM}_{\mathbf{curr}}$. The current forcing is not part of the source term calculations but is included in the wave kinematics [the left hand side of Eq. (1)], as shown in Eqs. (2)–(5).

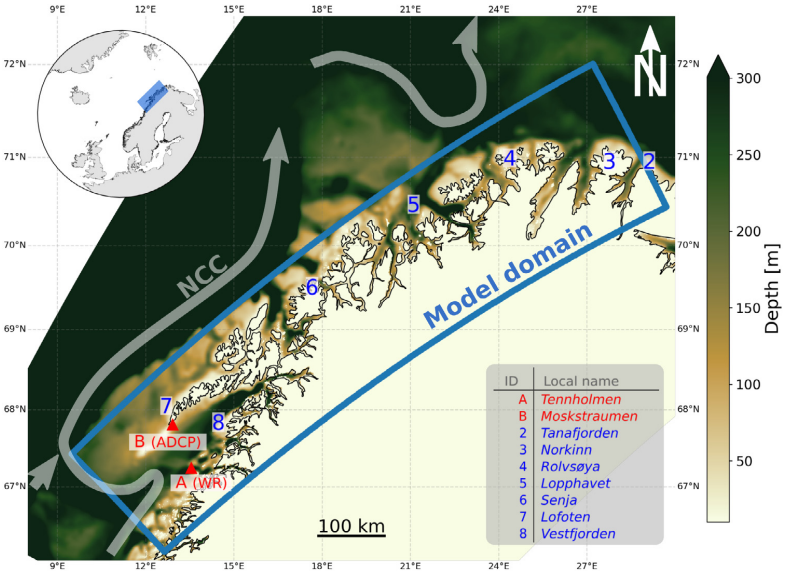

Fig. 1. The study area along the coast of Northern Norway. The Norwegian Atlantic Current (not shown) and the Norwegian coastal current (NCC) are the main ocean currents in the region, the latter guided northwards by the bathymetry. The WAM spectral wave model domain is outlined by the blue curvilinear polygon. Within the domain, two in situ measurement devices provided observations during the study period. These are the wave rider (WR) buoy outside A–*Tennholmen* and the ADCP located in the tidal current B–*Moskstraumen*. Additional local reference points are listed in the legend.

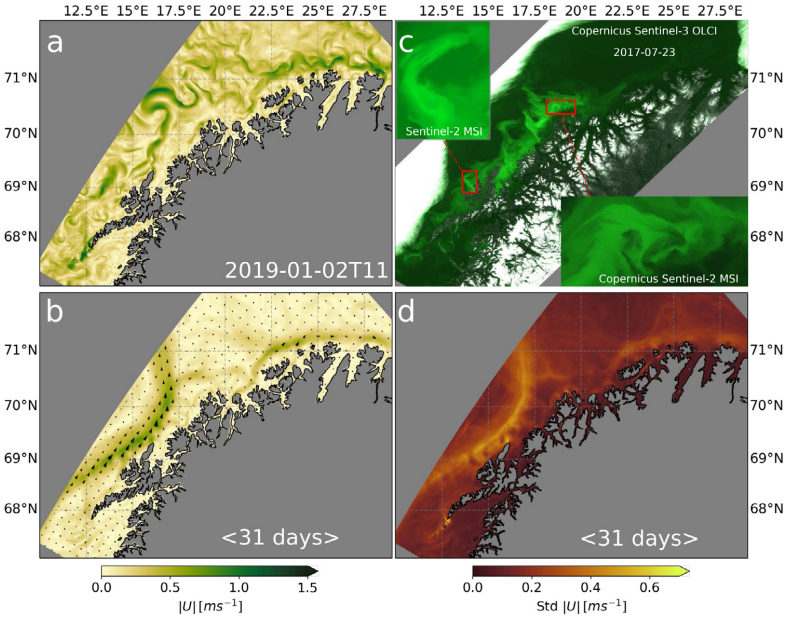

Fig. 2. A view of the Norkyst 800 m ROMS ocean model is given in panels (a), (b), and (d). Panel (c) illustrates the small scale variations of the Norwegian Coastal Current (NCC) during an algal bloom captured by the optical Copernicus Sentinel-2 and Sentinel-3 missions in 2017. The surface current speed, |**U**|, average speed, and standard deviation, are shown in panels (a), (b), and (d), respectively. Panel (a) show a snapshot of the ocean model surface current speed. The surface current mean flow (with directions) and the current variability (in terms of its standard deviation) are shown in panels (b) and (d), respectively. Here, the current statistics are computed for all days in January 2019.

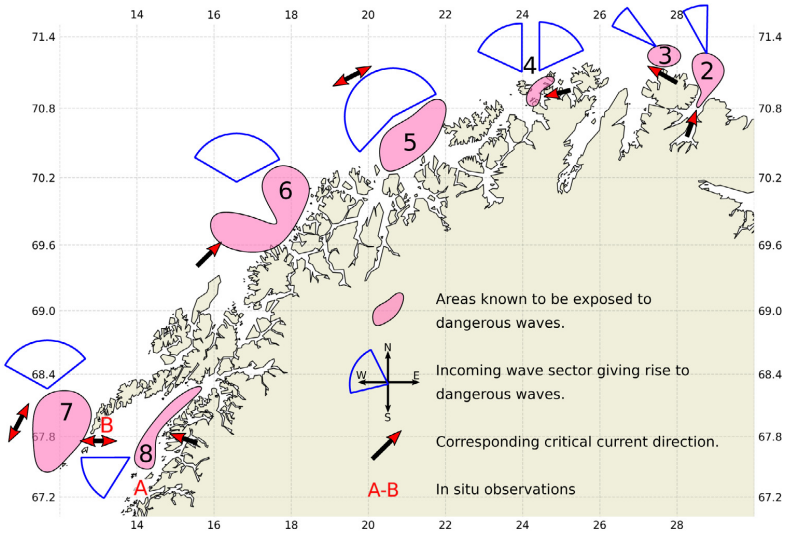

Fig. 3. An overview of the areas known for dangerous waves, according to the Norwegian Pilot Guide (Den norske los, 2018, NPG). Pink areas indicate the approximate horizontal extent of the critical areas (reproduced from the original publication), and their numbering is according to the original index. Area number 1 is outside the model domain and hence not included. Blue denotes the wave propagation sector associated with dangerous waves, and arrows denote the corresponding critical current direction.

2.1.3. Wave model forcing

NorKyst800 provided the ocean surface currents fields used to force $\mathrm{WAM}_{\mathbf{curr}}$. This is an operational configuration of the Regional Ocean Modelling System (ROMS, see Shchepetkin and McWilliams, 2005) operated by the Norwegian Meteorological Institute. It is a three-dimensional ocean circulation model (hereinafter ocean model) with 800 m horizontal resolution and 42 vertical levels using topography-following coordinates. The ocean model is forced at the boundaries by the Hybrid Coordinate Ocean Model, which is part of the TOPAZ system operated for the pan-European Copernicus Marine Service (https://cmems.met.no/ARC-MFC/). Eight tidal constituents are included in the barotropic boundary conditions. Further specifications of the ocean model setup are given by Albretsen et al. (2011).

The ocean model gives a good representation of the currents along the coast of Norway, which is dominated by the NAC and the NCC, together with the tides (Christensen et al., 2018; Kristensen and Gusdal, 2021). The NCC on average flows northwards (Fig. 2b), and is loosely following the isobaths of the continental shelf (Fig. 1). Smaller-scale dynamics includes sub-mesoscale eddies (i.e., of the order of 0.1–10 km, see McWilliams, 2016) originating from baroclinic instabilities (Fig. 2a), and inertial currents resulting from the wind forcing (Röhrs and Christensen, 2015). The appearance of eddies are readily observed indirectly by optical satellite instruments if algal blooms are present (Fig. 2c). Their exact location in the ocean model is, however, associated with larger uncertainty compared with the mean flow. Baroclinic dynamics associated with the NCC are also transient, as they are advected northwards by the mean flow. The variability of the NCC is also strongly modulated by the tides (Fig. 2d). Further to this, several areas close to the shoreline have high variability but with a weak mean flow. This includes *Moskstraumen* where OS21 found the horizontal extent, magnitude, direction and phase of the modeled current field to be in reasonable agreement with in situ and satellite observations.

Wind forcing was taken from the operational forecasts generated by the Arome Arctic numerical weather prediction model operated by the Norwegian Meteorological Institute. It is a 2.5 km horizontal resolution non-hydrostatic model with 65 vertical levels, and is primarily based on the High Resolution Limited Area Model (HIRLAM)–ALADIN Research on Mesoscale Operational NWP in Euromed (HARMONIE) AROME configuration. Further specifications are given in Müller et al. (2017). We used the surface wind fields, $\mathbf{U}_{10}$, as input to S_{in}.

2.1.4. In situ observations

Observations from two instruments located in the southern part of the model domain were available during the period studied (see A,B Fig. 1). The first, a Nortek Signature 500 acoustic Doppler current profiler (ADCP), was located east in *Moskstraumen*. These measurements were reported by OS21, where a more complete description of the data set and the area can be found. The observations include standard integrated wave parameters like significant wave height and the mean wave period, together with wave directional information. In addition, the ADCP measured the vertical profile of the current, which is barotropic during the tidal cycles (OS21). Wave measurements during two of the spring tide events were sometimes flagged as invalid at maximum current speed because the instrument tilted beyond the operating range (10° from zenith).

The second in situ instrument is a Datawell Mk3 waverider buoy (WR), moored near the island of *Tennholmen*. This buoy reported significant wave height and mean zero upcrossing period T_z with hourly temporal resolution.

For practical purposes, we denote both the observed and spectral estimate of significant wave height as H_s since they are very similar (Holthuijsen, 2007). The same applies for the mean wave period, hereafter denoted T_{m02}.

The maximum observed H_s values were about 8.5 m and 10.5 m from the ADCP and the WR, respectively (not shown).

2.1.5. Remote sensing observations

Several satellite altimeter missions are archived and openly accessible through the ESA Sea State Climate Change Initiative (CCI, https://data.ceda.ac.uk/neodc/esacci/sea_state/data/v1.1_release/l2p) and the Copernicus Marine Service (https://marine.copernicus.eu/). This includes the Copernicus Sentinel-3 missions together with the SARAL/AltiKa and Cryosat −2. It is common to filter and resample Level-2 20 Hz (approx. 350 m resolution) retrievals to Level-3 1 Hz (approx. 7 km resolution) (Bohlinger et al., 2019). For December 2018, we used the Level-3 multimission dataset from CCI. For January

and February 2019, we used the Sentinel-3 Level-3 data since the multi-mission dataset does not yet cover this period.

2.2. Verification

2.2.1. Verification metrics

For verification against observations, we computed the normalized root mean squared error (NRMSE) and normalized bias (NBIAS) using the same definition as that of Ardhuin et al. (2010),

$$\mathrm{NRMSE}(X) = \sqrt{\frac{\sum(X_\mathrm{o} - X_\mathrm{m})^2}{\sum X_\mathrm{o}^2}}, \tag{9}$$

$$\mathrm{NBIAS}(X) = \frac{\sum(X_\mathrm{o} - X_\mathrm{m})}{\sum X_\mathrm{o}}. \tag{10}$$

Here subscripts "o" and "m" denote observation and model, respectively, and X denotes the variable. For model intercomparison, we denote the absolute difference between the two wave model integrations as $\Delta X = \mathrm{WAM_{curr}} - \mathrm{WAM_{ref}}$. Relative changes between the model runs are denoted as

$$\mathrm{RC}(X) = \frac{\Delta X}{X_\mathrm{ref}}, \tag{11}$$

where the subscript "ref" indicates values from $\mathrm{WAM_{ref}}$. Instead of the NRMSE, we computed the RMSE in this respect. Further, we computed the mean, standard deviation (σ) and minimum/maximum difference.

2.2.2. Spatio-temporal variability

Since the ocean circulation within the model domain is dominated by the NCC, inertial currents, and the tides, we expect wave heights to be modulated on the associated temporal scales. For tides we consider the M_2 semidiurnal tidal constituent. The inertial frequency is the about the same as M_2 in the area, making it difficult to discriminate these in the open ocean. Close to shore, however, the topography cancels the inertial response. For baroclinic instabilities associated with the NCC, namely, fronts and eddies, we consider frequencies between hours to a couple of days, which generally reflect their life cycle (McWilliams, 2016). In order to separate the dominant temporal modes and their associated energy, we conducted a time series analysis for all grid points in our model domain, similar to the single point analysis by Gemmrich and Garrett (2012) and OS21. That is, power spectral densities (PSDs) for each model grid point, (i, j) were computed for a specific difference variable ΔX (i.e. $\mathrm{WAM_{curr}} - \mathrm{WAM_{ref}}$). We now compute the energy associated with the low-frequency band $[f_0, f_1]$, namely the NCC (denoted by index 1), and the high-frequency band $[f_2, f_3]$, namely M_2 (denoted by index 2), as

$$\hat{E}_{1,(i,j)} = \int_{f_0}^{f_1} \mathrm{PSD}(\Delta X)_{(i,j)}\, df, \tag{12}$$

$$\hat{E}_{2,(i,j)} = \int_{f_2}^{f_3} \mathrm{PSD}(\Delta X)_{(i,j)}\, df. \tag{13}$$

For convenience we here consider H_s since it is proportional to the square root of the wave energy. Note that $\hat{E}$ represents the variance of ΔX summed over a specific frequency range and should not be confused with the wave energy density E.

To help visualize the variability of the two frequency bands, we now create a red–green–blue (RGB) color composite showing the spatio-temporal variability of $\hat{E}$ as (R,G,B) = ($\hat{E}_1$, $\hat{E}_2$, $\hat{E}_1$). Variations associated with the low frequencies (1) appear as purple (equal amounts of red and blue), while variations associated with high frequencies (2) appear as green. Black then comes to represent zero variability while white means both temporal scales are present in equal amounts. This is a method which is frequently used in remote sensing applications for multitemporal change detection analysis (e.g. Marin et al., 2015), but to our knowledge has not been applied to spatial spectral analysis of wave model fields before.

Table 1
Bulk validation metrics for H_s and T_{m02} computed for the wave models vs. observations.

	NBIAS		NRMSE	
	$\mathrm{WAM_{curr}}$	$\mathrm{WAM_{ref}}$	$\mathrm{WAM_{curr}}$	$\mathrm{WAM_{ref}}$
H_s				
ADCP (N = 3767)	0.119	0.120	0.215	0.216
WR (N = 2133)	0.109	0.100	0.181	0.174
Altimeter (N = 1913)	0.05	0.05	0.21	0.21
T_{m02}				
ADCP (N = 3500)	0.185	0.194	0.170	0.175
WR (N = 2133)	0.134	0.115	0.181	0.174

3. Results

3.1. Wave model validation against observations

3.1.1. In situ observations and bulk validation

Energy fluctuations at each observation location are investigated through a power spectral density (PSD) analysis of ΔH_s (Fig. 4a) and H_s observations (Fig. 4b). For $\mathrm{WAM_{curr}}$ in *Moskstraumen*, the most distinct frequency peaks are located around the tidal constituents M_2 and M_4 as well as near the inertial frequency, f, which is about the same as M_2 in the area (Fig. 4a). This is in accordance with the observations, with pronounced peaks around M_2 and M_4 (Fig. 4b), where the latter is shifted slightly toward lower frequencies in $\mathrm{WAM_{curr}}$. At *Tennholmen*, the M_2 signal in ΔH_s is about two orders of magnitude smaller than *Moskstraumen*, which makes sense since the area is not exposed to strong tidal currents (Fig. 4).

For frequencies below M_2, the underlying causes for the inter-model discrepancies are many (Fig. 4a). Firstly, there is a delayed response in the mean flow due to the synoptic weather systems. OS21 found wave breaking in *Moskstraumen* to correspond well with the passage of such systems for frequencies below 0.75 cycles per day (see their Fig. 4c). Secondly, the refraction of wave action density due to eddies and whirls affects the wave height variability on longer time scales than those of the tides. This will be discussed in detail later. Thirdly, during one of the storms within our study period (e.g. $H_\mathrm{s} > 6$ m), ΔH_s exceeded 2 m in *Moskstraumen*. Thus, strong wave height modulations occurred infrequently. Such a storm event is further elaborated in Appendix.

In terms of verification metrics, the overall performance of the wave model compared against the observations is listed in Table 1. Both model runs have a negative bias of about 10% in H_s compared with the in situ observations. The NRMSEs are in the range 17–22%, and inter-model differences are below 1%. We find slightly higher differences in NBIAS and NRMSE for T_{m02} (Table 1). This is similar to the results of Palmer and Saulter (2016), who also reported inconclusive bulk validation metrics but found a more realistic representation of the wave field sub-regions dominated by tides. Model errors accumulate in such metrics if the spatio-temporal variations between model output and observations are slightly out of phase. Due to this, Ardhuin et al. (2012) found increasing wave model errors in tidal currents against a wave model forced with wind only.

3.1.2. Altimeter observations

When considering the entire domain, the NBIAS and NRSME against altimeter observations of H_s are virtually identical for both model runs (Table 1). However, sub-regions expected to have significant wave–current interaction (Fig. 5) do reveal a systematic improvement for all validation parameters for $\mathrm{WAM_{ref}}$ in *Vestfjorden* (location 8 in Fig. 1) with a 16% reduction in bias in December 2018 (P5, Table 2). Albeit a bit less, a decrease in model error and bias can also be seen for P5 from the CMEMS product. Here, there are twice as many samples as in December 2018 (N = 76 vs N = 29).

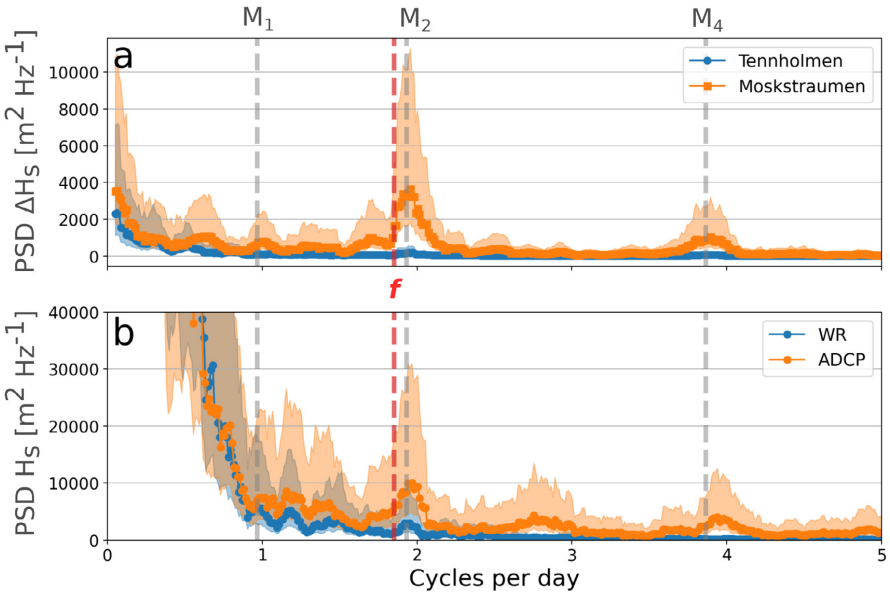

Fig. 4. Power spectral density (PSD) plots of ΔH_s (= WAM_{curr} - WAM_{ref}) and H_s time series at the in situ observation locations covering the study period. Panel (a) shows ΔH_s from grid points closest to the ADCP and wave rider (WR) locations. Panel (b) shows PSDs computed for the H_s observations in *Moskstraumen* (ADCP) and *Tennholmen* (WR). The shaded region around the PSDs indicates the 95% confidence limits. The tidal constituents M_1, M_2, and M_4 are plotted as vertical gray dashed lines for reference together with the inertial frequency, f (red dashed line).

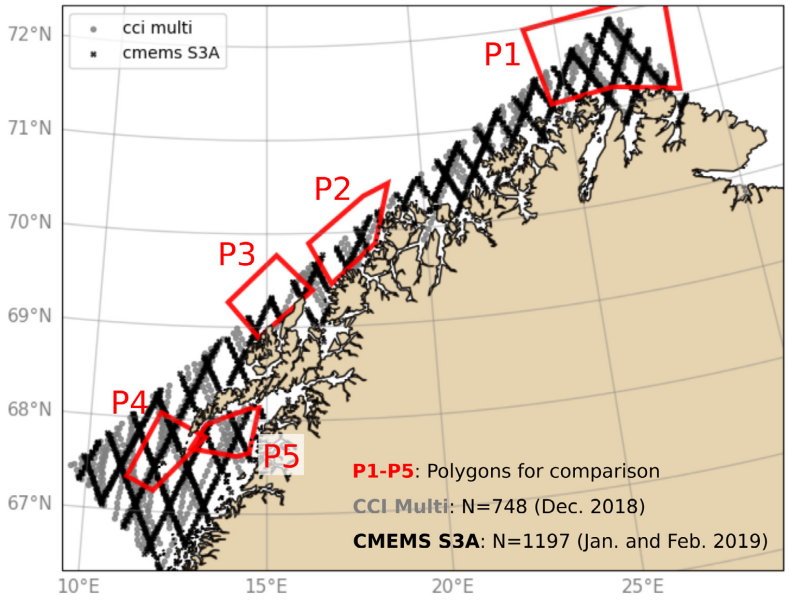

Fig. 5. Altimeter level-3 H_s observations within the model domain from the CCI multimission (gray) and CMEMS (black), together with polygons (P1–P5) for regional comparison.

3.2. Large-scale model inter-comparison

3.2.1. Temporal modes in horizontal H_s variability

In addition to the lowest frequencies (see Section 3.1.1), we find that ΔH_s exhibits two main temporal scales, controlled by the baroclinic instabilities associated with the NCC (T_e) and the M_2 semidiurnal tidal constituent (T_t). In general, the life-cycle of eddies and fronts lasts from hours to days depending on their generating mechanism and the prevailing conditions (McWilliams, 2016). In our domain we find that normally $T_e > T_t$ (not shown). Since the wind forcing is the same in

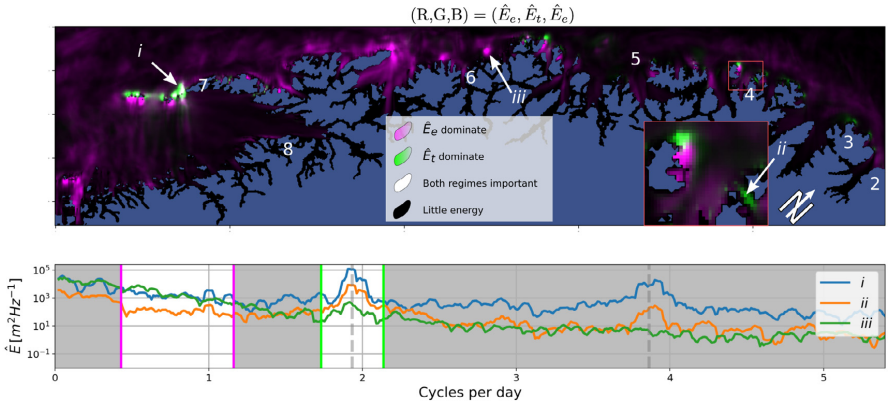

Fig. 6. Characterization of spatio-temporal variability in ΔH_s. The image consists of $\hat{E}_e$, $\hat{E}_t$, and $\hat{E}_c$ from Eqs (14)–(15) on the R, G, and B channels, respectively. Hence, shadings of purple signify areas where the variability is associated with $\hat{E}_e$ while shadings of green correspond to $\hat{E}_t$. White (black) show areas where both (none) of the modes have energy. The PSDs originate from a time series analysis for each model grid point. A few selected cases are shown in the lower panel for *Moskstraumen* (label *i*), *Breisundet* (label *ii*), and *Senja* (label *iii*). The gray shaded areas denote the frequencies that are excluded in the analysis, and the vertical dashed lines denote the M_2 and M_4 tidal constituents. Numbering 2–8 denote the dangerous wave areas from Fig. 3.

Table 2
Validation metrics computed for specific sub-regions (polygons P1–P5 in Fig. 5) against altimeter observations of H_s. Pearson correlation coefficient is denoted *r*.

	NBIAS		NRMSE		r	
	WAM_{curr}	WAM_{ref}	WAM_{curr}	WAM_{ref}	WAM_{curr}	WAM_{ref}
December 2018 CCI multimission						
P1 (N = 62)	0.18	0.17	0.21	0.21	0.91	0.91
P2 (N = 21)	0.00	−0.02	0.17	0.15	0.64	0.70
P3 (N = 37)	0.12	0.12	0.18	0.18	0.92	0.92
P4 (N = 165)	−0.01	−0.01	0.12	0.13	0.93	0.92
P5 (N = 29)	0.47	0.63	0.53	0.71	0.40	0.25
January–February 2019 CMEMS						
P1 (N = 88)	0.05	0.04	0.20	0.18	0.87	0.89
P2 (N = 93)	−0.04	−0.04	0.19	0.19	0.94	0.94
P3 (N = 106)	−0.01	−0.01	0.27	0.26	0.71	0.73
P4 (N = 344)	0.10	0.10	0.24	0.24	0.89	0.90
P5 (N = 76)	0.26	0.32	0.33	0.37	0.91	0.90

WAM_{curr} and WAM_{ref}, T_e and T_t should be resolved by WAM_{curr} only. We used Eqs (12)–(13) to discriminate these temporal modes as follows,

$$\hat{E}_{e,(i,j)} = \int_{\delta f_0}^{M_1+\delta f} \mathrm{PSD}(\Delta H_s)_{(i,j)}\, df, \tag{14}$$

$$\hat{E}_{t,(i,j)} = \int_{M_2-\delta f}^{M_2+\delta f} \mathrm{PSD}(\Delta H_s)_{(i,j)}\, df. \tag{15}$$

Here, δf_0 correspond to about 0.4 cycles per day and constitute a low pass filter, and δf correspond to about 3 h.

An RGB composite showing the spatio-temporal variability of ΔH_s is given in Fig. 6. It is clear that the tides impact the wave height in the area surrounding *Lofoten*, in particular in *Moskstraumen* (*i*,7 Fig. 6). Here, the energy modulation at M_2 is an order of magnitude larger compared with other areas dominated by tidal currents (lines *i* and *ii* Fig. 6). Furthermore, tidal processes mostly dominate close to the coast, including in narrow sounds and channels. In addition to bathymetric effects, some of these are also affected by corner effects that locally accelerate the tidal current. We also performed an analysis including the M_4 components, which gave more or less the same result (not shown).

In some regions, T_e and T_t appear simultaneously, but spatially separated, as in the highlighted box. In these cases, the wave height modulation is most often associated with the tides, but $\hat{E}(M_2)$ can be orders of magnitudes lower than $\hat{E}(M_1)$ (not shown). Thus, the wave–current interaction is dominated by tidal processes, but local topographic conditions like the corner effect can affect the flow field, and also and the incoming wave field. For the latter, refraction is very sensitive to the incoming wave direction, and waves can at times be refracted into sheltered areas.

Between areas 6 and 7, modulation on T_e is most pronounced (Fig. 6). Here, some places have a strong M_1 signal, while others are modulated on longer time scales, similar to the shallow banks outside *Senja* (see *iii*,6 Fig. 6).

Further away from the coast, T_e is more pronounced, but with less variability, as seen south and west of *Lofoten* (7– Fig. 6). This also includes the strip north of *Rolvsøya* (location 4– Figs. 1,6), where the NCC is meandering with strong eddy activity and large current variability (Figs. 2a,d). As expected, this suggests that wave refraction due to eddies and whirls is what drives the differences between the two wave model runs in such areas. Furthermore, it shows that wave–current interaction becomes more intense in areas close to the coast with strong tides than further away from the coast.

3.2.2. Statistical variability

There are some systematic differences in the twin model experiment. An area which stands out is *Vestfjorden* (8– Fig. 1), where on average $\Delta H_s > 0$ (i.e., $WAM_{curr} > WAM_{ref}$ in Fig. 7a). The region stands out even more clearly in terms of the relative change (RC), with mean ΔH_s values from +20% and above, and maximum values well above 100% (Figs. 8a,c). For ΔT_{m02}, the mean value in *Vestfjorden* is between 0.5 – 1 s with maxima around +3 s (not shown). Considering the Doppler shift and conservation of wave action, one would expect the increasing wave periods to be associated with decreasing wave amplitude. However, ΔH_s is positive, suggesting other dominating mechanisms (Figs. 7a, 8a).

Vestfjorden is sheltered from the strongest winds and has in general lower waves compared with the more exposed areas in the Lofoten archipelago. The systematic increase in H_s is mainly caused by advection of wave action due to the tidal oscillations and the NCC, together with current-induced refraction. To illustrate the impact of these effects, we inspect a case on 2019-01-05 shown in Fig. 9. Here, the area was dominated by eastward propagating swell and calm westerly winds and H_s about 0.1 m and 0.6 m in WAM_{ref} and WAM_{curr}, respectively (not shown). The wind sea wave height was more or less the same in both models (lower middle left panel of Fig. 9). The swell heights, however, were larger in WAM_{curr}, and the mean swell direction was

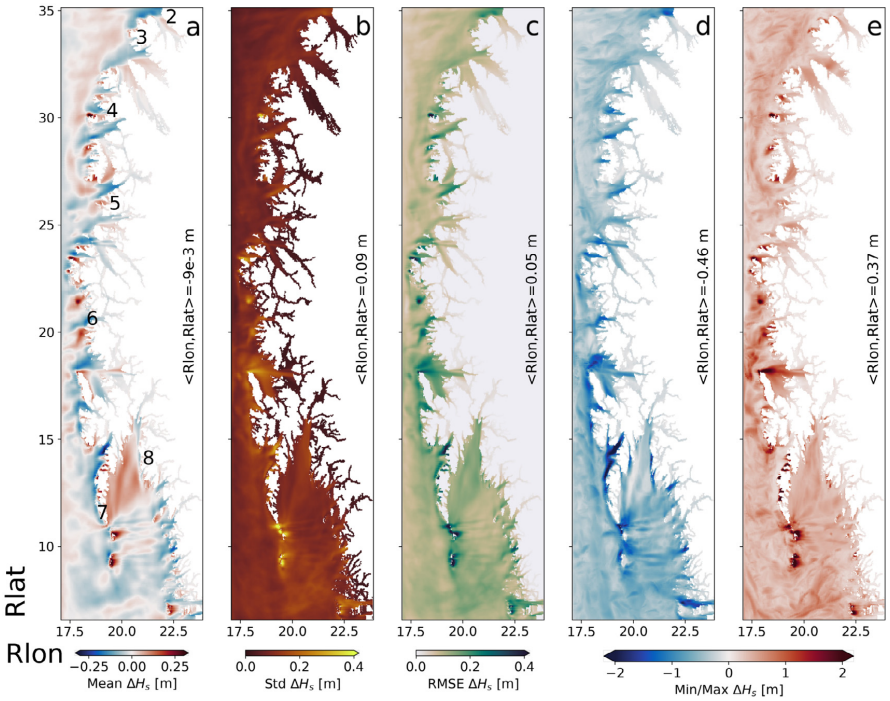

Fig. 7. Horizontal variability of ΔHs statistics including the mean (a), σ (b), RMSE (c) and minimum/maximum values [(d)/(e)]. All parameters are computed for the entire study period. The mean value for all grid points are denoted in each panel by "<Rlon, Rlat>". Minimum and maximum values denote the extremes for each grid cell and does not, necessarily, originate from the same time steps. Numbering 2–8 denote the dangerous wave areas from Fig. 3.

more northwards compared with WAM_{ref} (upper middle right panel of Fig. 9). Swell enters *Vestfjorden* through *Moskstraumen*, and meets strong current dipoles caused by the tidal current (see Fig. 9 OS21 and Fig. 8 Børve et al., 2021). Current-induced refraction is strongly connected to the vertical vorticity ζ of the current (Dysthe, 2001), and the dipoles thus have a strong influence on the wave propagation paths when propagating through *Moskstraumen*, as shown by OS21 (their Fig. 12). The influence of current refraction on swell can also explain the aforementioned mean increase in ΔT_{m02} with longer swell propagating into *Vestfjorden* in WAM_{curr} (upper right hand panel of Fig. 9). In addition to refraction in *Moskstraumen*, the advection of wave action from the south by the NCC (see Fig. 1) also modulates the wave field. The mean H_s difference for a 24 hour period was higher in WAM_{curr}, despite the changing vorticity field in *Moskstraumen* due to the tidal current (lower right panel of Fig. 9). The accumulation of wave action in *Vestfjorden* is in accordance with the results of Ardhuin et al. (2017), who found refraction and advection effects to dominate and partially cancel each other for scales larger than 30 km. Inclusion of current forcing tends to also reduce the horizontal difference in H_s across the *Lofoten* peninsula (not shown).

The shallow banks outside *Senja* reveal a positive mean and large maximum ΔH_s (location 6– Fig. 7). There are also several locations in lee of the mean NCC that exhibit substantial differences in wave energy connected to flow acceleration from corner effects (Fig. 7a). It is also interesting to note the separation between areas of positive and negative mean ΔH_s in the northernmost part of the model domain (e.g., between areas 3 and 4 in Fig. 7). Here, areas with on average positive ΔH_s are located away from the coast, i.e., collocated with regions of higher eddy activity and large current variability (Figs. 2a,d), and areas that are on average negative are located closer to the coast. The σ, RMSE, and min/max values indicate some hot spots mostly located close to the shoreline and associated with strong tidal currents (Fig. 7, panels b–e). These coincide with the strongest signal in the spatio-temporal analysis in Fig. 6.

3.3. Mapping regions with dangerous sea states

The regions identified by the NPG have been analyzed using the twin model experiment and observations (Fig. 3). We chose to investigate the areas where the ocean and wave models are expected to represent the dominating physical processes, and where the NPG gives a sufficient description of the phenomenon and underlying cause. Hence, area 2 is excluded in the analysis. In the subsequent sections, the regions are categorized according to their dominant cause. *Moskstraumen* (area 7) is highlighted because of the intense wave–current interactions as well as the availability of in situ observations.

3.3.1. Area 3 and 4: Opposing waves and tidal currents

Area 3 is exposed to the open ocean, as well as being subjected to a shallow plateau between 30–70 m (location 3 Fig. 1) which causes additional acceleration of the current. There is a clear tidal modulation of the wave field close to shore, where WAM_{curr} predicts higher mean wave height values (3– Figs. 6, 7a). The sharp transition to negative ΔH_s values further away from the coast is due to the mean flow direction of the NCC being eastward, together with waves primarily coming from west. In addition, the counter-flowing M_2 component is much weaker further out. Maximum increase in wave heights for this area was up to 40% in the period studied (Fig. 8c).

Although not confirmed with in situ measurements, the current in *Rolvsøysundet* and *Breisundet* (Rs and Bs in Fig. 10) is estimated to exceed 1 ms^{-1} (Den norske los, 2018). During spring tide, the current

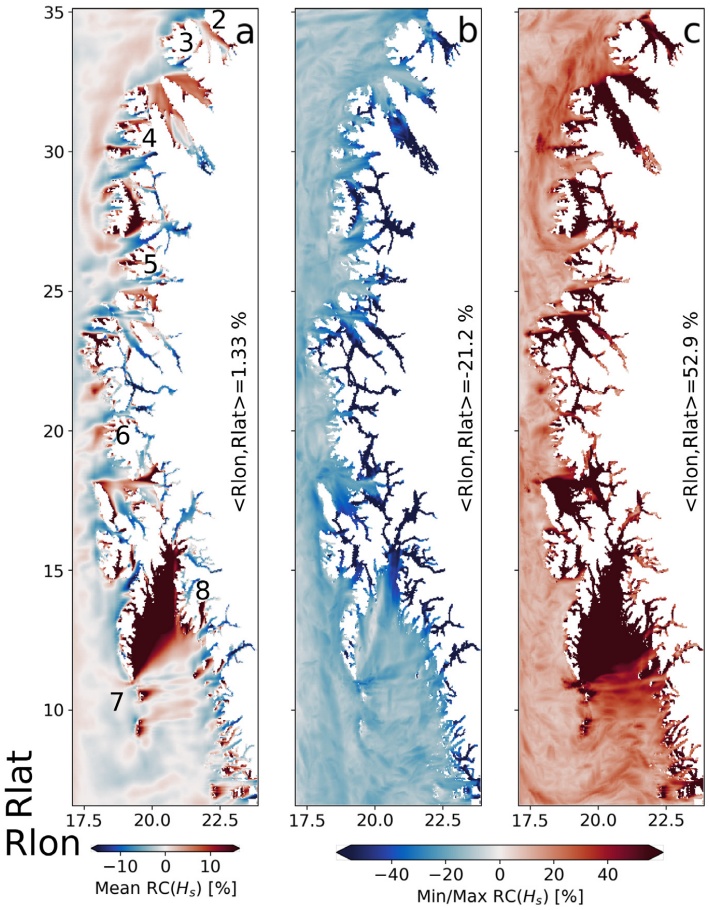

Fig. 8. Horizontal variability of relative change (RC) including the mean (a), and minimum/maximum values [(b)/(c)], computed for the entire study period.

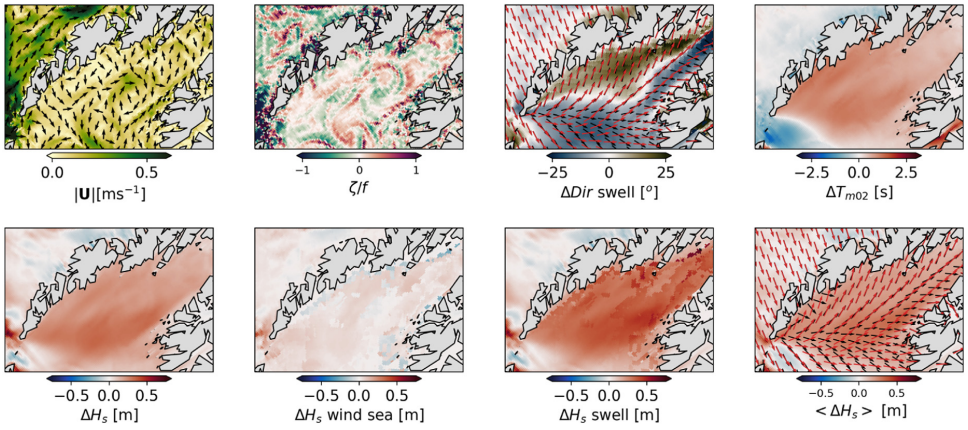

Fig. 9. Advection and current-induced refraction of wave energy in *Vestfjorden* at 2019-01-05T15:00 UTC. Upper panels from left denote the current speed, the vertical vorticity normalized by inertial frequency f, Δ swell direction (black arrows $\mathrm{WAM}_{\mathbf{ref}}$, red arrows $\mathrm{WAM}_{\mathbf{curr}}$), and ΔT_{m02}, respectively. Lower panels from left denote total ΔH_s, the difference for the wind sea, and swell components, and the mean difference for one day centered around 15:00UTC (together with mean swell propagation directions as above), respectively.

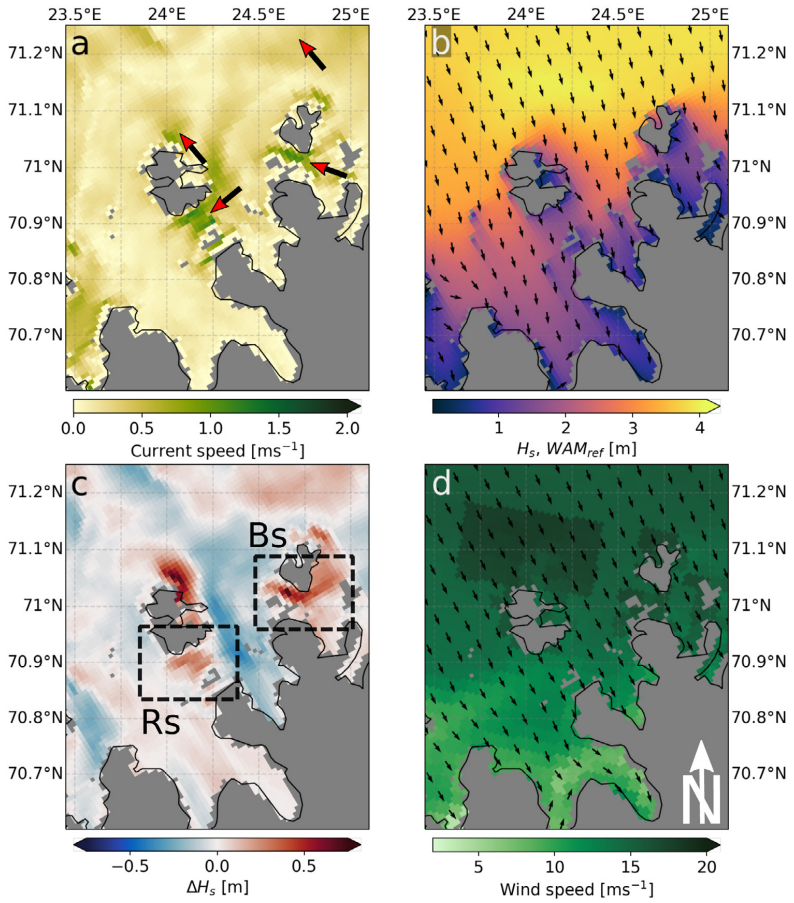

Fig. 10. Model snapshots at 2019-02-21T21 UTC for area 4 (see Fig. 3). Panels show: (a) the ocean current speed overlaid with tidal current direction (red arrows), (b) H_s with overlaid mean wave direction from WAM_{ref}, (c) ΔHs, and (d) wind speed with mean direction (black arrows). Wind, wave, and current conditions are similar to those reported to generate dangerous waves according to Den norske los (2018) in *Rolvsøysundet* (Rs) and *Breisundet* (Bs).

is reported to set up a rough sea state. A model snapshot is shown in Fig. 10. Here, the current meets the waves in Rs and Bs, resulting in an accompanying RC of about 20% and 40%, respectively. Maximum ΔH_s is about 0.7 m in Bs for the entire study period, and maximum RC is about 50%. The location of the areas with increased wave heights are well predicted by WAM_{curr}, together with their associated time scale, as seen in the highlighted rectangle in Fig. 6. The area with the largest positive ΔH_s, north of Rs, is not mentioned in the NPG. One reason could be that it is located on a shallow plateau with depths between 20–70 m, and is thus not used extensively for ship traffic.

3.3.2. Area 5 and 6: Refraction over shallows

Area 5 exhibits mostly positive mean RC over the shallows banks in the area, sometimes exceeding 25% (Figs. 1, 8). Even though the area is reported in NPG, the shallows are not denoted in the nautical charts provided by the Norwegian Mapping Authorities, contrary to all the other areas (https://norgeskart.no/#!?project=norgeskart&layers=1008). Nevertheless, the area is qualitatively resolved in terms of increased wave heights over the shallow regions according to the NPG

The shallow banks outside area 6 are also resolved in WAM_{curr}, with their on average positive RC in H_s up to 15% (Figs. 1, 8a). The shallow banks are also clearly visible in Fig. 6, with temporal modes associated with T_e. According to the NPG, dangerous waves occur when the tidal cycle is in phase with the NCC. The wave heights for northernmost shallow bank outside area 6 increase up to 40% (Fig. 8c). In order to quantify the impact of refraction, we conducted a wave ray-tracing analysis as shown in Fig. 11. Here we have implemented a wave ray-tracing solver for the Cartesian version of Eqs (2)–(5) to qualitatively assess the importance of refraction. Switching off the ambient current, the wave rays for a 14 s period swell converge over the shallow ridge due to depth-induced refraction (Fig. 11d). However, when currents are included, additional wave rays converge over the shallow due to current-induced refraction, causing the increase in H_s in WAM_{curr} (Fig. 11c). Thus, the ambient current acts as a wave guide towards the shallower regions by which the waves becomes trapped by the bathymetry, which in turn yield increasing wave heights.

3.3.3. Area 7: Moskstraumen

Intense wave–current interaction due to *Moskstraumen* occur on both sides of the southern tip of *Lofoten* (location 7– Fig. 1). The west side is known for the maximum H_s modulation, but the in situ observations were collected on the east side (B, Fig. 1). Here, the observed

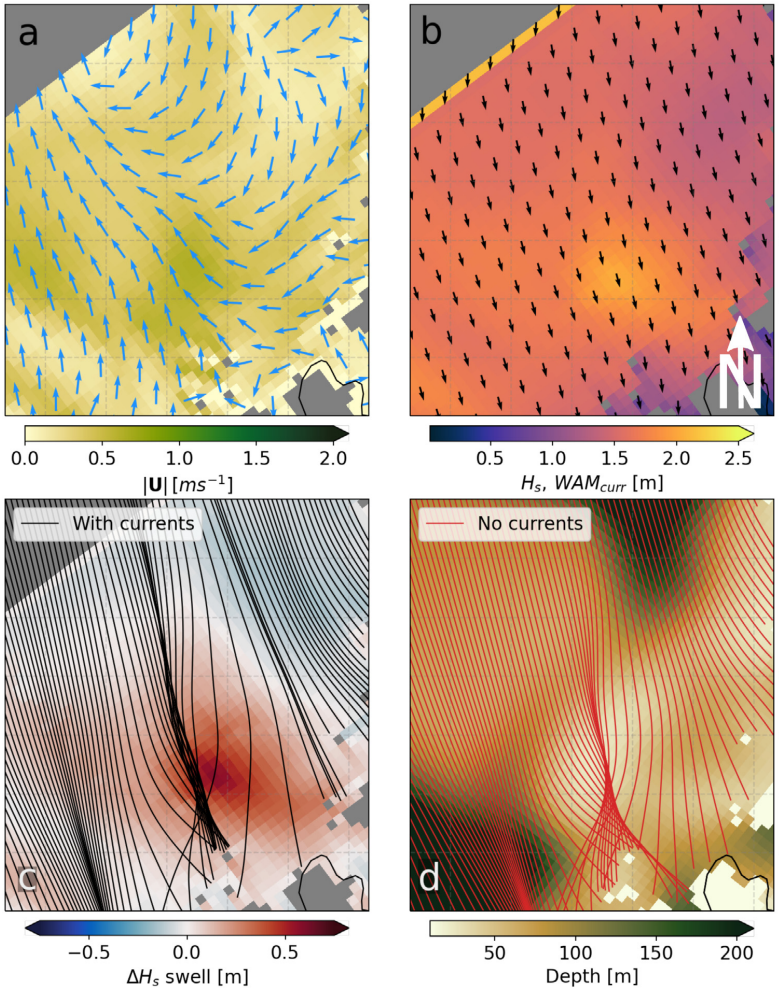

Fig. 11. The impact of current-induced refraction for the northernmost shallow bank in area 6 (see Fig. 3). A $T = 14\ s$ period wave is propagating against the current (panel a) according to the modeled mean swell direction (panel b) using a wave tracing solver. Panels (c) and (d) show the impact of current induced refraction (overlaid swell ΔH_s) and refraction due to bathymetry only (overlaid the depth profile), respectively.

interactions are presented first, followed by a detailed analysis on the west side.

The time series of H_s and the associated wave spectrum during an 8-day spring tide period in January 2019 are shown in Fig. 12. At the end of the period, $\text{WAM}_{\mathbf{curr}}$ H_s compares well with the observations at tidal cycles (see black triangles in Figs. 12a,g). Beginning on 23 January, the mean wave propagation direction gradually shifts from west to east following a shift in wind direction (Figs. 12c and d). Thus, wind waves and currents are coming into opposition as the current reaches its maximum. This leads to an increase in energy for the wind sea part of the observed and the $\text{WAM}_{\mathbf{curr}}$ spectrum (Figs. 12f,g). A current of 2 m s^{-1} (Fig. 12b) will block opposing wind waves with periods $T = 5$ s and shorter, which correspond well with the observed and modeled wind wave periods of around 0.2 Hz (Figs. 12f,g).

The modeled current maximum is more or less in phase with the observations (Fig. 12b). However, the peak after current maximum is at times out of phase (see black arrows Fig. 12b). Here, the northernmost part of the tidal current that has turned, as it turns westward before the rest of the tidal current (not shown). The turning induces a local horizontal shear of opposing surface currents, known locally as *Strinna*, which gives rise to a complicated sea state (Den norske los, 2018). Thus, for the first highlighted H_s peak, $\text{WAM}_{\mathbf{curr}}$ is out of phase with the observations as the eastward (not shown) propagating swell undergo an increase in wave energy due to *Strinna* (see lowest frequencies about 01-23T12:00 UTC Fig. 12f). Nevertheless, the 1D spectrum also reveal enhanced wave energy for the wind sea at current maximum, which corresponds well with the observations (Figs. 12f,g). However, at current maximum, the energy of the aforementioned swell decreases due to following waves and currents leading the decrease in H_s. In the context of numerical ocean modeling, a local phenomenon like *Strinna* can contaminate neighboring grid points due to limited horizontal resolution. This can in turn lead to a mismatch between wave predictions and observations, like in the case just described above. This highlights the challenges of comparing individual model grid points with observations.

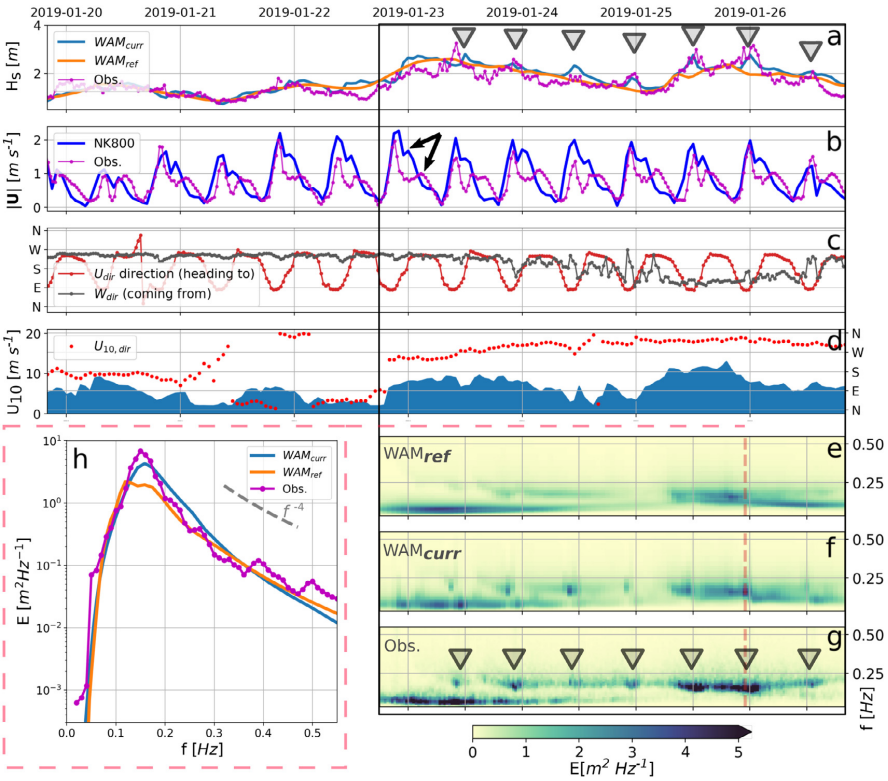

Fig. 12. Time series of modeled and measured wave, current, and wind conditions in *Moskstraumen* during spring tide in January 2019. Panels show: (a) H_s from WAM_{curr} (blue), WAM_{ref} (orange) and ADCP (magenta). Triangles denote when H_s is modulated due to the tidal current heading eastward during a rising tide. (b) modeled (blue) and observed (magenta) current speed (|**U**|). (c) Observed current (red) and mean wave propagation (gray) directions. (d) modeled wind speed (blue) and direction (red dots). The 2D wave energy density spectra from WAM_{ref}, WAM_{curr}, and the ADCP observations are given in panels (e), (f), and (g), respectively. (h) denote the 2D spectrum for a single point in time (see red line panels e–g).

Upon inspection of the 1D spectrum during current maxima we see that the wave energy around the peak frequency is two orders of magnitude larger in WAM_{curr} than WAM_{ref}, and correspond better with the observations (see Fig. 12h). However, the energy decay for the higher frequencies are less compared with the observations, suggesting that the wave dissipation parameterization is too conservative in cases like this.

Even though wave growth due to blocking waves seems to be the dominant mechanism, it most likely occurs in combination with the relative wind and the radiation stresses as also reported by Ardhuin et al. (2012), Vincent (1979). The impact of the relative wind is, however, not quantified in WAM_{curr} (Section 2.1.2). Nevertheless, the wind sea modulation at the peak of the tidal cycle corresponds well with the enhanced wave breaking reported by OS21 (see their Fig. 7). From Fig. 12c, it is perhaps not obvious that the waves and currents oppose each other near the current maximum since the observed mean wave direction can change erratically and sometimes record westward propagating waves. As the ADCP is an Eulerian measurement, these spikes around the current maximum are a result of blocked waves which are advected westward by the strong tidal current. Additional selected cases comparing observations with model results in *Moskstraumen* are given in Appendix.

From the twin experiment intercomparison, maximum H_s modulation in *Moskstraumen* occurs on the western side of *Lofoten*, when the tidal current is heading westward during a falling tide (see area 7 in Fig. 7e). A snapshot from 2019-01-24T05 UTC is shown in Fig. 13. Here, eastward propagating swell opposes the tidal current. Using the aforementioned wave ray-tracing method, a $T = 12$ s period wave train was propagated through the domain. This wave period is representative of the peak period in WAM_{curr} (not shown). We find the focusing of wave ray paths to agree with ΔH_s in the current branch (right panel Fig. 13). Local wind sea is also present, but the swell part of the spectrum is more strongly modulated by the tidal current (not shown). Trapped waves due to tidal currents were also reported by Ardhuin et al. (2012) from their field and model study in the Fromveur passage. In our case, however, the horizontal extent of the tidal current is not sufficiently long for the swell to be reflected back to the center from the edges of the current branch.

The largest ΔH_s west in *Moskstraumen* was about 90%. During periods of relatively calm winds, with H_s between 2–3 m, ΔH_s was about 1.5 m (not shown), giving a relative difference of about 50%. This implies that the current can modify the wave field to the same extent as that of the wind field variations. We also found minimum $\Delta T_{m02} < -3$ s in *Moskstraumen*, which is caused by the increase in wave frequency due to the Doppler shift (Eq. (7)).

4. Discussion

In *Moskstraumen*, the observed temporal scales of wave field modulations are resolved in WAM_{curr} (Figs. 4, 6). The wave energy density

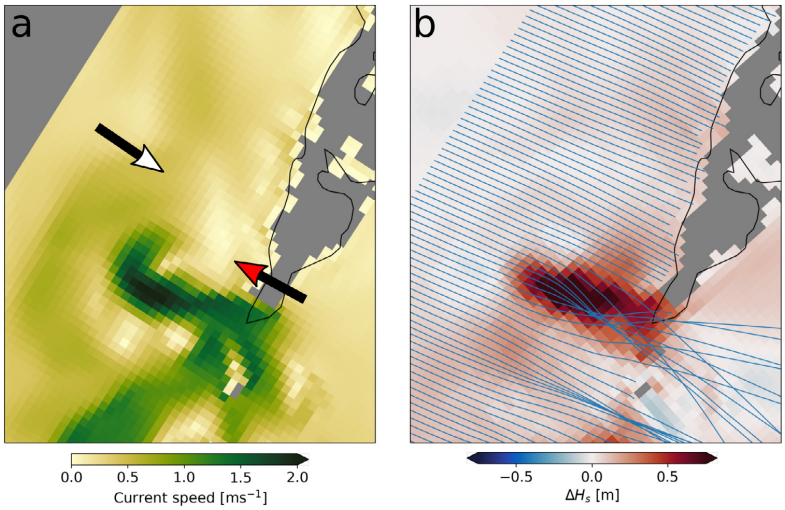

Fig. 13. Model snapshots (2019-01-24T05 UTC) during a falling tide in *Moskstraumen* (area 7 Fig. 3), when the tidal current is heading west. Panel (a) shows the current speed and direction (red arrow) and the dominant swell propagation direction (white arrow). Panel (b) show ΔHs with overlaid wave rays (blue) corresponding to eastward propagating swell with T = 12 s from a wave ray tracing solver.

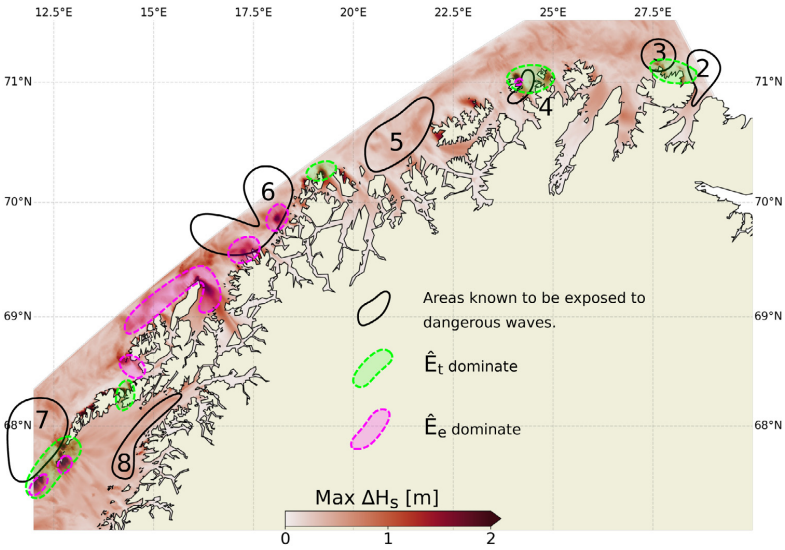

Fig. 14. Maximum ΔH_s for the entire study period (see Fig. 7e) overlaid with the areas known to be exposed to dangerous waves (black solid lines from Fig. 3) together with selected areas with strong temporal H_s variability at different temporal modes (see Fig. 6).

spectrum and the associated H_s are at times also correctly represented by $\mathrm{WAM_{curr}}$, contrary to $\mathrm{WAM_{ref}}$ (see Fig. 12). This is in agreement with Ardhuin et al. (2012), who also found their wave model capable of representing the current-induced effects using the same wave dissipation parameterization as in our study. Furthermore, and as shown explicitly in Appendix, the current forcing can impact the wave field to a similar degree to that of wind field, and also provide a more realistic representation of H_s during strong storms (U_{10} = 35 m s^{-1}, ΔH_s ~ 2 m, see Fig. 15d). We find that the largest wave height modulations in tidal currents occur when waves oppose the current. For wind sea, the increase in wave heights are due to wave blocking and energy bunching due to the Doppler shift, whereas refraction is most important for swell. This is also in agreement with previous work (e.g. Baschek, 2005; Ardhuin et al., 2012; Masson, 1996; Romero et al., 2017, 2020). However, deviations between observations and model results suggest that some wave–current interactions are not properly

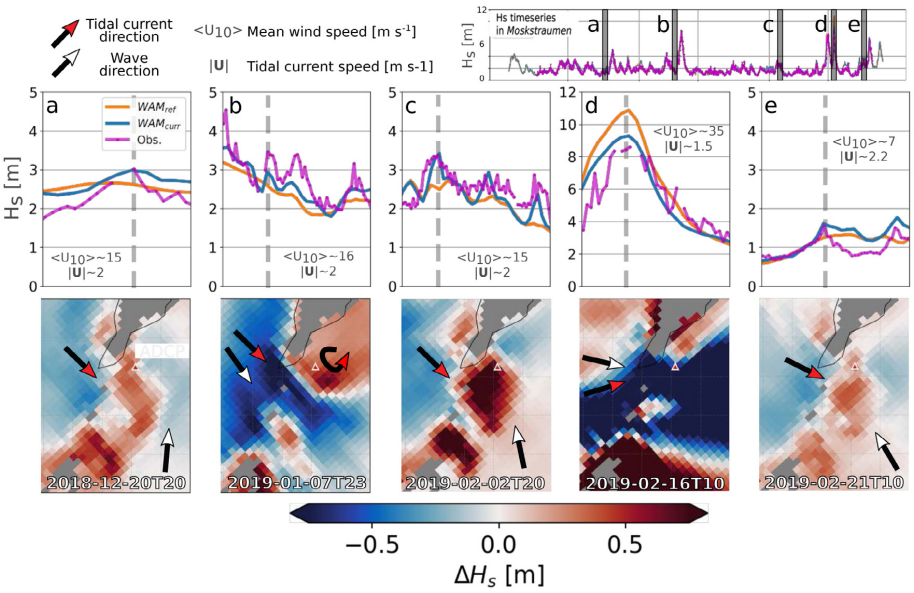

Fig. 15. Comparing H_s representation for selected segments in *Moskstraumen*. Columnwise, panels a-e show a zoomed view on H_s time series for a particular period, with a 2D ΔH_s snapshot associated with the vertical gray line. Arrows filled with red and white represent the tidal current direction and mean wave propagation direction, respectively. The approximate mean wind speed, $\langle U_{10} \rangle$, and maximum current speed, $|\mathbf{U}|$, for each of the snapshots are denoted in each time series panel. Red triangle denotes the location of the ADCP.

resolved by the wave model, which is expected due to the limitations of linear theory (Babanin et al., 2017). It is also a reminder of the inaccuracy of comparing single model grid cells with observations.

As the tidal cycles are well resolved WAM_{curr} (Fig. 12f), we consider it valid to extrapolate our analysis from *Moskstraumen* to other areas exposed to tidal currents, despite the lack of observations. This is of particular interest for dangerous wave areas (Fig. 3), and includes area 3, area 4 (Fig. 10), and the west side of *Moskstraumen* (Fig. 13) where we have no in situ measurements. For the latter, the model inter-comparison reveals an increase in H_s of up to 90% in the study period.

On longer time scales, WAM_{curr} qualitatively resolves areas 5 and 6 in the mean (Fig. 7a), but also for single cases (Fig. 11). We find the ambient current to act as a wave guide such that additional wave trains gets trapped by the local bathymetry, ultimately leading to increasing wave heights. The wave and current conditions correspond to what is reported in the NPG (Den norske los, 2018).

We find the proposed method of mapping the spatio-temporal variability differences between two runs in a twin experiment to be useful in identifying regions with intense wave–current interaction (Fig. 6). The information thus provided complements that from the maps of σ and RMSE (see Figs. 7b,c) by clearly distinguishing the dominant spectral regimes at work. When overlaying the most dominant areas in Fig. 6 with the maximum ΔH_s (Fig. 7e) together with the dangerous waves areas (Fig. 3), we see that those that are exposed to strong tidal currents stand out (Fig. 14). As all of these areas were characterized independently in the NPG, i.e. the areas 2–8, we conclude that this demonstrates the importance of including current forcing in high-resolution wave models in areas with strong currents. Their use is two-fold. First, the sort of twin-model runs shown here can be used to identify areas where the sea state is influenced by strong currents, and associated gradients. This can best be done by running twin-model hindcasts over sufficiently long periods and then analyze the difference fields of the two runs using the methodology presented here. In particular, mapping the average (Fig. 7) and maximum (Fig. 14) differences in significant wave height, ΔH_s, and assessing the associated spectral distribution through RGB composites (Fig. 6) are efficient ways to identify such potentially dangerous regions. Secondly, the same method can be employed for real-time forecasting, as is done operationally at the Norwegian Meteorological Institute. By providing maps of the wave height difference from such twin-model forecasts, it is immediately evident when and where situations with strong wave–current interaction can be expected.

In area 8 in *Vestfjorden*, we do not find spiky values in ΔH_s indicating large waves. However, we do find that WAM_{curr} reduces the bias and NRMSE in H_s against altimeter observations (P5 Table 2 and Figs. 5, 7, and 8). For the remainder of the domain, wave height variations mostly occur on shorter horizontal scales than the *Vestfjorden* basin (like P1-P4 in Fig. 5) such that the coarse resolution of Level-3 altimeter observations (about 7 km) is insufficient to reveal the differences. Utilizing Level-2 observations using novel filtering methods, such as Bohlinger et al. (2019) for characterizing wave height variability will be the focus of future studies.

An area that stands out with strong wave field modulation, which is not reported in the NPG, is located between area 6 and 7 in Fig. 3. Our findings show that $\hat{E}_t < \hat{E}_e$ (Fig. 14). However, $\hat{E}(\text{M}_1)$ is in the northernmost part similar to that in *Moskstraumen* (see line *i* Fig. 6). Further south, the wave field modulation occur on frequencies below M_1, suggesting that refraction due to eddies and whirls dominate. More field work experiments is needed to properly assess wave–current interaction in this area.

A limitation in the present study is the use of surface currents and not taking into account the vertical shear of the currents. Even though this can be considered a second order effect, it is expected to have an impact on the wave field (Quinn et al., 2017). On the other hand, tidal currents are often barotropic (like *Moskstraumen* see Fig. 7 in OS21), which justifies the use of surface currents in these areas.

To summarize, five out of seven areas known for dangerous waves are qualitatively resolved in WAM_{curr} in terms of increased wave heights (i.e. 3–7 Fig. 14). For these areas, the dominating cause leading to wave growth agrees with the reports in the NPG. The two remaining areas, i.e. 2 and 8, WAM_{curr} does neither indicate situations with particularly large waves in our study period, nor does it imply large, local horizontal wave height gradients. Nevertheless, the large mean relative H_s increase in *Vestfjorden* together with the bias reduction against altimeter observations show that the wave field representation in this region is improved in WAM_{curr}.

Based on the results and the discussion above we argue that current forcing should be included in wave forecasts in our study region. In particular tidal currents as they enforce the largest wave field variability and makes a large impact on the wave heights. Spectral wave models have for decades proven to yield good predictions of the sea state, including under extreme storm events (Aarnes et al., 2012). However, with the advent of high-resolution operational ocean models capable of faithfully resolving the tidal and baroclinic current field, the modulation of the wave field by spatially varying currents should also be taken into account.

5. Conclusion

In a twin wave model study in Northern Norway we have investigated the impact of current forcing in spectral wave models. This is an area exposed to waves from the open ocean, and an ocean circulation which is dominated by tides and energetic currents with associated eddies. We find the wave model with current forcing to qualitatively resolve several areas that are reported in the Norwegian Pilot Guide for their large, and sometimes dangerous, waves due to intense wave–current interaction. This is in contrast to the wave model without current forcing. The dominating physical mechanism leading to increased wave heights also correspond to the reports in the Pilot Guide. Further to this, our results indicate that some areas undergo strong wave height modulations, which are not reported in the Pilot Guide.

We find the proposed diagnostic method for mapping temporal variability in twin model experiments to be convenient in analyzing regions dominated by ocean dynamics on different time scales. It is easy to implement and simple to adjust in terms of frequency ranges of interest. In this work we focused mainly on the modulation of the significant wave height.

Tidal currents induce the largest absolute wave height discrepancies between the two model runs. We find the magnitude and phase in wave height variability to be well represented in *Moskstraumen*, which is one of the world's strongest tidal currents in the open ocean. Here, we find wave height deviations between the twin model runs up to 50% to corroborate with observations. Furthermore, and in absence of direct observations, we find inter model H_s differences up to 90% in tidal currents.

Maximum relative wave height discrepancies were found in areas sheltered from the open ocean and with less energetic currents, like *Vestfjorden*. Here, we find a better correspondence between altimeter observations of H_s and the wave model predictions with current forcing. Refraction and advection of wave action reduces the bias and RMSE by up to 16% and 18%, respectively, for specific periods. The spatial extent of *Vestfjorden* is also large enough to be sufficiently resolved by conventional Level-3 altimeter observations.

Inclusion of current forcing is still uncommon at operational centers (Palmer and Saulter, 2016; Staneva et al., 2015; Kanarik et al., 2021; Rapizo et al., 2018). We would suggest to include current forcing in the wave forecast models covering Northern Norway. Particularly in areas with strong tidal currents, the current forcing enforce an improved representation of the wave field for the end users.

CRediT authorship contribution statement

Trygve Halsne: Conceptualization, Methodology, Investigation, Writing – original draft. **Patrik Bohlinger:** Validation, Writing – original draft. **Kai Håkon Christensen:** Writing – original draft, Supervision. **Ana Carrasco:** Resources. **Øyvind Breivik:** Writing – original draft, Supervision.

Declaration of competing interest

The authors declare that they have no known competing financial interests or personal relationships that could have appeared to influence the work reported in this paper.

Acknowledgments

This research was partly funded by the Research Council of Norway through the project MATNOC, Grant No 308796. We greatly appreciate all the help from employees at Nortek AS and the Norwegian Coastal Administration who made possible the instrument deployment as well as acquiring, processing, and analyzing the ADCP data. ØB gratefully acknowledges the support by the Research Council of Norway through the Stormrisk project (Grant No 300608). TH would like to thank Thomas Lavergne for fruitful discussions concerning data visualization.

Appendix. Additional selected cases in Moskstraumen

Five additional segments to Section 3.3.3 concerning the impact of *Moskstraumen* on the wave field are presented in Fig. 15. All during rising tide, i.e. with an eastward oriented current. In Fig. 15a, H_s increases as wind waves meet an opposing current. Prior to this model snapshot, the H_s observations are invalid due to the tilt of the ADCP, here indicated by the missing line in the time series panel. Nevertheless, as the current speed starts decreasing, there is a good agreement between the observations and H_s predicted by WAM_{curr} during maximum current speed. Otherwise, WAM_{ref} is actually closer. There are, however, large horizontal gradients in ΔH_s as is evident from the two-dimensional (2D) views (lower panels in Fig. 15). Thus, comparing instead with neighboring grid points yielded slightly different results, except near the peak (not shown). Similarly, the event in Fig. 15c is also exposed to opposing wind waves and currents. The first and last peak in H_s are resolved by WAM_{curr} but not by WAM_{ref}.

For the event in Fig. 15b, both wave model runs predict a strong, large-scale gradient in H_s between the west (5 m) and east side (2 m) of the *Moskens Sound* (not shown). There is also a shear in the ocean current between the tidal current heading eastward, and a current following the coast west off *Lofotodden*, ending in a clockwise rotating eddy. The area sees frequent generation of eddies and dipoles due to the tidal current (see Fig. 9 OS21 and Fig. 8 Børve et al., 2021). The positive Doppler shift due to the wave-following tidal current stretches the waves and increases the wave period, with an accompanied decrease in wave amplitude in WAM_{curr}. Waves are also advected both by the tidal current and the NCC, giving rise to a region where wave action density accumulates. In addition, when escaping the tidal current, the waves experience a negative Doppler shift and thus an increase energy, as also reported by Romero et al. (2017).

The most extreme wave conditions in the study period occurred in late February, with H_s modeled to be around 9 m and 11 m by WAM_{curr} and WAM_{ref}, respectively (Fig. 15d). The observations were just below 8.5 m. The tidal current, although weaker than in the other cases, was oriented in the same overall direction as the waves, giving a strong reduction in H_s within the branch of the tidal current (negative ΔH_s region in Fig. 15d). There is an increase in H_s towards the coast, most likely due to refraction since the current speed is weaker towards the coast (Palmer and Saulter, 2016).

For the last event, the current exceeded 2 m s^{-1} and the wind speed was below 10 m s^{-1} heading north-west (Fig. 15e). Between the two

tidal cycles, both wave models over-predict H_s, but only WAM_{curr} resolved the wave height modulations. This example demonstrates that the tidal current can impact the wave field to a similar degree to that of the wind field, with variations in H_s of the order of 50%. The second peak in Fig. 15e covered the maximum relative change in our measurement period, which was 55.6% (at 2019-02-21T22 UTC).

References

Aarnes, O.J., Breivik, O., Reistad, M., 2012. Wave extremes in the northeast atlantic. J. Clim. 25 (5), 1529–1543. http://dx.doi.org/10.1175/JCLI-D-11-00132.1, Publisher: American Meteorological Society Section: Journal of Climate, URL: https://journals.ametsoc.org/view/journals/clim/25/5/jcli-d-11-00132.1.xml.

Albretsen, J., Sperrevik, A.K., Staalstrøm, A., Sandvik, A.D., Vikebø, F., Asplin, L., 2011. NorKyst-800 Report No. 1: User Manual and Technical Descriptions, Tech. Rep. 2. Technical Report, Institute of Marine Research, Bergen, Norway, URL: https://www.hi.no/en/hi/nettrapporter/fisken-og-havet/2011/fh_2-2011_til_web.

Ardhuin, F., Gille, S.T., Menemenlis, D., Rocha, C.B., Rascle, N., Chapron, B., Gula, J., Molemaker, J., 2017. Small-scale open ocean currents have large effects on wind wave heights. J. Geophys. Res. Oceans 122 (6), 4500–4517. http://dx.doi.org/10.1002/2016JC012413, _eprint: https://agupubs.onlinelibrary.wiley.com/doi/pdf/10.1002/2016JC012413, URL: https://agupubs.onlinelibrary.wiley.com/doi/abs/10.1002/2016JC012413.

Ardhuin, F., Rogers, E., Babanin, A.V., Filipot, J.-F., Magne, R., Roland, A., Westhuysen, A.v.d., Queffeulou, P., Lefevre, J.-M., Aouf, L., Collard, F., 2010. Semiempirical dissipation source functions for ocean waves. part I: Definition, calibration, and validation. J. Phys. Oceanogr. 40 (9), 1917–1941. http://dx.doi.org/10.1175/2010JPO4324.1, Publisher: American Meteorological Society Section: Journal of Physical Oceanography, URL: https://journals.ametsoc.org/view/journals/phoc/40/9/2010jpo4324.1.xml.

Ardhuin, F., Roland, A., Dumas, F., Bennis, A.-C., Sentchev, A., Forget, P., Wolf, J., Girard, F., Osuna, P., Benoit, M., 2012. Numerical wave modeling in conditions with strong currents: Dissipation, refraction, and relative wind. J. Phys. Oceanogr. 42 (12), 2101–2120. http://dx.doi.org/10.1175/JPO-D-11-0220.1, _eprint: https://journals.ametsoc.org/jpo/article-pdf/42/12/2101/4520148/jpo-d-11-0220_1.pdf.

Babanin, A.V., Rogers, W., De Camargo, R., Doble, M., Durrant, T., Filchuk, K., Ewans, K., Hemer, M., Janssen, T., Kelly-Gerreyn, B., MacHutchon, K., Mccomb, P., Qiao, F., Schulz, E., Skvortsov, A., Thomson, J., Vichi, M., violante carvalho, N., Wang, D., Young, I., 2019. Waves and swells in high wind and extreme fetches, measurements in the southern ocean. Front. Mar. Sci. 6, 361. http://dx.doi.org/10.3389/fmars.2019.00361.

Babanin, A.V., van der Weshuijsen, A., Chalikov, D., Rogers, W.E., 2017. Advanced wave modeling, including wave-current interaction. J. Mar. Res. 75 (3), 239–262. http://dx.doi.org/10.1357/002224017821836798.

Baschek, B., 2005. Wave–current interaction in tidal fronts. In: Rogue Waves: Proc. 14th 'Aha Huliko'a Hawaiian Winter Workshop. University of Hawaii at Manoa, Honolulu, HI, pp. 131–138.

Behrens, A., Staneva, J., Saetra, Ø., Janssen, P., 2013. Documentation of a Web Based Source Code Library for WAM. Technical Report, Helmholtz-Zentrum Geestacht,Geesthacht, Germany, URL: http://met-xpprod.customer.enonic.io/sokeresultat/_/attachment/inline/c1fdc351-1109-47fc-9d9e-65c9f31eaccb:b52dfe2b5953103564a339bb290b83c66b1315f6/MyWave_Report_D1.1.pdf.

Bohlinger, P., Breivik, Ø., Economou, T., Müller, M., 2019. A novel approach to computing super observations for probabilistic wave model validation. Ocean Model. 139, 101404. http://dx.doi.org/10.1016/j.ocemod.2019.101404, URL: https://www.sciencedirect.com/science/article/pii/S1463500319300435.

Børve, E., Isachsen, P.E., Nøst, O.A., 2021. Rectified tidal transport in Lofoten-Vesterålen, Northern Norway. Ocean Sci. Discuss. 1–33. http://dx.doi.org/10.5194/os-2021-41, Publisher: Copernicus GmbH, URL: https://os.copernicus.org/preprints/os-2021-41/.

Cavaleri, L., Fox-Kemper, B., Hemer, M., 2012. Wind waves in the coupled climate system. Bull. Am. Meteorol. Soc. 93 (11), 1651–1661. http://dx.doi.org/10.1175/BAMS-D-11-00170.1, Publisher: American Meteorological Society Section: Bulletin of the American Meteorological Society. URL: https://journals.ametsoc.org/view/journals/bams/93/11/bams-d-11-00170.1.xml.

Christensen, K.H., Sperrevik, A.K., Broström, G., 2018. On the variability in the onset of the Norwegian coastal current. J. Phys. Oceanogr. 48 (3), 723–738. http://dx.doi.org/10.1175/JPO-D-17-0117.1, Publisher: American Meteorological Society Section: Journal of Physical Oceanography. URL: https://journals.ametsoc.org/view/journals/phoc/48/3/jpo-d-17-0117.1.xml.

Den norske los, 2018. The Norwegian Pilot Guide—Sailing Directions for the Norwegian Coast, Svalbard and Jan Mayen. The Norwegian Mapping Authority, Stavanger, Norway.

Dysthe, K.B., 2001. Refraction of gravity waves by weak current gradients. J. Fluid Mech. 442, 157–159. http://dx.doi.org/10.1017/S0022112001005237, Publisher: Cambridge University Press. URL: https://www.cambridge.org/core/journals/journal-of-fluid-mechanics/article/abs/refraction-of-gravity-waves-by-weak-current-gradients/BCA46BDBE52EDC210719E9CC95DA7ECB.

Gemmrich, J., Garrett, C., 2012. The signature of inertial and tidal currents in offshore wave records. J. Phys. Oceanogr. 42 (6), 1051–1056. http://dx.doi.org/10.1175/JPO-D-12-043.1, Place: Boston MA, USA Publisher: American Meteorological Society. URL: https://journals.ametsoc.org/view/journals/phoc/42/6/jpo-d-12-043.1.xml.

Gjevik, B., Moe, H., Ommundsen, A., 1997. Sources of the melstrom. NAT 388, 837–838. http://dx.doi.org/10.1038/42159.

Hasselmann, S., Hasselmann, K., Allender, J.H., Barnett, T.P., 1985. Computations and parameterizations of the nonlinear energy transfer in a gravity-wave specturm. part II: Parameterizations of the nonlinear energy transfer for application in wave models. J. Phys. Oceanogr. 15 (11), 1378–1391. http://dx.doi.org/10.1175/1520-0485(1985)015<1378:CAPOTN>2.0.CO;2, Publisher: American Meteorological Society Section: Journal of Physical Oceanography. URL: https://journals.ametsoc.org/view/journals/phoc/15/11/1520-0485_1985_015_1378_capotn_2_0_co_2.xml.

Holthuijsen, L.H., 2007. Waves in Oceanic and Coastal Waters. Cambridge University Press, http://dx.doi.org/10.1017/CBO9780511618536.

Kanarik, H., Tuomi, L., Björkqvist, J.-V., Kärnä, T., 2021. Improving baltic sea wave forecasts using modelled surface currents. Ocean Dyn. 71 (6), 635–653. http://dx.doi.org/10.1007/s10236-021-01455-y.

Komen, G.J., Cavaleri, L., Doneland, M., Hasselmann, K., Hasselmann, S., Janssen, P.A.E.M. (Eds.), 1994. Dynamics and Modelling of Ocean Waves. Cambridge Univeristy Press, http://dx.doi.org/10.1017/CBO9780511628955.

Kristensen, N.M., Gusdal, Y., 2021. NorKyst800 Model Currents Validation. MET Report, (2/2021), Norwegian Meteorological Institute, p. 44, URL: https://www.met.no/publikasjoner/met-report/_/attachment/download/8b99ea1b-200f-4a09-9eb7-3ada0580e157:56ff9d6c44186aa495be038a1cc5dd84d3ca3f2a/MET-report-02-2021.pdf.

Marechal, G., Ardhuin, F., 2021. Surface currents and significant wave height gradients: Matching numerical models and high-resolution altimeter wave heights in the agulhas current region. J. Geophys. Res. Oceans 126 (2), http://dx.doi.org/10.1029/2020JC016564, e2020JC016564. _eprint: https://agupubs.onlinelibrary.wiley.com/doi/pdf/10.1029/2020JC016564. URL: https://agupubs.onlinelibrary.wiley.com/doi/abs/10.1029/2020JC016564.

Marin, C., Bovolo, F., Bruzzone, L., 2015. Building change detection in multitemporal very high resolution SAR images. IEEE Trans. Geosci. Remote Sens. 53 (5), 2664–2682. http://dx.doi.org/10.1109/TGRS.2014.2363548, Conference Name: IEEE Transactions on Geoscience and Remote Sensing.

Masson, D., 1996. A case study of wave–current interaction in a strong tidal current. J. Phys. Oceanogr. 26 (3), 359–372. http://dx.doi.org/10.1175/1520-0485(1996)026<0359:ACSOWI>2.0.CO;2, _eprint: https://journals.ametsoc.org/jpo/article-pdf/26/3/359/4424891/1520-0485(1996)026_0359_acswi_2_0_co_2.pdf.

Mathiesen, M., 1987. Wave refraction by a current whirl. J. Geophys. Res. Oceans 92 (C4), 3905–3912. http://dx.doi.org/10.1029/JC092iC04p03905, _eprint: https://agupubs.onlinelibrary.wiley.com/doi/pdf/10.1029/JC092iC04p03905. URL: https://agupubs.onlinelibrary.wiley.com/doi/abs/10.1029/JC092iC04p03905.

McWilliams, J.C., 2016. Submesoscale currents in the ocean. Proc. R. Soc. A Math. Phys. Eng. Sci. 472 (2189), 20160117. http://dx.doi.org/10.1098/rspa.2016.0117, Publisher: Royal Society. URL: https://royalsocietypublishing.org/doi/10.1098/rspa.2016.0117.

Mork, M., 1981. Circulation phenomena and frontal dynamics of the norwegian coastal current. Philos. Trans. R. Soc. Lond. Ser. A Math. Phys. Sci. 302 (1472), 635–647, Publisher: The Royal Society. URL: https://www.jstor.org/stable/37043.

Müller, M., Batrak, Y., Kristiansen, J., Køltzow, M.A., Noer, G., Korosov, A., 2017. Characteristics of a convective-scale weather forecasting system for the European arctic. Mon. Weather Rev. 145 (12), 4771–4787. http://dx.doi.org/10.1175/MWR-D-17-0194.1, Publisher: American Meteorological Society Section: Monthly Weather Review. URL: https://journals.ametsoc.org/view/journals/mwre/145/12/mwr-d-17-0194.1.xml.

Palmer, T., Saulter, A., 2016. Evaluating the Effects of Ocean Current Fields on a UK Regional Wave Model. Technical Report, (612), UK Met Office, Exeter, United Kingdom, p. 35, URL: https://library.metoffice.gov.uk/Portal/Default/en-GB/RecordView/Index/212801.

Quinn, B.E., Toledo, Y., Shrira, V.I., 2017. Explicit wave action conservation for water waves on vertically sheared flows. Ocean Model. 112, 33–47. http://dx.doi.org/10.1016/j.ocemod.2017.03.003, URL: https://www.sciencedirect.com/science/article/pii/S1463500317300288.

Rapizo, H., Durrant, T.H., Babanin, A.V., 2018. An assessment of the impact of surface currents on wave modeling in the Southern ocean. Ocean Dyn. 68 (8), 939–955. http://dx.doi.org/10.1007/s10236-018-1171-7.

Röhrs, J., Christensen, K.H., 2015. Drift in the uppermost part of the ocean. Geophys. Res. Lett. 42 (23), 10,349–10,356. http://dx.doi.org/10.1002/2015GL066733, _eprint: https://onlinelibrary.wiley.com/doi/pdf/10.1002/2015GL066733. URL: https://onlinelibrary.wiley.com/doi/abs/10.1002/2015GL066733.

Romero, L., Hypolite, D., McWilliams, J.C., 2020. Submesoscale current effects on surface waves. Ocean Model. 153, 101662. http://dx.doi.org/10.1016/j.ocemod.2020.101662, URL: http://www.sciencedirect.com/science/article/pii/S1463500320301645.

Romero, L., Lenain, L., Melville, W.K., 2017. Observations of surface wave–current interaction. J. Phys. Oceanogr. 47 (3), 615–632. http://dx.doi.org/10.1175/JPO-D-16-0108.1, _eprint: https://journals.ametsoc.org/jpo/article-pdf/47/3/615/4587128/jpo-d-16-0108_1.pdf.

Saetra, Ø., Halsne, T., Carrasco, A., Breivik, Ø., Pedersen, T., Christensen, K.H., 2021. Intense interactions between ocean waves and currents observed in the lofoten maelstrom. J. Phys. Oceanogr. -1 (aop), http://dx.doi.org/10.1175/JPO-D-20-0290.1, Publisher: American Meteorological Society Section: Journal of Physical Oceanography. URL: https://journals.ametsoc.org/view/journals/phoc/aop/JPO-D-20-0290.1/JPO-D-20-0290.1.xml.

Segtnan, O.H., 2014. Wave refraction analyses at the coast of Norway for offshore applications. Energy Procedia 53, 193–201. http://dx.doi.org/10.1016/j.egypro.2014.07.228, URL: https://linkinghub.elsevier.com/retrieve/pii/S1876610214011059.

Shchepetkin, A.F., McWilliams, J.C., 2005. The regional oceanic modeling system (ROMS): A split-explicit, free-surface, topography-following-coordinate oceanic model. JPO 9, 347–404. http://dx.doi.org/10.1016/j.ocemod.2004.08.002.

Staneva, J., Behrens, A., Wahle, K., 2015. Wave modelling for the German Bight coastal-ocean predicting system. J. Phys. Conf. Ser. 633, 012117. http://dx.doi.org/10.1088/1742-6596/633/1/012117, Publisher: IOP Publishing.

Vincent, C.E., 1979. The interaction of wind-generated sea waves with tidal currents. J. Phys. Oceanogr. 9 (4), 748–755. http://dx.doi.org/10.1175/1520-0485(1979)009<0748:TIOWGS>2.0.CO;2, Place: Boston MA, USA Publisher: American Meteorological Society. URL: https://journals.ametsoc.org/view/journals/phoc/9/4/1520-0485_1979_009_0748_tiowgs_2_0_co_2.xml.

Paper III

Ocean wave tracing v. 1: a numerical solver of the wave ray equations for ocean waves on variable currents at arbitrary depths

Trygve Halsne, Kai Håkon Christensen, Gaute Hope, and Øyvind Breivik
Geoscientific Model Development, **16**/**22** (2023)

III

Geosci. Model Dev., 16, 6515–6530, 2023
https://doi.org/10.5194/gmd-16-6515-2023

Geoscientific Model Development
Open Access
EGU

Ocean wave tracing v.1: a numerical solver of the wave ray equations for ocean waves on variable currents at arbitrary depths

Trygve Halsne[1,2], **Kai Håkon Christensen**[1,3], **Gaute Hope**[1], **and Øyvind Breivik**[1,2]

[1]Oceanography and Marine Meteorology, Norwegian Meteorological Institute, Oslo, Norway
[2]Geophysical Institute, University of Bergen, Bergen, Norway
[3]Department of Geosciences – Section for Meteorology and Oceanography, University of Oslo, Oslo, Norway

Correspondence: Trygve Halsne (trygve.halsne@met.no)

Received: 3 February 2023 – Discussion started: 23 March 2023
Revised: 17 August 2023 – Accepted: 2 October 2023 – Published: 14 November 2023

Abstract. Lateral changes in the group velocity of waves propagating in oceanic or coastal waters cause a deflection in their propagation path. Such refractive effects can be computed given knowledge of the ambient current field and/or the bathymetry. We present an open-source module for solving the wave ray equations by means of numerical integration in Python v3. The solver is implemented for waves on variable currents and arbitrary depths following the Wentzel–Kramers–Brillouin (WKB) approximation. The ray tracing module is implemented in a class structure, and the output is verified against analytical solutions and tested for numerical convergence. The solver is accompanied by a set of ancillary functions such as retrieval of ambient conditions using OPeNDAP, transformation of geographical coordinates, and structuring of data using community standards. A number of use examples are also provided.

1 Introduction

Ambient currents and varying water depth affect the propagation path of ocean waves through refraction. Such changes can induce substantial horizontal wave height variability and build complex sea states through crossing rays, leading to caustics (Fig. 1) (Holthuijsen, 2007). The linear theory of wave kinematics has been known for almost a century and applies the Wentzel–Kramers–Brillouin approximation (WKB, and sometimes WKBJ, where the last initial refers to Jeffreys) to characteristic wave and current conditions (Kenyon, 1971). That is, the changes in wave amplitude a, angular intrinsic frequency σ, and ambient medium are small over distances on the order of a wavelength λ. Such a treatment is known as the *geometrical optics approximation* and is applicable in various scientific branches dealing with the propagation of wave rays on different frequency scales. The resulting set of equations, typically referred to as the *wave ray equations*, only have analytical solutions for certain idealized cases; hence numerical integration is necessary to calculate the wave rays in arbitrary current fields and over arbitrary bathymetry (Kenyon, 1971; Mathiesen, 1987; Johnson, 1947). Such solvers have been available in the ocean wave community since the advent of spectral wave models but often as part of a large and complex model framework and not generally available as stand-alone applications.

Recent developments in the ocean modeling community, including assimilation of observations, have led to more realistic ocean-model output fields, which in turn have led to an increased interest in wave–current interaction studies (Babanin et al., 2017). Current-induced refraction has often been singled out as the principal mechanism leading to horizontal wave height variability at scales between 1 km and several hundred kilometers (e.g., Irvine and Tilley, 1988; Ardhuin et al., 2017, 2012). Thus, a number of recent studies employ wave ray equation solvers in order to quantify the impact of refraction (e.g., Romero et al., 2017, 2020; Ardhuin et al., 2012; Masson, 1996; Bôas et al., 2020; Halsne et al., 2022; Saetra et al., 2021; Sun et al., 2022; Gallet and Young, 2014; Rapizo et al., 2014; Kudryavtsev et al., 2017; Bôas and Young, 2020; Jones, 2000; Segtnan, 2014; Mapp et al., 1985; Wang et al., 1994; Liu et al., 1994). However, such implementations are rarely open to the community. To the best of our knowledge, there is no open-source solver available

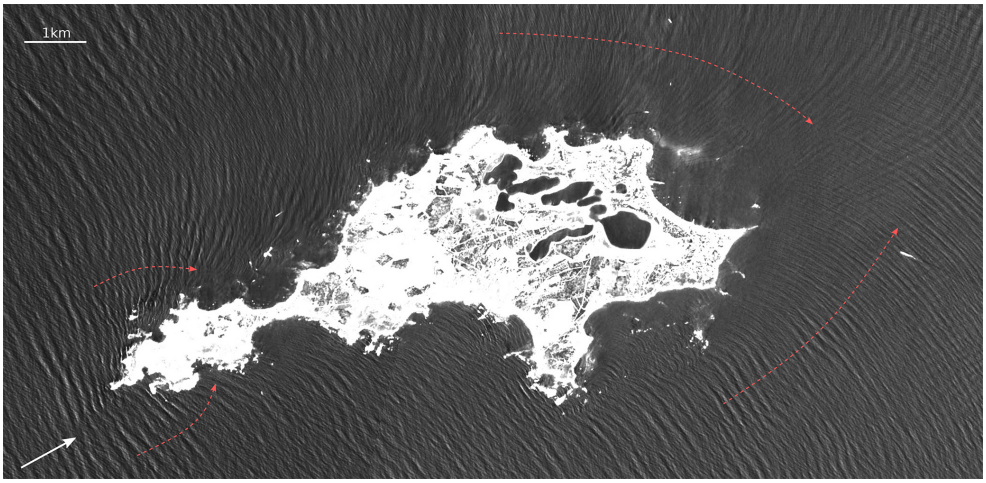

Figure 1. Depth refraction of swell against Rottnest Island off the coast of Western Australia depicted by the Copernicus Sentinel-2 mission, processed by ESA, in December 2021. The swell propagates northeastwards (white arrow) and interacts with the bathymetry when coming close to the island. Red arrows indicate the change in wave propagation direction, which is normal to the wave crest. An area subject to crossing waves is found on the east side of the island due to the change in wave propagation direction on both sides of the island.

in a high-level computer language to support such analyses. Furthermore, some of the solvers only focus on deep water where the wave ray equations are simplified since the topographic steering is negligible (e.g., Bôas and Young, 2020; Bôas et al., 2020; Mathiesen, 1987; Kenyon, 1971; Rapizo et al., 2014; Kudryavtsev et al., 2017). However, the joint effect of current- and depth-induced refraction at intermediate depth can be important (Romero et al., 2020; Halsne et al., 2022).

The scope of this paper is to present an open-source numerical solver of the wave ray equations implemented in Python. The paper is structured as follows: in Sect. 2 we present the theoretical background for the geometrical optics approximation of the wave ray equations on ambient currents and in variable depths. The numerical discretization and implementation of the equations and model are given in Sect. 3. Furthermore, some ancillary functions that support efficient workflows are also presented in Sect. 3. In Sect. 4, we compare the model output against analytical solutions and inspect the numerical convergence. A selection of examples using the ray tracing module, including idealized current fields and output from ocean circulation models, are presented in Sect. 5. Finally, a brief discussion and some concluding remarks are provided in Sect. 6.

2 Derivation of the wave ray equations

For simplicity, we first derive the wave ray equations in the x direction and then extend the results to both horizontal directions. We assume linear wave theory such that $ak \ll 1$, where a denotes the wave amplitude and $k = |\boldsymbol{k}| = |(k_x, k_y)|$ is the wave number. When considering the kinematics of wave trains through the geometrical optics approximation, it should be emphasized that diffraction is neglected. For a more complete description of the kinematics and dynamics of ocean waves, we refer the reader to Phillips (1977) and Komen et al. (1994).

2.1 The one-dimensional problem

A plane wave propagating in a slowly varying medium is given by

$$\eta(x,t) = ae^{i\chi}, \tag{1}$$

where $\chi = kx - \sigma t + \delta$ is the phase function. Here x, t, and δ denote position, time, and the phase, respectively, and σ is the wave angular intrinsic frequency given by the dispersion relation

$$\sigma = \sigma(k,x) = \sqrt{gk\tanh(kd)}, \tag{2}$$

where $d = d(x)$ is the water depth, which we assume to be constant in time. In the presence of an ambient current $U = U(x,t)$, the absolute wave angular frequency is

$$\omega = \Omega(k,x,t) = \sigma + kU, \tag{3}$$

which is often referred to as the *Doppler shift equation*. Consider now a phase function $\chi' = kx - \omega t + \delta$ in a frame of reference not moving with the current. Since $k = \partial\chi'/\partial x$ and

$\omega = -\partial\chi'/\partial t$, by cross-differentiating, we obtain the *conservation of wave crests* (see Note D, Holthuijsen, 2007, p. 339),

$$\frac{\partial k}{\partial t} + \frac{\partial \omega}{\partial x} = 0. \tag{4}$$

If we also assume local stationarity, i.e., $\partial/\partial t = 0$, k becomes constant in time and the frequency remains constant along the rays ($\partial\omega/\partial x = 0$). By taking the partial derivative of Eq. (3) while keeping t constant, we obtain

$$\frac{\partial \omega}{\partial x} = \frac{\partial \Omega}{\partial k}\frac{\partial k}{\partial x} + \frac{\partial \Omega}{\partial x}, \tag{5}$$

where $\partial\Omega/\partial k = c_\mathrm{g} + U$ is the advection velocity, which contains the wave group velocity $c_\mathrm{g} \equiv \partial\sigma/\partial k$. We define the material (or total) derivative as

$$\frac{\mathrm{d}}{\mathrm{d}t} = \frac{\partial}{\partial t} + (c_\mathrm{g} + U)\frac{\partial}{\partial x}. \tag{6}$$

Thus, advection of a wave group is simply

$$\frac{\mathrm{d}x}{\mathrm{d}t} = \frac{\partial \Omega}{\partial k} = c_\mathrm{g} + U. \tag{7}$$

This is the first of the wave ray equations. The evolution of the wave number k follows by inserting Eq. (5) into Eq. (4) such that

$$\frac{\mathrm{d}k}{\mathrm{d}t} = -\frac{\partial \Omega}{\partial x} = -\left(\frac{\partial \sigma}{\partial x} + k\frac{\partial U}{\partial x}\right), \tag{8}$$

which is the second of the wave ray equations. Using the same approach for ω, for a fixed bathymetry we get

$$\frac{\mathrm{d}\omega}{\mathrm{d}t} = \frac{\partial \Omega}{\partial t} = k\frac{\partial U}{\partial t}, \tag{9}$$

which reduces to

$$\frac{\mathrm{d}\omega}{\mathrm{d}t} = \frac{\partial \Omega}{\partial t} = 0 \tag{10}$$

for a stationary current $U(x, t = 0)$, since we consider ambient currents that vary slowly compared to a characteristic wave period. Thus, the absolute wave frequency is constant. Summarized, we have obtained the wave ray equations in one horizontal dimension as

$$\frac{\mathrm{d}x}{\mathrm{d}t} = c_\mathrm{g} + U, \tag{11}$$

$$\frac{\mathrm{d}k}{\mathrm{d}t} = -\left(\frac{\partial \sigma}{\partial x} + k\frac{\partial U}{\partial x}\right), \tag{12}$$

$$\frac{\mathrm{d}\omega}{\mathrm{d}t} = 0. \tag{13}$$

The wave ray equations constitute a set of coupled ordinary differential equations (ODEs) that define a characteristic curve in space and time. They can be solved as an initial value problem if defined with a starting point of $x^{n=0} \equiv x(t = 0)$ and an initial wave period of $T = T^{n=0}$ by using the dispersion relation from Eq. (2). In deep water, where the wavelength $\lambda \ll d/2$, the first term on the right-hand side of Eq. (12) vanishes since $\tanh(kd) \to 1$ in Eq. (2). Under such conditions the evolution of k is only a function of the horizontal gradients in the ambient current.

2.2 The two-dimensional problem

In 2D we denote the position vector $\boldsymbol{x} = (x, y)$ and the ambient current vector $\boldsymbol{U} = (U, V)$. We define the horizontal gradient operator as

$$\nabla_\mathrm{h} \equiv \hat{\mathbf{i}}\frac{\partial}{\partial x} + \hat{\mathbf{j}}\frac{\partial}{\partial y}, \tag{14}$$

where $\hat{\mathbf{i}}$ and $\hat{\mathbf{j}}$ denote the unit vectors for x and y, respectively. Now, the absolute angular frequency,

$$\omega = \Omega(t, \boldsymbol{k}, \boldsymbol{x}) = \sigma + \boldsymbol{k}\cdot\boldsymbol{U}(t, \boldsymbol{x}), \tag{15}$$

and the wave ray equations for a stationary current field become

$$\frac{\mathrm{d}\boldsymbol{x}}{\mathrm{d}t} = \boldsymbol{c}_\mathrm{g} + \boldsymbol{U}, \tag{16}$$

$$\frac{\mathrm{d}\boldsymbol{k}}{\mathrm{d}t} = -\nabla_\mathrm{h}\sigma - \boldsymbol{k}\cdot\nabla_h\boldsymbol{U}, \tag{17}$$

$$\frac{\mathrm{d}\omega}{\mathrm{d}t} = 0. \tag{18}$$

In the context of spectral wave modeling, the dynamical evolution of the wave field is governed by the wave action balance equation,

$$\frac{\partial N}{\partial t} + \nabla_\mathrm{h}\cdot\left(\dot{\boldsymbol{x}}N\right) + \nabla_k\cdot\left(\dot{\boldsymbol{k}}N\right) = \frac{S}{\sigma}. \tag{19}$$

Here, $N \equiv E/\sigma$ is the wave action density, which is a conserved quantity in the presence of currents (Bretherton and Garrett, 1968). The wave action density contains the wave variance density E, which is $\propto a^2$. The right-hand side of Eq. (19) represents sources and sinks of wave action. The wave number gradient operator is

$$\nabla_\mathrm{k} \equiv \hat{\mathbf{i}}\frac{\partial}{\partial k_x} + \hat{\mathbf{j}}\frac{\partial}{\partial k_y}. \tag{20}$$

The wave ray equations (Eqs. 16–17) model the terms written (for brevity) with overdots in Eq. (19), i.e.,

$$\dot{\boldsymbol{x}} \equiv \frac{\mathrm{d}\boldsymbol{x}}{\mathrm{d}t}, \tag{21}$$

$$\dot{\boldsymbol{k}} \equiv \frac{\mathrm{d}\boldsymbol{k}}{\mathrm{d}t}. \tag{22}$$

There is thus a connection between the wave field dynamics and kinematics where $\dot{\boldsymbol{x}}$ represents the advection of wave action in physical space and $\dot{\boldsymbol{k}}$ represents the refraction ("advection" in $\boldsymbol{k}$ space). The wave action balance (Eq. 19) is solved by third-generation spectral wave models but then discretized either by wave number k or frequency f and direction θ (Komen et al., 1994).

3 Numerical implementation

3.1 Finite-difference discretization

The wave ray equations (Eqs. 16–17) are well suited for numerical integration. The `ocean_wave_tracing` module offers two finite-difference numerical schemes: a fourth-order Runge–Kutta scheme and a forward Euler scheme through its `solver` method. For readability, the latter is used here to present the discretization of the wave ray equations. The advection (Eq. 16) becomes

$$x^{n+1}_{(l,j)} = x^{n}_{(l,j)} + \Delta t\, f_{\boldsymbol{x}}\left(x^{n}_{(l,j)}, y^{n}_{(l,j)}, k^{n}_{(l,j)}, k^{n}_{x,(l,j)}, U^{n}_{(l,j)}\right), \quad (23)$$

$$y^{n+1}_{(l,j)} = y^{n}_{(l,j)} + \Delta t\, f_{\boldsymbol{x}}\left(x^{n}_{(l,j)}, y^{n}_{(l,j)}, k^{n}_{(l,j)}, k^{n}_{y,(l,j)}, V^{n}_{(l,j)}\right). \quad (24)$$

Here n denotes the discrete time index, with $n = 0, 1, \ldots, N$ and $\Delta t = t_{n+1} - t_n$. Discrete horizontal indices are given by $l = 0, 1, \ldots, N_x$; $j = 0, 1, \ldots, N_y$; and $\Delta x = x_{l+1} - x_l$, $\Delta y = y_{l+1} - y_l$. The $f_{\boldsymbol{x}}$ is a function of the group velocity and ambient current and becomes (skipping time and horizontal indices for readability)

$$f_{\boldsymbol{x}}(x, y, k, k_x, U) = \begin{cases} c_{\mathrm{g}}(k, d[x, y])\,\frac{k_x}{k} + U(x, y), \\ \text{in } x \text{ direction}, \\ c_{\mathrm{g}}(k, d[x, y])\,\frac{k_y}{k} + V(x, y), \\ \text{in } y \text{ direction}. \end{cases} \quad (25)$$

The evolution in wave number (Eq. 17) becomes

$$k^{n+1}_{x,(l,j)} = k^{n}_{x,(l,j)} + \Delta t\, f_{\boldsymbol{k}}\left(k^{n}_{x,(l,j)}, k^{n}_{y,(l,j)}, \frac{\partial}{\partial x}\sigma(k^{n}_{l,j}, d_{l,j}), \frac{\partial}{\partial x}U^{n}_{l,j}, \frac{\partial}{\partial x}V^{n}_{l,j}\right), \quad (26)$$

$$k^{n+1}_{y,(l,j)} = k^{n}_{y,(l,j)} + \Delta t\, f_{\boldsymbol{k}}\left(k^{n}_{x,(l,j)}, k^{n}_{y,(l,j)}, \frac{\partial}{\partial y}\sigma(k^{n}_{l,j}, d_{l,j}), \frac{\partial}{\partial y}U^{n}_{l,j}, \frac{\partial}{\partial y}V^{n}_{l,j}\right). \quad (27)$$

Here, $f_{\boldsymbol{k}}$ is a function of the horizontal derivatives of σ and $\boldsymbol{U}$. Horizontal derivatives are discretized using a central difference scheme, such that $f_{\boldsymbol{k}}$ becomes

$$f_{\boldsymbol{k}}(x, y, k_x, k_y, U, V) = \begin{cases} -\frac{\sigma^{n}_{l+1,j} - \sigma^{n}_{l-1,j}}{2\Delta x} - k^{n}_{x,(l,j)} \\ \frac{U^{n}_{l+1,j} - U^{n}_{l-1,j}}{2\Delta x} - k^{n}_{y,(l,j)} \\ \frac{V^{n}_{l+1,j} - V^{n}_{l-1,j}}{2\Delta x}, \text{in } x \text{ direction}, \\ -\frac{\sigma^{n}_{l,j+1} - \sigma^{n}_{l,j-1}}{2\Delta y} - k^{n}_{x,(l,j)} \\ \frac{U^{n}_{l,j+1} - U^{n}_{l,j-1}}{2\Delta y} - k^{n}_{y,(l,j)} \\ \frac{V^{n}_{l,j+1} - V^{n}_{l,j-1}}{2\Delta y}, \text{in } y \text{ direction}. \end{cases} \quad (28)$$

3.2 Stability condition

A constraint for hyperbolic equations in finite-difference numerical schemes is the Courant–Friedrichs–Lewy (CFL) condition, which for a process with advection velocity W demands that the non-dimensional Courant number be defined as

$$C \equiv W\frac{\Delta t}{\Delta r} \leq 1, \quad (29)$$

where $\Delta r = \sqrt{\Delta x^2 + \Delta y^2}$. If $C > 1$, the process will advect a distance larger than the grid point resolution over a period Δt, leading to instabilities in the numerical solution. A dedicated method, `check_CFL`, is implemented in the `Wave_tracing` class and added to the `set_initial_condition` method (Fig. 2). The Courant number is written to the log file as

$$C_{\text{logfile}} = \begin{cases} \text{info}, & \text{if } C \leq 1, \\ \text{warning}, & \text{if } C > 1. \end{cases} \quad (30)$$

The advection velocity (the absolute group velocity as seen from a fixed point) in Eq. (29) is implemented as

$$W = \max(|\boldsymbol{U}|) + \max(\boldsymbol{c}^{n=0}_{\mathrm{g}}), \quad (31)$$

which is a good proxy for the magnitude of the maximum advection speed. It may, however, exceed W for $n > 0$ for waves starting in shallow water and propagating towards deeper water. In the `check_CFL`, $\Delta r = \min(\Delta x, \Delta y)$.

3.3 Model simulation workflow

The wave ray equations are implemented in Python 3 in the `ocean_wave_tracing` module available on GitHub at https://github.com/hevgyrt/ocean_wave_tracing (last access: 6 November 2023) under a GPL v.3 license. It is based on common native Python libraries and open-source projects. Key open-source projects include *numpy* (numerical Python – https://numpy.org/, last access: 6 November 2023), *matplotlib* (https://matplotlib.org/, last access: 6 November 2023), and *xarray* (https://docs.xarray.dev/en/stable/, last access: 6 November 2023). The latter library is a large project, which has become a de facto standard in geophysical sciences for analyzing and dealing with multi-dimensional data. The wave ray tracing tool is a class instance, and the `Wave_tracing` object contains multiple auxiliary methods before and after performing the numerical integration. Here, we will focus on the workflow, input fields, implementation, and the ancillary methods enclosing the wave ray tracing `solver` method.

3.3.1 Operating conditions

A set of fixed conditions are specified for the `ocean_wave_tracing` module. The most important conditions include the following:

Algorithm 1 Generic workflow code example.

```
import numpy as np
import maplotlib.pyplot as plt
from ocean_wave_tracing import Wave_tracing

# Defining some properties of the medium
nx = 100; ny = 100 # number of grid points in x- and y-direction
x = np.linspace(0,2000,nx) # size x-domain [m]
y = np.linspace(0,3500,ny) # size y-domain [m]
T = 250 # simulation time [s]
U=np.zeros((nx,ny))
U[nx//2:,:]=1

# Define a wave tracing object
wt = Wave_tracing(U=U,V=np.zeros((ny,nx)),
  nx=nx, ny=ny, nt=150,T=T,
  dx=x[1]-x[0],dy=y[1]-y[0],
  nb_wave_rays=20,
  domain_X0=x[0], domain_XN=x[-1],
  domain_Y0=y[0], domain_YN=y[-1],
  )

# Set initial conditions
wt.set_initial_condition(wave_period=10,
  theta0=np.pi/8)
# Solve
wt.solve()
```

- The model domain must be rectangular and in Cartesian coordinates with a uniform horizontal resolution in each direction.
- Units must follow the SI system with length scale units of meters (m) and seconds (s). The angular units are radians (rad). Wave propagation direction θ follows a right handed coordinate system with $\theta = 0$ being parallel to the x axis and propagating in the positive x direction.
- Variable names, structures, and metadata are, to a large extent, based on the Climate and Forecast (CF) metadata convention (https://cfconventions.org/, last access: 6 November 2023).

3.3.2 Ray tracing model initialization

A flowchart of the model simulation workflow is given in Fig. 2 and an associated code example in Alg. 1. Firstly, a wave ray tracing object `Wave_tracing` is initialized by an `__init__` method. The input variables define the ambient conditions and include

- the ambient current `U,V` = $\boldsymbol{U}$;
- the bathymetry `depth` (optional);
- the boundaries `X0`, `XN`, `Y0`, and `YN` and horizontal resolution `dx` and `dy` of the domain;
- the number of time steps `nt` and total duration time for wave propagation `T`;
- the number of wave rays `nb_wave_rays`.

The current is allowed to vary in time by setting `temporal_evolution=True`, but it is up to the user to make sure that $\boldsymbol{U}(t, \boldsymbol{x})$ is not violating Eq. (18) by $\partial \boldsymbol{U}/\partial t \simeq 0$. If the bathymetry is not specified, the model assumes deep-water waves and sets a fixed uniform depth at 10^5 m. Depth values are defined as positive, implying that negative values will be treated as land if both negative and positive values are present through a dedicated bathymetry checker (`check_bathymetry`), which is invoked within `__init__`. Furthermore, the input velocity field is checked and *xarray* datasets are created for the bathymetry and velocity field as class variables following the CF convention.

3.3.3 Setting the initial conditions

Before the numerical integration, initial conditions for the ODEs are specified in a dedicated `set_initial_condition()` method (Alg. 1, Fig. 2). Here the initial wave period $T^{n=0}$, wave propagation direction $\theta = \theta^{n=0}$, and initial position $\mathbf{r}(t = 0, \boldsymbol{x}) = (x^{n=0}, y^{n=0})$ are specified. By utilizing the rectangular model domain, the initial position can most easily be given as one of the sides of the domain, i.e.,

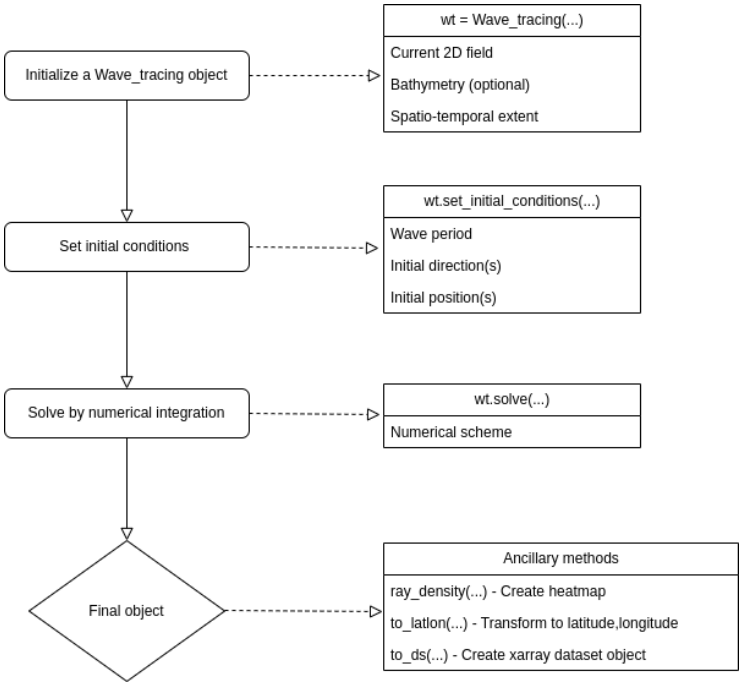

Figure 2. Flowchart of the workflow from initializing a ray tracing object to solving the wave ray tracing equations. The left column denotes the most important steps in the workflow, and the right column highlights the most important parameters and supporting methods under each step.

`top`, `bottom`, `left`, or `right`, where `left` is default (see Alg. 1). In such cases, the number of wave rays is spread uniformly on the selected boundary. Another option is to specify initial grid points `ipx` and `ipy` for each wave ray. Similarly, $\theta = \theta^{n=0}$ can also be specified for each ray, or a single uniform direction can be given for all rays. Such examples are provided later.

The model is solved for a single wave frequency, dictated by the initial wave period $T^{n=0}$. The wave number k is retrieved from $T^{n=0}$ using Eq. (2), which in intermediate depths requires an iterative solver. Using the approximation by Eckart (1952), the error in k is less than 5 % (Holthuijsen, 2007).

3.3.4 Numerical integration

Numerical integration of Eqs. (23)–(28) is initiated by invoking the `solver` method. Here, $\nabla_h \boldsymbol{U}$ is computed prior to the integration using the *numpy gradient* method. The integration is performed iteratively in a Lagrangian sense by computing the next position $\mathbf{r}^{n+1}$ from the current position $\mathbf{r}^n$ for each wave ray. Thus, the `solver` keeps track of the horizontal indices l and j for every time step and for each wave ray in the model domain. Hence, the numerical integration for the wave rays can follow a vectorized approach, which is conceptually visualized in Fig. 3. For a given position $\mathbf{r}$, the properties of the ambient medium, i.e., the current and bathymetry, are selected using a nearest-neighbor approach.

Even though $\nabla_h \boldsymbol{U}$ is static for each model field, $\nabla_\mathrm{h}\sigma$ in Eq. (28) must be computed for each iteration n since the wave number k evolves in time. Furthermore, for each iteration of n, the wave propagation direction θ^n is computed from $\boldsymbol{k}^n$ using the *numpy atan2* function.

After a successful call of the `solve()` function, the `Wave_tracing` object will have populated its class variables for the wave rays being (`ray_x`, `ray_y`), (`ray_kx`, `ray_ky`), `ray_k`, `ray_theta`, `ray_cg`, and (`ray_U`, `ray_V`), which are the horizontal position vector, wave number vector, wave number, wave propagation direction, wave group velocity, and ambient current vector, respectively. All of the aforementioned class variables have the dimensions `number_of_wave_rays`$\times N$.

The numerical scheme used in the `solver` method is configurable by the user, and the default is a fourth-order Runge–Kutta scheme. That is, the numerical scheme is generic and detached from the wave ray equations. The schemes are

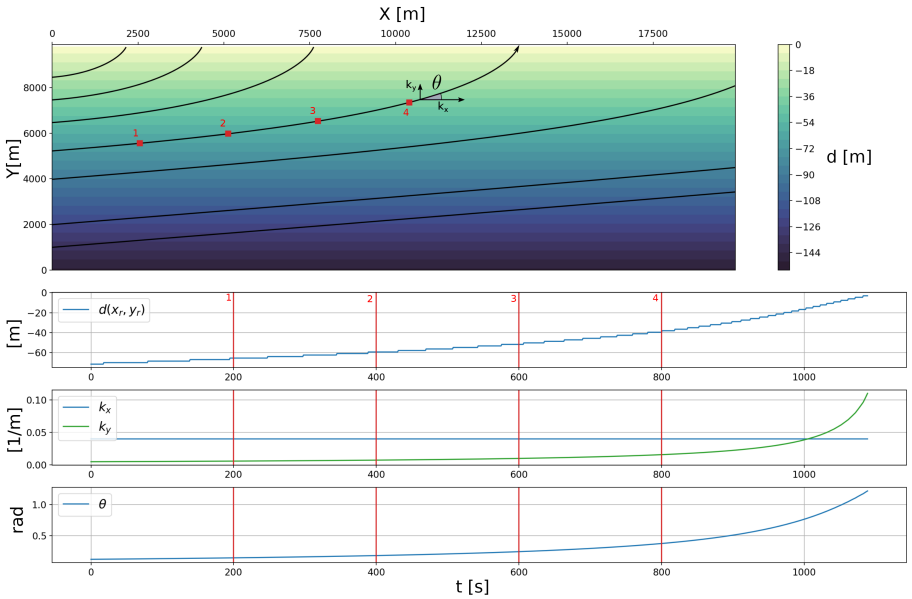

Figure 3. A conceptual figure highlighting the workflow strategy of the model. Here, depth refraction of a $T = 10$ s period wave propagating from left with an initial angle $\theta^{n=0} = 0.1$ rad is shown for seven different rays (black lines). The propagation path for each wave ray is computed simultaneously through vectorization. The lower panels denote the change in depth, evolution in $\boldsymbol{k}$, and corresponding wave propagation direction, θ, in time along one of the rays. As expected, the wave rays deflect towards shallower regions due to the increase in the k_y wave number component.

available in a separate utility function `util_solvers`, which contains (currently two) numerical schemes which are defined Python classes in a hierarchy with a generic ODE solver as the top node. That is, each sub-class has its own *advance* method, which corresponds to the numerical scheme. This approach is to a large extent built on material from Langtangen (2016). Furthermore, the `util_solvers` also contain the advection and wave number evolution functions in Eq. (25) and Eq. (28), respectively.

3.4 Ancillary methods and testing

3.4.1 Ancillary functions

Ancillary functions include methods which are considered useful for the user community. The current version has four methods, three within the `Wave_tracing` object and one outside the object.

The method outside the `Wave_tracing` object is targeted for data preparation before model initialization. It is not strictly a Python method, but it is a generic workflow for data retrieval. More specifically, since the ray tracing model is focused on ocean currents and bathymetry, it is natural to exploit variable fields from ocean circulation models. It is common for oceanographic centers to disseminate model results under a free and open data policy and to enable the Open-source Project for a Network Data Access Protocol (OPeNDAP – https://www.opendap.org/, last access: 6 November 2023) on the data distribution server (e.g., THREDDS – https://www.unidata.ucar.edu/software/tds/current/, last access: 6 November 2023 or HYRAX – https://www.opendap.org/software/hyrax-data-server, last access: 6 November 2023). The OPeNDAP enables spatio-temporal subsetting to be carried out on the server side and thus avoids the problem of downloading huge amounts of data prior to use. Such user-defined subsets can be accessed directly via data streaming by using common netCDF4 readers (https://www.unidata.ucar.edu/software/netcdf/, last access: 6 November 2023), which are available in *xarray*. The ancillary method, or workflow, is provided in the Jupyter notebook `extract_ocean_model_data.ipynb`. Here, the user can plot and check the user-defined area and temporal extent prior to writing the subset to disk or initiating the `Wave_tracing` object directly. It is common for ocean circulation models to have output variable fields with hourly temporal resolution such that $\boldsymbol{U}(t, \boldsymbol{x})$ is unlikely to violate Eq. (18). However, it is up to the user to understand the lim-

itations of the model if simulating wave rays for very long shallow-water waves like tsunamis and tidal waves.

The first of the three class methods within the `Wave_tracing` object is a transformation method from projection coordinates to latitude and longitude values, which is called `to_latlon()` (see Fig. 2). That is, when using ocean-circulation-model field variables as input data, it is not readily possible to compare the `Wave_tracing` output with other sources of data since ocean-model field variables are most often in a specific projection. In this context, using latitude and longitude coordinates is often much more convenient. The method requires the *proj4* string of the ocean-model domain and performs coordinate transformation using the *pyproj* (https://pyproj4.github.io/pyproj/stable/, last access: 6 November 2023) library in Python. Even if not required, it is common that the *proj4* string is listed in the `grid_mapping` variable in a CF-compliant ocean-model dataset.

The second ancillary function is based on the wave ray density method by Rapizo et al. (2014) and is called `ray_density()`. It computes the relative number of wave rays within user-defined grid boxes, which can be considered proportional to the wave height and thus the horizontal wave height variability. The method returns a 2D grid and the associated ray density variable.

The third method takes care of converting all the characteristic `Wave_tracing` class variables into an *xarray* dataset, including latitude and longitude if the *proj4* string is given as input. The method is called `to_ds()`. The output *xarray* dataset follows the CF convention for metadata. Thus, the data can utilize all the functionality within *xarray*, including the plotting and writing of data to disk. Examples using all the methods listed above will be shown later in Sect. 5.

3.4.2 Tests

The `ocean_wave_tracing` repository is equipped with unit tests written in the framework of Pythons `pytest`. Unit tests are tailored for the methods within and used by the `Wave_tracing` class and typically check the numerical implementation against known solutions. For instance, the computation of wave celerity for deep and shallow water is tested against analytical solutions.

For integration tests, a set of example scripts running the entire chain of operations is embedded in the `test` folder. Such tests are also implicitly inherent in the scripts provided in the `notebooks` and `verification` folders, since these notebooks run the entire chain. Moreover, continuous integration tests are embedded in the repository utilizing the *poetry* project (https://python-poetry.org/, last access: 6 November 2023).

4 Model validation

Here we verify the output of the `Wave_tracing` solver against analytical solutions for idealized cases for depth- and current-induced refraction. Model differences are given as the absolute relative difference between the analytical solution A and the numerical model solution B for an arbitrary variable z as

$$\Delta(z) = \left| \frac{z_\mathrm{A} - z_\mathrm{B}}{z_\mathrm{A}} \right| \times 100, \tag{32}$$

given in the units of percentage.

4.1 Snell's law

When only considering the bathymetry, Snell's law,

$$\frac{\sin(\phi_1)}{\sin(\phi_2)} = \frac{c_1}{c_2}, \tag{33}$$

applies for parallel depth contours (see Note 7A, Holthuijsen, 2007, p. 207). Here, subscripts 1 and 2 indicate the properties of the wave and medium before and after being transmitted through an interface, which here are lines of different bathymetry, and c is the phase speed. The ϕ_1 denotes the incidence angle between the wave ray and the normal to the interface, and ϕ_2 is the angle of refraction after the interaction.

In the presence of ambient currents, Snell's law can be written for a horizontally sheared current $V = V(x)$ (Kenyon, 1971),

$$\sin(\phi_2) = \frac{\sin(\phi_1)}{(1 - \frac{V}{c_1}\sin(\phi_1))^2}. \tag{34}$$

Verification of the wave ray tracing model results against Eqs. (33) and (34) is shown in the upper and lower panels of Fig. 4, respectively. For the idealized bathymetry, the wave ray tracing was performed for a shallow-water wave with wavelength $\lambda = 10\,000\,\mathrm{m}$ propagating towards a stepwise shallower region.

Here, $\Delta\phi_2$ was computed for each new depth regime (upper panel Fig. 4a). For the horizontally sheared current (Fig. 4b), a $T = 10\,\mathrm{s}$ period deep-water wave propagated through the current field where

$$V(X) = \begin{cases} 0 & \text{if } X < 2000\,\mathrm{m}, \\ 2,\mathrm{m\,s^{-1}} & \text{if } X \geq 2000\,\mathrm{m}. \end{cases} \tag{35}$$

The relative differences in both the idealized bathymetry and horizontally sheared current cases listed above were $\Delta(\theta_2) \sim 10^{-1}\,\%$ (Fig. 4). The script producing Fig. 4 and computing the analytical results is available as a Jupyter notebook under `verification/snells_law.ipynb`.

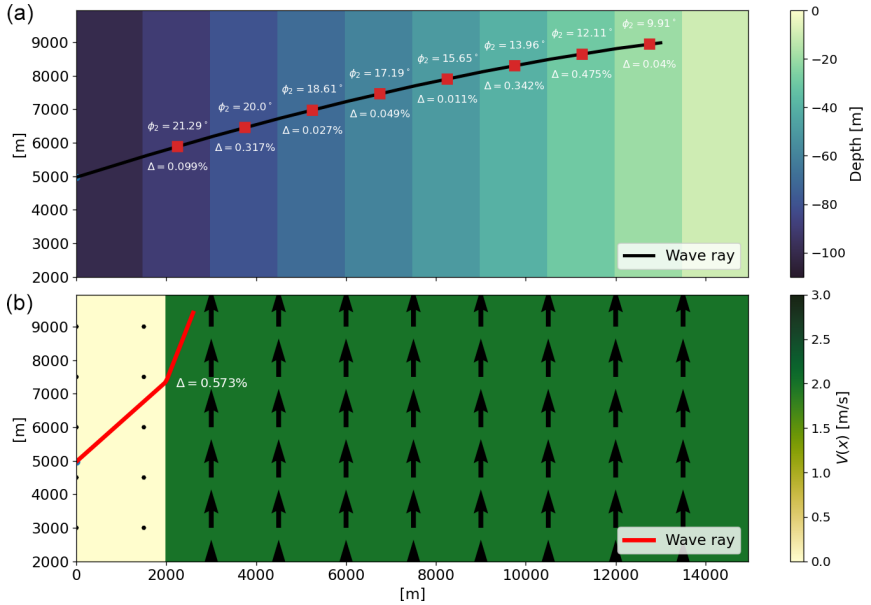

Figure 4. Verifying the analytical solutions of Snell's law against the wave ray tracing solver for cases with idealized bathymetry (Eq. 33) **(a)** and a shear current (Eq. 34) **(b)**. The relative differences in $\Delta\theta_2$ (Eq. 32) are given as insert text for both cases.

4.2 Wave deflection

For deep-water waves, there is a direct relation between wave ray curvature and the vertical vorticity (henceforth vorticity) $\zeta = \partial v/\partial x - \partial u/\partial y$ (Kenyon, 1971; Dysthe, 2001):

$$\nu = \frac{\zeta}{c_g}, \tag{36}$$

valid for $|\boldsymbol{U}|/c_g \ll 1$. Here, positive vorticity will deflect a wave to the left relative to its wave propagation direction and to the right for negative vorticity. The ratio with the wave group velocity also entails that shorter waves will deflect more compared with longer waves.

An approximate wave deflection angle can be computed from Eq. (36) by adding a characteristic $\zeta = \zeta_0$ and length scale l such that (Gallet and Young, 2014)

$$\theta_\nu \simeq \frac{\zeta_0 l}{c_g}. \tag{37}$$

We use the idealized horizontally sheared current,

$$U(X, Y) = \begin{cases} 0, & \text{if } X < 2500\,\text{m}, \\ 3\alpha, & \text{if } X \geq 2500\,\text{m}, \end{cases} \tag{38}$$

where α increases linearly from $\alpha = 0$ at $y = 0$ to $\alpha = 1\,\text{m s}^{-1}$ at $y = Y$ such that ζ values are constant within the regions. An assessment of θ_ν for a $T = 10\,\text{s}$ period deep-water wave propagated through Eq. (38) is shown in Fig. 5. Here, the solution in the lower panel also uses Eq. (38) but with a minus sign in front of α. Relative differences between the model and analytical solution are $\Delta(\theta_\nu) \sim 10^0\,\%$. The difference is a sum of the numerical errors together with the approximate equality in Eq. (37). Furthermore, the difference between the simulation of the negative and positive vorticity ζ is also due to the advection of the current. Furthermore, the deflection direction for negative and positive ζ is readily seen in Fig. 5. The full analysis is available in the `verification/wave_deflection.ipynb` notebook in the GitHub repository.

4.3 Numerical convergence

The numerical convergence for decreasing values of the CFL number C is tested for the conservation of absolute frequency ω in Eq. (18). For the idealized case of a deep-water wave propagating in the x direction from a region with $U = 0$ to a region with an opposing current $U = -1\,\text{m s}^{-1}$, Eq. (18) requires

$$\omega = \sigma + kU = \text{const.} = \omega_0, \tag{39}$$

where subscript 0 denotes the region with $U = 0$. For deep water, the phase speed $c = \sigma/k$ such that Eq. (39) can be

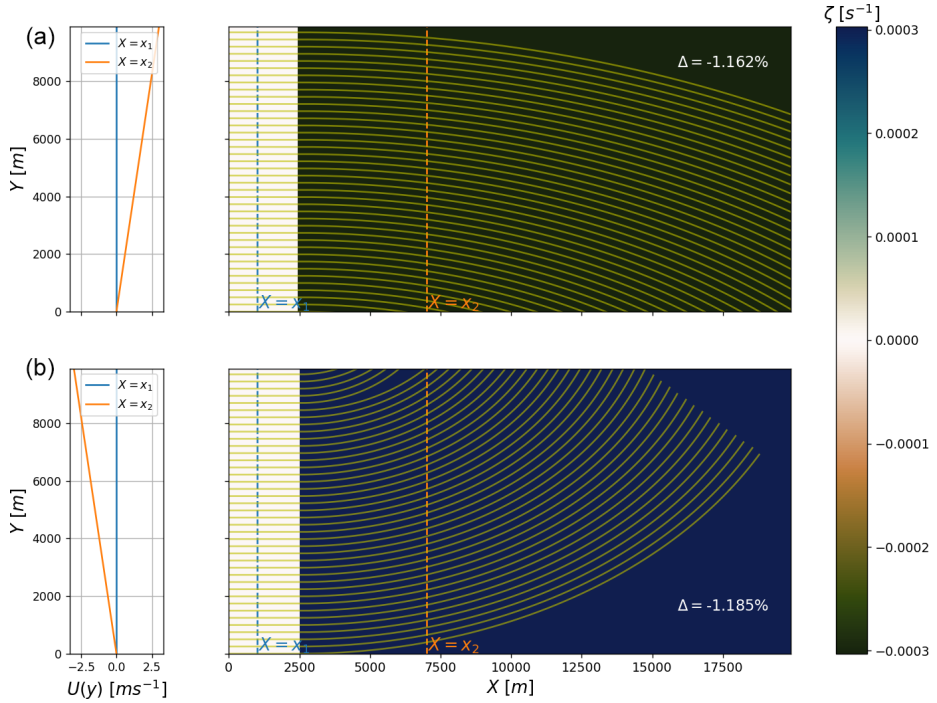

Figure 5. Verifying the approximate solutions of wave deflection (Eq. 37) against the wave ray tracing output for cases with idealized negative **(a)** and positive vorticity ζ **(b)**. The associated velocity field $\boldsymbol{U} = (U(x, y), 0)$ at $X = x_1, x_2$ is given in the left column plots. The relative differences $\Delta\theta_v$ [Eq. 32] using $l = 2500$ m are given for both cases (see insert text). Yellow lines denote the wave rays.

rearranged and

$$k = \frac{k_0 c_0}{U + c}. \tag{40}$$

In our example, $k = 0.046\,\mathrm{m}^{-1}$ for a $T = 10$ s period wave propagating into the region $U = -1\,\mathrm{m\,s}^{-1}$. The numerical convergence for Eq. (18) is shown in Fig. 6. Here, the error $\Delta\omega$ decreases with decreasing C due to the increasing number of time steps N. The error does not decrease monotonically, however, since k must be solved sufficiently many times within the region where $\partial U/\partial x \neq 0$ to obtain its correct value. Nevertheless, the solution converges to the analytical solution with decreasing C (see k_{an} in Fig. 6). The test on the numerical convergence is available in the GitHub repository in the `verification/numerical_convergence_omega.ipynb` notebook.

5 Examples of usage

Here we provide some use examples of the wave ray tracing model, which include simulations under idealized current and bathymetry fields and ambient conditions retrieved from an ocean circulation model. The code for running the tool is similar to the generic example given in Alg. 1 but with different ambient and initial conditions. The idealized current fields are part of the repository as a netCDF4 file and reproducible in the `notebooks/create_idealized_current_and_bathymetry.ipynb` notebook. The examples include specifying different initial conditions as well as utilizing the ancillary functions described in Sect. 3.4.1.

5.1 Idealized cases

Cases with depth-induced refraction are shown in Fig. 7. Here the idealized cases show the expected veering of wave rays towards shallower regions when the deep-water limit $\lambda/2 \gg d$ is no longer applicable. The examples also show how the initial position $\mathbf{r}^{n=0}$ can be set differently using the different sides of the domain (i.e., `left` and `bottom` in Fig. 7a, c, d) and from a single point with the initial propagation angle uniformly distributed in a sector (Fig. 7b).

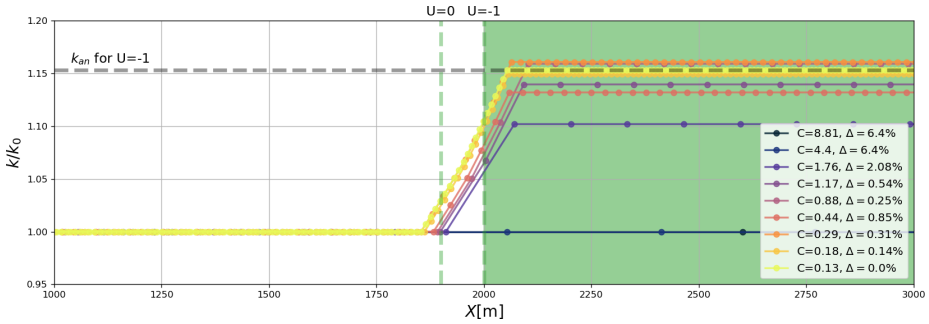

Figure 6. The numerical convergence tested for conservation of absolute frequency ω in Eq. (18). The convergence is tested for an increasing number of discrete time indices n with an accompanied decreasing Courant number C. Here, a domain with velocity field $U = 0$ for $X < 2000$ and $U = -1$ for $X \geqq 2000$, where $\Delta X = 100$ m (see dashed vertical lines), was used. The analytical value k_{an} is obtained from Eq. (40). The relative error $\Delta = (\omega_0 - \omega)/\omega_0$ decreases with C. The results here are obtained by using the RK4 scheme, but similar results are obtained using the FE (not shown).

Cases with current-induced refraction in deep water are shown in Fig. 8. Examples of wave trains both following and opposing a horizontally sheared current are provided (Fig. 8a, b). The ambient current causes areas of converging and crossing wave rays, which are known as caustics or focal points. Furthermore, an example of waves propagating through an idealized oceanic eddy is shown (Figs. 8c, d).

The joint effect of current- and depth-induced refraction at intermediate depth is shown in Fig. 9. Here, the `ray_density` method is used to highlight the different focal points obtained in deep water and when the waves are also influenced by the bathymetry.

All the examples listed above are available in the `notebooks/idealized_examples.ipynb` notebook.

5.2 Ocean-model output

Examples of using surface currents and bathymetry extracted from the operational coastal ocean circulation model at the Norwegian Meteorological Institute (Albretsen et al., 2011) as input in wave tracing simulations are shown for different regions in Fig. 10. Here, the `to_latlon()` method has been used together with `to_ds()` in order to visualize the output on a georeferenced map. Figure 10b denotes the refraction due to currents and bathymetry (red rays), compared with bathymetry only (yellow rays). There are clear differences between the wave rays with and without currents. The current field used here spanned four model output time steps with an hourly temporal resolution. Figure 10c and d show how the wave kinematics are affected by a barotropic tidal current under two characteristic cycles. In the lower left panel, the tidal current gives rise to a focal point and crossing wave rays. Cases similar to the latter two were investigated in Halsne et al. (2022), comparing the results with output from a spectral wave model (Eq. 19). The examples provided here are available in the `notebooks/ocean_model_example.ipynb` notebook.

The famous textbook example of trapped waves in the Agulhas Current east of South Africa is shown in Fig. 11. Here, the wave tracing simulations used the surface current from the ESA's GlobCurrent project (https://data.marine.copernicus.eu/product/MULTIOBS_GLO_PHY_REP_015_004/description, last access: 6 November 2023). The particular point in time for the simulation is the same as used in Kudryavtsev et al. (2017) (i.e., 4 January 2016, see their Figs. 14–15) but here with an apparently coarser horizontal resolution in the current forcing.

6 Discussion and concluding remarks

We have presented a Python-based, open-source, finite-difference ray tracing model for arbitrary depths at variable currents. The `Wave_tracing` module has been tested and verified against analytical solutions and tested for numerical convergence. The solver comes with a set of ancillary functions aimed at supporting relevant workflows for data retrieval, transformation, and visualization in the scientific community as well as being compatible with the standardized Climate and Forecast (CF) metadata conventions. Such workflows have been documented and are available in the repository as examples for the end users.

To the best of our knowledge, no such modeling tool is openly available in a high-level computing language despite its usefulness for the investigation and quantification of the impact of ambient currents and bathymetry on the wave field (e.g., Romero et al., 2017, 2020; Ardhuin et al., 2012; Masson, 1996; Bôas et al., 2020; Halsne et al., 2022; Saetra et al.,

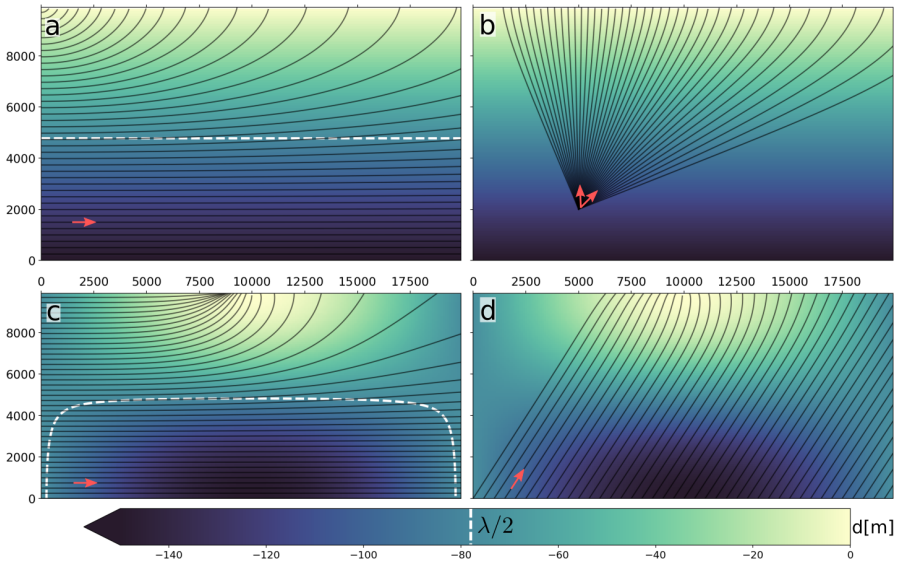

Figure 7. Examples of depth refraction of a long crested 10 s period wave using various initial positions and initial propagation directions (red arrows), for two different depth profiles in the upper **(a, b)** and lower panels **(c, d)**. Waves with $\frac{\lambda}{2} \ll d$ ($\lambda = 156$ m on deep water, white contour lines) will not "feel" the bottom and thus not be refracted.

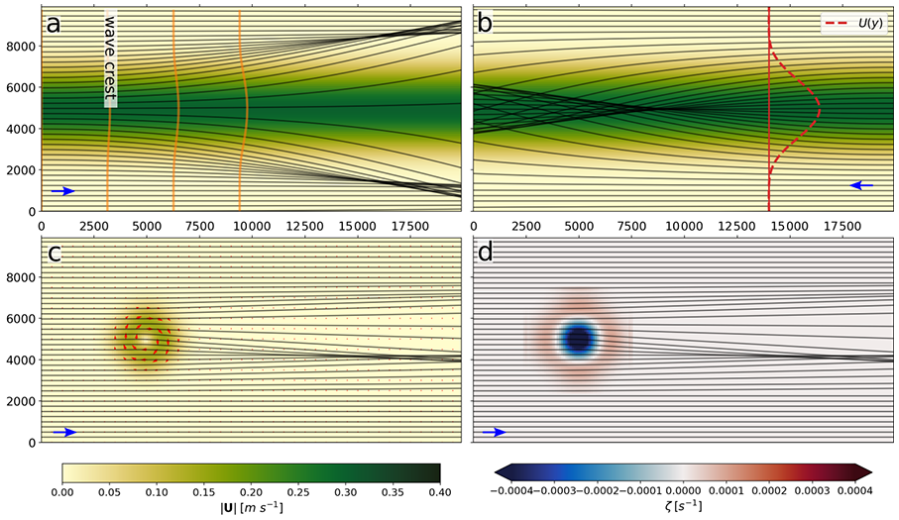

Figure 8. Examples of current-induced refraction under different flow regimes and initial propagation directions (blue lines). Panel **(a)** denotes the evolution of the wave crest (orange lines) as it rides along a current jet (see current profile $U(y)$ in **b**). In panel **(b)** the current jet is opposing the waves, inducing focal points in the middle of the jet. Panel **(c)** shows how a characteristic current whirl impacts the wave propagation paths, and **(d)** denotes the relation between deflection angle and the vorticity, ζ.

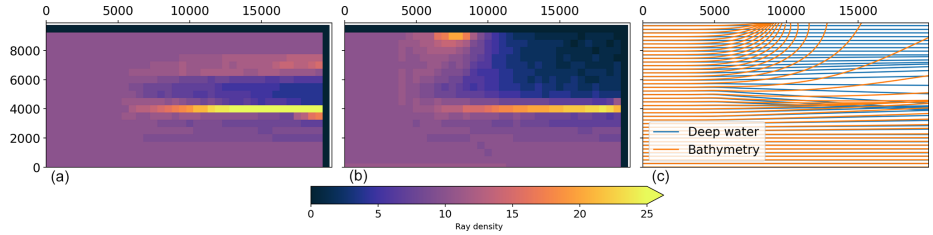

Figure 9. The impact of depth and current refraction on horizontal wave height variability as seen through wave ray density plots. Panel **(a)** shows results using the wave ray density method for a current whirl on deep water (see Fig. 8c). Panel **(b)** shows the impact on wave ray density for the same current whirl but on intermediate depths, i.e., adding the bathymetry in Fig. 7c. Panel **(c)** denotes the difference in the wave ray paths between the two cases.

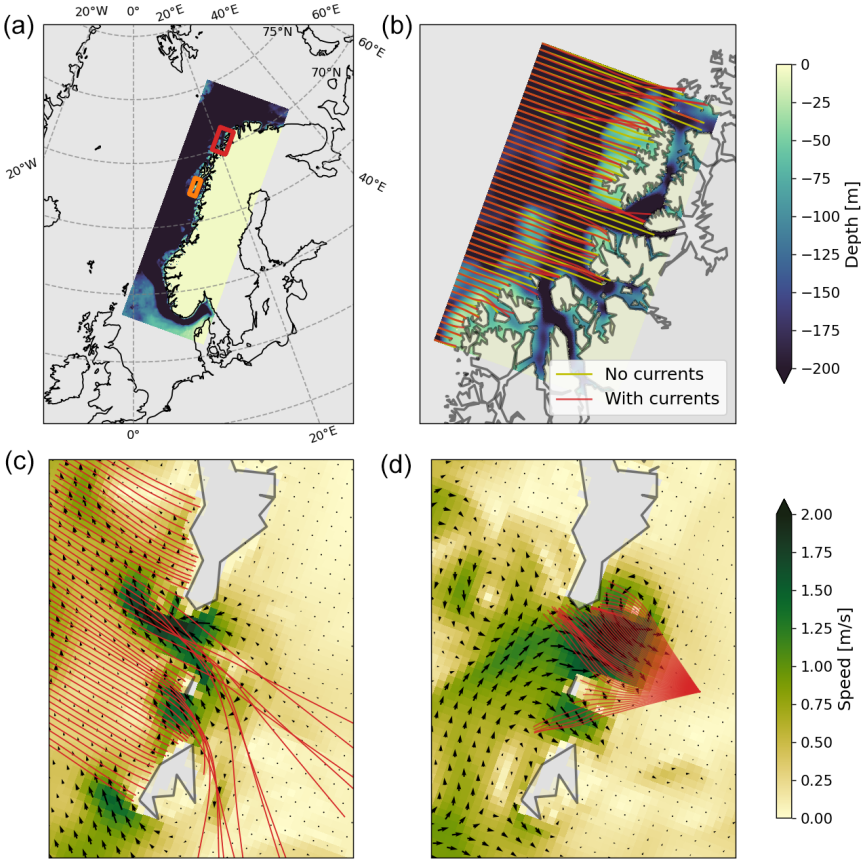

Figure 10. The impact of currents and bathymetry on wave propagation paths using current and bathymetry fields from an 800 m resolution Regional Ocean Modeling System (ROMS) model in Northern Norway **(a)**. **(b)** Subset in the red rectangle in **(a)**; it shows how time-varying surface currents (i.e., four model time steps) impact the wave propagation paths for a $T = 10$ s period wave (red rays) when compared to refraction due to bathymetry only (yellow rays). **(c, d)** Subset in the orange rectangle in **(a)**; panels **(c)** and **(d)** show the impact of a tidal current on the wave propagation paths for a $T = 10$ s period wave **(c)** and a $T = 7$ s period wave **(d)**. Here, arrows denote the direction of the ambient current.

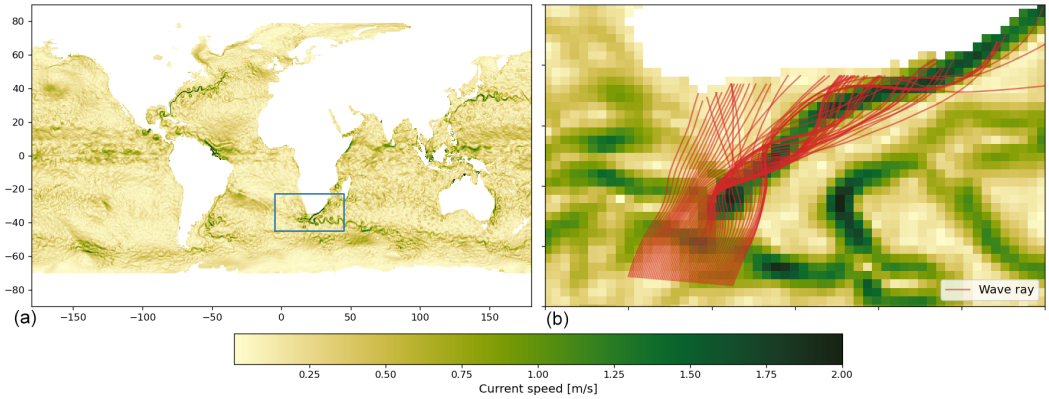

Figure 11. Focusing of wave rays by the Agulhas Current. Here, surface current data from the GlobCurrent project are used from 4 January 2016 **(a)**. The data are originally given in spherical latitude and longitude coordinates but are approximated here in the area of interest to equidistant Cartesian coordinates with 22 and 28 km spatial resolution in the x and y directions, respectively. The famous trapping of wave rays within the branch of the Agulhas Current is shown in **(b)** using a $T = 10$ s period wave. The duration of the run was 62 h, and 18 consecutive model output times (temporal resolution of 3 h) were used.

2021; Sun et al., 2022; Gallet and Young, 2014; Rapizo et al., 2014; Kudryavtsev et al., 2017; Bôas and Young, 2020).

The solver is applicable to waves in finite depth, which is in contrast to previously reported models which handle only current-induced refraction in deep water (e.g., Bôas and Young, 2020; Bôas et al., 2020; Mathiesen, 1987; Kenyon, 1971; Rapizo et al., 2014; Kudryavtsev et al., 2017). For intermediate depths, the joint effect of current- and depth-induced refraction can be very important for the wave height variability (Fig. 9). Such examples were presented in Halsne et al. (2022) and Romero et al. (2020), where the combined refraction of wave rays due to the ambient current and bathymetry caused focusing, which led to a significant increase in the local wave height (see Fig. 11 in Halsne et al., 2022 and Fig. 14 in Romero et al., 2020).

The effect of vertically sheared currents is usually neglected in coupled wave model simulations since it is a second-order effect. However, in strong baroclinic environments, such shear may strongly affect the absolute angular frequency (Zippel and Thomson, 2017). In `ocean_wave_tracing`, the impact of vertically sheared currents can be accounted for by computing an effective depth-integrated current (e.g., Kirby and Chen, 1989). Such an extension is easy to add as an optional method in the ray tracing model initialization due to the class structure (see Sect. 3.3.2), given that the input ambient current field is three-dimensional. However, and as shown by Calvino et al. (2022), care should be taken since numerical errors can be introduced in the computation of an effective current from horizontally varying 3D sheared currents with coarse vertical resolution. An implementation of the effective current is planned as a future extension in `ocean_wave_tracing`.

The `ocean_wave_tracing` module does not support wave reflection. Such processes are complex but could be added later. This means that wave rays can essentially propagate through land and out of the model domain. Such effects are, however, circumvented by using *numpy*'s masked arrays and not-a-number (NaN) values. For instance in the `bathymetry_checker`, negative bathymetry values will be treated as land and set to a *numpy* NaN. When plotting, `NaN` values do not appear. Furthermore, masked values are often standard in ocean circulation models, and thus wave rays "stop" when entering land grid points (see Fig. 10).

Solving the ray equation using a high-level language such as Python gives added execution time and memory usage compared to lower-level languages. However, execution times are normally on the order of 10^1 s but will obviously increase with the number of time steps `nt`. It is possible to further speed up the code by utilizing other modules and by making the code base more dense in terms of reducing the amount of code. However, the objective of the wave ray tracing tool described here is neither to create a substitute to wave models nor to optimize it for large and/or long simulations. It is rather to provide a framework that is easy to understand and simple to run. In addition, a comprehensible code base makes the tool suitable for further development by other contributors. Furthermore, best practices like vectorization have been used in order to speed up the solver, without loss of general readability of the code.

Code and data availability. The source code is available at https://github.com/hevgyrt/ocean_wave_tracing (last access: 6 November 2023) under a GPL v.3 license with DOI

https://doi.org/10.5281/zenodo.7602540 (Halsne et al., 2023). ROMS data from MET Norway is available on under a free an open data policy at https://thredds.met.no/thredds/fou-hi/norkyst800v2.html?dataset=norkyst800m_1h_be (Albretsen et al., 2011). This study has been conducted using E.U. Copernicus Marine Service Information, specifically using the ESA GlobCurrent dataset; https://doi.org/10.48670/moi-00050 (GlobCurrent E.U. Copernicus Marine Service Information, 2022).

Supplement. The supplement related to this article is available online at: https://doi.org/10.5194/gmd-16-6515-2023-supplement.

Author contributions. TH designed and implemented the software, including the formal analysis and model validation, and wrote the manuscript draft. GH supported the development and GitHub integration. GH, KHC, and ØB reviewed and edited the manuscript.

Competing interests. The contact author has declared that none of the authors has any competing interests.

Disclaimer. Publisher's note: Copernicus Publications remains neutral with regard to jurisdictional claims made in the text, published maps, institutional affiliations, or any other geographical representation in this paper. While Copernicus Publications makes every effort to include appropriate place names, the final responsibility lies with the authors.

Acknowledgements. This research was partly funded by the Research Council of Norway through the project MATNOC (grant no. 308796). Trygve Halsne and Øyvind Breivik are grateful for additional support from the Research Council of Norway through the StormRisk project (grant no. 300608).

Financial support. This research has been supported by the Norges Forskningsråd (grant nos. MATNOC 308796 and Stormrisk 300608).

Review statement. This paper was edited by P. N. Vinayachandran and reviewed by Leonel Romero and one anonymous referee.

References

Albretsen, J., Sperrevik, A. K., Staalstrøm, A., Sandvik, A. D., Vikebø, F., and Asplin, L.: NorKyst-800 report no. 1: User manual and technical descriptions, Tech. Rep. 2, Institute of Marine Research, Bergen, Norway, https://www.hi.no/en/hi/nettrapporter/fisken-og-havet/2011/fh_2-2011_til_web (last access: 6 November 2023), 2011.

Ardhuin, F., Roland, A., Dumas, F., Bennis, A.-C., Sentchev, A., Forget, P., Wolf, J., Girard, F., Osuna, P., and Benoit, M.: Numerical Wave Modeling in Conditions with Strong Currents: Dissipation, Refraction, and Relative Wind, J. Phys. Oceanogr., 42, 2101–2120, https://doi.org/10.1175/JPO-D-11-0220.1, 2012.

Ardhuin, F., Gille, S. T., Menemenlis, D., Rocha, C. B., Rascle, N., Chapron, B., Gula, J., and Molemaker, J.: Small-scale open ocean currents have large effects on wind wave heights, J. Geophys. Res.-Oceans, 122, 4500–4517, https://doi.org/10.1002/2016JC012413, 2017.

Babanin, A. V., van der Weshuijsen, A., Chalikov, D., and Rogers, W. E.: Advanced wave modeling, including wave-current interaction, J. Mar. Res., 75, 239–262, https://doi.org/10.1357/002224017821836798, 2017.

Bretherton, F. P. and Garrett, C. J. R.: Wavetrains in Inhomogeneous Moving Media, P. Roy. Soc. Lond. A Mat., 302, 529–554, ISSN 0080-4630, 1968.

Bôas, A. B. V. and Young, W. R.: Directional diffusion of surface gravity wave action by ocean macroturbulence, J. Fluid Mech., 890, 1469–7645, https://doi.org/10.1017/jfm.2020.116, 2020.

Bôas, A. B. V., Cornuelle, B. D., Mazloff, M. R., Gille, S. T., and Ardhuin, F.: Wave-Current Interactions at Meso- and Submesoscales: Insights from Idealized Numerical Simulations, J. Phys. Oceanogr., 50, 3483–3500, https://doi.org/10.1175/JPO-D-20-0151.1, 2020.

Calvino, C., Dabrowski, T., and Dias, F.: Theoretical and applied considerations in depth-integrated currents for third-generation wave models, AIP Adv., 12, 015017, https://doi.org/10.1063/5.0077871, 2022.

Dysthe, K. B.: Refraction of gravity waves by weak current gradients, J. Fluid Mech., 442, 157–159, https://doi.org/10.1017/S0022112001005237, 2001.

Eckart, C.: The propagation of gravity waves from deep to shallow water, https://ui.adsabs.harvard.edu/abs/1952grwa.conf..165E (last access: 6 November 2023), U. S. National Bureau of Standards, 1952.

Gallet, B. and Young, W. R.: Refraction of swell by surface currents, J. Mar. Res., 72, 105–126, https://doi.org/10.1357/002224014813758959, 2014.

GlobCurrent E.U. Copernicus Marine Service Information (CMEMS): Global Total Surface and 15m Current (COPERNICUS-GLOBCURRENT) from Altimetric Geostrophic Current and Modeled Ekman Current Reprocessing, Marine Data Store (MDS) [data set], https://doi.org/10.48670/moi-00050, 2022.

Halsne, T., Bohlinger, P., Christensen, K. H., Carrasco, A., and Breivik, Ø.: Resolving regions known for intense wave–current interaction using spectral wave models: A case study in the energetic flow fields of Northern Norway, Ocean Model., 176, 102071, https://doi.org/10.1016/j.ocemod.2022.102071, 2022.

Halsne, T., Christensen, K. H., Hope, G., and Breivik, Ø.: Model repository, Zenodo [code], https://doi.org/10.5281/zenodo.7602540, 2023.

Holthuijsen, L. H.: Waves in Oceanic and Coastal Waters, Cambridge University Press, https://doi.org/10.1017/CBO9780511618536, 2007.

Irvine, D. E. and Tilley, D. G.: Ocean wave directional spectra and wave-current interaction in the Agulhas from the Shuttle Imaging Radar-B synthetic aperture radar, J. Geophys. Res.-Oceans, 93, 15389–15401, https://doi.org/10.1029/JC093iC12p15389, 1988.

Johnson, J. W.: The refraction of surface waves by currents, Eos, Transactions American Geophysical Union, 28, 867–874, https://doi.org/10.1029/TR028i006p00867, 1947.

Jones, B.: A Numerical Study of Wave Refraction in Shallow Tidal Waters, Estuar. Coast. Shelf Sci., 51, 331–347, https://doi.org/10.1006/ecss.2000.0679, 2000.

Kenyon, K. E.: Wave refraction in ocean currents, Deep-Sea Res., 18, 1023–1034, https://doi.org/10.1016/0011-7471(71)90006-4, 1971.

Kirby, J. T. and Chen, T.-M.: Surface waves on vertically sheared flows: Approximate dispersion relations, J. Geophys. Res.-Oceans, 94, 1013–1027, https://doi.org/10.1029/JC094iC01p01013, 1989.

Komen, G. J., Cavaleri, L., Doneland, M., Hasselmann, K., Hasselmann, S., and Janssen, P. A. E. M. (Eds.): Dynamics and Modelling of Ocean Waves, Cambridge Univeristy Press, https://doi.org/10.1017/CBO9780511628955, 1994.

Kudryavtsev, V., Yurovskaya, M., Chapron, B., Collard, F., and Donlon, C.: Sun glitter imagery of surface waves. Part 2: Waves transformation on ocean currents, J. Geophys. Res.-Oceans, 122, 1384–1399, 2017.

Langtangen, H. P.: A Primer on Scientific Programming with Python, vol. 6 of Texts in Computational Science and Engineering, Springer, Berlin, Heidelberg, ISBN 978-3-662-49886-6 978-3-662-49887-3, https://doi.org/10.1007/978-3-662-49887-3, 2016.

Liu, A. K., Peng, C. Y., and Schumacher, J. D.: Wave-current interaction study in the Gulf of Alaska for detection of eddies by synthetic aperture radar, J. Geophys. Res.-Oceans, 99, 10075–10085, https://doi.org/10.1029/94JC00422, 1994.

Mapp, G. R., Welch, C. S., and Munday, J. C.: Wave refraction by warm core rings, J. Geophys. Res., 90, 7153, https://doi.org/10.1029/JC090iC04p07153, 1985.

Masson, D.: A Case Study of Wave–Current Interaction in a Strong Tidal Current, J. Phys. Oceanogr., 26, 359–372, https://doi.org/10.1175/1520-0485(1996)026<0359:ACSOWI>2.0.CO;2, 1996.

Mathiesen, M.: Wave refraction by a current whirl, J. Geophys. Res.-Oceans, 92, 3905–3912, https://doi.org/10.1029/JC092iC04p03905, 1987.

Phillips, O. M.: The Dynamics of the Upper Ocean, Cambridge University Press, Cambridge, 2 edn., https://doi.org/10.1002/zamm.19790590714, 1977.

Rapizo, H., Babanin, A., Gramstad, O., and Ghantous, M.: Wave Refraction on Southern Ocean Eddies, in: 19th Australasian Fluid Mechanics Conference, Melbourne, Australia, 8–11 December 2014, 18, 46–50, ISBN 978-1-5108-2684-7, 2014.

Romero, L., Lenain, L., and Melville, W. K.: Observations of Surface Wave–Current Interaction, J. Phys. Oceanogr., 47, 615–632, https://doi.org/10.1175/JPO-D-16-0108.1, 2017.

Romero, L., Hypolite, D., and McWilliams, J. C.: Submesoscale current effects on surface waves, Ocean Model., 153, 101662, https://doi.org/10.1016/j.ocemod.2020.101662, 2020.

Saetra, Ø., Halsne, T., Carrasco, A., Breivik, Ø., Pedersen, T., and Christensen, K. H.: Intense interactions between ocean waves and currents observed in the Lofoten Maelstrom, J. Phys. Oceanogr., 51, 3461–3476, https://doi.org/10.1175/JPO-D-20-0290.1, 2021.

Segtnan, O. H.: Wave Refraction Analyses at the Coast of Norway for Offshore Applications, Energy Proced., 53, 193–201, https://doi.org/10.1016/j.egypro.2014.07.228, 2014.

Sun, R., Villas Bôas, A. B., Subramanian, A. C., Cornuelle, B. D., Mazloff, M. R., Miller, A. J., Langodan, S., and Hoteit, I.: Focusing and Defocusing of Tropical Cyclone Generated Waves by Ocean Current Refraction, J. Geophys. Res.-Oceans, 127, e2021JC018112, https://doi.org/10.1029/2021JC018112, 2022.

Wang, D. W., Liu, A. K., Peng, C. Y., and Meindl, E. A.: Wave-current interaction near the Gulf Stream during the Surface Wave Dynamics Experiment, J. Geophys. Res.-Oceans, 99, 5065–5079, https://doi.org/10.1029/93JC02714, 1994.

Zippel, S. and Thomson, J.: Surface wave breaking over sheared currents: Observations from the Mouth of the Columbia River, J. Geophys. Res.-Oceans, 122, 3311–3328, https://doi.org/10.1002/2016JC012498, 2017.

Paper IV

IV

Wave modulation in a strong tidal current and its impact on extreme waves

Trygve Halsne, Alvise Benetazzo, Francesco Barbariol, Kai Håkon Christensen, Ana Carrasco, and Øyvind Breivik
Journal of Physical Oceanography, **54/1** (2023)

Wave Modulation in a Strong Tidal Current and Its Impact on Extreme Waves

TRYGVE HALSNE,[a,b] ALVISE BENETAZZO,[c] FRANCESCO BARBARIOL,[c] KAI HÅKON CHRISTENSEN,[a,d] ANA CARRASCO,[a] AND ØYVIND BREIVIK[a,b]

[a] *Norwegian Meteorological Institute, Oslo, Norway*
[b] *University of Bergen, Bergen, Norway*
[c] *Institute of Marine Sciences, Italian National Research Council, Venice, Italy*
[d] *University of Oslo, Oslo, Norway*

(Manuscript received 24 March 2023, in final form 30 October 2023, accepted 1 November 2023)

ABSTRACT: Accurate estimates of extreme waves are central for maritime activities, and stochastic wave models are the best option available for practical applications. However, the way currents influence the statistics of space–time extremes in spectral wave models has not been properly assessed. Here we demonstrate impacts of the wave modulation caused by one of the world's strongest open ocean tidal currents, which reaches speeds of at least 3 m s^{-1}. For a bimodal swell and wind sea state, we find that most intense interactions occur when the wind sea opposes the tidal current, with an increase in significant wave height and spectral steepness up to 45% and 167%, respectively. The steepness modulation strengthens the second-order Stokes contribution for the normalized extreme crests, which increases between 5% and 14% during opposing wind sea and current. The normalized extreme wave heights have a strong dependence on the narrow-bandedness parameter, which is sensitive to the variance distribution in the bimodal spectrum, and we find an increase up to 12% with currents opposing the wind sea. In another case of swell opposing a tidal jet, we find the spectral steepness to exceed the increase predicted by a simplified modulation model. We find support in single-point observations that using tidal currents as forcing in wave models improves the representation of the expected maximum waves, but that action must be taken to close the gap of measurements in strong currents.

SIGNIFICANCE STATEMENT: The purpose of this study is to investigate how a very strong tidal current affects the surface wave field, and how it changes the stochastic extreme waves formulated for a space–time domain. Our results suggest that the expected maximum waves become more realistic when tidal currents are added as forcing in wave models. Here, the expected extremes exceed traditional model estimates, i.e., without current forcing, by more than 10%. These differences have implications for maritime operations, both in terms of planning of marine structures and for navigational purposes. However, there is a significant lack of observations in environments with such strong currents, which are needed to further verify our results.

KEYWORDS: Oceanic waves; Spectral analysis/models/distribution; Wave properties; Tides; In situ oceanic observations; Ocean models

1. Introduction

Strong wave field modulations are caused by periodic tidal currents and at river inlets (Baschek 2005; Tolman 1990; Guillou 2017; Zippel and Thomson 2017; Saetra et al. 2021; Ho et al. 2023; Chawla and Kirby 2002). The interaction between waves and tidal currents dictates the horizontal wave height variability and may cause dangerous sea states (Ardhuin et al. 2012; Masson 1996; Rapizo et al. 2017; Halsne et al. 2022). Such interactions are also linked to the generation of extreme waves, which poses a severe threat for maritime activities due to their random occurrence and abnormal size (e.g., Lavrenov 1998; Toffoli et al. 2011; Onorato et al. 2011). However, the influence of tidal currents on the extreme wave statistics have yet to be properly investigated. In this paper we demonstrate and discuss the impact by a strong tidal current in northern Norway on the short-term extreme wave statistics, by taking advantage of the recent implementation of space–time extremes in spectral wave models (Benetazzo et al. 2021b; Barbariol et al. 2017) in combination with tidal current forcing.

Extreme wave estimates for a given sea state have traditionally been computed using stochastic models defined for a single point in space over a certain time duration, such that the wave field can be considered a statistically stationary process. It is, however, recognized that the maximum sea surface elevation within a certain horizontal area is generally higher than what is measured in a single point (Forristall 2007, 2008; Krogstad et al. 2008; Fedele et al. 2011). Therefore, recent works have focused on extending the traditional time extreme approaches to take into account the three-dimensional space–time domain (e.g., Boccotti 2000; Fedele 2012; Fedele et al. 2013; Benetazzo et al. 2015). The maximum wave crests η and crest–to–trough heights H in such domains are referred to as the space–time extremes (STEs). Recent studies have found good agreement between observations of extreme waves and expected STEs based on higher-order Stokes waves (Benetazzo et al. 2015, 2021a; Fedele et al. 2017; Barbariol et al. 2019;

Denotes content that is immediately available upon publication as open access.

Corresponding author: Trygve Halsne, trygve.halsne@met.no

DOI: 10.1175/JPO-D-23-0051.1

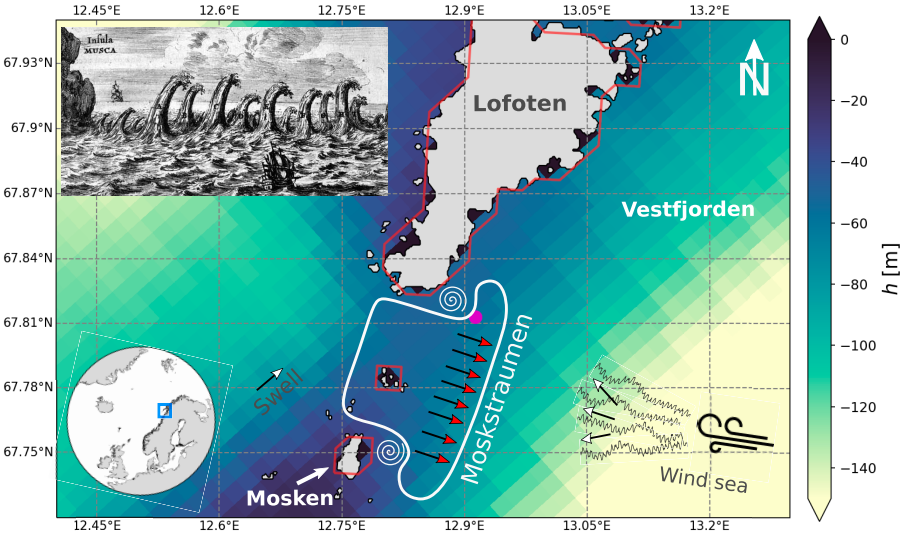

FIG. 1. A cartoon representation of the Moskstraumen tidal current during incoming tide (red colored arrows denote direction), which is located between the southern tip of the Lofoten Peninsula and the island of Mosken in northern Norway. The magenta dot shows the location of the ADCP. Red contours denote the land mask from the wave model. The bimodal sea state during one of our periods of investigation had easterly wind sea and a southwesterly swell component. During incoming tide, Moskstraumen takes the form of a broad, uniform current with eddies in its vicinity. Here the shape of Moskstraumen is exaggerated for illustrative purposes. Moskstraumen has been renowned for centuries for its strength and ferocity, and here the sea surface manifestation of Moskstraumen by Johannes Herbinius from 1678 is included.

Benetazzo et al. 2017). Although the impact by currents on extreme waves has been studied following deterministic approaches (e.g., Toffoli et al. 2011; Onorato et al. 2011; Hjelmervik and Trulsen 2009), currents in stochastic extreme wave models have been given little attention.

Expected extreme waves in short-term statistics are dictated by sea state parameters computed from the 2D wave spectrum. Four of these are particularly important in a space–time domain (Benetazzo et al. 2021a): (i) the significant wave height (H_s), (ii) the spectral steepness (ε), which represents a measure of the nonlinearity of the sea state, (iii) the average number of waves within the space–time domain (N_{3D}), which represents the sample size, and (vi) the narrow-bandedness parameter (ϕ^*), which characterizes the width of the frequency spectrum. Barbariol et al. (2015) demonstrated how the linear (i.e., with steepness $\varepsilon = 0$) stochastic crest heights in space–time increased on a countercurrent due to the increase in N_{3D}, caused by the frequency shift, and vice versa on cocurrents. They considered Pierson–Moskowitz and JONSWAP spectra and an idealized current in one direction. Consequently, the effect of current-induced refraction on the extreme crests was not taken into account. Moreover, the recent work by Benetazzo et al. (2015) takes into account weakly nonlinear random wave fields up to second order in ε, which has not been analyzed in the presence of currents.

To the best of our knowledge, no previous works have addressed the influence by currents on the stochastic wave heights in space–time. Ying et al. (2011) investigated the role of currents on the traditional *time* extreme wave height distribution proposed by Longuet-Higgins (1957). They proposed to add a scaling term to the probability distribution due to the change in statistics caused by focal points due to current-induced refraction, which were derived based on the results by White and Fornberg (1998), such that the probability of extreme wave heights increases in caustics. However, since the stochastic extreme wave formulations considered here are formulated for space–time, we hypothesize that the local changes in wave statistics caused by currents are implicitly taken into account by the N_{3D} parameter. Furthermore, and building upon the quasi-determinism theory by Boccotti (2000), the maximum STE wave height depend on characteristic shape of the wave spectrum, also when reduced from the space–time to a single-point time domain, where the narrow-bandedness parameter ϕ^* is used as a measure.

Our study takes place in the Loften Maelstrom (Fig. 1), locally referred to as *Moskstraumen* ("straum" is current in Norwegian), a very strong open-ocean tidal current which can at least reach a speed of 3 m s^{-1}. Moskstraumen, which the tidal current will be referred to hereafter, has been infamous for centuries for its strength and for the occurrence of large and steep waves (Gjevik et al. 1997; Moe et al. 2002). Saetra et al. (2021) presented the first simultaneous measurements of waves and currents in Moskstraumen, which they used to verify an ocean model representation of the tidal current.

Halsne et al. (2022) used the wave observations and found a better agreement with the wave field predicted by a WAM spectral wave model forced with model currents than an identical model without currents. Here we use a similar setup, but take advantage of a more recent WAM version that includes the STE computations (Benetazzo et al. 2021b). We consider two periods with different met-ocean conditions, one where young wind sea opposes a broad uniform tidal current and another where swell opposes a tidal jet. Under these characteristic conditions, we assess the impact by wave straining (to be introduced later) and current-induced refraction, two important wave–current interaction (WCI) mechanisms, on the sea state by, among others, comparing against a quasi-stationary idealized theoretical solution. We evaluate the influence of Moskstraumen on the 2D spectrum, the key spectral parameters listed above, and ultimately on the STEs.

The paper is structured as follows. In the following section 2 we present the theoretical framework for currents effects on the wave field under quasi-stationary conditions. In section 3, the stochastic extreme wave formulations in a space–time domain is presented together with the homogeneity assumption for short term statistics. In section 4, we describe the study region and model specifications. The results for each of the cases are presented in section 5 and further discussed in section 6. Then our concluding remarks are presented in section 7.

2. Current-induced wave field transformation

Here we present the wave straining mechanism by first considering the impact by a horizontally uniform current on the wave variance density E, and second on wave steepness. We consider an ambient, quasi-stationary, current field $\mathbf{U}(t, \mathbf{x}) \simeq \mathbf{U}(\mathbf{x}) = [u(\mathbf{x}), v(\mathbf{x})]$, where $\mathbf{x}$ is the horizontal position vector.

The Doppler shift equation

$$\omega = \sigma + \mathbf{k} \cdot \mathbf{U}, \tag{1}$$

governs the shift in wave frequency. Here, ω is the absolute wave frequency as seen from a fixed point, σ is the intrinsic frequency (following the current), and $\mathbf{k} = (k_x, k_y)$ is the wavenumber vector. Under quasi-stationary conditions, the number of wave crests is conserved in a fixed control volume [Phillips 1977, Eq. (2.6.2)]. This requires that the wavenumber $k = |\mathbf{k}|$ must change when exposed to a changing ambient current through the intrinsic frequency dispersion relation

$$\sigma^2 = gk\tanh(kh), \tag{2}$$

where g is the gravitational constant and h is the water depth. We define the effective current

$$U_{\text{eff}} = U\vartheta, \tag{3}$$

where $U = |\mathbf{U}|$, and the degree of opposition between the waves and the currents, ϑ, is computed by

$$\vartheta = \cos(\theta_c - \theta_w). \tag{4}$$

Here, θ_c, θ_w denote the current direction and the wave direction, respectively, using the same convention. Thus, values of 1, 0, and −1 indicate following, perpendicular, and opposing, respectively.

Consider a wave train propagating along the x axis on deep water from an area with $U_{\text{eff}} = u_0 = 0$ to an opposing current $U_{\text{eff}} < 0$. In the following, subscript 0 denotes the wave characteristics where $U_{\text{eff}} = 0$. In such a case, $\omega = \sigma_0 = \text{const.}$ due to wave crest conservation. To compensate for the loss in the $\mathbf{k} \cdot \mathbf{U}$ term of (1), there must be an accompanied increase in k. Increasing k implies a shortening in the wavelength $\lambda = 2\pi/k$. In the presence of currents, E is not a conserved quantity (Longuet-Higgins and Stewart 1964). However, the wave action density $N = N(\mathbf{x}, t) = E/\sigma$ is conserved and takes the general form (Bretherton and Garrett 1968)

$$\frac{\partial N}{\partial t} + \nabla \cdot (\dot{\mathbf{x}} N) = 0. \tag{5}$$

Here, $\mathbf{x} = \mathbf{c}_g + \mathbf{U}$ is the absolute wave group velocity vector, and $\mathbf{c}_g = (\mathbf{k}/k)(\partial\sigma/\partial k)$ the intrinsic group velocity vector. Solving (5) with respect to E for a constant current according to the above considerations we obtain [Phillips 1977, Eq. (3.7.11)]

$$\frac{E}{E_0} = \frac{c_0^2}{c^2(1 + 2U_{\text{eff}}/c)}. \tag{6}$$

Here, the impact by the currents is reflected in the denominator, and E increases toward the singularity $U_{\text{eff}} \to -c/2$, implying that the waves have been blocked by the current. At the blocking point, $U_{\text{eff}} = -c_0/4$. According to (6), E will increase when the waves are propagating into an opposing current, and decrease for a following current. The theory is valid in the absence of wave breaking and while $U_{\text{eff}} > -c_0/4$. In the absence of a clear naming convention, we denote the effect in (6) "wave straining," by following Holthuijsen and Tolman (1991). Wave straining is the combined effect of the "concertina effect" (Ardhuin et al. 2017; Wang and Sheng 2018), referring to the change in wavenumber, and the accompanied "energy bunching" (Baschek 2005). It is similar to shoaling, which occurs when waves propagate from deep to intermediate and shallow waters.

If we consider the wave steepness $\varepsilon = \sqrt{E}k$, since E is proportional to the square of the wave amplitude a, we can rewrite (6) (Rapizo et al. 2017)

$$\frac{\varepsilon}{\varepsilon_0} = \frac{(1 - kU_{\text{eff}}/\omega)^3}{\sqrt{1 + 2U_{\text{eff}}/c}}. \tag{7}$$

Here, the kU_{eff}/ω term in the nominator expresses the effect by the current on the wave steepness, which can be recognized by considering (1):

$$\frac{kU_{\text{eff}}}{\omega} = \frac{\omega - \sigma}{\omega} = \frac{\Delta\omega}{\omega}. \tag{8}$$

Thus, $\Delta\omega < 0$ implies a growth in (7), and the k dependence denotes the sensitivity of wave straining to the initial wavelength. For example, for waves directly opposing a current $U_{\text{eff}} = -1.0\ \text{m s}^{-1}$ from a reference of $U_{\text{eff}} = 0$, the increase in ε is 26% and 95% for a $T = 12$ s and a $T = 5$ s period

TABLE 1. Wave parameter modulation due to wave straining on steady currents according to (7). The left and right sides show the ratio in wave variables (subscript 0 means zero current) for a 5- and 12-s period wave, respectively. In all cases, $a_0 = 1$ m. Each row denotes different effective currents U_{eff}.

	$T_0 = 5$ s			$T_0 = 12$ s		
U_{eff} (m s^{-1})	a/a_0	k/k_0	$\varepsilon/\varepsilon_0$	a/a_0	k/k_0	$\varepsilon/\varepsilon_0$
1.5	0.74	0.74	0.55	0.87	0.87	0.75
1	0.81	0.8	0.65	0.91	0.91	0.82
0.5	0.89	0.89	0.79	0.95	0.95	0.9
−0.5	1.16	1.15	1.33	1.06	1.06	1.12
−1	1.41	1.39	1.95	1.13	1.12	1.26
−1.5	1.95	1.82	3.55	1.21	1.2	1.45

wave, respectively. A summary for different values of U_{eff} and wave periods are given in Table 1. From the above considerations, both k and $\sqrt{E}$ are modulated simultaneously by wave straining, and consequently ε is very sensitive to the ambient current (Vincent 1979).

3. Statistical models for extreme waves in a space–time domain

The zero mean sea surface elevation is denoted $\eta(t, \mathbf{x})$. The sea state can be characterized by $H_s = 4\beta$, where β is the standard deviation of $\eta(t, \mathbf{x})$. Building upon the results by Fedele (2012), Benetazzo et al. (2015), and Boccotti (2000), we consider a 3D space–time domain $\Gamma = XYD$, where X and Y are the size of the sides of a rectangular surface area and D is the duration of a time interval (see Fig. 1 in Fedele 2012). Here fundamental properties of the STE models are described, with particular focus on the sea state parameters that are essential for the STEs.

a. Expected extreme wave crests and heights

Assuming a Gaussian probability distribution of η for every point within Γ, then the maximum individual crest height η_{MAX} can be defined in terms of an exceedance probability by a threshold z:

$$P_{\text{ST,MAX}} = \Pr\{\eta_{\text{MAX}} > z | (x, y, t) \in \Gamma\}, \tag{9}$$

where subscript ST stands for space–time. The STE model for η_{MAX} is based on the so-called "Euler characteristics" valid for n dimensions (Adler and Taylor 2007), which was first reduced to $n = 3$ and verified for ocean waves in a space–time domain by Fedele (2012), and thereafter further developed by Benetazzo et al. (2015) to take into account weakly nonlinear random wave fields up to second order in ε. With regards to the maximum crest-to-trough wave height (H_{MAX}), we consider the linear quasi-determinism theory by Boccotti (2000) which takes into account the narrow-bandedness of the sea state. These maxima can be deduced from their expected value using integrated spectral parameters, provided that the sea state is temporally stationary and spatially homogeneous (Adler and Taylor 2007). Such assumptions may be altered in a rapidly varying tidal current and will be treated in the subsequent section.

In essence, the STEs are proportional to H_s, and subsequently modified by parameters that constitute the average number of waves ($N_{3\text{D}}$), wave steepness (ε), and spectral bandwidth (ϕ^*), which will now be introduced in that order (Benetazzo et al. 2021a). First, the average number of waves within Γ is (Fedele 2012)

$$N_{3\text{D}} = \frac{XYD}{L_x L_y T_m}\sqrt{1 - \alpha_{xt}^2 - \alpha_{xy}^2 - \alpha_{yt}^2 + 2\alpha_{xt}\alpha_{xy}\alpha_{yt}}, \tag{10}$$

where L_x, L_y, T_m denote length scales associated with the mean crest length (in the X and Y direction) and the zero-crossing mean period, respectively. Furthermore, the average number of waves at the boundaries and at the edges of Γ reads

$$N_{2\text{D}} = \frac{XD}{L_x T_m}\sqrt{1 - \alpha_{xt}^2} + \frac{YD}{L_y T_m}\sqrt{1 - \alpha_{yt}^2} + \frac{XY}{L_x L_y}\sqrt{1 - \alpha_{xy}^2}, \tag{11}$$

$$N_{1\text{D}} = \frac{X}{L_x} + \frac{Y}{L_y} + \frac{D}{T_m}, \tag{12}$$

respectively. Studies have shown that the average number of waves within the interior of the space–time domain, i.e., $N_{3\text{D}}$, dominate over the others for large-sized space–time domains, and is therefore considered here (Fedele 2012; Benetazzo et al. 2021a). The degree of organization in the space–time wave field is characterized by the expression containing the square root in (10):

$$A = \sqrt{1 - \alpha_{xt}^2 - \alpha_{xy}^2 - \alpha_{yt}^2 + 2\alpha_{xt}\alpha_{xy}\alpha_{yt}}, \tag{13}$$

which originates from the determinant of the covariance matrix of $\eta(t, \mathbf{x})$ [see Eqs. (5)–(7) by Benetazzo et al. (2021a)]. The variables in A are commonly referred to as the "irregularity parameters" (Baxevani and Rychlik 2006). These parameters can be computed from spectral moments as

$$\alpha_{xt} = \frac{m_{101}}{\sqrt{m_{200} m_{002}}}, \tag{14}$$

$$\alpha_{yt} = \frac{m_{011}}{\sqrt{m_{020} m_{002}}}, \tag{15}$$

$$\alpha_{xy} = \frac{m_{110}}{\sqrt{m_{200} m_{020}}}, \tag{16}$$

where

$$m_{ijl} = \int\int k_x^i k_y^j \sigma^l E(\sigma, \theta)\, d\sigma\, d\theta. \tag{17}$$

From (10), it follows that $N_{3\text{D}}$ is maximized for $A = 1$ and minimized for $A = 0$. More details about the spectral distributions associated with A are found in Baxevani and Rychlik (2006).

The degree of nonlinearity for a weakly nonlinear sea state is determined by the spectral steepness ε, which is related to the skewness coefficient of the sea state (i.e., the third-order moment of its probability density function). A characteristic ε for deep water is (Fedele and Tayfun 2009)

$$\varepsilon = \frac{\beta\sigma_1^2}{g}(1 - \nu + \nu^2), \tag{18}$$

where $\sigma_1 = m_{001}/m_{000}$ is the average angular frequency and

$$\nu = \sqrt{m_{002}m_{000}/m_{001}^2 - 1}, \tag{19}$$

is a spectral bandwidth parameter proposed by Longuet-Higgins (1975). For simplicity, the wave steepness is denoted by ε in (7) and (18), even though the first represents a monochromatic wave field and the second is a measure of the spectral steepness with finite bandwidth.

The bandwidth parameter ϕ^* draws upon the quasi-determinism theory of Boccotti (2000) and characterizes the narrow-bandedness of the sea state. Formally, it stems from the autocovariance function for $\eta(t)$,

$$\phi(\tau) = \langle \eta(t)\,\eta(t+\tau)\rangle. \tag{20}$$

Here, τ and angle brackets $\langle\cdot\rangle$ denote time lag and temporal mean, respectively. The narrow-bandedness is defined as

$$\phi^* \equiv \frac{\phi(\tau^*)}{\phi(0)}, \tag{21}$$

where

$$\phi(\tau) = \int E(\sigma)\cos(\sigma\tau)\,d\sigma, \tag{22}$$

and τ^* is the time lag of the first minimum of $\phi(\tau)$. Typical values for ϕ^* are -1 for an infinitely narrow frequency spectrum and in the range $[-0.75, -0.65]$ for wind-sea conditions (Boccotti 2000).

The expected maximum wave crest within a space–time domain Γ can be derived from the exceedance probability (9). Corrected to second order in ε, it is defined as (Benetazzo et al. 2021a)

$$\overline{\eta}_{\mathrm{MAX,ST}} = \beta\left(h_1 + \frac{\varepsilon}{2}h_1^2\right) + \beta\gamma\left[(1+\varepsilon h_1) \times \left(h_1 - \frac{2N_{3D}h_1 + N_{2D}}{N_{3D}h_1^2 + N_{2D}h_1 + N_{1D}}\right)^{-1}\right], \tag{23}$$

where subscript ST stands for space–time and expected values are denoted by the overbar operator $\overline{(\cdot)}$. Here, h_1 is the normalized mode of the probability density function of the linear STE (see appendix A in Benetazzo et al. 2017), and the Euler–Mascheroni constant $\gamma \simeq 0.5772$ is obtained by following the asymptotic extreme distribution by Gumbel (1958). For a single point in space, i.e., $X = Y = 0$, (23) reduces to the time-extreme model proposed by Tayfun (1980), which in turn reduces to the model proposed by Longuet-Higgins (1957) for $\varepsilon = 0$. The expected maximum linear crest-to-trough wave heights within Γ can be computed from the linear $\overline{\eta}_{\mathrm{MAX,ST}}$, i.e., with $\varepsilon = 0$, (Boccotti 2000),

$$\overline{H}_{\mathrm{MAX,ST}} = \beta\left[h_1 + \gamma\left(h_1 - \frac{2N_{3D}h_1 + N_{2D}}{N_{3D}h_1^2 + N_{2D}h_1 + N_{1D}}\right)^{-1}\right] \times \sqrt{2(1-\phi^*)}. \tag{24}$$

Here, the expected extreme height increases with decreasing ϕ^*. Thus, $\overline{H}_{\mathrm{MAX}}$ is maximized for an infinitely narrow sea state where $\phi^* = -1$ (Boccotti 2000).

In general, $\overline{\eta}_{\mathrm{MAX,ST}}$ in (23) increases with increasing $\beta = H_s/4$, N_{3D}, and ε, and vice versa (Benetazzo et al. 2021a). Similar modulations are found for $\overline{H}_{\mathrm{MAX,ST}}$ in (24) through the parameters β, N_{3D}, and $|\phi^*|$ ($|\cdot|$ denotes the absolute value). Thus, (23) and (24) can be written in a simplified form as (Benetazzo et al. 2021a)

$$\frac{\overline{\eta}_{\mathrm{MAX,ST}}}{H_s} = F_\eta(\varepsilon, N_{3D}), \tag{25}$$

$$\frac{\overline{H}_{\mathrm{MAX,ST}}}{H_s} = F_H(|\phi^*|, N_{3D}), \tag{26}$$

where F_η and F_H denote the functional dependence with respect to the maximum η and H, respectively.

b. *Sea state homogeneity under ambient currents*

The wave spectrum $E(\sigma, \theta)$, and associated integrated variables, from a wave record at a single point x_i, y_i can be computed if the sea surface elevation $\eta(t, x_i, y_i)$ can be considered a stationary Gaussian process. Such an assumption generally holds for wave records with maximum duration D = 15–30 min (Holthuijsen 2007, p. 56). Similarly, homogeneous means that variables are statistically invariant in space so that $E(\sigma, \theta)$, computed over a duration interval D, does not change within the area. Such an assumption generally holds for square areas with sides of about 10 wavelengths in the open ocean (Boccotti 2000, p. 251). In wave modeling, the homogeneity condition in space and time is satisfied by keeping X and Y within $\mathcal{O}(10^2)$ m, and smaller than the model grid size (Benetazzo et al. 2021b).

With regards to ambient currents, we consider mean flows with spatiotemporal variability much less than the characteristic length scales for ocean waves. This can be formalized by requiring (Peregrine 1976)

$$\max\left|\frac{1}{U}\frac{\partial U}{\partial t}\right| \ll \sigma, \ \max\left|\frac{1}{U}\nabla_h U\right| \ll k, \tag{27}$$

where ∇_h denotes the horizontal gradient operator.

4. Model specifications, study region, and observations

a. *Spectral wave model and oceanic current forcing*

To assess the impact by Moskstraumen on the wave field, we used the WAM third-generation spectral wave model

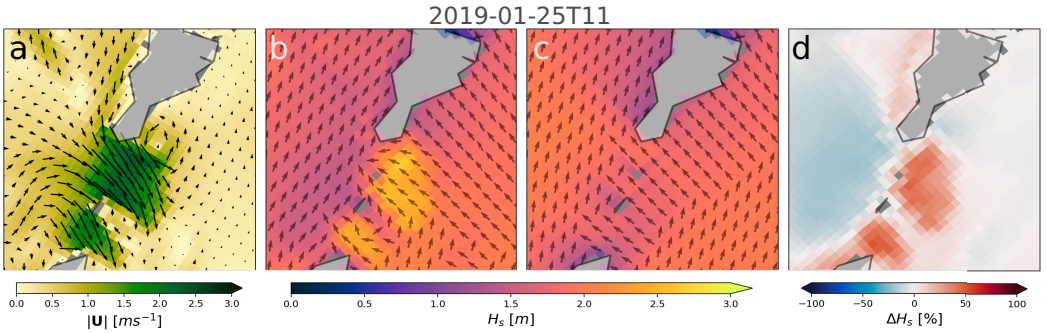

FIG. 2. Snapshots of Moskstraumen during maximum speed and its impact on the wave field. Panels denote (a) the current speed and direction, (b) H_s from W+C, (c) H_s from W, and (d) their relative difference according to (31). Black arrows in (b) and (c) denote the peak wave direction.

(Komen et al. 1994). In WAM, the sea state is modeled by solving the wave action evolution equation, i.e., a spectral representation of $N = N(\sigma, \theta; \mathbf{x}, t)$ with a nonzero right hand side of (5), which in deep water takes the form (Komen et al. 1994)

$$\frac{\partial N}{\partial t} + \nabla_h(\dot{\mathbf{x}}N) + \nabla_k(\dot{\mathbf{k}}N) = \frac{S_{\text{in}} + S_{\text{nl}} + S_{\text{ds}}}{\sigma}. \tag{28}$$

Here, ∇_k is the wavenumber gradient operator and the wave kinematics on the left hand side are

$$\dot{\mathbf{x}} = \frac{d\mathbf{x}}{dt} = \mathbf{c}_g + \mathbf{U}(t, \mathbf{x}), \tag{29}$$

$$\dot{\mathbf{k}} = \frac{d\mathbf{k}}{dt} = -\mathbf{k} \cdot \nabla_h \mathbf{U}(t, \mathbf{x}). \tag{30}$$

Here, (29) is the advection of wave action density and (30) models refraction and the change in wavenumber components as the wave propagation direction is normal to the wavenumber vector. The wind input S_{in} and the wave breaking S_{ds} together with the nonlinear quadruple wave–wave interaction S_{nl} make up the source terms in (28).

Two 800-m resolution WAM simulations were carried out. The first included only wind forcing and lateral spectral boundary conditions from a coarser (4 km) outer wave model. Wind forcing was taken from the operational 2.5-km resolution Arome Arctic NWP model operated by the Norwegian Meteorological Institute, with further specifications given in Müller et al. (2017). The second run also included surface current forcing from MET Norway's operational ROMS (Regional Ocean Modeling System; Shchepetkin and McWilliams 2005) model, also at an 800-m horizontal resolution. The ocean surface current was included in the wave kinematics, (29) and (30). The two model simulations are hereafter referred to as W and W+C, which stand for wind and wind + currents, respectively. These simulations are based on the same model setup as reported by Halsne et al. (2022), which provide more details about the forcing fields and wave model specifications. However, the WAM simulations were further extended by including the computation of STEs (Benetazzo et al. 2021b). Here, the dimensions of the space–time domain $\Gamma = XYD$ were $X = Y = 200$ m, and the duration was $D = 1200$ s, after the general recommendations in Benetazzo et al. (2021b).

b. *Moskstraumen and characteristic met-ocean conditions*

The Lofoten region is located within the belt of westerlies and thus characterized by westerly waves coming from the open ocean, which include local wind sea and the near constant presence of remotely generated swell. On the east side of the strait, we find the Vestfjorden basin, which is about 100 km wide in the east–west direction (Fig. 1). The Lofoten area is therefore not exposed to swell from the east, but will become subject to local easterly wind sea under certain synoptic situations.

There is an asymmetry in the flow field when Moskstraumen is flowing west and east (Børve et al. 2021). When flowing west, Moskstraumen takes the form of a narrow jet with eddies occurring in the vicinity regions with strong shear. Flowing east, Moskstraumen is much broader in extent, and thus characterized with a more uniform flow field. This flow field is exemplified in Fig. 1 but also seen in the 800-m ocean model (Fig. 2a). Even though the ocean model is able to provide a qualitatively good representation of Moskstraumen, it is incapable of resolving all the complex subgrid processes. For example, when the current turns from flowing eastward to westward at slack tide, the northern part turns first and then gradually further south, which results in an area of strong horizontal shear (Halsne et al. 2022). The gradual turning is resolved in the ocean model, but the timing and magnitude of the gradients are not always correct. The phases when Moskstraumen is flowing west and east are hereafter referred to as outgoing tide and incoming tide, respectively. An example of Moskstraumen during maximum speed at incoming tide, together with its impact on the wave field in WAM, is shown in Fig. 2.

c. *ADCP observations*

Three months during winter 2019, concurrent wave and current measurements from a bottom-mounted Nortek Signature 500-kHz acoustic Doppler velocity profiler (ADCP) were

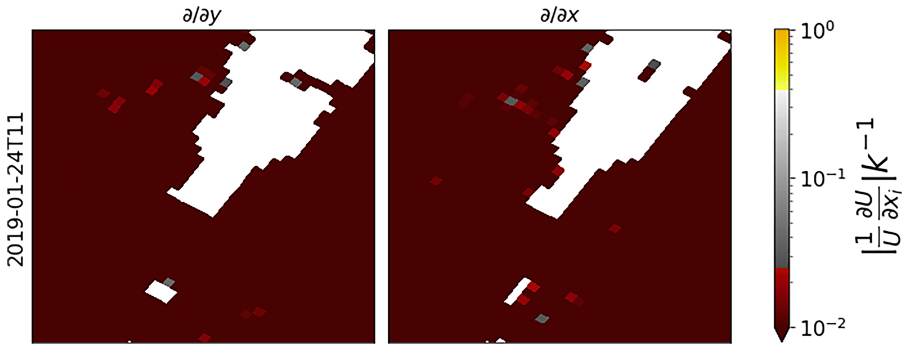

FIG. 3. Computing the criteria for the horizontal homogeneity according to (27) under maximum current speed for a $T = 6$ s period wave. Panels show the horizontal current gradient in the (left) y ($x_i = x_2$) and (right) x direction ($x_i = x_1$) on a logarithmic scale.

available on the east side of Lofoten (see magenta dot in Fig. 1). Here, wave measurements at 2 Hz from a five-beam configuration (one vertical and four slanted) in burst mode were acquired every 30 min, and each burst lasted 17 min. Vertical current profiles were also acquired simultaneously at 2 Hz with vertical resolution of 2 m, together with average mode measurements made up by 60 samples every 10 min with similar vertical resolution. These measurements were presented by Saetra et al. (2021) and Halsne et al. (2022).

In addition to the subgrid processes, the complex environment with its irregular coastline and strong currents makes it challenging to obtain an accurate spatiotemporal collocation of the model data and the observations. Another source causing spatial shift in model grid point values is the interpolation of the ROMS current field onto the WAM model grid projection. Furthermore, the coastline in the two models are slightly different (not shown). In our analysis, we found better agreement in both phase and magnitude for wave parameters at model grid points in the vicinity of the ADCP location rather than in the exact location (not shown). We have selected the nearest grid point with 2D wave spectral output, about 2 km southwest of the ADCP location.

5. Results

In the following we first consider a period at the end of January 2019, where a local easterly wind sea from Vestfjorden was opposing the broad and uniform eastward current (Fig. 2). The situation lasted for about 5 days and was due to a high pressure ridge of about 1022 hPa located over Lofoten which set up wind speeds U_{10} of 3–12 m s^{-1} from east-southeast (not shown). Here, the sea state was bimodal with a local wind sea component together with a gentle southwesterly swell with $1 < H_s < 3$ m (Figs. 1 and 2). This period was the only time during the 3-month ADCP deployment when easterly wind conditions lasted more than 2 days. This particular period was also investigated by Halsne et al. (2022). We then consider a period in early January with prevailing northwesterly swell opposing Moskstraumen, now shaped as a narrow jet on the offshore side at outgoing tide. Most emphasis is put on the first period, since there the observations are in the region of strong wave–current interaction.

The spectral parameters used for the extreme wave analysis should be computed from the intrinsic spectrum $E(f_i, \theta)$ ($f_i = \sigma/2\pi$). Thus, a transformation had to be applied on the wave model output since it is given in absolute frequencies, $f_a = \omega/2\pi$. The transformation from an absolute to an intrinsic reference frame is presented in the appendix.

The relative difference for a variable X between the two wave models is defined as

$$\mathrm{RD}(X) = \frac{X_{\mathrm{W+C}} - X_{\mathrm{W}}}{X_{\mathrm{W}}}. \tag{31}$$

a. Sea state modulation in Moskstraumen

1) SEA STATE HOMOGENEITY

The horizontal homogeneity condition in (27) is treated in Fig. 3, by using a representative wind sea peak period of 6 s. The ratios $|(1/U)(\partial U/\partial x_i)|k^{-1} \ll 1$, where $i = 1, 2$ denote the x and y direction, respectively. The horizontal homogeneity condition was also satisfied during other stages in the tidal cycle, and during swell and tidal jet conditions (not shown).

For the stationarity condition in (27), time derivatives from the observed current using representative intrinsic frequencies for the swell and wind sea components are presented in Fig. 4. Also here, the criterion of a current field varying much slower than a characteristic wave scale, $|(1/U)(\partial U/\partial t)|\sigma^{-1} \ll 1$, was fulfilled. To further support the stationarity condition, wave observations were analyzed by computing the variance β^2, and its potential drift during the 17-min burst period for different stages in the tidal cycle. Here, no significant deviations were found during each burst period (not shown).

2) TIDAL MODULATION OF THE WAVE FIELD AND THE UNI- AND DIRECTIONAL SPECTRUM

When the easterly wind sea opposed the broad uniform current, the wave model with current (W+C) showed a region

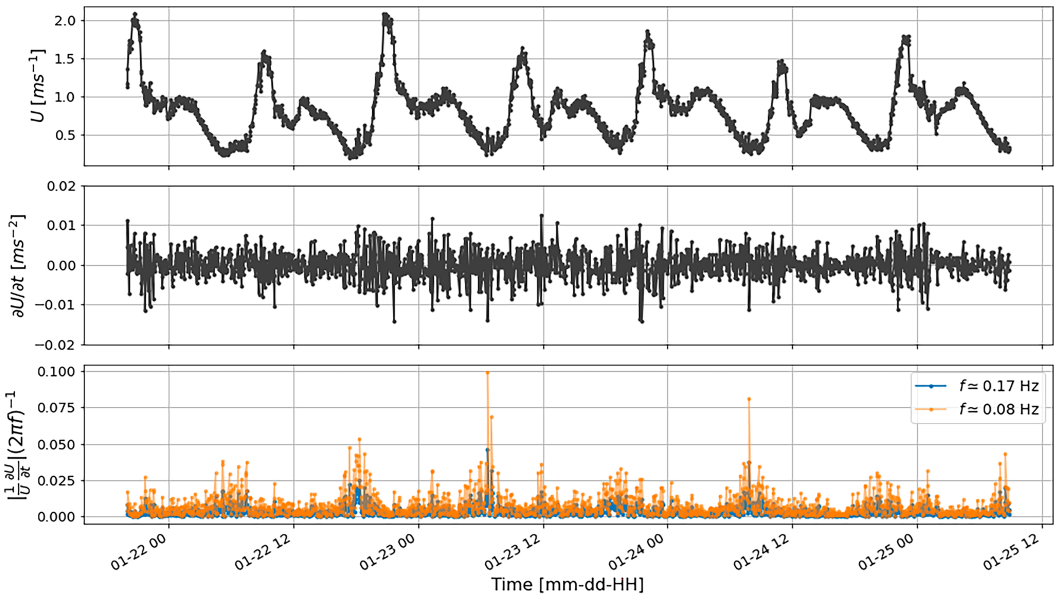

FIG. 4. Computing the criteria for the slowly varying current assumption in time (27). (top) The time series of the measured current speed U and (middle) the time derivative for 7 tidal cycles. (bottom) The scaled time derivative of U on a $T = 13$ s period wave (orange) and a $T = 6$ s period wave (blue).

of increased H_s with a shape similar to the tidal current (Fig. 2b). The met-ocean conditions suggests that wave straining is the dominating mechanism for three reasons: that is, (i) its sensitivity to higher frequencies in (1), (ii) the horizontal current gradients are strongest at the edges of the broad current and more uniform in the center (not shown) and consequently less exposed to caustics compared with a narrow jet (Kenyon 1971; Dysthe 2001), and (iii) both the active wind forcing and the short-crested nature of the wind sea are working against the veering of the rays, and consequently the impact of refraction is more diffuse compared with a narrow swell spectrum (Rapizo et al. 2016; Holthuijsen and Tolman 1991). However, and even if the wave straining mechanism dominate in the model when the wind sea opposes Moskstraumen, it does not imply that wave straining was the dominating mechanism in the observations since there are processes like wave breaking and strong shear going on below scales of 800 m.

The observed and W+C unidirectional spectra had a similar relative variance distribution on the wind sea and swell components in the bimodal spectrum (Figs. 5e,f). The semidiurnal M_2 modulation of the wind sea was well predicted by W+C, but the magnitude, and thus H_s, was at times off by about 1 m. There may be several reasons for such deviations, but the one around 1200 UTC 23 January (see red arrows in Fig. 5g) was due to the grid point resolution in the ROMS model. Here, Moskstraumen turned 180° prior to the observed current and opposed the swell, resulting in an increase in H_s. Furthermore, the wave energy was at times located on lower frequencies in the model compared with the observations, as seen from about 1200 UTC 26 January and throughout the period in the lower panel in Figs. 5e and 5f. Here, the U_{10} decreased to about 3 m s^{-1} in the atmospheric model (not shown). Another limitation with the measured 2D spectra was the cutoff in directional measurements at 0.2 Hz (Fig. 5c), related to the 500-kHz carrier frequency of the ADCP.

Snapshots of the temporal evolution of the modeled wave spectrum are shown in Fig. 6. Here, the wind sea broadened in direction and increased in frequency up to 0.3 Hz due to the opposing current (middle row). The spectra from the W simulation were stationary during incoming tide (top row). Clearly, the energy on the swell components reduced when propagating in the current direction (bottom row). Considering the unidirectional spectrum, both the energy and mean frequency level increased in W+C (rightmost column). The current speed reached 2 m s^{-1}, which exceeds the blocking velocity for the 5-s wave present in W, which according to (6) is -1.95 m s^{-1}.

3) INTEGRATED SPECTRAL PARAMETERS

Time evolution in the key sea state parameters from (25) and (26) are shown in Fig. 7, and the intermodel differences are listed in Table 2. An increase in H_s and ε occurred when the wind sea was opposing the current, except for H_s during the first tidal cycle around 1200 UTC 23 January as mentioned in the previous section (Fig. 5g). The phase of the modulation in ε was in general accordance with the observations with a correlation coefficient between ε from W+C and the observations of 0.80. Note that the observed sea state parameters are

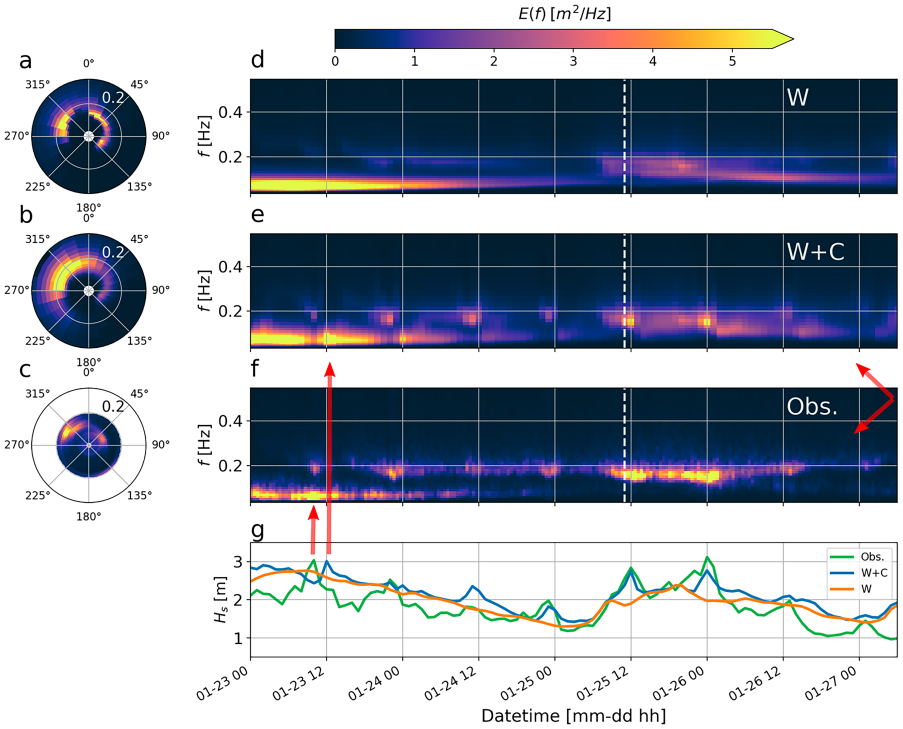

FIG. 5. Comparing (left) snapshots of modeled and observed 2D spectrum, together with (right) the temporal evolution in the 1D spectra and H_s. Snapshots of 2D spectra are taken from 1100 UTC 25 January (see vertical dashed line). Output from the wave model forced with (a),(d) wind (W), (b),(e) wind and current (W+C), and (c),(f) the ADCP observations (Obs.). At 50-m depth, the ADCP cannot measure wave directions for frequencies above 0.2 Hz [see (c)]. A more complete frequency coverage is provided by the observed 1D spectrum [see (f)]. (g) The spectral significant wave height H_s is shown for the observations (green line), W+C (blue line), and W (orange line). Red arrows around 1200 UTC 23 January denote the shift in the wave energy caused by the observed current turning before the model current, and the red arrows around 0000 UTC 27 January denote the different spectral wave energy distribution in the model vs the observations. Note that the color scale for the 2D spectra represents a scaled version of the 1D spectra, as the units are scaled by degrees.

computed from the intrinsic unidirectional spectrum. The H_s in W+C exceeded the W simulation by up to 44%, and ε by 167% (Table 2).

The average number of waves N_{3D} from (10) also increased with currents opposing the wind sea due to the shift in frequency to shorter waves (Fig. 7c). Consequently, L_x, L_y, T_m all decreased (not shown). The impact by the degree of organization in the space–time wave field A on N_{3D} was less systematic during the tidal phases, which made the influence by the tidal current difficult to interpret (not shown). Less systematic differences were also found for the absolute narrow-bandedness $|\phi^*|$ (Fig. 7d). We recall that $|\phi^*| \to 0$ implies a more broad-banded sea state, and that typical values for a wind-sea spectrum are in the range (0.65, 0.75). The lower $|\phi^*|$ in W+C than in W during the first tidal cycle was a result of the swell and wind sea having a similar energy level due to Moskstraumen opposing the latter, which thus caused a broadening the 1D spectrum (Fig. 7d). For the last two tidal cycles, when $U_{10} \simeq 3$ m s^{-1}, the energy on the swell and remaining wind sea was equally partitioned during outgoing tide, leading to the decrease in $|\phi^*|$ in W+C. By contrast, for some of the intermediate opposing cycles, the strong shift in variance density to the wind sea components caused a more narrow-banded sea state (Figs. 5e,f). Furthermore, the observations and W+C model predictions show some similar fluctuations, but often have quite different values, which is to be expected since the energy distributions in the spectra were at times quite different (Figs. 5e–g).

4) STEEPNESS MODULATION AND SIMPLIFIED QUASI-STATIONARY MODEL

The deep water spectral steepness in (18) can be rewritten

$$\varepsilon = \frac{\beta\sigma_1^2}{g}(1 - \nu + \nu^2) = \sqrt{E}k_1\psi, \tag{32}$$

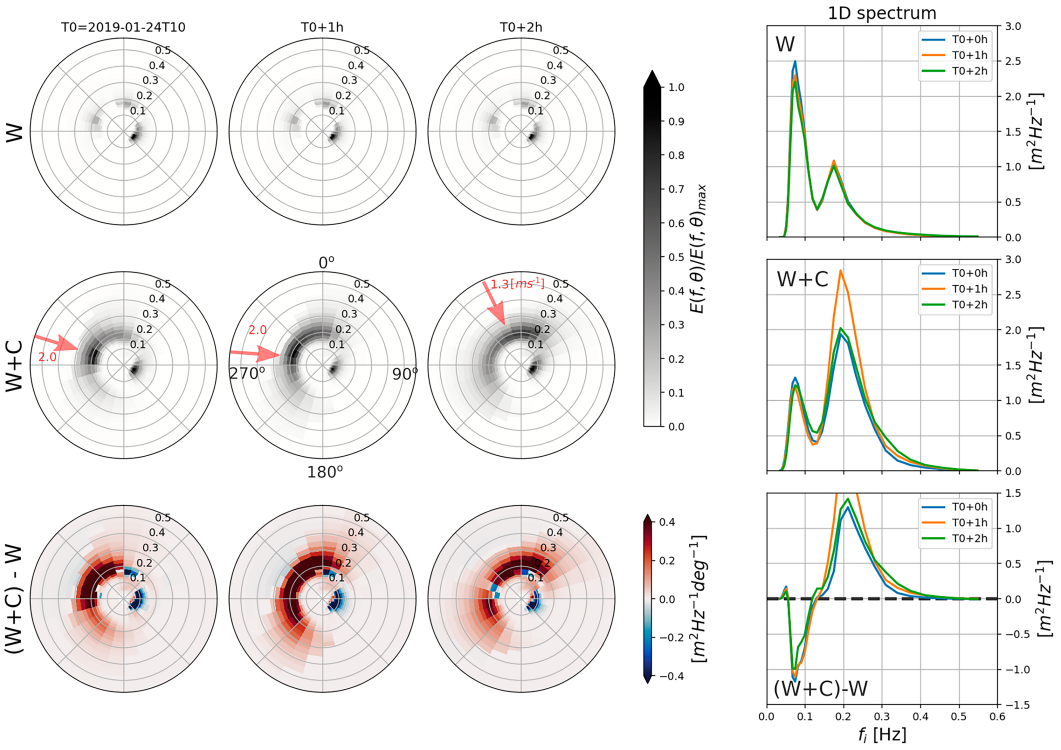

FIG. 6. Snapshots of the currents impact on the intrinsic wave spectrum during incoming tide (see Figs. 1 and 2). Rows show the normalized wave spectrum from the wave model forced with (top) wind (W), (middle) wind and currents (W+C), and (bottom) their difference. Columns on the left denote subsequent time steps, where the center column indicates the maximum current speed. The red arrows show the current direction, and the current speed (m s^{-1}) is denoted with red text. The rightmost column denotes the nonnormalized 1D spectrum.

where $k_1 = \sigma_1^2/g$ through (2), $\psi \in [0.75, 1]$, and $\beta = \sqrt{E}$. The global minimum for the parabolic function ψ is obtained for $\nu = 0.5$, and similar values were obtained in W+C and W such that $\psi_{W+C}/\psi_W \simeq 1$ (not shown). Thus, (32) can be further simplified, and we obtain the intermodel ratio

$$\frac{\varepsilon}{\varepsilon_0} \simeq \frac{\left(\sqrt{E}k_1\right)_{W+C}}{\left(\sqrt{E}k_1\right)_W}, \tag{33}$$

which can be evaluated against the quasi-stationary model for steepness modulation (7).

The comparison is shown in Fig. 8 by using k_1 from T_{m01} in W. Here, (7) gave similar results as the intermodel ratio. The spiky overshoots from (7) can be attributed to the lack of wave dissipation in the simplified model. Also, when comparing (7) against $\varepsilon_{W+C}/\varepsilon_W$ from the partitioned wind sea part of the spectrum (using the spectral partitioning algorithm from https://github.com/metocean/wavespectra – accessed 17 August 2022), the "troughs" were also realistically captured, which were due to the lengthening of waves on following currents (see green lines). The troughs were not present for the full bimodal spectrum, since then the swell part opposed the current and consequently increased in energy. The similarity between (33) and (7) also suggests that wave straining was the dominating WCI mechanism.

b. Extreme wave modulation

1) TIDAL MODULATION OF EXTREMES

The ratio $\overline{\eta}_{MAX,ST}/H_s$ increased when waves and currents were opposing and largely followed the curve of ε with a correlation coefficient of 0.92 in W+C (Figs. 7b and 9a). Maximum values mostly coincided with the maximum of ε, and the W+C predictions exceeded W up to 14% (Table 2). The intermodel difference between the linear predictions in W+C and W, i.e., considering $F_\eta(\varepsilon = 0, N_{3D})$ in (25), demonstrate the contribution by N_{3D} (see dashed lines Fig. 9a). The fluctuations, however small, in the linear $\overline{\eta}_{MAX,ST}/H_s$ correspond to the N_{3D}, and the increase on counter currents is due to the wave lengths becoming shorter by the frequency shift, which is in line with the results by Barbariol et al. (2015). The offset

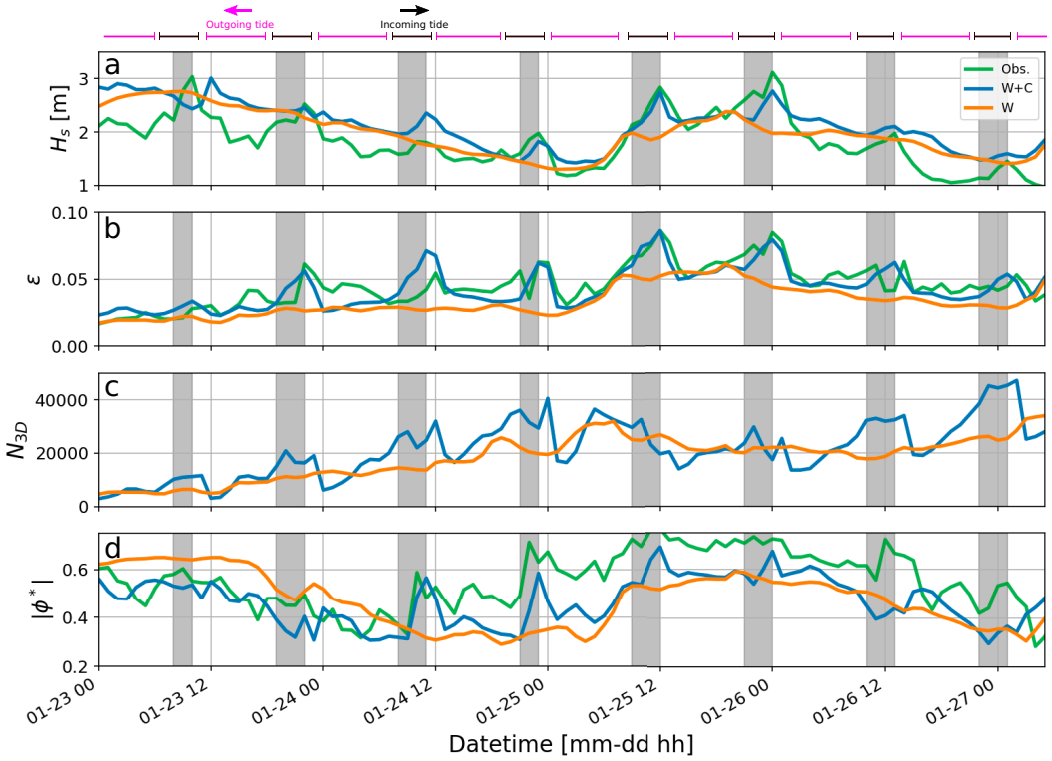

FIG. 7. Temporal evolution in the key integrated spectral parameters (a) H_s, (b) ε, (c) N_{3D}, and (d) $|\phi^*|$ from W+C (blue line), W (orange line), and observations (Obs., green line). Observed sea state parameters are computed from the unidirectional spectrum and averaged over an hour. Black and magenta horizontal lines on top denote the phase of Moskstraumen, and the arrows its approximate east (right) and west (left) direction. Gray vertical bins denote when the current and wind waves were opposing with $\vartheta < -0.5$ [see (4)].

between the linear and nonlinear $\overline{\eta}_{\mathrm{MAX,ST}}/H_s$ (i.e., solid and dashed lines) imply that for an on-average high N_{3D}, $\overline{\eta}_{\mathrm{MAX,ST}}$ is more sensitive to the nonlinear ε contribution than further increasing the number of waves due to currents.

TABLE 2. Intermodel relative differences in integrated spectral variables and normalized expected extreme waves according to (31). The mean, maximum (max) and standard deviation (std) are given columnwise. The relative differences are given in percentage units (%). Values reflect the time periods in Figs. 7 and 9.

	Mean	Max	Std
Integrated variables			
H_s	7.9	44.5	10.0
E	34.5	167.4	36.0
N_{3D}	33.3	141.3	103.0
$\lvert\phi^*\rvert$	1.5	79.2	21.0
Extreme estimates			
$\overline{\eta}_{\mathrm{MAX,ST}}/H_s$	3.1	13.9	3.0
$\overline{H}_{\mathrm{MAX,ST}}/H_s$	0.3	11.7	3.0

Expected extremes over a domain of variable size were also analyzed to further elucidate their sensitivity to ε and $|\phi^*|$. Following Benetazzo et al. (2021a), we define such a domain by forcing $X = L_x$, $Y = L_y$, and $D = 100T_m$. Then, only one wave, on average, is included in the horizontal space domain, and consequently $N_{3D} \approx 100A$. Such a choice also allows to assess the impact by A, ε, and $|\phi^*|$ in different sea states. As mentioned, there was an unsystematic modulation in A during the tidal cycles, and the values were also often similar in W and W+C. Consequently, the tidal modulation was governed by the modulation in ε and $|\phi^*|$. The resulting $\overline{\eta}_{\mathrm{MAX,VS}}/H_s$, with subscript VS for variable size, is given in Fig. 9b. Here the linear $\overline{\eta}_{\mathrm{MAX,VS}}/H_s$ [i.e., $F_\eta(\varepsilon = 0, N_{3D})$ from (25)] were similar for W+C and W (see dashed blue and orange lines). Thus, the intermodel differences in the second order $\overline{\eta}_{\mathrm{MAX,VS}}/H_s$ were governed by ε, now with a correlation of 0.98 in W+C, and consequently the most extreme conditions occurred when the wind sea opposed Moskstraumen.

The $\overline{H}_{\mathrm{MAX,ST}}/H_s$ had less of a systematic tidal modulation during the tidal cycles (Fig. 9c). That is, the extremes from W+C were sometimes lower during opposing wind sea and

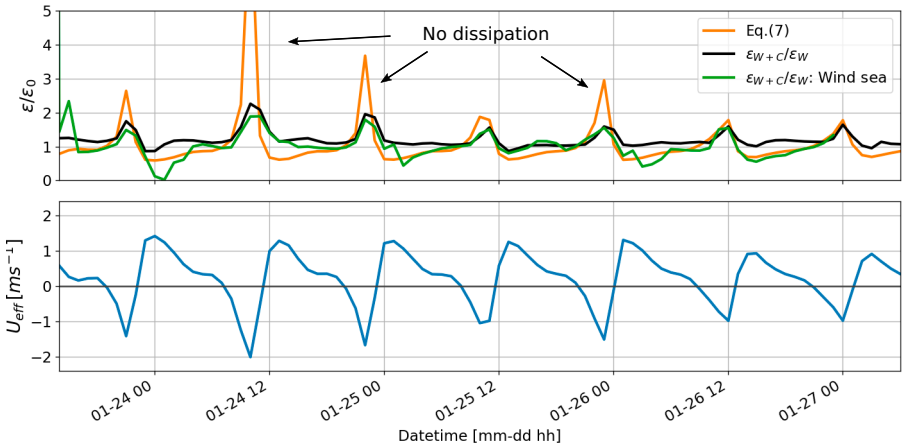

FIG. 8. Comparing $\varepsilon/\varepsilon_0$ from (33) using W+C and W and the simplified wave straining model in (7). (top) The intermodel ratio, i.e., $\varepsilon_{W+C}/\varepsilon_W$ (black line), and the output from (7) (orange line) using k_1 computed from T_{m01} in W. (bottom) U_{eff} from (3). Since the wave spectrum was bimodal (Fig. 6), we also added $\varepsilon_{W+C}/\varepsilon_W$ from the wind sea partition of the spectrum (green line).

currents, and sometimes higher. We find a correlation coefficient with $|\phi^*|$ of 0.74 in W+C, and consequently the modulation in $\overline{H}_{MAX,ST}/H_s$ during the first and two last tidal cycles was due to the similar energy levels on the bimodal components (see Fig. 5). The predictions from the variable size domain, $\overline{H}_{MAX,VS}/H_s$, are shown in Fig. 9d, with values that to a large extent followed the fluctuations in $|\phi^*|$, now with a correlation coefficient of 0.97 for W+C (Fig. 7d).

2) HORIZONTAL VARIABILITY IN EXPECTED EXTREMES

When wind sea opposed Moskstraumen, $\overline{\eta}_{MAX,ST}/H_s$ became most severe at the edges of the broad current (Figs. 10a,b). Here the intermodel ratio reveal a 10%–15% increase in $\overline{\eta}_{MAX,ST}/H_s$ (Fig. 10b). Similar horizontal variability was also found for the other tidal cycles (not shown).

The $\overline{H}_{MAX,ST}/H_s$ became most severe within the region of increased H_s (Figs. 10c,d), with a uniform horizontal distribution. We find an increase in $\overline{H}_{MAX,ST}/H_s$ of about 5%–10% when adding currents as forcing (Fig. 10d). During the two last tidal cycles in the period of interest, the time series analysis showed a decrease in $\overline{H}_{MAX,ST}/H_s$ during maximum opposing wind sea and current (Fig. 9c). In the field view, however, the decrease was confined to the northern part of the current, while further south a similar modulation and shape was obtained (not shown). At the southern part, the remaining wind sea was more dominating compared with farther north, as well as being more sheltered to the swell (not shown).

3) TIME EXTREMES FROM OBSERVATIONS

The single point observations presented here provide limited statistics due to the seldom occurrence of easterly wind situations. Moreover, the observations also include the signal of complex small-scale variability unresolved in the ocean and wave model (Fig. 5). Nevertheless, and despite such limitations, they can be used to consider the trends in the expected extremes during co- and counterflow situations. However, only the temporal extremes, i.e., with $X = Y = 0$, can be compared.

Stochastic time extremes from the ADCP observations were computed following the procedure outlined by Barbariol et al. (2019). That is, each 17-min burst, acquired twice per hour, was split into three equal subsegments, i.e., each with a duration of approximately 5.5 min. In each subsegment, the η_{MAX} and H_{MAX} were computed from a zero crossing analysis, and the $\overline{\eta}_{MAX,T}$ and $\overline{H}_{MAX,T}$ by taking the mean of the three realizations. This is a block maxima approach to assessing the expected maxima. These maxima will be independent and identically distributed under the assumption that the time series is statistically stationary (Coles 2001). Furthermore, values from the two bursts every hour were resampled to an hourly mean value. The expected extremes from W+C and W were computed over the same time interval. Since observations and model predictions were at times out of phase (e.g., Fig. 7), we applied the quantitative *dynamic time warping* method. Here, a distance metric d_{dtw} is computed from a point-to-point matching of indices in a monotonically increasing sequence. Peaks that are out of phase will be matched if they are within a certain window size. Typical applications of the dynamic time warping method is found in automatic speech recognition, where sequences with different speeds can be matched. Lower values of d_{dtw} indicate shorter distances and a better fit.

A comparison between the model and observations is given in Fig. 11. Here, distinct local peaks in skewness occur for at least five out of the eight tidal cycles when the wind sea and current were opposing. The $\overline{\eta}_{MAX,T}$ from W+C mimic the increase from the observations at the M_2 frequency when the wind sea opposed Moskstraumen (Fig. 11b), however often underestimating the magnitude. Note that here $\overline{\eta}_{MAX,T} \propto H_s$,

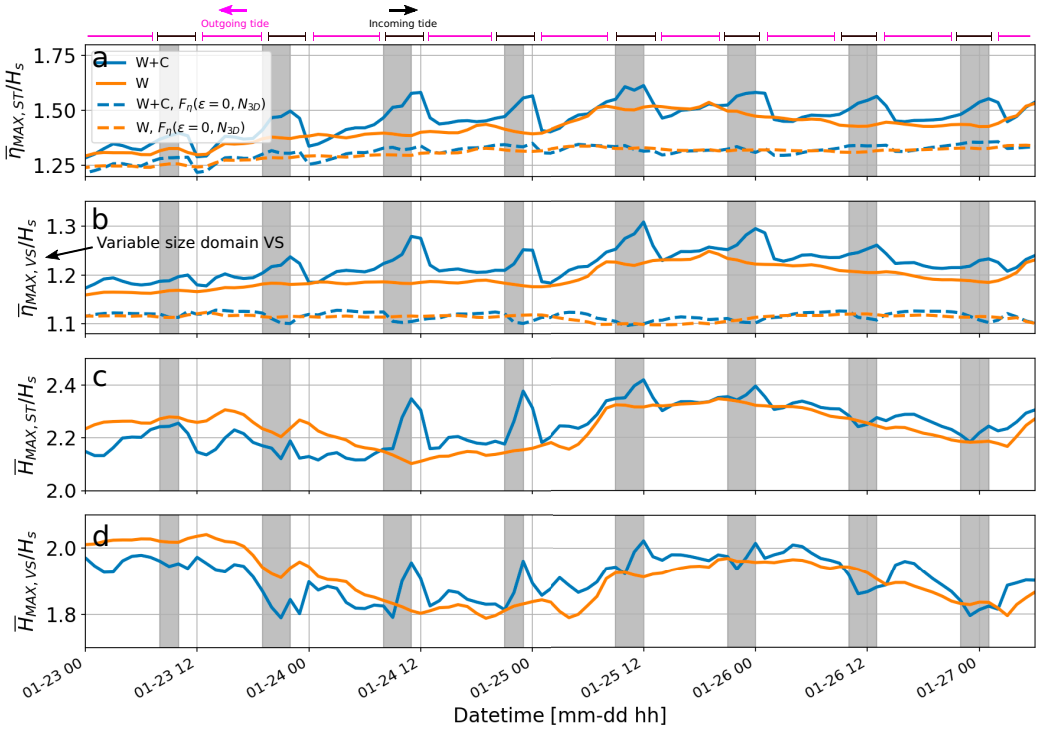

FIG. 9. Temporal evolution in expected extremes computed from the 2D spectra. Panels show (a) $\overline{\eta}_{\mathrm{MAX,ST}}/H_s$ from (23), (b) $\overline{\eta}_{\mathrm{MAX,VS}}/H_s$ using a domain of variable size (subscript VS), i.e., $X = L_x$, $Y = L_y$ and $D = 100T_m$, (c) $\overline{H}_{\mathrm{MAX,ST}}/H_s$ from (24), and (d) $\overline{H}_{\mathrm{MAX,VS}}/H_s$. Dashed lines in (a) and (b) denote the linear versions, i.e., $\overline{\eta}_{\mathrm{MAX,ST}}/H_s = F_\eta(\varepsilon = 0, N_{3\mathrm{D}})$. Labels and layout are similar to that in Fig. 7.

with a correlation of 0.95 and 0.99 for the observations and W+C, respectively. Even though the H_s from W+C and the observations were quite similar (Fig. 5g), the underestimation may be linked to energy being larger on the wind sea components in the observed spectra than the W+C (see the two first tidal cycles in Figs. 5e,f). From the normalized $\overline{\eta}_{\mathrm{MAX},T}/H_s$, there is also an underestimation in the ratio (not shown). Nevertheless, the trend is that the expected maximum wave crests increase when the wind sea opposes Moskstraumen. The observed extremes, according to the common definition of $\eta/H_s > 1.25$ (Dysthe et al. 2008), also occurred for the wind sea on counter currents (see red dots). For $\overline{\eta}_{\mathrm{MAX},T}$: $d_{\mathrm{dtw,W+C}} = 2.96$ and $d_{\mathrm{dtw,W}} = 3.19$.

For $\overline{H}_{\mathrm{MAX},T}$, we find a similar tendency in M_2 modulation between W+C and the observations (Fig. 11c). The $d_{\mathrm{dtw,W+C}} = 3.93$ and $d_{\mathrm{dtw,W}} = 4.52$, implying a better fit for the former. However, the observed extremes, according to the definition of $H/H_s > 2$, occurred when the swell partition opposed Moskstraumen during outgoing tide (see red dots in Fig. 11c). Moreover, the peaks were also here underestimated by the model, and there was no clear M_2 modulation in the normalized $\overline{H}_{\mathrm{MAX},T}/H_s$ (not shown).

c. *Opposing swell and tidal jet during outgoing tide*

The other interesting case of characteristic wave and tidal current occurs when Moskstraumen is flowing westward. The Moskstraumen now takes the form of a narrow jet (Fig. 12a). Since swell conditions often prevail on the offshore side, the spectrum is often unimodal. A summary of the swell (wave age $c_p/U_{10} \simeq 18/7.5 > 1$, where c_p is phase speed) and tidal current conditions during a period in early January 2019 is given in Fig. 12. Unfortunately, no observations were available on the offshore side of the Lofoten archipelago.

The tidal jet clearly modulated the spectrum at the M_2 frequency, which led to a more energetic wave field compared with no current forcing (Figs. 12c,d). Solving the wave ray equations (29) and (30) numerically using the method by Halsne et al. (2023) and the tidal current field and bathymetry as input, the convergence of wave rays suggests that current-induced refraction was the dominating WCI mechanism (Fig. 12b). Moreover, the wave straining mechanism becomes less dominant the longer the waves are (Table 1), and here the peak period was at times 13 s. The wave field became much more energetic during these episodes with

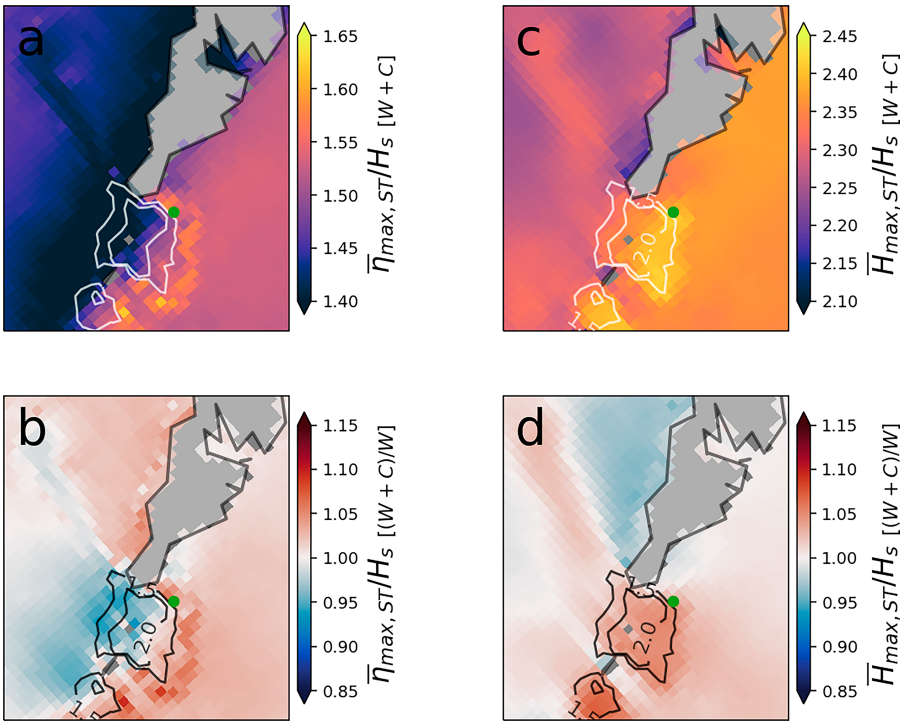

FIG. 10. Horizontal variability in normalized extreme wave crests (a),(b) $\overline{\eta}_{\mathrm{MAX,ST}}/H_s$ and (c),(d) $\overline{H}_{\mathrm{MAX,ST}}/H_s$ during maximum incoming tide. The expected extremes from (top) W+C and (bottom) its ratio with W. Green dots denote the location of the ADCP. Contour lines indicate current speed (m s^{-1}).

swell opposing the tidal jet, with an increase in H_s up to 90% (Fig. 13a). In addition to the increase in energy, the 2D spectrum also underwent significant directional broadening (not shown).

The maximum increase in ε by the tidal jet exceeded the wind-only simulation (W) by a factor 2 (not shown). We observe that the analytical wave straining model (7) is mostly incapable of capturing the modulation in ratio $\varepsilon_{\mathrm{W+C}}/\varepsilon_{\mathrm{W}}$, as seen from the excess in yellow color shading in Fig. 13b. The excess can be understood if we consider ε as in (32) to be the product of wave amplitude and wavenumber only (i.e., skipping the finite bandwidth measure ψ). Then, the convergence of wave energy due to caustics leads to an increase in the wave amplitude part, while the wavenumber is less modulated. These results suggest that different WCI mechanisms may modulate the extreme wave crest statistics differently, due to the aforementioned sensitivity in ε. The ratio $\overline{\eta}_{\mathrm{MAX,VS}}/H_s$ (note variable size VS) changed due to Moskstraumen, particularly under opposing swell and current situations, and the relative difference between W+C and W exceeded 10% (Fig. 13c). Similar changes were found in $\overline{\eta}_{\mathrm{MAX,ST}}/H_s$, but we do not consider the N_{3D} parameter since ε dominates the variability. The correlation between $\overline{\eta}_{\mathrm{MAX,VS}}/H_s$ and ε in W+C was 0.99. Following the reasoning about the impact by refraction on ε, the increase in H_s also constrain the ratio $\overline{\eta}_{\mathrm{MAX,VS}}/H_s$.

For the $\overline{H}_{\mathrm{MAX,VS}}/H_s$, the expected extremes followed the curve of $|\phi^*|$, with a correlation coefficient of 0.98 in W+C (Figs. 13d,e). During counterflow situations when refraction seemed to dominate, one may expect that the sea state would become broader in frequency due to the crossing sea state and nonlinear redistribution of energy across scales (Tamura et al. 2008; Rapizo et al. 2016). This appeared to be the case during certain tidal cycles (see around 5 January 2019 in Fig. 13d), but certainly not for all. However, when the sea state became broader, there was an accompanying decrease in $\overline{H}_{\mathrm{MAX,VS}}/H_s$.

Maximum $\overline{\eta}_{\mathrm{MAX,ST}}/H_s$ were located at the edges of the tidal jet during maximum current speed at outgoing tide, and not within the current jet itself (left column Fig. 14). In the vicinity of the jet, we find a 5%–15% increase in $\overline{\eta}_{\mathrm{MAX,ST}}/H_s$ compared with W (Fig. 14b). The $\overline{H}_{\mathrm{MAX,VS}}/H_s$ was generally higher outside the current jet (Fig. 14c), and decreased around 5% within the area of strong currents (Fig. 14d). Similar horizontal variability was also found for the other tidal cycles (not shown).

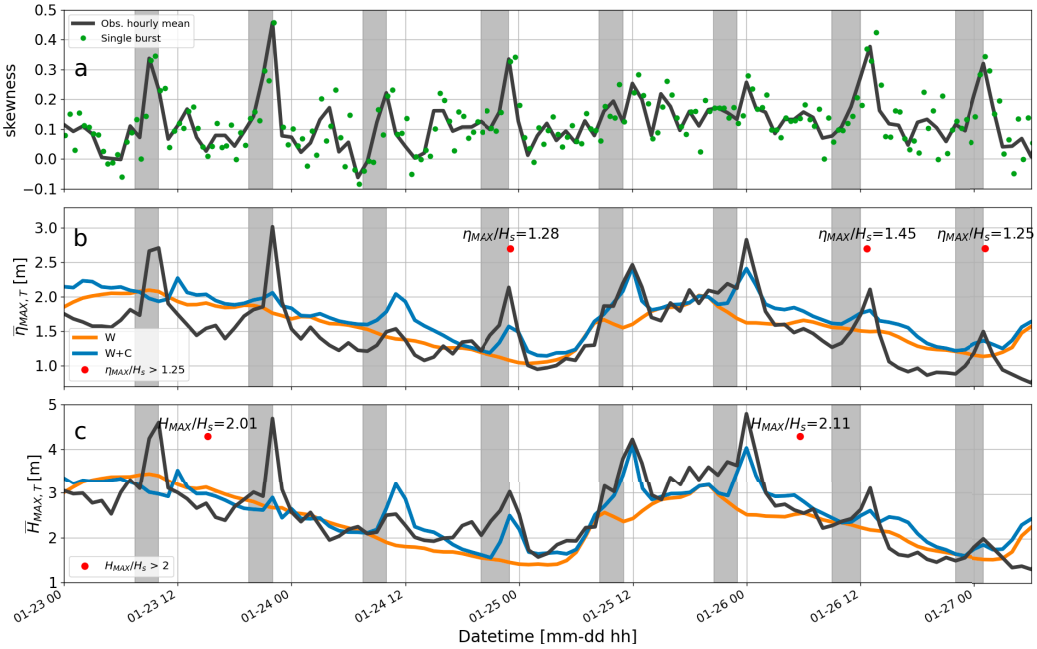

FIG. 11. Comparing time series of expected time extremes from wave model against observations. (a) The skewness computed from the 17-min burst observations (green dots) and the hourly mean (solid black line); the expected maximum wave (b) crests and (c) heights in time (i.e., single point) in its dimensional form from the observations (solid black line), W+C (blue line), and W (orange line). Here, red dots show the cases where extreme events occurred according to the definition.

6. Discussion

a. *Steepness modulation and the impact of Moskstraumen on* $\overline{\eta}_{\mathrm{MAX}}$

We find $\overline{\eta}_{\mathrm{MAX,ST}}$ to be more sensitive to the current-induced modulations in ε than those in $N_{3\mathrm{D}}$ (Figs. 9a,b and 13c). In both the cases considered, the expected extreme crests increased most when the waves were opposing Moskstraumen. Consequently, our results suggest that the simultaneous increase in the components of ε due to wave straining is an important factor in modulating $\overline{\eta}_{\mathrm{MAX,ST}}$ in young, short-crested sea states on horizontally homogeneous tidal currents. Under conditions where refraction is likely to dominate, however, the ratio $\varepsilon_{\mathrm{W+C}}/\varepsilon_{\mathrm{W}}$ suggests that convergence of wave energy due to caustics provide an additional contribution to the steepness modulation (Fig. 13b), which indicates that the current-induced extreme wave modulations are sensitive to the underlying WCI mechanisms.

Interestingly, $\overline{\eta}_{\mathrm{MAX,VS}}/H_s$ reached 1.31 during opposing wind sea and broad current (Fig. 9b) and 1.32 during the opposing swell and tidal jet (Fig. 13c). It seems plausible that the significant increase in H_s in the latter case constrained the ratio $\overline{\eta}_{\mathrm{MAX,VS}}/H_s$. For the space–time extremes, the contribution from $N_{3\mathrm{D}}$ increased $\overline{\eta}_{\mathrm{MAX,VS}}/H_s$ to 1.61 for the former (Fig. 9a) and 1.56 for the latter (not shown). The higher values for the former was due to the on-average shorter wind waves, such that more waves fitted into the space–time domain compared with the latter swell case. Therefore, our findings indicate that under conditions similar to the former, when wave straining is a prominent mechanism, a sea state exposed to more severe extremes can be reached.

The horizontal variability of $\overline{\eta}_{\mathrm{MAX,ST}}/H_s$ corroborate the findings by Hjelmervik and Trulsen (2009), suggesting that extreme waves become more severe at the edges of the current where the horizontal current gradients are strongest and H_s has not reached its maximum value (left panels of Figs. 10 and 14).

In the case where our observations coincided with the region of strong wave–current interaction, we also found a similar trend in the tidal modulation of $\overline{\eta}_{\mathrm{MAX},T}$ from the wave model with current forcing and the observations, contrary to the wave model without current forcing (Fig. 11). Long-term single point observations in extreme environments are very rare in themselves due to the harsh conditions, and the ADCP measurements used here are the first of its kind in Moskstraumen (Saetra et al. 2021). Consequently, observations spanning both space and time under similar conditions are even more rare. Obtaining such measurements requires development and innovation in instrument deployment setups and operating methods.

Summarized, our results show that STE crests are very sensitive to the current-induced modulation in ε, and also suggests that including tidal current forcing in spectral wave models provides more realistic modulation of the expected

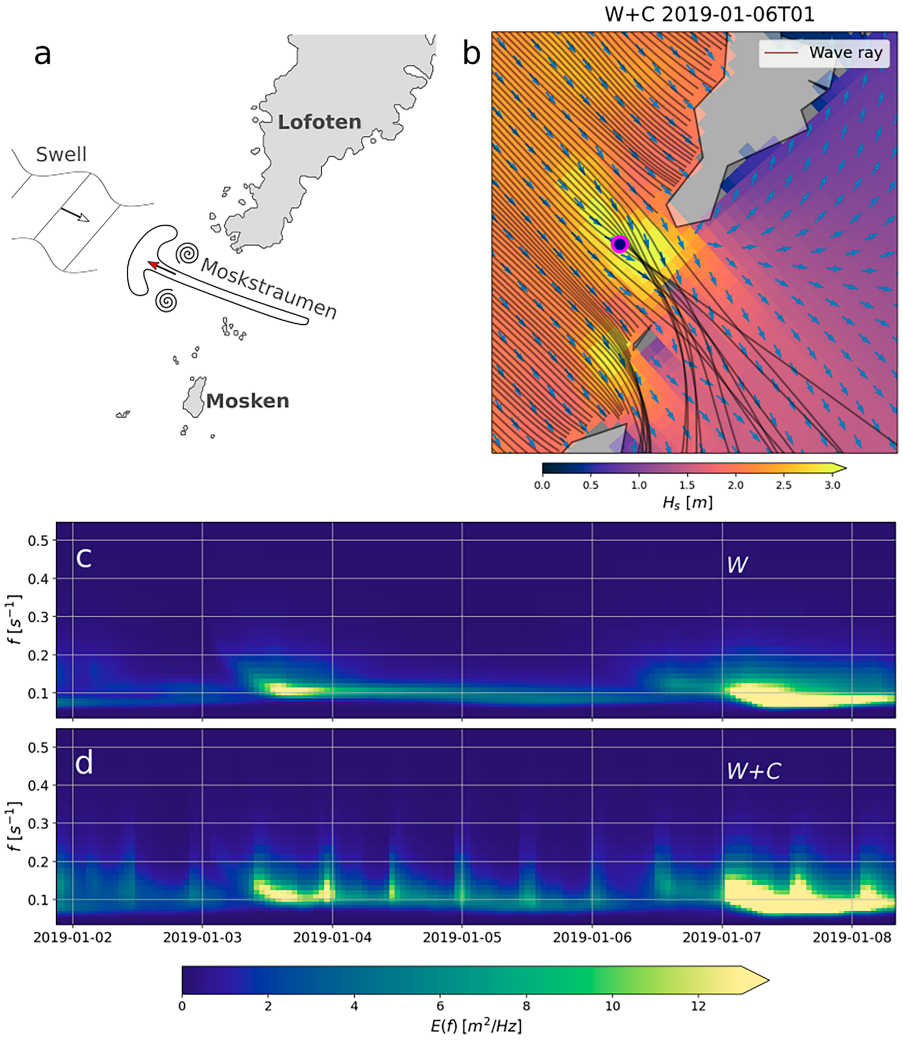

FIG. 12. (a) Summary of the predominant north westerly swell and tidal current conditions on the west side of Lofoten 2–8 Jan 2019. During outgoing tide, Moskstraumen takes the form as a narrow tidal jet, and (b) a snapshot of the swell and tidal jet interaction from W+C is, where blue arrows indicate peak wave direction. Wave rays are computed for a $T = 13$ s period wave. (c),(d) Time series of the unidirectional spectra from W and W+C [taken from the magenta/black dot in (b)] are shown.

maximum wave crests. Consequently, the expected maximum space–time wave crest parameters now available in spectral wave models can be useful in nearshore wave forecasting and in engineering applications like wave load analysis of tidal power facilities and other marine structures.

b. *Narrow-bandedness and* $\overline{H}_{\mathrm{MAX}}$

The modulation in $|\phi^*|$ from the bimodal spectra, and its impact on $\overline{H}_{\mathrm{MAX,ST}}$ was at times difficult to interpret. Here, $|\phi^*|$ was sensitive to the relative variance distribution on the swell and wind sea components in the spectrum, while becoming easier to interpret when the wind sea dominated, i.e., during the intermediate tidal cycles in the period (Figs. 5, 7, and 9). In their deterministic approach, Hjelmervik and Trulsen (2009) found that the amount of freak waves increased on uniform countercurrents for both narrow- and broad-banded sea states. Such an increase is difficult to conclude from our results since the bimodal partitions were at times propagating against each

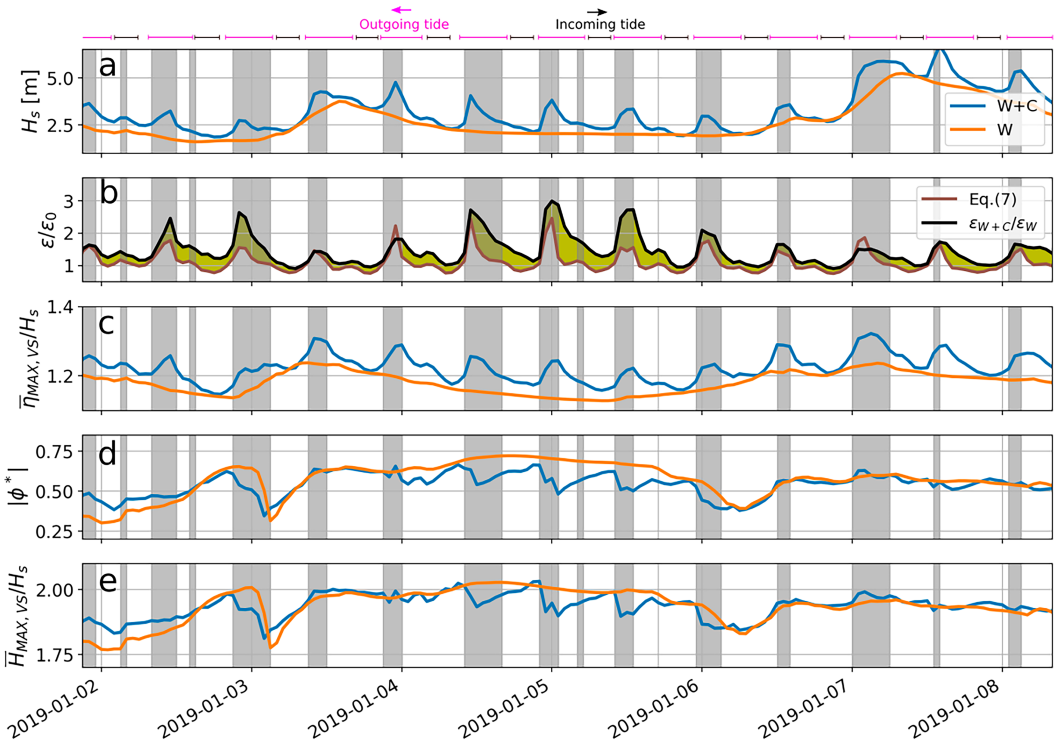

FIG. 13. Time series of key sea state parameters and associated expected extremes over a variable size domain during swell and tidal jet interactions. Panels show (a) H_s, (b) $\varepsilon/\varepsilon_0$ as in Fig. 8 (yellow shading shows the excess of the inter model ratio), (c) $\overline{\eta}_{\mathrm{MAX,VS}}/H_s$, (d) $|\phi^*|$, and (e) $\overline{H}_{\mathrm{MAX,VS}}/H_s$.

other (Fig. 6). However, when the wind sea dominated, we found an increase in $\overline{H}_{\mathrm{MAX,ST}}/H_s$ when it opposed the tidal current (Figs. 9c,d, and 10c,d).

The decrease in $\overline{H}_{\mathrm{MAX,VS}}/H_s$ during the opposing swell and tidal jet is contrary to the results of Ying et al. (2011) (Fig. 13e), which suggested that caustics caused by refraction increased the probability of extremes. Our results corroborate the findings by Hjelmervik and Trulsen (2009), which found it less likely to encounter extreme wave heights in the center of an opposing narrow tidal jet compared with its edges due to the reduction in the kurtosis, even though the wave heights were higher in the center (Figs. 14c,d). However, proper measurements are needed to further evaluate the impact by tidal jets and broad uniform currents on $\overline{H}_{\mathrm{MAX,ST}}/H_s$. Moreover, such studies should also include areas subject to met-ocean conditions that are not present in the Lofoten area, like swell on collinear tidal jets.

7. Conclusions

We have investigated the wave, and extreme wave, modulation by one of the strongest open ocean tidal currents in the world, namely, the Moskstraumen in northern Norway. The study has considered the influence by Mosktraumen under two characteristic met-ocean conditions where (i) a bimodal sea state encountered a broad, uniform countercurrent, and (ii) a swell system encountered an opposing tidal jet. Methods and data include output from a spectral wave model with and without current forcing, accompanied by a simplified quasi-stationary model for wave steepness modulation, and in situ observations. The largest wave modulations occurred when the waves were opposing Moskstraumen, in both cases, where key parameters like the significant wave height H_s and spectral steepness ε increased.

The second-order non-Gaussian contribution through ε in the expected maximum space–time wave crests $\overline{\eta}_{\mathrm{MAX,ST}}$ increased when the wind sea in (i), and the swell in (ii), were opposing Moskstraumen. Consequently, the ratio $\overline{\eta}_{\mathrm{MAX,ST}}/H_s$ also increased, which was more sensitive to ε than the average number of waves within the space–time domain $N_{3\mathrm{D}}$ from Eq. (26). We found a similar trend in tidal modulation when comparing time extremes from model and observations, although the model underestimated the magnitude of the expected extremes. Nevertheless, our results suggest that extreme wave crests in a time and space–time domain become more likely in the

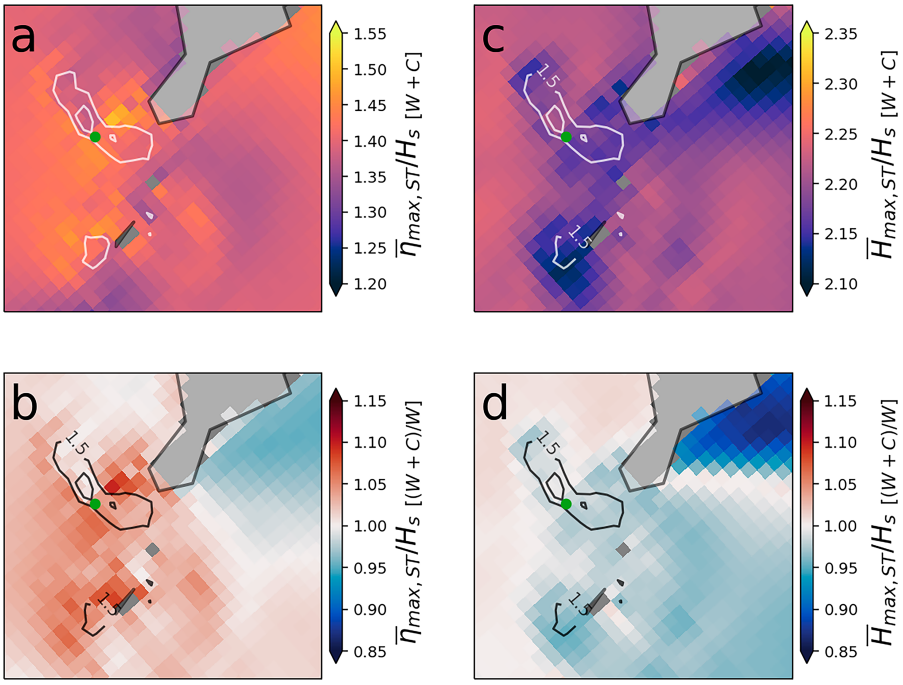

FIG. 14. Horizontal variability in normalized extreme wave crests (a),(b) $\overline{\eta}_{\mathrm{MAX,ST}}/H_s$ and (c),(d) $\overline{H}_{\mathrm{MAX,ST}}/H_s$ during maximum outgoing tide at 0100 UTC 6 January 2019. The expected extremes from (top) W+C and (bottom) its ratio with W. Green dots denote the location of the time series data at the offshore location. Innermost contour lines indicate current speed at 2 m s^{-1}.

presence of a strong opposing tidal current, and that using tidal current forcing in wave models improves their estimates.

Current-induced modulations in the expected space–time wave heights $\overline{H}_{\mathrm{MAX,ST}}$ corresponded strongly to the value of the narrow-bandedness parameter $|\phi^*|$ during both (i) and (ii). The intermodel differences were very sensitive to the relative distribution of the variance density on the wind sea and swell components during (i). When the wind sea dominated, $\overline{H}_{\mathrm{MAX,ST}}/H_s$ increased when the waves opposed the tidal current, but vice versa when the wind sea and swell components had similar variance density. During (ii), $\overline{H}_{\mathrm{MAX,ST}}/H_s$ often decreased when the swell encountered the opposing tidal jet. Thus, our results suggest that the impact of strong tidal currents on the spectral shape is key for the accompanied modulation in $\overline{H}_{\mathrm{MAX,ST}}/H_s$.

Our findings indicate that current-induced modulations in expected extremes are sensitive to the underlying WCI mechanism. For instance, wave straining will increase ε and $N_{3\mathrm{D}}$ for short waves encountering a broad countercurrent, i.e., similar to the conditions in (i), and a strong increase in ε and H_s are found during (ii), where refraction seemingly dominates. For the latter, however, the increase in H_s constrains the ratios $\overline{\eta}_{\mathrm{MAX}}/H_s$ and $\overline{H}_{\mathrm{MAX}}/H_s$, and our results suggests that more severe extremes can be expected when wave straining dominate. However, more work is required to further understand the role of tidal currents on extreme waves. Such work should in particular involve more extensive measurement campaigns with simultaneous spatial sampling over longer time periods, and should also include areas where other combinations of characteristic tidal current flow fields and wave conditions occur.

Acknowledgments. This research was partly funded by the Research Council of Norway through the project MATNOC (Grant 308796). TH and ØB are grateful for additional support from the Research Council of Norway through the StormRisk project (Grant 300608). AB and FB acknowledge the contribution from the Korea Institute of Ocean Science and Technology in the context of the project ASTROWAVES.

Data availability statement. The ROMS model data are available from https://thredds.met.no/thredds/dodsC/sea/norkyst800m/1h/aggregate_be. WAM and ADCP data are available from the Norwegian Meteorological Institute upon request.

APPENDIX

Transformation from Absolute to Intrinsic Frequencies

Since the wave variance density is conserved, the transformation from an absolute to an intrinsic wave spectrum involves solving the Jacobian. For a 2D wave spectrum, the wavenumber vector $\mathbf{k} = (k_x, k_y)$ and the velocity vector $\mathbf{U} = (u, v)$ must be considered. The wavenumber $k = |\mathbf{k}|$, and the angle between k_x and k_y is θ_w. The Jacobian $\partial\omega/\partial\sigma$ becomes

$$\frac{\partial\sigma + \mathbf{k}\cdot\mathbf{U}}{\partial\sigma} = 1 + u\frac{\partial k_x}{\partial\sigma} + v\frac{\partial k_y}{\partial\sigma}. \tag{A1}$$

Inserting for the wavenumber components, we get

$$1 + u\frac{\partial k\cos(\theta_w)}{\partial\sigma} + v\frac{\partial k\sin(\theta_w)}{\partial\sigma} = 1 + \frac{u\cos(\theta_w)}{c_g} + \frac{v\sin(\theta_w)}{c_g}. \tag{A2}$$

Using trigonometry, $[\cos(\theta_w), \sin(\theta_w)] = \mathbf{k}/k$ (i.e., the adjacent and opposite divided by the hypotenuse, respectively), we write

$$\frac{\partial\omega}{\partial\sigma} = 1 + \frac{1}{c_g}[u\cos(\theta_w) + v\sin(\theta_w)] = 1 + \frac{\mathbf{k}\cdot\mathbf{U}}{kc_g}. \tag{A3}$$

The result is the same as that obtained in the WW3 user manual [see p. 14 in version 7.00 of The WAVEWATCH III Development Group (2019)], which also applies for the Jacobian $\partial f_a/\partial f_i$ since

$$E_i(f_i, \theta_w) = 2\pi E_i(\sigma, \theta_w) = 2\pi\left(1 + \frac{\mathbf{k}\cdot\mathbf{U}}{kc_g}\right)E_a(\omega, \theta_w)$$
$$= \left(1 + \frac{\mathbf{k}\cdot\mathbf{U}}{kc_g}\right)E_a(f_a, \theta_w). \tag{A4}$$

To compute the Jacobian using the spectra from WAM, $\mathbf{k}$, $\mathbf{u}$, k, and c_g must be computed for every direction $\theta_{w,j}$ in the discrete spectrum. The group velocity is defined

$$c_g = \frac{\partial\omega}{\partial k} = n\frac{\sigma}{k}, \tag{A5}$$

where $n = 0.5 + [kd/\sinh(2kd)]$. Furthermore, the directionality for all discrete $\mathbf{k}$ vectors must be considered such that $\mathbf{k}_j = \mathbf{k}_j(\theta_w)$. Once the Jacobian is computed, the variance density for each frequency for each must be remapped from the absolute to intrinsic frequencies from the Doppler shift equation (1). The remapping was performed by using linear interpolation.

REFERENCES

Adler, R. J., and J. E. Taylor, 2007: Excursion probabilities for smooth fields. *Random Fields and Geometry*, Springer Monographs in Mathematics, Vol. 115, Springer, 349–386, https://doi.org/10.1007/978-0-387-48116-6_14.

Ardhuin, F., and Coauthors, 2012: Numerical wave modeling in conditions with strong currents: Dissipation, refraction, and relative wind. *J. Phys. Oceanogr.*, **42**, 2101–2120, https://doi.org/10.1175/JPO-D-11-0220.1.

——, S. T. Gille, D. Menemenlis, C. B. Rocha, N. Rascle, B. Chapron, J. Gula, and J. Molemaker, 2017: Small-scale open ocean currents have large effects on wind wave heights. *J. Geophys. Res. Oceans*, **122**, 4500–4517, https://doi.org/10.1002/2016JC012413.

Barbariol, F., A. Benetazzo, S. Carniel, and M. Sclavo, 2015: Space–time wave extremes: The role of metocean forcings. *J. Phys. Oceanogr.*, **45**, 1897–1916, https://doi.org/10.1175/JPO-D-14-0232.1.

——, and Coauthors, 2017: Numerical modeling of space-time wave extremes using WAVEWATCH III. *Ocean Dyn.*, **67**, 535–549, https://doi.org/10.1007/s10236-016-1025-0.

——, J.-R. Bidlot, L. Cavaleri, M. Sclavo, J. Thomson, and A. Benetazzo, 2019: Maximum wave heights from global model reanalysis. *Prog. Oceanogr.*, **175**, 139–160, https://doi.org/10.1016/j.pocean.2019.03.009.

Baschek, B., 2005: Wave-current interaction in tidal fronts. *Rogue Waves: Proc. 14th 'Aha Huliko'a Hawaiian Winter Workshop*, Honolulu, HI, University of Hawai'i at Mānoa, 131–138, http://www.soest.hawaii.edu/PubServices/2005pdfs/Baschek.pdf.

Baxevani, A., and I. Rychlik, 2006: Maxima for Gaussian seas. *Ocean Eng.*, **33**, 895–911, https://doi.org/10.1016/j.oceaneng.2005.06.006.

Benetazzo, A., F. Barbariol, F. Bergamasco, A. Torsello, S. Carniel, and M. Sclavo, 2015: Observation of extreme sea waves in a space–time ensemble. *J. Phys. Oceanogr.*, **45**, 2261–2275, https://doi.org/10.1175/JPO-D-15-0017.1.

——, B. Francesco, B. Filippo, C. Sandro, and S. Mauro, 2017: Space-time extreme wind waves: Analysis and prediction of shape and height. *Ocean Modell.*, **113**, 201–216, https://doi.org/10.1016/j.ocemod.2017.03.010.

——, F. Barbariol, F. Bergamasco, L. Bertotti, J. Yoo, J.-S. Shim, and L. Cavaleri, 2021a: On the extreme value statistics of spatio-temporal maximum sea waves under cyclone winds. *Prog. Oceanogr.*, **197**, 102642, https://doi.org/10.1016/j.pocean.2021.102642.

——, and Coauthors, 2021b: Towards a unified framework for extreme sea waves from spectral models: Rationale and applications. *Ocean Eng.*, **219**, 108263, https://doi.org/10.1016/j.oceaneng.2020.108263.

Boccotti, P., 2000: *Wave Mechanics for Ocean Engineering*. Elsevier Oceanography Series, Vol. 64, Elsevier, 520 pp., https://doi.org/10.1016/S0422-9894(00)80024-0.

Børve, E., P. E. Isachsen, and O. A. Nøst, 2021: Rectified tidal transport in Lofoten-Vesterålen, northern Norway. *Ocean Sci.*, **17**, 1753–1773, https://doi.org/10.5194/os-2021-41.

Bretherton, F. P., and C. J. R. Garrett, 1968: Wavetrains in inhomogeneous moving media. *Proc. Roy. Soc. London*, **302A**, 529–554, https://doi.org/10.1098/rspa.1968.0034.

Chawla, A., and J. T. Kirby, 2002: Monochromatic and random wave breaking at blocking points. *J. Geophys. Res.*, **107**, 3067, https://doi.org/10.1029/2001JC001042.

Coles, S., 2001: *An Introduction to Statistical Modeling of Extreme Values*. Springer Series in Statistics, Vol. 208, Springer, 225 pp.

Dysthe, K. B., 2001: Refraction of gravity waves by weak current gradients. *J. Fluid Mech.*, **442**, 157–159, https://doi.org/10.1017/S0022112001005237.

Dysthe, K., H. E. Krogstad, and P. Müller, 2008: Oceanic rogue waves. *Annu. Rev. Fluid Mech.*, **40**, 287–310, https://doi.org/10.1146/annurev.fluid.40.111406.102203.

Fedele, F., 2012: Space–time extremes in short-crested storm seas. *J. Phys. Oceanogr.*, **42**, 1601–1615, https://doi.org/10.1175/JPO-D-11-0179.1.

——, and M. A. Tayfun, 2009: On nonlinear wave groups and crest statistics. *J. Fluid Mech.*, **620**, 221–239, https://doi.org/10.1017/S0022112008004424.

——, A. Benetazzo, and G. Z. Forristall, 2011: Space-time waves and spectra in the Northern Adriatic Sea via a wave acquisition stereo system. *Structures, Safety and Reliability*, Vol. 2, *30th International Conference on Ocean, Offshore and Arctic Engineering*, American Society of Mechanical Engineers, 651–663, https://doi.org/10.1115/OMAE2011-49924.

——, ——, G. Gallego, P.-C. Shih, A. Yezzi, F. Barbariol, and F. Ardhuin, 2013: Space–time measurements of oceanic sea states. *Ocean Modell.*, **70**, 103–115, https://doi.org/10.1016/j.ocemod.2013.01.001.

——, C. Lugni, and A. Chawla, 2017: The sinking of the El Faro: Predicting real world rogue waves during Hurricane Joaquin. *Sci. Rep.*, **7**, 11188, https://doi.org/10.1038/s41598-017-11505-5.

Forristall, G. Z., 2007: Wave crest heights and deck damage in Hurricanes Ivan, Katrina, and Rita. *OTC Offshore Technology Conf. 2007*, Houston, TX, OnePetro, OTC-18620-MS, https://doi.org/10.4043/18620-MS.

——, 2008: Maximum crest heights over an area and the air gap problem. *Safety and Reliability; Materials Technology; Douglas Faulkner Symposium on Reliability and Ultimate Strength of Marine Structures*, Vol. 3, *25th International Conference on Offshore Mechanics and Arctic Engineering*, American Society of Mechanical Engineers, 11–15, https://doi.org/10.1115/OMAE2006-92022.

Gjevik, B., H. Moe, and A. Ommundsen, 1997: Sources of the Maelstrom. *Nature*, **388**, 837–838, https://doi.org/10.1038/42159.

Guillou, N., 2017: Modelling effects of tidal currents on waves at a tidal stream energy site. *Renewable Energy*, **114**, 180–190, https://doi.org/10.1016/j.renene.2016.12.031.

Gumbel, E. J., 1958: *Statistics of Extremes*. Columbia University Press, 378 pp., https://doi.org/10.7312/gumb92958.

Halsne, T., P. Bohlinger, K. H. Christensen, A. Carrasco, and Ø. Breivik, 2022: Resolving regions known for intense wave–current interaction using spectral wave models: A case study in the energetic flow fields of northern Norway. *Ocean Modell.*, **176**, 102071, https://doi.org/10.1016/j.ocemod.2022.102071.

——, K. H. Christensen, G. Hope, and Ø. Breivik, 2023: Ocean wave tracing v.1: A numerical solver of the wave ray equations for ocean waves on variable currents at arbitrary depths. *Geosci. Model Dev.*, **16**, 6515–6530, https://doi.org/10.5194/gmd-16-6515-2023.

Hjelmervik, K. B., and K. Trulsen, 2009: Freak wave statistics on collinear currents. *J. Fluid Mech.*, **637**, 267–284, https://doi.org/10.1017/S0022112009990607.

Ho, A., S. Merrifield, and N. Pizzo, 2023: Wave–tide interaction for a strongly modulated wave field. *J. Phys. Oceanogr.*, **53**, 915–927, https://doi.org/10.1175/JPO-D-22-0166.1.

Holthuijsen, L. H., 2007: *Waves in Oceanic and Coastal Waters*. Cambridge University Press, 405 pp., https://doi.org/10.1017/CBO9780511618536.

——, and H. L. Tolman, 1991: Effects of the Gulf Stream on ocean waves. *J. Geophys. Res.*, **96**, 12 755–12 771, https://doi.org/10.1029/91JC00901.

Kenyon, K. E., 1971: Wave refraction in ocean currents. *Deep-Sea Res. Oceanogr. Abstr.*, **18**, 1023–1034, https://doi.org/10.1016/0011-7471(71)90006-4.

Komen, G. J., L. Cavaleri, M. Donelan, K. Hasselmann, S. Hasselmann, and P. A. E. M. Janssen, 1994: *Dynamics and Modelling of Ocean Waves*. Cambridge University Press, 339 pp., https://doi.org/10.1017/CBO9780511628955.

Krogstad, H. E., J. Liu, H. Socquet-Juglard, K. B. Dysthe, and K. Trulsen, 2008: Spatial extreme value analysis of nonlinear simulations of random surface waves. *23rd Int. Conf. on Offshore Mechanics and Arctic Engineering*, Vol. 2, American Society of Mechanical Engineers, 285–295, https://doi.org/10.1115/OMAE2004-51336.

Lavrenov, I. V., 1998: The wave energy concentration at the Agulhas Current off South Africa. *Nat. Hazards*, **17**, 117–127, https://doi.org/10.1023/A:1007978326982.

Longuet-Higgins, M. S., 1957: The statistical analysis of a random, moving surface. *Philos. Trans. Roy. Soc. London*, **A249**, 321–387, https://doi.org/10.1098/rsta.1957.0002.

——, 1975: On the joint distribution of the periods and amplitudes of sea waves. *J. Geophys. Res.*, **80**, 2688–2694, https://doi.org/10.1029/JC080i018p02688.

——, and R. w. Stewart, 1964: Radiation stresses in water waves; a physical discussion, with applications. *Deep-Sea Res. Oceanogr. Abstr.*, **11**, 529–562, https://doi.org/10.1016/0011-7471(64)90001-4.

Masson, D., 1996: A case study of wave–current interaction in a strong tidal current. *J. Phys. Oceanogr.*, **26**, 359–372, https://doi.org/10.1175/1520-0485(1996)026<0359:ACSOWI>2.0.CO;2.

Moe, H., A. Ommundsen, and B. Gjevik, 2002: A high resolution tidal model for the area around the Lofoten Islands, northern Norway. *Cont. Shelf Res.*, **22**, 485–504, https://doi.org/10.1016/S0278-4343(01)00078-4.

Müller, M., Y. Batrak, J. Kristiansen, M. A. Ø. Køltzow, G. Noer, and A. Korosov, 2017: Characteristics of a convective-scale weather forecasting system for the European Arctic. *Mon. Wea. Rev.*, **145**, 4771–4787, https://doi.org/10.1175/MWR-D-17-0194.1.

Onorato, M., D. Proment, and A. Toffoli, 2011: Triggering rogue waves in opposing currents. *Phys. Rev. Lett.*, **107**, 184502, https://doi.org/10.1103/PhysRevLett.107.184502.

Peregrine, D. H., 1976: Interaction of water waves and currents. *Advances in Applied Mechanics*, Vol. 16, C.-S. Yih, Ed., Elsevier, 9–117, https://doi.org/10.1016/S0065-2156(08)70087-5.

Phillips, O. M., 1977: *The Dynamics of the Upper Ocean*. 2nd ed. Cambridge University Press, 336 pp.

Rapizo, H., T. Waseda, A. V. Babanin, and A. Toffoli, 2016: Laboratory experiments on the effects of a variable current field on the spectral geometry of water waves. *J. Phys. Oceanogr.*, **46**, 2695–2717, https://doi.org/10.1175/JPO-D-16-0011.1.

——, A. V. Babanin, D. Provis, and W. E. Rogers, 2017: Current-induced dissipation in spectral wave models. *J. Geophys. Res. Oceans*, **122**, 2205–2225, https://doi.org/10.1002/2016JC012367.

Saetra, Ø., T. Halsne, A. Carrasco, Ø. Breivik, T. Pedersen, and K. H. Christensen, 2021: Intense interactions between ocean waves and currents observed in the Lofoten Maelstrom. *J. Phys. Oceanogr.*, **51**, 3461–3476, https://doi.org/10.1175/JPO-D-20-0290.1.

Shchepetkin, A. F., and J. C. McWilliams, 2005: The Regional Oceanic Modeling System (ROMS): A split-explicit, free-surface, topography-following-coordinate oceanic model. *Ocean Modell.*, **9**, 347–404, https://doi.org/10.1016/j.ocemod.2004.08.002.

Tamura, H., T. Waseda, Y. Miyazawa, and K. Komatsu, 2008: Current-induced modulation of the ocean wave spectrum and the role of nonlinear energy transfer. *J. Phys. Oceanogr.*, **38**, 2662–2684, https://doi.org/10.1175/2008JPO4000.1.

Tayfun, M. A., 1980: Narrow-band nonlinear sea waves. *J. Geophys. Res.*, **85**, 1548–1552, https://doi.org/10.1029/JC085iC03p01548.

The WAVEWATCH III Development Group, 2019: User manual and system documentation of WAVEWATCH III R version 6.07. NOAA/NWS/NCEP/MMAB Tech. Note 333, 465 pp., https://raw.githubusercontent.com/wiki/NOAA-EMC/WW3/files/manual.pdf.

Toffoli, A., and Coauthors, 2011: Occurrence of extreme waves in three-dimensional mechanically generated wave fields propagating over an oblique current. *Nat. Hazards Earth Syst. Sci.*, **11**, 895–903, https://doi.org/10.5194/nhess-11-895-2011.

Tolman, H. L., 1990: The influence of unsteady depths and currents of tides on wind-wave propagation in shelf seas. *J. Phys. Oceanogr.*, **20**, 1166–1174, https://doi.org/10.1175/1520-0485(1990)020<1166:TIOUDA>2.0.CO;2.

Vincent, C. E., 1979: The interaction of wind-generated sea waves with tidal currents. *J. Phys. Oceanogr.*, **9**, 748–755, https://doi.org/10.1175/1520-0485(1979)009<0748:TIOWGS>2.0.CO;2.

Wang, P., and J. Sheng, 2018: Tidal modulation of surface gravity waves in the Gulf of Maine. *J. Phys. Oceanogr.*, **48**, 2305–2323, https://doi.org/10.1175/JPO-D-17-0250.1.

White, B. S., and B. Fornberg, 1998: On the chance of freak waves at sea. *J. Fluid Mech.*, **355**, 113–138, https://doi.org/10.1017/S0022112097007751.

Ying, L. H., Z. Zhuang, E. J. Heller, and L. Kaplan, 2011: Linear and nonlinear rogue wave statistics in the presence of random currents. *Nonlinearity*, **24**, R67, https://doi.org/10.1088/0951-7715/24/11/R01.

Zippel, S., and J. Thomson, 2017: Surface wave breaking over sheared currents: Observations from the mouth of the Columbia River. *J. Geophys. Res. Oceans*, **122**, 3311–3328, https://doi.org/10.1002/2016JC012498.

A Wave models with current forcing: Parametrizations and numerics

In this thesis, ambient currents have only been considered as forcing fields of wave kinematics in the spectral wave models. Two remaining aspects, namely the numerics and physical parametrizations, will be presented briefly here, starting with the former.

A.1 Numerical constraints

In order to resolve currents in wave modeling, sufficient internal resolution is needed to properly propagate and distribute the variance within the model domain. At scales below 30 km, *Marechal and Ardhuin* (2021) found that the number of directional bins should be at least 48 in order to properly resolve current-induced refraction. *Rapizo et al.* (2018) present an interesting discussion on the horizontal resolution in current forcing fields, and how representative such fields are in terms of submesoscale scatterers. They conclude that typical resolutions of global reanalysis products are too coarse, and as a consequence cannot realistically refract waves. In contrast, they claim that in model simulations including coarse resolution current forcing (i.e., above 0.5 degree resolution), effects like the relative wind (to be introduced below) are more appropriately represented.

A.2 Model parametrizations in the presence of currents

In the action balance equation (2.17), the wave kinematics appear from the governing equations while the dynamics, in the form of source terms, represent physical processes that are parameterized. The understanding, and thus parameter description, of these processes has evolved rapidly during the last decades—particularly the S_{in} and S_{ds} (e.g., *Ardhuin et al.*, 2010; *Babanin et al.*, 2010; *Rogers et al.*, 2012). Due to the focus of this thesis, I only give a brief summary of the influence by currents on the source terms on the right-hand-side of (2.17).

A.2.1 Wave generation by wind

Wind–waves are fed by the momentum transfer from the surface wind $\mathbf{U}_{10}$. Although many parametrizations exists, recent models usually consider $S_{\text{in}} \propto \mathbf{U}_{10}^2$ (*Holthuijsen*, 2007, ch. 6.4.3). However, the ambient current affects the wind stress such that the *relative* wind can be written

$$\mathbf{U}_{10,\text{r}} = \mathbf{U}_{10} + \alpha\mathbf{U}, \tag{A.1}$$

where $\alpha \in [0, 1]$. *Hersbach and Bidlot* (2008) suggested it be most realistic to choose $\alpha < 1$, since $\alpha = 1$ it will not take into account the adjustment of the atmosphere to the ocean currents. A simplified analysis on the impact by the relative wind on H_{s} can be done by considering $H_{\text{s}} \propto \mathbf{U}_{10}^2/\text{g}$ and $\gamma = |\mathbf{U}|/|\mathbf{U}_{10}| \ll 1$ (*Gemmrich and Garrett*, 2012). Then, by considering $\Delta H_{\text{s}} = H_{\text{s}} - H_{\text{s,r}}$ we obtain

$$\frac{\Delta H_{\text{s}}}{H_{\text{s}}} = \frac{2\alpha\mathbf{U}}{\mathbf{U}_{10}} + \mathcal{O}(\gamma^2). \tag{A.2}$$

If we only consider one direction with $U_{10} = 12$ m s^{-1} and $u = 0.7$ m s^{-1}, (A.2) contributes 12% and 6% for $\alpha = 1$ and 0.5, respectively. *Rapizo et al.* (2018) recently reported the relative wind effect to reduce the positive wave height bias in the Southern Ocean. On shorter scales, *Guimarães et al.* (2022) found that it was difficult to validate the effect on short wind wave growth because of errors within the wind forcing fields. Furthermore, *Romero et al.* (2020) demonstrated that the horizontal variability due to the relative wind was much lower compared with the contribution from the wave kinematics. Moreover, *Ardhuin et al.* (2012) used $\alpha = 1$ and found the relative wind to give a 25 % increase in H_s—which (according to the authors) is an overestimation of the true effect. In summary: The relative wind matters, but its impact is expected to be less than those of wave kinematics. Moreover, it is difficult to properly quantify the magnitude of the effect.

A.2.2 Nonlinear wave-wave interaction

The nonlinear wave–wave interaction is a conservative term; it is responsible for reshuffling wave energy within the wave spectrum. Currents are therefore not represented directly within the S_{nl} term. Nevertheless, the redistribution of energy within the spectrum becomes increasingly active when currents are included; this was recently reported in the idealized numerical studies by *Tamura et al.* (2008) and in the laboratory experiments by *Rapizo et al.* (2016). That is, currents may not cause large changes in lower order spectral moments *locally*. However, they may cause substantial "internal" shifts within the spectrum. Therefore, there is a push in the community to replace the traditional *discrete interaction approximation* (*Hasselmann and Hasselmann*, 1985)—which heavily reduces the computational time compared with the exact S_{nl} solution—with more accurate approximations. It is expected that such an effort will provide more realistic spectra in the presence of currents.

A.2.3 Wave dissipation: Wave breaking

Waves breaking is the most important dissipative process in the wave action balance equation. The bottom friction process is also affected by tidal currents (e.g., *Guillou et al.*, 2016). However, since it is a less dominant dissipative process than white capping, it is not considered in more detail here.

Wave breaking is a nonlinear process related to the wave steepness (e.g., *Zippel and Thomson*, 2015). Recent wave dissipation parametrizations are therefore functions of wave steepness, which can be computed from the directional spectrum. However, the steepness formulations vary between the parametrizations. In relation to currents, this was discussed in detail by *Ardhuin et al.* (2012). In essence, since shorter waves steepen more than longer waves according to (2.18), the choice of parametrization, including the steepness formulation, affect the wave breaking statistics. Moreover, in the perspective of the spectrum, it is not intuitive what is a representative wave steepness for multimodal sea states (*Støle-Hentschel et al.*, 2020). Therefore, *Davison et al.* (2022) recently proposed a new bulk steepness formulation in crossing sea states.

Ambient currents influence the wave breaking intensity. Conceptually, the work by *Phillips* (1984) argues that the current-induced steepness modulation is more local than that of H_s, since the high frequency part of the spectrum saturates first for a given current speed. In the so-called Λ-distribution, first proposed by *Phillips* (1985), the white cap coverage is the 2nd order moment of the probability density function, and

consequently sensitive to currents following the reasoning above (*Romero*, 2019; *Romero et al.*, 2020). Based on the sensitivity to currents, *Rapizo et al.* (2017) proposed to add another breaking term to the so-called "ST4" physics (*Rogers et al.*, 2012) based on the wave straining mechanism (2.18). They argued that the current-induced wave steepening needed to be accounted for in the wave breaking dissipation, and found better agreement with observations in a tidal current when compared with other traditional parametrizations. Similar reports have been given by *Chawla and Kirby* (2002), *Ris and Holthuijsen* (1996), and *Westhuysen* (2012), who also proposed new bulk wave breaking formulations. *Davidson et al.* (2008) proposed a conceptual model for tidal damping only considering parallel currents and waves to justify the *tidal push* observed by recreational surfers that waves become larger on shoreward propagating tidal waves, i.e., increasing the mean sea level.

B Steady waves and currents: An order of magnitude analysis

Inspired by *Ardhuin* (2020), I provide an order of magnitude analysis on the effect by steady currents on deep water waves. However, instead of considering the change in σ, this treatment is more in line with the work by *Phillips* (1977). Consider waves propagating parallel to the x–axis. For a steady current in deep water, the kinematic condition (i.e., conservation of number of wave crests, see Eq. 2.6.2 in *Phillips*, 1977) allows us to write the Doppler shift equation (2.12)

$$\omega = \sigma + \kappa u = \text{const.} = \omega_0. \tag{B.1}$$

I use the same notation as in Section 2.3.1, with subscript 0 belonging to the area with $u = 0$ and no subscript belongs to the area where $u = u(x) \neq 0$. From the dispersion relation $\omega_0 = \sqrt{g\,\kappa_0}$, if $u = 0$. We rearrange (B.1) by using $c = \sigma/\kappa$ such that

$$\kappa(u + c) = \kappa_0 c_0. \tag{B.2}$$

Since $c = \sqrt{g/\kappa}$ and $c_0 = \sqrt{g/\kappa_0}$, we can insert and rearrange Eq. (B.2);

$$\frac{c^2}{c_0^2} = \frac{\kappa_0}{\kappa} = \frac{c}{c_0} + \frac{u}{c_0}. \tag{B.3}$$

This can be rewritten as a second-order equation in c;

$$c^2 - cc_0 - c_0 u = 0, \tag{B.4}$$

with solutions

$$c = \frac{c_0}{2}\left(1 \pm \sqrt{1 + 4u/c_0}\right). \tag{B.5}$$

The positive solution is the correct one, since $c = c_0$ for $u = 0$. Now, I rewrite (B.5) using the relative current–wave ratio (now normalized by the phase speed) $\delta_{\mathrm{r,c}} = u/c_0$ as

$$c = \frac{c_0}{2}\left(1 + \sqrt{1 + 4\delta_{\mathrm{r,c}}}\right). \tag{B.6}$$

Wave blocking occurs if $\delta_{\mathrm{r,c}} \leq -0.25$; then u exceeds $-c_0/4$ and

$$\frac{u}{c} = u\frac{2}{c_0} = (-\frac{c_0}{4})\frac{2}{c_0} = -\frac{1}{2}. \tag{B.7}$$

Thus, the current velocity is equal and opposite to the group velocity ($u = -c/2 = -c_g$). More detailed considerations about this problem is given by *Peregrine* (1976), where he shows that wave reflection may also occur.

In order to obtain an order of magnitude estimate, I assume $|\delta_{\mathrm{r,c}}| \ll 1$. Then (B.6) is simplified by applying a Taylor series expansion on the square root expression $g(\delta_{\mathrm{r,c}}) = \sqrt{1 + 4\delta_{\mathrm{r,c}}}$:

$$T|g(\delta_{\mathrm{r,c}})|_{\mathrm{r,c}=0} = 1 + 2\delta_{\mathrm{r,c}} - 2\delta_{\mathrm{r,c}}^2 + \mathcal{O}(\delta_{\mathrm{r,c}}^3). \tag{B.8}$$

Corrected to second-order in $\delta_{\mathrm{r,c}}$, and by using $c = g/\sigma$

$$c = c_0(1 + \delta_{\mathrm{r,c}}),\ \sigma = 2\omega_0. \tag{B.9}$$

For a steady wave train, the conservation of wave action reduces to (2.18) (note $u_0 = 0$)

$$\frac{E}{E_0} = \frac{c_0^2}{c^2(1 + 2\delta_{\mathrm{r,c}})}. \tag{B.10}$$

If considering the wave energy density proportional to the square of the wave amplitude, we obtain the same result as in *Phillips* (1977) (see Eq. [2.7.11] therein). Inserting (B.9), the right hand side becomes

$$\frac{1}{(1 + \delta_{\mathrm{r,c}})^2(1 + 2\delta_{\mathrm{r,c}})}. \tag{B.11}$$

Then, corrected to $\mathcal{O}(\delta_{\mathrm{r,c}}^2)$, (B.10) becomes

$$\frac{E}{E_0} = \frac{1}{(1 + 4\delta_{\mathrm{r,c}})}. \tag{B.12}$$

Finally, I rewrite in terms of $\delta_{\mathrm{r}} = u/c_{g,0}$, and obtain

$$\frac{E}{E_0} = \frac{1}{(1 + 2\delta_{\mathrm{r}})}. \tag{B.13}$$

C Mapping spatio-temporal variability

As highlighted in Section 3.2.1, the ocean dynamics outside Northern Norway change on various temporal scales; the shortest are the semidiurnal tides and the longest belongs to the NwAC and NCC. To map the associated variability in the wave field in space and time, a new diagnostic method was proposed in Paper II. The method involves a spectral analysis of the difference in any field variable between two slightly different models, for the grid points of interest within in the domain. Formally, two energy modes $\mathcal{M}_k$ $(k = 1, 2)$ are computed by integrating a spectrum (note: Not the wave variance spectrum) at different frequency bands in the range $f \in [f_{\mathrm{low,k}}, f_{\mathrm{high,k}}]$ as

$$\mathcal{M}_{k,(i,j)} = \int_{f_{\mathrm{low,k}}}^{f_{\mathrm{high,k}}} P(\Delta X)_{(i,j)}\, df, \tag{C.1}$$

where P is the power spectral density at grid point (i, j) of the difference Δ in the field variable X. The two modes $\mathcal{M}_1, \mathcal{M}_2$ are therefore associated with different temporal scales. Their spatio-temporal variability can be visualized by an RGB-composite, where the red (R) and blue (B) bands are composed by $\mathcal{M}_1$, and the green band (G) by $\mathcal{M}_2$. As a consequence, $\mathcal{M}_1 \gg \mathcal{M}_2$ appear as purple, $\mathcal{M}_1 \ll \mathcal{M}_2$ as green, $\mathcal{M}_1 \sim \mathcal{M}_2 \gg 0$ as white, and $\mathcal{M}_1 \sim \mathcal{M}_2 \simeq 0$ as black. Note that the two modes might be disproportional in magnitude, such that a scaling might be necessary in order to obtain a meaningful plot.

In Paper II, I expected current-induced wave height modulations (i.e., $\Delta X = \Delta H_{\mathrm{s}}$) associated with submesoscale eddies and tides. Therefore, $f_{\mathrm{low,1}}$ corresponded to periods longer than sub-daily, and $f_{\mathrm{high,1}} \sim$ daily, and $[f_{\mathrm{low,2}}, f_{\mathrm{high,2}}]$ was concentrated around the M_2 tidal constituent.

Bibliography

Aarnes, O. J., Ø. Breivik, and M. Reistad (2012), Wave Extremes in the Northeast Atlantic, *Journal of Climate*, *25*(5), 1529–1543. 23

Adler, R. J. (1981), *The Geometry of Random Fields*, John Wiley. 8

Albretsen, J., A. K. Sperrevik, A. Staalstrøm, A. D. Sandvik, F. Vikebø, and L. Asplin (2011), NorKyst-800 report no. 1: User manual and technical descriptions, Tech. Rep. 2, *Tech. rep.*, Institute of Marine Research, Bergen, Norway. 28

Allahdadi, M. N., R. He, and V. S. Neary (2023), Impact of the Gulf Stream on ocean waves, *Deep Sea Research Part II: Topical Studies in Oceanography*, *208*, 105,239. 14

Alpers, W. (1985), Theory of radar imaging of internal waves, *Nature*, *314*, 245–247. 16

Ardhuin, F. (2020), Ocean waves in geosciences, *Book, not official published.* 123

Ardhuin, F., E. Rogers, A. V. Babanin, J.-F. Filipot, R. Magne, A. Roland, A. v. d. Westhuysen, P. Queffeulou, J.-M. Lefevre, L. Aouf, and F. Collard (2010), Semiempirical Dissipation Source Functions for Ocean Waves. Part I: Definition, Calibration, and Validation, *Journal of Physical Oceanography*, *40*(9), 1917–1941. 13, 119

Ardhuin, F., A. Roland, F. Dumas, A.-C. Bennis, A. Sentchev, P. Forget, J. Wolf, F. Girard, P. Osuna, and M. Benoit (2012), Numerical Wave Modeling in Conditions with Strong Currents: Dissipation, Refraction, and Relative Wind, *Journal of Physical Oceanography*, *42*(12), 2101–2120. 2, 9, 12, 14, 16, 17, 33, 36, 120

Ardhuin, F., S. T. Gille, D. Menemenlis, C. B. Rocha, N. Rascle, B. Chapron, J. Gula, and J. Molemaker (2017), Small-scale open ocean currents have large effects on wind wave heights, *Journal of Geophysical Research: Oceans*, *122*(6), 4500–4517. 1, 2, 10, 17, 18, 29

Babanin, A. V., K. N. Tsagareli, I. R. Young, and D. J. Walker (2010), Numerical Investigation of Spectral Evolution of Wind Waves. Part II: Dissipation Term and Evolution Tests, *Journal of Physical Oceanography*, *40*(4), 667–683. 119

Babanin, A. V., A. van der Weshuijsen, D. Chalikov, and W. E. Rogers (2017), Advanced wave modeling, including wave-current interaction, *Journal of Marine Research*, *75*(3), 239–262. 2

Babanin, A. V., W. Rogers, R. De Camargo, M. Doble, T. Durrant, K. Filchuk, K. Ewans, M. Hemer, T. Janssen, B. Kelly-Gerreyn, K. MacHutchon, P. Mccomb, F. Qiao, E. Schulz, A. Skvortsov, J. Thomson, M. Vichi, N. violante carvalho, D. Wang, and I. Young (2019), Waves and Swells in High Wind and Extreme Fetches, Measurements in the Southern Ocean, *Frontiers in Marine Science*, *6*, 361. 2

Barbariol, F., A. Benetazzo, S. Carniel, and M. Sclavo (2015), Space–Time Wave Extremes: The Role of Metocean Forcings, *Journal of Physical Oceanography*, *45*(7), 1897–1916. 34

Barbariol, F., J.-H. G. M. Alves, A. Benetazzo, F. Bergamasco, L. Bertotti, S. Carniel, L. Cavaleri, Y. Y. Chao, A. Chawla, A. Ricchi, M. Sclavo, and H. Tolman (2017), Numerical modeling of space-time wave extremes using WAVEWATCH III, *Ocean Dynamics*, *67*(3), 535–549. 3, 9, 28

Barnes, M. A., and C. Rautenbach (2020), Toward Operational Wave-Current Interactions Over the Agulhas Current System, *Journal of Geophysical Research: Oceans*, *125*(7), e2020JC016,321. 1

Baschek, B. (2005), Wave-current interaction in tidal fronts, in *Rogue Waves: Proc. 14th 'Aha Huliko'a Hawaiian Winter Workshop*, pp. 131–138, Honolulu, HI, University of Hawaii at Manoa. 2, 3, 13, 34, 36

Baschek, B., D. M. Farmer, and C. Garrett (2006), Tidal fronts and their role in air-sea gas exchange, *Journal of Marine Research*, *64*(4), 483–515. 13

Behrens, A., J. Staneva, Ø. Saetra, and P. Janssen (2013), Documentation of a web based source code library for WAM, *Tech. rep.*, Helmholtz-Zentrum Geestacht,Geesthacht, Germany. 28

Benetazzo, A., F. Barbariol, F. Bergamasco, A. Torsello, S. Carniel, and M. Sclavo (2015), Observation of Extreme Sea Waves in a Space–Time Ensemble, *Journal of Physical Oceanography*, *45*(9), 2261–2275. 8

Benetazzo, A., F. Barbariol, P. Pezzutto, J. Staneva, A. Behrens, S. Davison, F. Bergamasco, M. Sclavo, and L. Cavaleri (2021), Towards a unified framework for extreme sea waves from spectral models: rationale and applications, *Ocean Engineering*, *219*, 108,263. 3, 9, 28

Bitner-Gregersen, E. M., O. Gramstad, K. Trulsen, A. K. Magnusson, S. Støle-Hentschel, O. J. Aarnes, and Ø. Breivik (2024), Rogue waves: Results of the ExWaMar project, *Ocean Engineering*, *292*, 116,543. 7

Boccotti, P. (1982), Relations between characteristic sea wave parameters, *Journal of Geophysical Research: Oceans*, *87*(C6), 4267–4268. 8

Boccotti, P. (2000), *Wave Mechanics for Ocean Engineering*, *Elsevier Oceanography Series*, vol. 64, Elsevier, doi:10.1016/S0422-9894(00)80024-0. 8

Breivik, Ø., K. Mogensen, J.-R. Bidlot, M. A. Balmaseda, and P. A. E. M. Janssen (2015), Surface wave effects in the NEMO ocean model: Forced and coupled experiments, *Journal of Geophysical Research: Oceans*, *120*(4), 2973–2992. 37

Bretherton, F. P., and C. J. R. Garrett (1968), Wavetrains in Inhomogeneous Moving Media, *Proceedings of the Royal Society of London. Series A, Mathematical and Physical Sciences*, *302*(1471), 529–554. 12

Bôas, A. B. V., and W. R. Young (2020), Directional diffusion of surface gravity wave action by ocean macroturbulence, *Journal of Fluid Mechanics*, *890*. 17, 33, 36

Bôas, A. B. V., B. D. Cornuelle, M. R. Mazloff, S. T. Gille, and F. Ardhuin (2020), Wave-Current Interactions at Meso- and Submesoscales: Insights from Idealized Numerical Simulations, *Journal of Physical Oceanography*, *50*(12), 3483 – 3500. 10, 17, 36

Børve, E., P. E. Isachsen, and O. A. Nøst (2021), Rectified tidal transport in Lofoten–Vesterålen, northern Norway, *Ocean Science*, *17*(6), 1753–1773. 1, 21

Cavaleri, L., and P. M. Rizzoli (1981), Wind wave prediction in shallow water: Theory and applications, *Journal of Geophysical Research: Oceans*, *86*(C11), 10,961–10,973. 10

Chawla, A., and J. T. Kirby (2002), Monochromatic and random wave breaking at blocking points, *Journal of Geophysical Research: Oceans*, *107*(C7), 4–1–4–19. 13, 14, 17, 121

Christakos, K. (2021), Wind-Generated Waves in Fjords and Coastal Areas, Doctoral thesis, The University of Bergen, accepted: 2021-08-25T11:45:37Z ISBN: 9788230866290. 10

Christensen, K. H., A. K. Sperrevik, and G. Broström (2018), On the Variability in the Onset of the Norwegian Coastal Current, *Journal of Physical Oceanography*, *48*(3), 723–738. 23

Davidson, M. A., T. J. O'Hare, and K. J. George (2008), Tidal Modulation of Incident Wave Heights: Fact or Fiction?, *Journal of Coastal Research*, *24*(sp2), 151–159. 2, 121

Davison, S., A. Benetazzo, F. Barbariol, G. Ducrozet, J. Yoo, and M. Marani (2022), Space-time statistics of extreme ocean waves in crossing sea states, *Frontiers in Marine Science*, *9*. 120

Den norske los (2018), *The Norwegian Pilot Guide—Sailing Directions for the Norwegian coast, Svalbard and Jan Mayen*, The Norwegian Mapping Authority, Stavanger, Norway. 20, 21, 23, 32

Dokken, S. T., and T. Wahl (1995), ERS-1 SAR observations of tidal currents in the Moskenes sound, *FFI rapport 23*, Norwegian Defence Research Establishment. 22

Dokken, S. T., R. Olsen, T. Wahl, and M. V. Tantillo (2001), Identification and characterization of internal waves in SAR images along the coast of Norway, *GRL*, *28*, 2803–2806. 22

Dysthe, K., H. E. Krogstad, and P. Müller (2008), Oceanic Rogue Waves, *Annual Review of Fluid Mechanics*, *40*(1), 287–310. 2, 7, 8

Dysthe, K. B. (2001), Refraction of gravity waves by weak current gradients, *Journal of Fluid Mechanics*, *442*, 157–159. 10, 16, 17

Ellingsen, S. Å., and Y. Li (2017), Approximate Dispersion Relations for Waves on Arbitrary Shear Flows, *Journal of Geophysical Research: Oceans*, *122*(12), 9889–9905. 37

Fedele, F. (2012), Space–Time Extremes in Short-Crested Storm Seas, *Journal of Physical Oceanography*, *42*(9), 1601–1615. 8

Fedele, F., A. Benetazzo, G. Gallego, P.-C. Shih, A. Yezzi, F. Barbariol, and F. Ardhuin (2013), Space–time measurements of oceanic sea states, *Ocean Modelling*, *70*, 103–115. 8

Forristall, G. Z. (1978), On the statistical distribution of wave heights in a storm, *Journal of Geophysical Research: Oceans*, *83*(C5), 2353–2358. 8

Forristall, G. Z. (2000), Wave Crest Distributions: Observations and Second-Order Theory, *Journal of Physical Oceanography*, *30*(8), 1931–1943. 8

Gallet, B., and W. R. Young (2014), Refraction of swell by surface currents, *Journal of Marine Research*, *72*(2), 105–126. 17, 33

Gemmrich, J., and C. Garrett (2012), The Signature of Inertial and Tidal Currents in Offshore Wave Records, *Journal of Physical Oceanography*, *42*(6), 1051 – 1056. 17, 29, 36, 119

Gjevik, B. (2009), *Flo og fjære langs kysten av Norge og Svalbard.*, Farleia Forlag. 19, 21, 22

Gjevik, B., H. Moe, and A. Ommundsen (1997), Sources of the Melstrom, *NAT*, *388*, 837–838. 1, 20, 31

Grachev, A. A., and C. W. Fairall (2001), Upward Momentum Transfer in the Marine Boundary Layer, *Journal of Physical Oceanography*, *31*(7), 1698–1711. 7

Guerber, H. A. (1909), *Myths of the Norsemen - From the Eddas and Sagas*, George G. Harrap and Company Limited. 19

Guillou, N., G. Chapalain, and S. P. Neill (2016), The influence of waves on the tidal kinetic energy resource at a tidal stream energy site, *Applied Energy*, *180*, 402–415. 120

Guimarães, P. V., F. Ardhuin, Y. Perignon, A. Benetazzo, M.-N. Bouin, V. Garnier, J.-L. Redelsperger, M. Accensi, and J. Thomson (2022), Relative current effect on short wave growth, *Ocean Dynamics*. 29, 120

Haakenstad, H., Ø. Breivik, M. Reistad, and O. J. Aarnes (2020), NORA10EI: A revised regional atmosphere-wave hindcast for the North Sea, the Norwegian Sea and the Barents Sea, *International Journal of Climatology*, *40*(10), 4347–4373. 23

Halsne, T., L. Ferrighi, B. Saadatnejad, N. Budewitz, F. Dinessen, L.-A. Breivik, and Ø. Godøy (2019), The Norwegian National Ground Segment; Preservation, Distribution and Exploitation of Sentinel Data, *Data Science Journal*, *18*(1), 61. 27

Hansen, M. W., V. Kudryavtsev, B. Chapron, C. Brekke, and J. A. Johannessen (2016), Wave Breaking in Slicks: Impacts on C-Band Quad-Polarized SAR Measurements, *IEEE Journal of Selected Topics in Applied Earth Observations and Remote Sensing*, *9*(11), 4929–4940. 36

Hasselmann, K., T. Barnett, E. Bouws, H. Carlson, D. Cartwright, K. Enke, J. Ewing, H. Gienapp, D. Hasselmann, P. Kruseman, A. Meerburg, P. Müller, D. Olbers, K. Richter, W. Sell, and H. Walden (1973), Measurements of wind-wave growth and swell decay during the Joint North Sea Wave Project (JONSWAP). 1, 8

Hasselmann, S., and K. Hasselmann (1985), Computations and Parameterizations of the Nonlinear Energy Transfer in a Gravity-Wave Spectrum. Part I: A New Method for Efficient Computations of the Exact Nonlinear Transfer Integral, *Journal of Physical Oceanography*, *15*(11), 1369–1377. 120

Hersbach, H., and J.-R. Bidlot (2008), The relevance of ocean surface current in the ECMWF analysis and forecast system, in *Proc. ECMWF Workshop on Ocean-atmosphere interactions*, vol. 6173, Reading, UK. 119

Hjermann, D. Ø., A. Melsom, G. E. Dingsør, J. M. Durant, A. M. Eikeset, L. P. Røed, G. Ottersen, G. Storvik, and N. C. Stenseth (2007), Fish and oil in the Lofoten–Barents Sea system: synoptic review of the effect of oil spills on fish populations, *Marine Ecology Progress Series*, *339*, 283–299. 1

Ho, A., S. Merrifield, and N. Pizzo (2023), Wave–Tide Interaction for a Strongly Modulated Wave Field, *Journal of Physical Oceanography*, *53*(3), 915–927. 2, 10

Holthuijsen, L. H. (2007), *Waves in Oceanic and Coastal Waters*, Cambridge University Press, doi:10.1017/CBO9780511618536. 1, 9, 119

Holthuijsen, L. H., and H. L. Tolman (1991), Effects of the Gulf Stream on ocean waves, *Journal of Geophysical Research: Oceans*, *96*(C7), 12,755–12,771. 2, 13, 14, 15, 16

Homer (1919), *The Odyssey*, London : W. Heinemann; New York : G.P. Putnam's sons, 1919. 19

Huang, N. E., D. T. Chen, C.-C. Tung, and J. R. Smith (1972), Interactions between Steady Won-Uniform Currents and Gravity Waves with Applications for Current Measurements, *Journal of Physical Oceanography*, *2*(4), 420–431. 13

Hypolite, D., L. Romero, J. C. McWilliams, and D. P. Dauhajre (2021), Surface Gravity Wave Effects on Submesoscale Currents in the Open Ocean, *Journal of Physical Oceanography*, *51*(11), 3365–3383. 37

Irvine, D. E., and D. G. Tilley (1988), Ocean wave directional spectra and wave-current interaction in the Agulhas from the Shuttle Imaging Radar-B synthetic aperture radar, *Journal of Geophysical Research: Oceans*, *93*(C12), 15,389–15,401. 17

Johnson, J. W. (1947), The refraction of surface waves by currents, *Eos, Transactions American Geophysical Union*, *28*(6), 867–874. 14, 16

Kanarik, H., L. Tuomi, J.-V. Björkqvist, and T. Kärnä (2021), Improving Baltic Sea wave forecasts using modelled surface currents, *Ocean Dynamics*, *71*(6), 635–653. 2, 29

Kenyon, K. E. (1971), Wave refraction in ocean currents, *Deep Sea Research and Oceanographic Abstracts*, *18*(10), 1023–1034. 10, 16, 17

Kirby, J. T., and T.-M. Chen (1989), Surface waves on vertically sheared flows: Approximate dispersion relations, *Journal of Geophysical Research: Oceans*, *94*(C1), 1013–1027. 37

Komen, G. J., L. Cavaleri, M. Doneland, K. Hasselmann, S. Hasselmann, and P. A. E. M. Janssen (Eds.) (1994), *Dynamics and Modelling of Ocean Waves*, Cambridge Univeristy Press, doi:10.1017/CBO9780511628955. 12, 27

Krogstad, H. E., J. Liu, H. Socquet-Juglard, K. B. Dysthe, and K. Trulsen (2004), Spatial Extreme Value Analysis of Nonlinear Simulations of Random Surface Waves, pp. 285–295, American Society of Mechanical Engineers Digital Collection, doi:10.1115/OMAE2004-51336. 8

Kudryavtsev, V., M. Yurovskaya, B. Chapron, F. Collard, and C. Donlon (2017), Sun glitter imagery of surface waves. Part 2: Waves transformation on ocean currents, *Journal of Geophysical Research: Oceans*, *122*(2), 1384–1399. 2, 36

Kudryavtsev, V. N., S. A. Grodsky, V. A. Dulov, and A. N. Bol'shakov (1995), Observations of wind waves in the Gulf Stream frontal zone, *Journal of Geophysical Research: Oceans*, *100*(C10), 20,715–20,727. 1, 2

Lai, R. J., S. R. Long, and N. E. Huang (1989), Laboratory studies of wave-current interaction: Kinematics of the strong interaction, *Journal of Geophysical Research: Oceans*, *94*(C11), 16,201–16,214. 13

Lamb, H. (1932), *Hydrodynamics*, 6 ed., Cambridge Mathematical Library. 8

Lavrenov, I. (1998), The wave energy concentration at the Agulhas current off South Africa, *Natural hazards*, *17*(2), 117–127. 2

Lenain, L., and N. Pizzo (2021), Modulation of Surface Gravity Waves by Internal Waves, *Journal of Physical Oceanography*, *51*(9), 2735–2748. 16, 22

Lenain, L., B. K. Smeltzer, N. Pizzo, M. Freilich, L. Colosi, S. Å. Ellingsen, L. Grare, H. Peyriere, and N. Statom (2023), Airborne Remote Sensing of Upper-Ocean and Surface Properties, Currents and Their Gradients From Meso to Submesoscales, *Geophysical Research Letters*, *50*(8), e2022GL102,468. 17, 36

Longuet-Higgins, M. (1952), On the statistical distribution of the heights of sea waves, *Journal of Marine Research*, *11*(3). 7

Longuet-Higgins, M. S., and R. Stewart (1961), The changes in amplitude of short gravity waves on steady non-uniform currents, *Journal of Fluid Mechanics*, *10*(4), 529–549. 11, 13, 14

Longuet-Higgins, M. S., and R. Stewart (1964), Radiation stresses in water waves; a physical discussion, with applications, *Deep-Sea Res II*, *11*(4), 529–562. 11

Longuet-Higgins, M. S., and R. W. Stewart (1960), Changes in the form of short gravity waves on long waves and tidal currents, *Journal of Fluid Mechanics*, *8*(4), 565–583. 11

Longuet-Higgins, M. S., and R. W. Stewart (1962), Radiation stress and mass transport in gravity waves, with application to 'surf beats', *Journal of Fluid Mechanics*, *13*(4), 481–504. 11

Lynge, B. K., J. Berntsen, and B. Gjevik (2010), Numerical studies of dispersion due to tidal flow through Moskstraumen, northern Norway, *Ocean Dyn.*, *60*, 907–920. 1, 19

Mackay, E. B. L., and J. P. Hardwick (2022), Joint Extremes of Waves and Currents at Tidal Energy Sites in the English Channel, American Society of Mechanical Engineers Digital Collection, doi:10.1115/OMAE2022-79348. 36

Malila, M. P., F. Barbariol, A. Benetazzo, Ø. Breivik, A. K. Magnusson, J. Thomson, and B. Ward (2023), Statistical and Dynamical Characteristics of Extreme Wave Crests Assessed with Field Measurements from the North Sea, *Journal of Physical Oceanography*, *53*(2), 509–531. 8

Marechal, G., and F. Ardhuin (2021), Surface Currents and Significant Wave Height Gradients: Matching Numerical Models and High-Resolution Altimeter Wave Heights in the Agulhas Current Region, *Journal of Geophysical Research: Oceans*, *126*(2), e2020JC016,564. 17, 29, 119

Masson, D. (1996), A Case Study of Wave–Current Interaction in a Strong Tidal Current, *Journal of Physical Oceanography*, *26*(3), 359–372. 2, 13, 16, 17, 36

Mathiesen, M. (1987), Wave refraction by a current whirl, *Journal of Geophysical Research: Oceans*, *92*(C4), 3905–3912. 10, 15, 16

McWilliams, J. C. (2016), Submesoscale currents in the ocean, *Proceedings of the Royal Society A: Mathematical, Physical and Engineering Sciences*, *472*(2189), 20160,117. 23

Moe, H., A. Ommundsen, and B. Gjevik (2002), A high resolution tidal model for the area around The Lofoten Islands, northern Norway, *CRS*, *22*, 485–504. 1, 19, 20, 21, 24, 31

Mork, K. A., and Ø. Skagseth (2010), A quantitative description of the Norwegian Atlantic Current by combining altimetry and hydrography, *Ocean Science*, *6*(4), 901–911. 23

Munk, W. H. (1950), Origin and generation of waves, *Coastal Engineering Proceedings*, (1), 1–1. 5

Naess, A. (1985), On the distribution of crest to trough wave heights, *Ocean Engineering*, *12*(3), 221–234. 8

Olabarrieta, M., J. C. Warner, and N. Kumar (2011), Wave-current interaction in Willapa Bay, *Journal of Geophysical Research: Oceans*, *116*(C12). 37

Olabarrieta, M., J. C. Warner, B. Armstrong, J. B. Zambon, and R. He (2012), Ocean–atmosphere dynamics during Hurricane Ida and Nor'Ida: An application of the coupled ocean–atmosphere–wave–sediment transport (COAWST) modeling system, *Ocean Modelling*, *43-44*, 112–137. 29

Ommundsen, A. (2002), Models of cross shelf transport introduced by the Lofoten Maelstrom, *CRS*, *22*, 93–113. 1

Onorato, M., D. Proment, and A. Toffoli (2011), Triggering Rogue Waves in Opposing Currents, *Physical Review Letters*, *107*(18), 184,502. 2

Palmer, T., and A. Saulter (2016), Evaluating the effects of ocean current fields on a UK regional wave model., *Technical Report 612*, UK Met Office, Exeter, United Kingdom. 2, 29

Peregrine, D. H. (1976), Interaction of Water Waves and Currents, in *Advances in Applied Mechanics*, vol. 16, edited by C.-S. Yih, pp. 9–117, Elsevier, doi:10.1016/S0065-2156(08)70087-5. 9, 15, 123

Phillips, O. M. (1977), *The Dynamics of the Upper Ocean*, 2 ed., Cambridge University Press, Cambridge. 11, 123, 124

Phillips, O. M. (1984), On the Response of Short Ocean Wave Components at a Fixed Wavenumber to Ocean Current Variations, *Journal of Physical Oceanography*, *14*(9), 1425–1433. 13, 16, 17, 18, 120

Phillips, O. M. (1985), Spectral and statistical properties of the equilibrium range in wind-generated gravity waves, *Journal of Fluid Mechanics*, *156*, 505–531. 13, 120

Piterbarg, V. I. (1996), *Asymptotic Methods in the Theory of Gaussian Processes and Fields*, *Translations of Mathematical Monographs*, vol. 148. 8

Poe, E. A. (1841), *A descent into the Maelström*, published: Graham's Magazine. 19

Quilfen, Y., and B. Chapron (2019), Ocean Surface Wave-Current Signatures From Satellite Altimeter Measurements, *Geophysical Research Letters*, *46*(1), 253–261. 2, 15, 17

Quilfen, Y., M. Yurovskaya, B. Chapron, and F. Ardhuin (2018), Storm waves focusing and steepening in the Agulhas current: Satellite observations and modeling, *Remote Sensing of Environment*, *216*, 561 – 571. 2

Quinn, B. E., Y. Toledo, and V. I. Shrira (2017), Explicit wave action conservation for water waves on vertically sheared flows, *Ocean Modelling*, *112*, 33–47. 37

Rapizo, H., A. Babanin, O. Gramstad, and M. Ghantous (2014), Wave Refraction on Southern Ocean Eddies, in *19th Australasian Fluid Mechanics Conference,*. 15

Rapizo, H., T. Waseda, A. V. Babanin, and A. Toffoli (2016), Laboratory Experiments on the Effects of a Variable Current Field on the Spectral Geometry of Water Waves, *Journal of Physical Oceanography*, *46*(9), 2695–2717. 16, 120

Rapizo, H., A. V. Babanin, D. Provis, and W. E. Rogers (2017), Current-induced dissipation in spectral wave models, *Journal of Geophysical Research: Oceans*, *122*(3), 2205–2225. 14, 36, 121

Rapizo, H., T. H. Durrant, and A. V. Babanin (2018), An assessment of the impact of surface currents on wave modeling in the Southern Ocean, *Ocean Dynamics*, *68*(8), 939–955. 2, 17, 29, 119, 120

Rascle, N., F. Nouguier, B. Chapron, A. Mouche, and A. Ponte (2016), Surface Roughness Changes by Finescale Current Gradients: Properties at Multiple Azimuth View Angles, *Journal of Physical Oceanography*, *46*(12), 3681 – 3694. 18

Rascle, N., J. Molemaker, L. Marié, F. Nouguier, B. Chapron, B. Lund, and A. Mouche (2017), Intense deformation field at oceanic front inferred from directional sea surface roughness observations, *Geophysical Research Letters*, *44*(11), 5599–5608. 18

Rascle, N., F. Nouguier, B. Chapron, and F. J. Ocampo-Torres (2018), Sunglint images of current gradients at high resolution: Critical angle and directional observing strategy, *Remote Sensing of Environment*, *216*, 786–797. 18, 36

Reistad, M., Ø. Breivik, H. Haakenstad, O. J. Aarnes, B. R. Furevik, and J.-R. Bidlot (2011), A high-resolution hindcast of wind and waves for the North Sea, the Norwegian Sea, and the Barents Sea, *Journal of Geophysical Research: Oceans*, *116*(C5). 28

Ris, R., and L. Holthuijsen (1996), Spectral modelling of current induced wave-blocking, in *Coastal Engineering 1996*, pp. 1247–1254. 13, 121

Rogers, W. E., A. V. Babanin, and D. W. Wang (2012), Observation-consistent input and whitecapping dissipation in a model for wind-generated surface waves: Description and simple calculations, *Journal of Atmospheric and Oceanic Technology*, *29*(9), 1329–1346. 14, 119, 121

Romero, L. (2019), Distribution of Surface Wave Breaking Fronts, *Geophysical Research Letters*, *46*(17-18), 10,463–10,474. 121

Romero, L., L. Lenain, and W. K. Melville (2017), Observations of Surface Wave–Current Interaction, *Journal of Physical Oceanography*, *47*(3), 615–632. 2, 33, 34, 36

Romero, L., D. Hypolite, and J. C. McWilliams (2020), Submesoscale current effects on surface waves, *Ocean Modelling*, *153*, 101,662. 1, 2, 17, 18, 29, 33, 120, 121

Rusu, L., and C. Guedes Soares (2011), Modelling the wave–current interactions in an offshore basin using the SWAN model, *Ocean Engineering*, *38*(1), 63–76. 13

Röhrs, J., and K. H. Christensen (2015), Drift in the uppermost part of the ocean, *Geophysical Research Letters*, *42*(23), 10,349–10,356. 23

Saruwatari, A., D. M. Ingram, and L. Cradden (2013), Wave–current interaction effects on marine energy converters, *Ocean Engineering*, *73*, 106–118. 36

Shchepetkin, A. F., and J. C. McWilliams (2005), The Regional Oceanic Modeling System (ROMS): A split-explicit, free-surface, topography-following-coordinate oceanic model, *JPO*, *9*, 347–404. 28

Smit, P. B., and T. T. Janssen (2019), Swell Propagation through Submesoscale Turbulence, *Journal of Physical Oceanography*, *49*(10), 2615–2630. 15, 17

Spaans, R. (2023), 'My Eyes Have Never Yet Beheld Him.' Demythologising Arctic Sea Monsters in the Poetry of the Norwegian Priest and Fish Merchant Petter Dass (1647–1707), in *Ichthyology in Context (1500–1880)*, pp. 420–453, Brill, doi:10.1163/9789004681187_015, section: Ichthyology in Context (1500–1880). 20

Staneva, J., A. Behrens, and K. Wahle (2015), Wave modelling for the German Bight coastal-ocean predicting system, *Journal of Physics: Conference Series*, *633*, 012,117. 2

Stewart, R. H., and J. W. Joy (1974), HF radio measurements of surface currents, *Deep Sea Research and Oceanographic Abstracts*, *21*(12), 1039–1049. 37

Strand, K., Ø. Breivik, G. Pedersen, F. B. Vikebø, S. Sundby, and K. H. Christensen (2020), Long-term Statistics of Observed Bubble Depth versus Modeled Wave Dissipation, *JGRO*, *125*(2), e2019JC015,906. 28

Støle-Hentschel, S., K. Trulsen, J. C. Nieto Borge, and S. Olluri (2020), Extreme Wave Statistics in Combined and Partitioned Windsea and Swell, *Water Waves*, *2*(1), 169–184. 120

Sun, R., A. B. Villas Bôas, A. C. Subramanian, B. D. Cornuelle, M. R. Mazloff, A. J. Miller, S. Langodan, and I. Hoteit (2022), Focusing and Defocusing of Tropical Cyclone Generated Waves by Ocean Current Refraction, *Journal of Geophysical Research: Oceans*, *127*(1), e2021JC018,112. 33

Tamura, H., T. Waseda, Y. Miyazawa, and K. Komatsu (2008), Current-Induced Modulation of the Ocean Wave Spectrum and the Role of Nonlinear Energy Transfer, *Journal of Physical Oceanography*, *38*(12), 2662–2684. 120

Tamura, H., T. Waseda, and Y. Miyazawa (2009), Freakish sea state and swell-windsea coupling: Numerical study of the Suwa-Maru incident, *Geophysical Research Letters*, *36*(1). 2

Tan, K., L. Xie, P. Bai, Q. Zheng, J. Li, Y. Xu, and M. Li (2023), Modulation Effects of Mesoscale Eddies on Sea Surface Wave Fields in the South China Sea Derived From a Wave Spectrometer Onboard the China-France Ocean Satellite, *Journal of Geophysical Research: Oceans*, *128*(1), e2021JC018,088. 17

Tayfun, M. A. (1980), Narrow-band nonlinear sea waves, *Journal of Geophysical Research: Oceans*, *85*(C3), 1548–1552. 8

Tayfun, M. A., and F. Fedele (2007), Wave-height distributions and nonlinear effects, *Ocean Engineering*, *34*(11), 1631–1649. 8

Toffoli, A., L. Cavaleri, A. V. Babanin, M. Benoit, E. M. Bitner-Gregersen, J. Monbaliu, M. Onorato, A. R. Osborne, and C. T. Stansberg (2011), Occurrence of extreme waves in three-dimensional mechanically generated wave fields propagating over an oblique current, *Natural Hazards and Earth System Sciences*, *11*(3), 895–903. 2

Tolman, H. L. (1990a), Wind wave propagation in tidal seas, phdthesis, Delft University of Technology. 2, 16

Tolman, H. L. (1990b), The Influence of Unsteady Depths and Currents of Tides on Wind-Wave Propagation in Shelf Seas, *Journal of Physical Oceanography*, *20*(8), 1166–1174. 10

Vagle, S., and D. Farmer (1998), A comparison of four methods for bubble size and void fraction measurements, *IEEE Journal of Oceanic Engineering*, *23*(3), 211–222. 28

Verne, J. (1891), *Vingt Mille Lieues sous les mers*, published: Magasin d'éducation et de récrátion. 19

Vikebø, F., C. Jørgensen, T. Kristiansen, and Ø. Fiksen (2007), Drift, growth, and survival of larval Northeast Arctic cod with simple rules of behaviour, *Marine Ecology Progress Series*, *347*, 207–219. 1

Vincent, C. E. (1979), The Interaction of Wind-Generated Sea Waves with Tidal Currents, *Journal of Physical Oceanography*, *9*(4), 748 – 755. 2, 13, 16

Wang, D., H. Wijesekera, E. Jarosz, W. Teague, and W. Pegau (2016), Turbulent diffusivity under high winds from acoustic measurements of bubbles, *JPO*, *46*(5), 1593–1613. 28

Wang, D. W., A. K. Liu, C. Y. Peng, and E. A. Meindl (1994), Wave-current interaction near the Gulf Stream during the Surface Wave Dynamics Experiment, *Journal of Geophysical Research: Oceans*, *99*(C3), 5065–5079. 16

Wang, P., and J. Sheng (2018), Tidal Modulation of Surface Gravity Waves in the Gulf of Maine, *Journal of Physical Oceanography*, *48*(10), 2305–2323. 10, 14, 29, 36

Westhuysen, A. J. v. d. (2012), Spectral modeling of wave dissipation on negative current gradients, *Coastal Engineering*, *68*, 17 – 30. 121

Whitham, G. B. (1965), A general approach to linear and non-linear dispersive waves using a Lagrangian, *Journal of Fluid Mechanics*, *22*(2), 273–283. 12

WW3DG (2019), User manual and system documentation of WAVEWATCH III R version 6.07, college Park, MD, USA, 465 pp. + Appendices. 12

Ying, L. H., Z. Zhuang, E. J. Heller, and L. Kaplan (2011), Linear and nonlinear rogue wave statistics in the presence of random currents*, *Nonlinearity*, *24*(11), R67. 15

Zippel, S., and J. Thomson (2015), Wave breaking and turbulence at a tidal inlet, *Journal of Geophysical Research: Oceans*, *120*(2), 1016–1031. 120

Zippel, S., and J. Thomson (2017), Surface wave breaking over sheared currents: Observations from the Mouth of the Columbia River, *Journal of Geophysical Research: Oceans*, *122*(4), 3311–3328. 37

Graphic design: Communication Division, UiB / Print: Skipnes Kommunikasjon AS

uib.no

ISBN: 9788230849453 (print)
9788230864166 (PDF)